Department of Exploration Geophysics

INVERSION FOR THE ELASTIC PARAMETERS OF LAYERED TRANSVERSELY ISOTROPIC MEDIA

Ruiping Li

This thesis is presented as part of the requirements for the award of the Degree of Doctor of Philosophy of Curtin University of Technology

September 2002

Declaration

This thesis contains no material which has been accepted for the award of any other degree or diploma in any university.

To the best of my knowledge and belief this thesis contains no material previously published by any other person except where due acknowledgment has been made.

Signature: …….

Date: ……...

DEDICATION

To my father Professor Laizheng Li for his eternal encouragement.

To my husband Roger Luo, and my lovely daughters Jingjing and Joanne.

ABSTRACT

In most cases of seismic processing and interpretation, elastic isotropy is assumed. However, velocity **anisotropy** is found to exist in most subsurface media. Hence, there exists a fundamental inconsistency between theory on the one hand, and practice on the other. If not recognised, this can invalidate interpretation of seismic data.

In this thesis, inversion methods for elastic parameters are developed to quantify the degree of velocity anisotropy of multi-layered transversely isotropic media. This primarily involves examining the velocity fields of layered media using anisotropic elastic wave propagation theory, and developing inversion programs to recover elastic parameters from those velocity fields. The resolved elastic parameter information is used in carrying out further studies on the effects of seismic anisotropy on normal moveout (NMO). Mathematical analyses, numerical simulations, and physical modelling experiments are used in this research for verification purposes before application to field survey data.

Numerical studies show the transmission velocity field through layered media appears to be equivalent to that through a single-layered medium, within the practical offset limits in field surveys. The elastic parameters, which describe the property of such equivalent single-layered media, can be used as apparent elastic parameters to describe the collective mechanical property of the layered media. During this research, Snell's law was used in ray tracing to determine ray paths through the interface between any two component layers.

By analyzing the signals recorded by any receiver in a walkaway VSP survey, the apparent transmission velocity field for the layered media above this receiver depth was inverted. Software was developed to recover the apparent elastic parameters for the layered media above this receiver depth using the transmission velocity field as input.

Based on a two-layered model, another method was developed to recover the interval elastic parameters for an individual layer of interest, using the signals recorded by receivers on the upper and lower surfaces of this layer.

The recovered elastic parameters may be considerably different from the real values if a transversely isotropic medium with a tilted symmetry axis (TTI) is treated as a transversely isotropic medium with a vertical symmetry axis (VTI). A large angle of tilt of the symmetry axis significantly influences the recorded velocity field through the medium. An inversion program was written to recover the value of the tilt angle of a TTI medium, and the elastic parameters of the medium.

Programs were also developed to combine information from P, SV, and SH-waves in an inversion procedure. This capability in inversion programs enables us to use the additional information provided by a multi-component VSP survey to obtain accurate estimates of the elastic parameters of geological formations.

Software testing and development was carried out on numerically generated input data. Up to 10 milliseconds of random noise in travel time was added to the input to confirm the stability of the inversion software. Further testing was carried out on physical model data where the parameters of the model were known from direct measurements. Finally the inversion software was applied to actual field data and found to give plausible results.

In software testing in the physical modelling laboratory, other practical problems were encountered. System errors caused by the disproportionately large size of the transducers used affected the accuracy of the inversion results obtained. Transducer performance was studied, and it was found that reducing the size of transducers or making offset corrections would decrease the errors caused by the disproportionately large transducer dimensions.

In using the elastic parameters recovered, it was found that the elastic parameter d significantly influences the seismic records from a horizontal reflector. The normal moveout velocity was found to show variations from the zero-offset normal moveout velocity depending on the value and sign of elastic parameter d. New approximate

expressions for anisotropic normal moveout, phase and ray velocity functions at short offsets were developed. The value of anisotropic parameter d was found to be the major factor controlling these relations. If the recovered parameter d has a large negative value, analytical and numerical studies demonstrated that the new expression for moveout velocity developed herein should be used instead of Thomsen's normal moveout equation.

ACKNOWLEDGMENTS

I wish to express my thanks to all those who have contributed in any way towards the completion of this thesis:

I am very grateful to my supervisors Professor Norman F. Uren, and Dr. Partrick Okoye for their valuable guidance, fruitful suggestions, encouragement and friendship towards my PhD thesis accomplishment. Special gratitude goes to Professor Norman F. Uren for his patient guidance and critical instruction during my thesis preparation. Thanks also go to Professor John A. McDonald, Chairman of my PhD supervising panel, for stimulating discussions and constructive suggestions during the period of my PhD research.

I am pleased to have worked in a friendly environment with all staff and graduate students in the Department of Exploration Geophysics. In particular, I am sincerely grateful to Dr. Milovan Urosevic for his constructive discussions and help with field seismic data. He made coal field data available that allowed me to test my inversion programs. I thank Dr. Bruce Hartley for his help with computer programming and laboratory experiments. I also thank Mr. Murray Hill and Mr. Robert Verstandig for their help in accessing computing facilities. I acknowledge Woodside Petroleum Ltd. for allowing me to use their field petroleum data from the Timor Sea.

I particularly thank my husband Roger. He was the first person to read most of my thesis drafts. His correction of language problems for my thesis is highly appreciated.

This project was financially supported by the Australian Postgraduate Award with Stipend (APAWS), and partially supported by a grant from the Australian Society of Exploration Geophysicists (ASEG) Research Foundation. I also acknowledge Australian Petroleum Cooperative Research Centre (APCRC), Curtin Reservoir Geophysics Consortium (CRGC), and Australian Federation of University Women (WA) for their financial support for my project. I thank these organizations very much.

TABLE OF CONTENTS

LIST OF TABLES

LIST OF FIGURES

CHAPTER 1

INTRODUCTION

Seismic is sound in rocks. The basic technique of seismic exploration geophysics consists of emitting artificially generated seismic waves, which propagate through the Earth, and recording the arrivals from the source with a set of geophones. From the recorded travel times and the velocities of seismic waves, the shapes and characteristics of underground structures may be found to assist us to predict the presence or absence of petroleum or minerals. In the application of geophysical methods to petroleum exploration, the seismic reflection method and VSP (Vertical Seismic Profiling) are amongst the most commonly used techniques.

In most seismic processing and interpretation cases, we usually assume that a medium has the same physical properties regardless the direction of measurement, i.e., **isotropy**. However, **anisotropy** is found to exist in many subsurface media (Levin, 1978; Jolly, 1956; Jones and Wang, 1981), and their properties such as seismic velocity *do* have a dependence on direction. Ignoring anisotropy may introduce erroneous seismic imaging in some cases (e.g., Banik, 1984; Ensley, 1989; Urosevic, 2000).

1.1 Introduction

According to Sheriff's definition (Sheriff, 1991), seismic anisotropy is the "variation of seismic velocity depending on the direction in which it is measured".

When anisotropy is present, errors in processing and imaging procedures may be introduced. Anisotropy may cause a departure from hyperbolic moveout in CDP (common-depth-point) gather reflection curves. Incorrect velocity determination will cause erroneous depth estimations (Crampin and Radovich, 1982). The velocities estimated from common midpoint gathers and well logs may show mismatches (Levin, 1978, and 1979). Dip moveout (DMO) may not be able to correct the reflector point dispersal phenomenon (Uren et al., 1990a). The spatial resolution in

an anisotropic medium may be affected by its degree of anisotropy (Okoye, 1994). The undetected presence of anisotropy could introduce errors in interpretation issues, such as the definition of subsurface lithology.

The detection of the presence of anisotropy, and its degree, is significant in the inversion of seismic survey data and the creation of seismic depth images. Measures of the degree of anisotropy can also be used as a good discriminator of lithology, and in fracture detection. For example, Larner and Cohen (1993) improved the quality of seismic sections by applying anisotropic corrections. Uren et al. (1990b) made NMO (normal moveout) corrections for elliptically anisotropic media. Urosevic (2000) used anisotropy as an important aid in determining fracture direction.

Three main types of seismic anisotropy in sedimentary rocks have been reported so far, and they are transverse isotropy, orthorhombic anisotropy, and monoclinic anisotropy (Ebrom and Sheriff, 1992).

Transverse isotropy is defined as having the same property (e.g. velocity) when measured within a plane that is normal to an axis, but having a different value when measured at some other angle to that axis (Levin, 1990). This axis is a direction, designated as the symmetry axis. If the individual layer thickness is much less than the wavelength of the passing seismic wave, horizontally bedded fine-layered sedimentary rocks can be modelled as transversely isotropic media with vertical axes of symmetry (VTI) (Postma, 1955; Backus, 1962). A single parallel set of planar vertical cracks will often be modelled as a transversely isotropic medium with a horizontal symmetry axis (HTI) (Winterstein, 1990).

In the top few kilometres of the upper mantle beneath oceans and continents, anisotropy principally results from a thin layer of aligned sequences (Crampin et al., 1984). Around a petroleum reservoir of interest, sandstones, shales, or shale-rich sequences generally exhibit transverse isotropy due to their layered characters. Transverse isotropy is chosen as the focus of this research because of its widespread occurrence in the sedimentary rocks commonly encountered in oil exploration.

Many exploration geophysicists have worked on transverse isotropy, for example, Geoltrain (1988), Crampin (1986), Helbig (1984, 1994), Winterstein (1990), Uren (1989), Uren et al. (1990a, 1990b, 1991), Thomsen (1986, 1993), Tsvankin (1996, 1997), Okoye (1994). Thomsen (1986) proposed a convenient five-parameter model to describe seismic wave propagation in a transversely isotropic medium. This model has been widely used in research into transverse isotropy.

1.2 Problem Definition

For a transversely isotropic medium, we need five elastic parameters (instead of 21 for the general anisotropic form, or 2 for isotropy) to describe wave propagation (White, 1965; Helbig, 1984; Thomsen, 1986), due to its dependence on direction. Using these five elastic parameters or stiffness coefficients, wave propagation through a transversely isotropic medium may be specified (Thomsen, 1986).

The elastic parameters of a stratified multi-layered medium with thin individual layers can be expressed in terms of thickness-weighted averages of functions of the elastic parameters of its constituents (Helbig and Schoenberg, 1987). However, the thickness of sedimentary rock layers may well be much greater than a seismic wavelength. Structures composed of transversely isotropic layers or of isotropic layers with the thickness of each of the component layers far greater than the wavelength, need further examination. Okoye et al. (1997) directly extended the results for layered models with thin layers to layered models with thicker layers. They presumed an effective elastic parameter to be a weighted average value of the individual layer parameters for a multi-layered model in the physical modelling laboratory, but did not examine the applicability of this assumption. Actually, we do not know whether the overall velocity field of such a model is equivalent to that for a single transversely isotropic medium. The specific contribution to the values of the apparent elastic parameters of a composite thick layer model from each layer's parameters is uncertain.

The velocity field of wave propagation through a multi-layered medium with thick individual layers needs to be examined. After obtaining the overall velocity field, we need to ask ourselves:

- *Can we treat a multi-layered medium with thick components as a single-layered transversely isotropic medium?*
- *Can we obtain average or apparent elastic parameters which adequately represent a multi-layered model?*

Since the major task of geophysical surveys is to understand or make quantitative statements about a subsurface target, inversion for the elastic parameters of sedimentary rocks from observations is of great interest to us. This is the main goal of this research. A brief review of some inversion methods for the determination of elastic parameters follows.

Elastic parameter recovery

One method of measuring the elastic parameters of a transversely isotropic medium is from slowness surfaces. A slowness surface is defined as "the surface obtained by taking the reciprocals of all the points on the phase velocity surface" (Sheriff, 1991). Hsu and Schoenberg (1991) recovered the polarisation and slowness surfaces for P and SV-waves near the receiver region by measuring the travel time differences between adjacent sources and receivers. By best fitting the polarisation and slowness surfaces from these observations, the elastic parameters for the region around the receivers were successfully determined. Horne and Leaney (2000) also inverted the elastic parameters from the polarization and the slowness components in a walkaway VSP experiment shot in the Java Sea region. According to Kebaili et al. (1996), assumptions were made that the region between receivers was homogeneous, the borehole was vertical while the surface was horizontal. However, this method may not be effective if such a region is heterogeneous, and parameter values change within the region between the receivers. The effects due to the deviation of the borehole from the vertical or of the topography of the surface need careful correction. For a thin layer interval, the error in the determination of slowness,

which is inversely proportion to the layer's thickness, may also be too great to obtain an accurate measurement (Kebaili et al., 1996).

Non-hyperbolic reflection moveout has been used to invert for the elastic parameters of a transversely isotropic medium. A series of papers has been published in this area, e.g. Tsvankin and Thomsen (1994, 1995), Ball (1995), Tsvankin (1996, 1997), Alkhalifah and Tsvankin (1995), Alkhalifah et al. (1996), Alkhalifah (1997), Grechka et al. (1999). The accuracy of inversion results "depends largely on the departure of the moveout from hyperbolic and its sensitivity to the estimated parameters" (Alkhalifah, 1997).

The elastic parameters of a transversely isotropic medium may also be measured in a laboratory using ultrasonic transmission experiments (e.g., Dellinger and Vernik, 1994; Vestrum, 1994; Vernik and Nur, 1992; Lo et al., 1986; Jones and Wang, 1981). Conventionally, measurements are made on sets of cylindrical cores cut at angles of $0°$, $45°$ and $90°$ to the symmetry axis, with the core width and height being normally several centimetres. The elastic parameters are obtained by analysing the travel times in these three directions. As pointed out by Thomsen (1986), errors in measuring velocities will be great, because the sample needs to be cut accurately and its heterogeneity (as distinct from anisotropy) also becomes significant in small samples. The errors in these three velocity measurements will also result in cumulative errors in the determination of parameters as discussed by Thomsen (1986).

Okoye et al. (1996) developed a P-wave inversion method for a single-layered VTI model. They used large numbers of observations in the inversion process. Their inversion program recovered some of the elastic parameters from seismic P-wave transmission experiments, while fixing other parameters as presumed values. Their approach works in the laboratory for a one-layered model, but it is hard to apply to real walkaway VSP survey data because they required a value for horizontal velocity. Obviously there is difficulty in obtaining horizontal velocity information from layered media in the field, and more parameters than they studied need to be recovered from the survey data.

Layered media may not be horizontal, but may have angles of dip from the horizontal direction. If so, the symmetry axis may not be vertical, i.e. it may have an angle of dip or tilt from the vertical direction (Urosevic, 2000). Such a medium will be termed a tilted transversely isotropic (TTI) medium having a tilted symmetry axis. Knowledge of the angle of inclination of the symmetry axis is very important in understanding the fine structure of rocks, such as fracture orientation or local bedding directions. There is a need to develop an inversion procedure to directly recover the angle of tilt of the symmetry axis from observed velocity field measurements.

S-waves convey additional information about the anisotropic properties of rocks, and cannot be ignored (Crampin, 1986). S-waves may not exist within the pore fluids in rocks, but P-waves commonly do. "The P-waves preferably respond to gross velocity structure (global information about geology), while S-waves carry information about 3D structure along the ray path (local information)" (Urosevic, 1985). P and S-waves "can provide much more information about a reservoir than can be provided by either alone" (Caldwell, 1999). There is a need to develop an inversion procedure that recovers the elastic parameters of a transversely isotropic medium from the velocity fields of more than one wave type, in order to make use of the additional information in these recordings.

From the above discussions, there is a need to examine anisotropic wave behavior in multi-layered subsurface media, and to develop inversion methods for the detection and quantification of anisotropy in layered media.

In the proposed research, both forward and inverse problems will be studied. Forward modelling is an essential step in the study of the behavior of transverse isotropy. With a good knowledge of seismic wave propagation in transversely isotropic media, it should be possible to develop inversion methods to recover the elastic parameters. The inverse problem is substantially harder than its corresponding forward problem. As stated by Menke (1989), there are many different solutions to inverse problems, and there are different criteria by which the goodness of those solutions can be judged. The determination of the anisotropic properties of a subsurface target — the inverse problem — is ambiguous, and they

can only be estimated. The solution to an inverse problem may be non-unique and uncertain. Every bit of relevant information must be used to determine the most accurate image of a target structure in an attempt to reduce ambiguity.

To be of practical use, an iterative inversion program must be stable, convergent, and efficient. For a set of measurement data, convergence is a common problem one may come across. The inversion program should avoid any repeated iteration with which no further improvement is made for the trial parameters. Any result from an inversion program does not mean we have solved this inversion problem. The inversion result only suggests possible best-fit parameters for the estimated model. Verification procedures should be carried out to see whether the estimated model is likely or reasonable.

A practical inversion method also needs to be applicable to numerical simulation experiments, laboratory experiments and field walkaway VSP surveys. Applicability will be a key issue for the development of inversion methods in this thesis.

If the elastic parameters of a transversely isotropic medium are correctly estimated, a velocity model describing seismic wave transmission can be determined. Then, for example, we should be able to use the estimated elastic parameters to make moveout corrections in seismic data processing. For a seismic surface survey, Thomsen (1986) derived an equation for zero-offset NMO velocity for transverse isotropy based on values of the elastic parameters. This equation has been used as an NMO velocity for short offsets (Tsvankin, 1996; Alkhalifah et al., 1996). As it is an approximation when used in this way, the accuracy of this equation for short offsets needs to be examined. Okoye et al. (1998) showed experimentally that the accuracy and the validity of this NMO equation for short offsets depends on the nature and the degree of anisotropy prevailing in a given sedimentary area. Further theoretical studies and numerical analysis are needed.

The ability to quantify the degree of subsurface velocity anisotropy and incorporate this in moveout corrections should lead to a more accurate data interpretation and an improved seismic resolution. This should not only be of economic importance to the

drilling industry, but also should be useful in reservoir volume estimations on which drilling decisions are made.

1.3 Research Proposals

It is proposed to:

- Examine the velocity field of waves propagating through multi-layered media, using elastic wave propagation theory.
- Develop inversion methods to recover the elastic parameters of layered media from measured velocity fields.
- Test inversion methods using the data from numerical simulation experiments, physical modelling experiments and field walkaway VSP surveys.
- Incorporate the recovered elastic parameters into moveout corrections of numerical seismic data at short offsets.

Because "the nature of depositional processes tends to produce transverse isotropy with a vertical symmetry axis in undisturbed, horizontal, plane-layered sedimentary rocks" (Jakobsen and Johansen, 2000), this research will be mainly limited to horizontally layered transversely isotropic media. For multi-layered media, the individual layers will be isotropic media or transversely isotropic media with a vertical symmetry axis. However, for recovering the apparent elastic parameters, the research will extend to transversely isotropic media with a tilted symmetry axis. Only the simplest case — the two-dimensional case with the seismic line along the dip direction — will be studied.

Four approaches will be adopted to carry out this proposed research:

- *theoretical analysis,*
- *computer simulation experiments,*
- *physical modelling experiments, and*
- *field seismic surveys.*

The transmission and the reflection of seismic waves in transversely isotropic media is not as simple as that in isotropic media. The analytical method to be applied will

involve using Snell's law (Sheriff, 1991) and the exact elastic wave equations (Musgrave, 1970; Thomsen, 1986) to determine a velocity field and deduce approximate expressions for the moveout velocity at short-offsets. The mathematical formulae for wave propagation are important tools for describing the anisotropic nature of sedimentary rocks.

Because of the mathematical complexity in anisotropic media, it is hard to deduce explicit expressions for seismic wave propagation through the interface between layered transversely isotropic media. Numerical modelling experiments will be employed to carry out quantitative analysis in wave propagation. Furthermore, the inversion methods that will be developed in this research will be tested first on numerical modelling data before being applied to a field survey. Validation of methods will then be possible, as the inversion results should be consistent with the known modelling parameters.

Physical modelling is a useful tool for studying seismic wave propagation in anisotropic models. The frequency of the ultrasonic sources used in the laboratory (around 1 MHz) is much higher than that in the field (around 10 – 100 Hz) (Walton, 1996). Scaling factors will need to be used in the laboratory to make the scaled frequency utilized lie within the range of that expected in actual fieldwork. Physical modelling experiments will be used for trials and testing of inversion software.

Real field data will be used to assess whether the inversion methods that will be developed in this research are applicable in practice. In applying inversion methods to seismic shot records, they should provide plausible estimates of the elastic parameters for a survey area.

1.4 Outline of the Thesis

In Chapter 2, the theory of seismic wave propagation is reviewed. Some examples of seismic waves transmitted through sedimentary rocks will be described.

In Chapter 3, the overall velocity field of multi-layered models composed of transversely isotropic media or isotropic media will be numerically examined. An inversion method will be developed to recover the apparent elastic parameters from P, SV, and SH-wave transmission velocity fields for a layered medium.

In Chapter 4, a new method will be presented to recover the interval elastic parameters of a layer of interest. The method will provide a useful tool to estimate the elastic parameters of a layer of interest.

In Chapter 5, the inversion methods developed in Chapters 3 will be applied to physical modelling experiments. The effects of transducer size in the laboratory will be studied through both physical modelling experiments, and numerical simulation experiments.

In Chapter 6, the inversion methods developed in Chapters 3 and 4 will be applied to coal and petroleum seismic field data.

In Chapter 7, recovered elastic parameters will be used to apply moveout corrections at short offsets. P-wave propagation behavior at small offsets will be examined analytically. The applicability of Thomsen's normal moveout equation will also be studied.

In Chapter 8, the major outcomes of this research will be reviewed and recommendations for further study will be given.

CHAPTER 2
THEORETICAL REVIEW

Inversion for the elastic parameters of layered transversely isotropic media is the major topic of this research. Before we begin the research, a theoretical review of inversion theory and wave propagation through a transversely isotropic medium is appropriate for those aspects that have a bearing on the proposed research.

In this chapter, general concepts of forward and inverse problems will be described first. A brief description of the relevant theory of seismic wave propagation that is involved in this research will also be given. The fundamental equations, which will be used in later chapters, are listed in this chapter. For reason of clarity, wave propagation equations using direction cosines will be derived here. Some examples of wave propagation through real sedimentary rocks will be given in this chapter to provide a realistic picture of anisotropy.

2.1 Forward and Inverse Theory

According to Menke (1989), forward theory is defined as "the process of predicting the results of measurements (predicting data) on the basis of some general principle or model and a set of specific conditions relevant to the problem at hand". Inverse theory addresses the reverse problem: "starting with data and a general principle or model, it determines estimates of the model parameters". The procedures for solving an inverse problem invariably incorporate the procedures of solving a forward problem. Figure 2.1 offers a view of the forward and inverse problems. Non-linear inversion normally involves an iterative convergence process. The estimated model from the inversion may differ from the true model. "It is essential to somehow quantify the error between the estimated model and the true model" (Scales and Snieder, 2000).

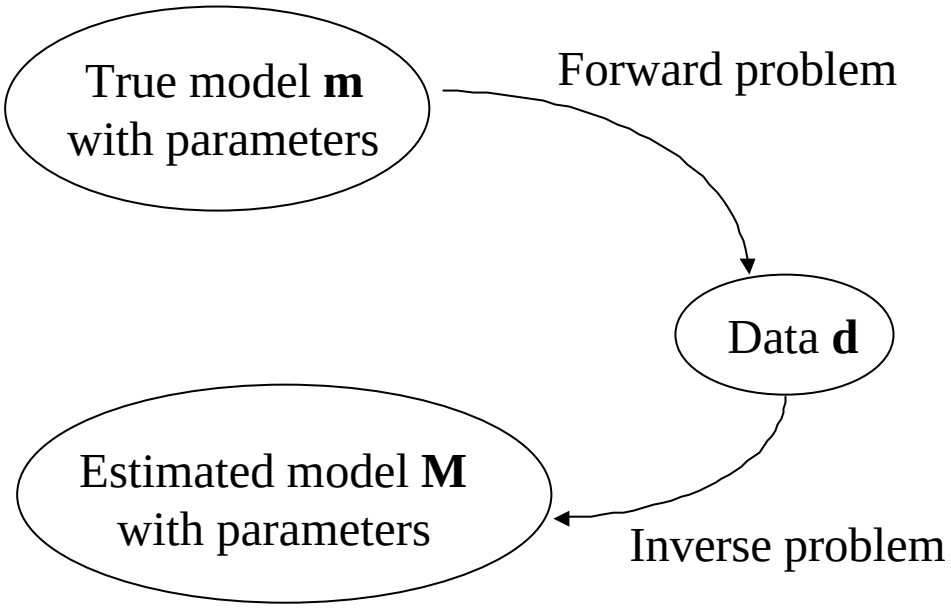

Figure 2.1 A view of inverse problems. The solution to the forward problem is unique. However, the solution to the inverse problem is non-unique. It is quite possible that the estimated model **M** differs from the true model **m**, though forward modelling of both will generate data **d**.

Inversion methods to obtain the elastic parameters of transversely isotropic media from the measured velocity field are the major focus of this research. To solve these inversion problems, we should examine the effects of elastic parameters on the seismic velocity field. That is, we must consider the forward problem as an essential part of the inverse problem.

Inversion procedure

The mathematical relationships for seismic wave propagation through anisotropic media are generally non-linear. An iterative procedure is normally used when solving such inversion problems.

For an observational velocity field, we select an estimated model. Using guessed parameters, we obtain a calculated velocity field using forward theory. We then find the differences between the calculated velocity field and that from observations. These differences are then used to update the model parameters to provide a better estimate of the correct values. The procedure then goes back again to calculate the velocity field with the new model parameters and do the comparison once more. Such iteration steps keep going on until the difference between the calculated velocity field and that from observation reaches an acceptable minimum. The procedure is then concluded to give finally these best estimates of the elastic parameters.

In practice, there are three ways to terminate the iteration circle and output the inversion result, as follows. One is when the differences between the observed and calculated velocity fields change by a very small value from the previous iteration. Another is when the increment values in the model parameters are very small. In these two cases, we cannot improve the best-fitting parameters very much even if we continue the iteration. Finally, if the iteration has been running a large number of times, it must be compulsorily stopped to avoid a useless long time running without convergence.

Error analysis

The velocity error between the observed and calculated velocity field for each iteration may be simply defined as the average error: $\Delta = \sum_{i=1}^{n} \frac{\left| v_{gcal}(i) - v_{gobs}(i) \right|}{n}$, or the relative error: $\Omega = \frac{1}{n} \sum_{i=1}^{n} \frac{\left| v_{g}(i) - v_{gobs}(i) \right|}{v_{gobs}(i)}$. Here, $v_{gcal}(i)$ and $v_{gobs}(i)$ represent the calculated velocity field and the observations.

Once we obtain an inversion result, the uncertainties in the model parameters can be calculated from the diagonal elements of the covariance matrix (Press et al., 1992a; Bevington, 1969).

Result analysis

The iteration procedure may converge on a set of parameters that differ from the true parameters. According to Tarantola (1987), for a non-linear model, "there is no warranty that the maximum likelihood point is unique, or that a given point which is a local maximum, is the absolute maximum". It should also be pointed out that the observation data are subject to measurement errors. "Typical data never exactly fit the model that is being used, even when the model is correct. We need the means to assess whether or not the model is appropriate" (Press et al., 1992a). A verification procedure needs to be carried out after we obtain the inversion solution.

The approach *"chi-by-eye"* may be used to find a fit which is acceptable if a graph of the data and that calculated from the recovered model looks good (Press et al., 1992a). The calculated velocity field, computed from the estimated elastic parameters, should be compared with the observational velocity field. Agreement between these two velocity fields indicates that the estimated model is a suitable model to describe the velocity field of the observation area. If the model is an unlikely match to the data, then the estimated model is probably not the right one, and the recovered elastic parameters are probably inappropriate.

It is also possible that the iteration procedure may not converge at all. The divergence of the inversion process may suggest that a wrong model may have been used in the inversion. For example, if we inaccurately assume transverse isotropy for the survey region which actually has complex fracturing and heterogeneity, the inversion process may not provide any suitable result.

2.2 Seismic Wave Propagation

Named for Robert Hooke (1635-1703), an English physicist, Hooke's law was formulated in 1660 (Love, 1927). When seismic waves propagate through rocks, mechanical displacements in the media are in accord with Hooke's law. Provided the stress is below a certain limiting value, the "elastic limit", the strain is recoverable, and the stress is linearly dependent on the strain. For infinitesimal displacement u_i, Hooke's law is given as follows (Nye, 1993):

$$s_{ij} = c_{ijkl} e_{kl} . \tag{2.1}$$

Where, e_{kl} is the strain tensor:

$$e_{kl} = \frac{1}{2}\left(\frac{\partial u_k}{\partial x_l} + \frac{\partial u_l}{\partial x_k}\right), \tag{2.2}$$

and s_{ij} is the stress tensor. The stress, as well as the strain, is a symmetric tensor ($s_{ij} = s_{ji}$, $e_{ij} = e_{ji}$). c_{ijkl} represents the stiffness tensor. There is a maximum of $3^4 = 81$ stiffness constants. These stiffness coefficients are also symmetric ($c_{ijkl} = c_{ijlk} = c_{jikl} = c_{klji}$). As a consequence, there are only 21 independent stiffness constants. Using the Voigt recipe (Musgrave, 1970; Nye, 1993), the fourth-order stiffness tensor can be rewritten as a second-order symmetric matrix:

$$c_{ijkl} \Rightarrow c_{mn},$$

where,

ij	or	kl	:	11	22	33	32=23	31=13	12=21
↓		↓		↓	↓	↓	↓	↓	↓
m		n		1	2	3	4	5	6

The equation of wave propagation then has the form:

$$c_{ijkl}\frac{\partial^2 u_k}{\partial x_l \partial x_j} - r\frac{\partial^2 u_i}{\partial t^2} = 0. \tag{2.3}$$

Assume a plane-wave solution for equation 2.3 as:

$$u_k = Ap_k \exp[iw(\frac{n_l}{v_p}x_l - t)] = Ap_k \exp[iw(s_l x_l - t)], \tag{2.4}$$

where:

A is the amplitude factor,

p_k is the unit polarisation vector, $p_k = (p_1, p_2, p_3)$,

w is angular frequency,

v_p is the phase velocity, a vector describing the expanding speed of wavefronts,

n_l is the unit velocity direction vector,

s_l is defined as the slowness vector:

$$s_l = \frac{n_l}{v_p}. \tag{2.5}$$

The direction of the slowness vector is the same as that of phase velocity, i.e. the wavefront normal.

Inserting equation 2.4 into equation 2.3, we obtain:

$$\left(c_{ijkl}n_l n_j - r{v_p}^2 d_{ik}\right)p_k = 0. \tag{2.6}$$

Here,

The above equation can be re-written as the Kelvin-Christoffel equation (Musgrave, 1970):

$$\begin{bmatrix} \Gamma_{11} - rv_p^2 & \Gamma_{12} & \Gamma_{13} \\ \Gamma_{21} & \Gamma_{22} - rv_p^2 & \Gamma_{23} \\ \Gamma_{31} & \Gamma_{32} & \Gamma_{33} - rv_p^2 \end{bmatrix}\begin{bmatrix} p_1 \\ p_2 \\ p_3 \end{bmatrix} = 0. \tag{2.7}$$

Here, the Kelvin-Christoffel stiffnesses are defined as:

$$\Gamma_{ik} = c_{ijkl}n_l n_j. \tag{2.8}$$

For non-zero solutions of p_k, the determinant of the above equation should be zero. This is the eigenvalue equation:

$$\begin{vmatrix} \Gamma_{11} - rv_p^2 & \Gamma_{12} & \Gamma_{13} \\ \Gamma_{21} & \Gamma_{22} - rv_p^2 & \Gamma_{23} \\ \Gamma_{31} & \Gamma_{32} & \Gamma_{33} - rv_p^2 \end{vmatrix} = 0. \quad (2.9)$$

In anisotropic media, the **group velocity** is defined as the "velocity of energy transport in the direction radially outward from a point source" (Sheriff, 1991). It is also called the **ray velocity**. The phase velocity and the group (or ray) velocity generally differ in magnitude and direction. The group velocity is the vector sum of the phase velocity and another vector perpendicular to the phase velocity direction as follows (Achenbach, 1973):

$$v_g = v_p + w(dv_p/dw). \quad (2.10)$$

For seismic wave propagation through multi-layered media, the boundary condition is Snell's law which is stated as follows*: the component of the slowness, tangent to the surface, is identical for the incident, reflected and refracted waves,* and written mathematically as:

$$\frac{\sin q_i}{v_{pi}(q_i)} = \frac{\sin q_r}{v_{pr}(q_r)} = \frac{\sin q_t}{v_{pt}(q_t)}. \quad (2.11)$$

Where, the indices *i, r, t* represent the incident, reflected and transmitted waves, respectively. "Snell's law holds for the angles measured between an interface and the wavefronts, using phase velocities" (Sheriff, 1991).

2.3 Wave Propagation in a Transversely Isotropic Medium

Transverse isotropy is also often known as hexagonal anisotropy. For a transversely isotropic medium with a vertical symmetry axis, any two directions within the horizontal plane are equivalent to each other. The elastic stiffness matrix has five independent components, as follows (Musgrave, 1970; Thomson, 1986):

$$C \equiv \begin{bmatrix} c_{11} & (c_{11}-2c_{66}) & c_{13} & 0 & 0 & 0 \\ (c_{11}-2c_{66}) & c_{11} & c_{13} & 0 & 0 & 0 \\ c_{13} & c_{13} & c_{33} & 0 & 0 & 0 \\ 0 & 0 & 0 & c_{44} & 0 & 0 \\ 0 & 0 & 0 & 0 & c_{44} & 0 \\ 0 & 0 & 0 & 0 & 0 & c_{66} \end{bmatrix}. \qquad (2.12)$$

Considering the cylindrical symmetry of a transversely isotropic medium, wave propagation in three-dimensional space can be simplified to a two-dimensional plane. Since the *x* and *y* axes are equivalent for a transversely isotropic medium, we can arbitrarily confine ourselves to the two-dimensional cross section in the *x*-*z* plane. Figure 2.2 shows a sketch of the phase angle q, ray angle f, and the phase velocity v_p, ray velocity v_g for transversely isotropy with a vertical symmetry axis. The phase and ray velocities are equal only in the direction of the symmetry axis and perpendicular to it.

Let the phase velocity be in the direction *n*, at an angle q from the symmetry axis. The direction is represented by direction cosines:

$$n=(\sin q,\ 0,\ \cos q). \qquad (2.13)$$

For a transversely isotropic medium with stiffness from equation 2.12, equation 2.7 will have the following forms:

$$\begin{bmatrix} c_{11}\sin^2 q + c_{44}\cos^2 q - rv_p^2 & 0 & (c_{13}+c_{44})\sin q\cos q \\ 0 & c_{66}\sin^2 q + c_{44}\cos^2 q - rv_p^2 & 0 \\ (c_{13}+c_{44})\sin q\cos q & 0 & c_{44}\sin^2 q + c_{33}\cos^2 q - rv_p^2 \end{bmatrix} \begin{bmatrix} p_1 \\ p_2 \\ p_3 \end{bmatrix} = 0. \qquad (2.14)$$

When $p_1=p_3=0$, which means the polarization direction is along the *y* axis, we have:

$$rv_p^2 = c_{66}\sin^2 q + c_{44}\cos^2 q\ . \qquad (2.15)$$

This velocity is for a pure shear wave, called the SH-wave or S1-wave. The polarization direction is perpendicular to the plane containing the symmetry axis and the ray path.

When $p_2=0$, the eigenvalue equation becomes:

$$\begin{vmatrix} c_{11}\sin^2 q + c_{44}\cos^2 q - rv_p^2 & (c_{13}+c_{44})\sin q\cos q \\ (c_{13}+c_{44})\sin q\cos q & c_{44}\sin^2 q + c_{33}\cos^2 q - rv_p^2 \end{vmatrix} = 0. \qquad (2.16)$$

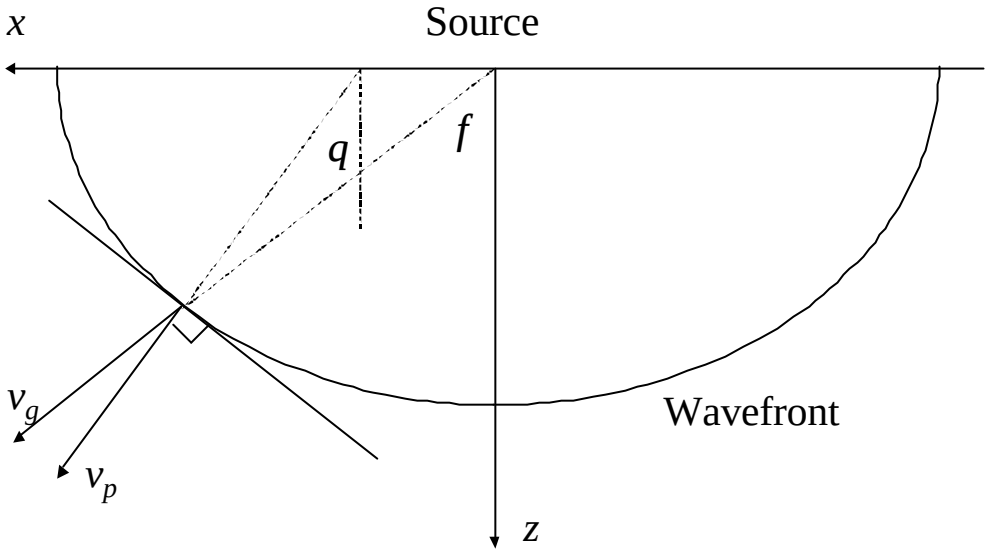

Figure 2.2 The definition of the phase angle q, phase velocity v_p, ray angle f, and ray (group) velocity v_g. The direction of phase velocity v_p is orthogonal to the wavefront (after Thomsen, 1986). Phase velocity is equal in magnitude and direction to ray velocity in directions parallel and perpendicular to the symmetry axis.

The solution to this eigenvalue equation is:

$$rv_p^2 = \frac{1}{2}\{(c_{11}+c_{44})\sin^2 q + (c_{33}+c_{44})\cos^2 q \pm \sqrt{[(c_{11}+c_{44})\sin^2 q + (c_{33}+c_{44})\cos^2 q]^2 + 4(c_{13}+c_{44})^2 \sin^2 q \cos^2 q - 4(c_{11}\sin^2 q + c_{44}\cos^2 q)(c_{44}\sin^2 q + c_{33}\cos^2 q)}\}. \quad (2.17)$$

This solution represents two phase velocities, for both P and SV (or S2) waves. The polarization directions of these two waves are orthogonal to each other, and within the plane that contains the symmetry axis and the raypath. The polarization directions of P and SV-waves can be determined by inserting equation 2.17 into equation 2.14. Because the polarization directions of P and SV waves are generally not along the raypath or orthogonal to the raypath, these P and SV waves should strictly be called quasi-P and quasi-SV waves (Sheriff, 1991; Tsvankin, 1996). For simplicity, P and SV waves will be used in this thesis to represent these two waves, without adding the prefix "quasi-".

Thomsen (1986) introduced a notation to simplify the wave propagation equations. He defined five-parameters as follows:

The velocities for P-waves and S-waves along the vertical symmetry axis direction are, respectively:

$$a_0 = \sqrt{c_{33}/r}\ , \quad (2.18)$$

$$b_0 = \sqrt{c_{44}/r}\ . \quad (2.19)$$

The non-dimensional anisotropic parameters are:

$$\text{P-wave anisotropy: } e \equiv \frac{c_{11}-c_{33}}{2c_{33}} = \frac{v_p^2(\frac{p}{2}) - a_0^2}{2a_0^2}, \quad (2.20)$$

$$\text{near-vertical anisotropy: } d \equiv \frac{(c_{13}+c_{44})^2 - (c_{33}-c_{44})^2}{2c_{33}(c_{33}-c_{44})}, \quad (2.21)$$

$$\text{S-wave anisotropy: } g \equiv \frac{c_{66}-c_{44}}{2c_{44}}. \quad (2.22)$$

Another alternative parameter d^* (instead of d) is defined as:

$$d^* \equiv \frac{1}{2c_{33}^2}\left[2(c_{13}+c_{44})^2 - (c_{33}-c_{44})(c_{11}+c_{33}-2c_{44})\right]. \quad (2.23)$$

Then, the directional dependencies of the three phase velocities are (Thomsen, 1986):

$$v_p^2(q) = a_0^2[1 + e\sin^2 q + D^*(q)], \tag{2.24}$$

$$v_{sv}^2(q) = b_0^2[1 + \frac{a_0^2}{b_0^2} e\sin^2 q - \frac{a_0^2}{b_0^2} D^*(q)], \tag{2.25}$$

$$v_{sh}^2(q) = b_0^2[1 + 2g\sin^2 q], \tag{2.26}$$

where, the phase angle q is the angle between the normal to the wavefront and the vertical axis. *D*(q)* is defined as

$$D^*(q) \equiv \frac{1}{2}(1 - \frac{b_0^2}{a_0^2})\left\{\left[1 + \frac{4d^*}{(1 - b_0^2/a_0^2)^2}\sin^2 q\cos^2 q + \frac{4(1 - b_0^2/a_0^2 + e)e}{(1 - b_0^2/a_0^2)^2}\sin^4 q\right]^{1/2} - 1\right\} \tag{2.27}$$

For P, or SV, or SH-waves, the relationship between the ray velocity $v_g(f)$ at a ray angle f from the vertical direction and its corresponding phase velocity $v_p(q)$ is given by (Berryman, 1979; Thomsen, 1986):

$$v_g^2(f) = v_p^2(q) + \left(\frac{dv_p(q)}{dq}\right)^2, \tag{2.28}$$

$$\tan f = \frac{\tan q + \frac{1}{v_p(q)} \cdot \frac{dv_p(q)}{dq}}{1 - \tan q \cdot \frac{1}{v_p(q)} \cdot \frac{dv_p(q)}{dq}}. \tag{2.29}$$

In the direction of the symmetry axis:

$$q = f = 0,$$

$$v_p = v_g(P) = a_0, v_{SV} = v_g(SV) = b_0, v_{SH} = v_g(SH) = b_0.$$

In the direction perpendicular to the symmetry axis:

$$q = f = \pm\frac{p}{2},$$

$$v_p = v_g(P) = a_0\sqrt{(1 + 2e)}, v_{SV} = v_g(SV) = b_0, v_{SH} = v_g(SH) = b_0\sqrt{(1 + 2g)}.$$

Normally for any other specific ray direction f, it is hard to obtain an explicit expression for ray velocity $v_g(f)$ from the equations 2.24 — 2.29. The ray velocity $v_g(f)$ for any wave mode is also a non-linear function of the anisotropic parameters e, d, and g.

Thomsen (1986) presented measured anisotropic parameters for a number of sedimentary rocks. "Most of these rocks have anisotropy in the order of weak-to-moderate range", whose anisotropic parameters (e, d, g) are less than 0.2.

If the elastic parameters a_0, b_0, e, d, g, and density r are known, then the stiffness coefficients of c_{11}, c_{33}, c_{44}, c_{66}, and c_{13} can be easily obtained using the following equations:

$$\begin{aligned} c_{33} &= r a_0^2, \\ c_{44} &= r b_0^2, \\ c_{11} &= 2c_{33}(e + \tfrac{1}{2}) = 2 r a_0^2 (e + \tfrac{1}{2}), \\ c_{66} &= 2c_{44}(g + \tfrac{1}{2}) = 2 r b_0^2 (g + \tfrac{1}{2}), \\ c_{13} &= r a_0 \sqrt{(a_0^2 - b_0^2)(2d + 1 - b_0^2 / a_0^2)} - r b_0^2. \end{aligned} \tag{2.30}$$

Helbig and Schoenberg (1987) examined the stability conditions under transverse isotropy. The stability conditions are listed as follows:

$$\begin{aligned} &c_{44} > 0, \\ &c_{66} > 0, \\ &c_{11} - c_{66} > 0, \\ &c_{33}(c_{11} - c_{66}) - c_{13}^2 > 0. \end{aligned} \tag{2.31}$$

2.4 Examples of Wave Propagation in a Transversely Isotropic Medium

To provide an intuitive image of seismic wave propagation through a transversely isotropic medium with a vertical symmetry axis, wave characteristics in some sedimentary rocks are calculated and shown in this section. These include phase and ray velocities, slowness surfaces, wave polarization directions, and P, SV, and SH-waves wavefronts. The four representative sedimentary rocks, which will be used in my numerical experiments in this thesis, are chosen as examples. They are Taylor sandstone (Figure 2.3), Dog Creek shale (Figure 2.4), Mesaverde (5501) clayshale (Figure 2.5), and Green River shale (Figure 2.6).

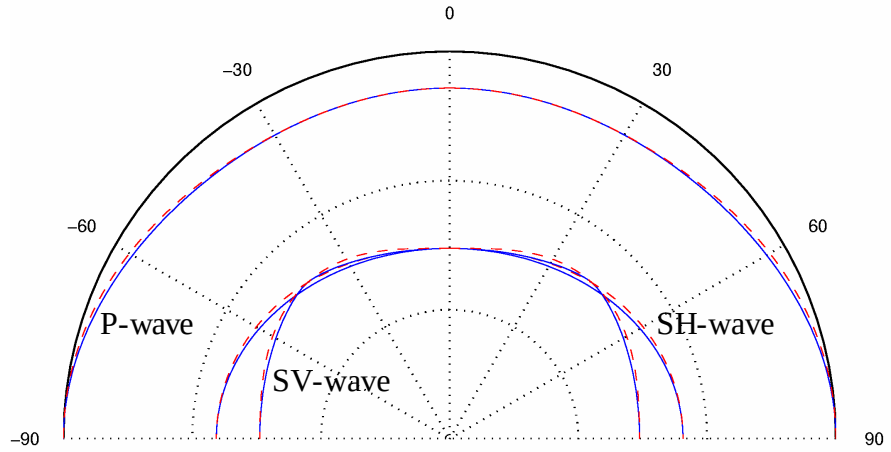

(a)

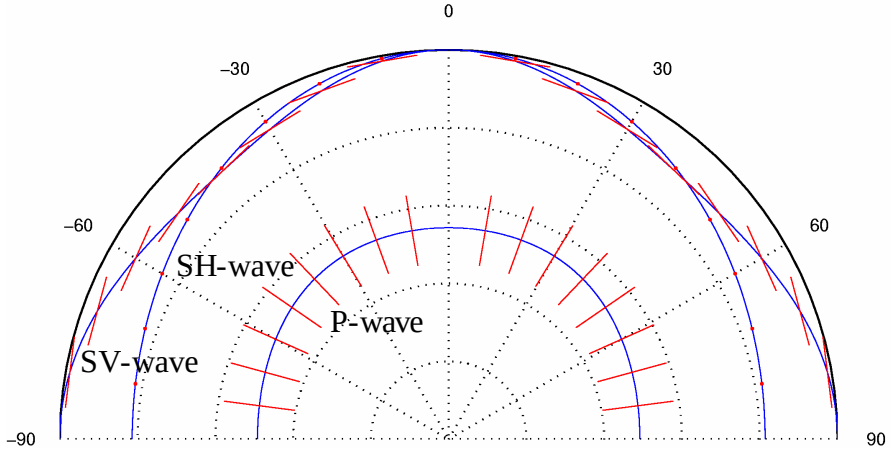

(b)

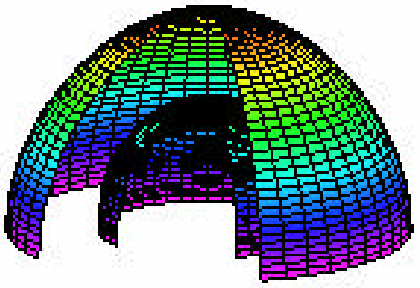

(c)

Figure 2.3 Characteristics of P, SV, and SH-waves in Taylor sandstone. (a) Phase velocity fields (red dashed curves) and group velocity fields (blue curves). (b) Slowness surfaces (blue curves) and the wave polarization directions (red lines). (c) Group velocity surfaces. The values of its anisotropic parameters are $e=0.110$, $d=-0.035$, $g=0.255$ (parameters are from Thomsen, 1986).

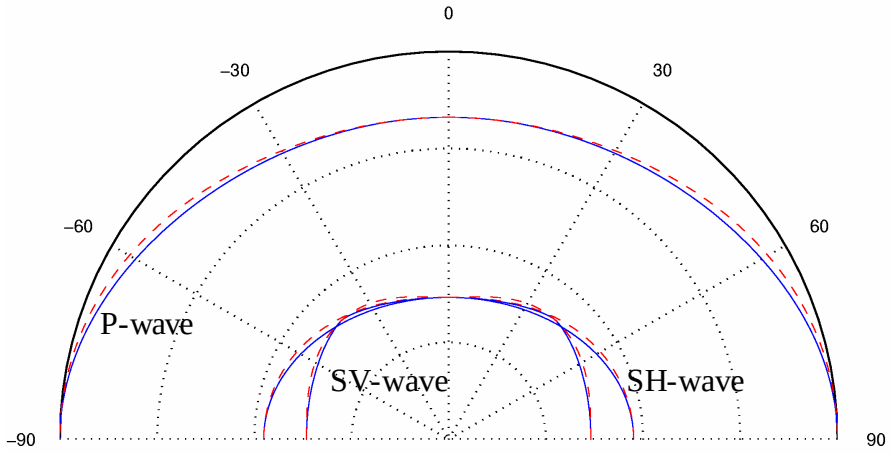

(a)

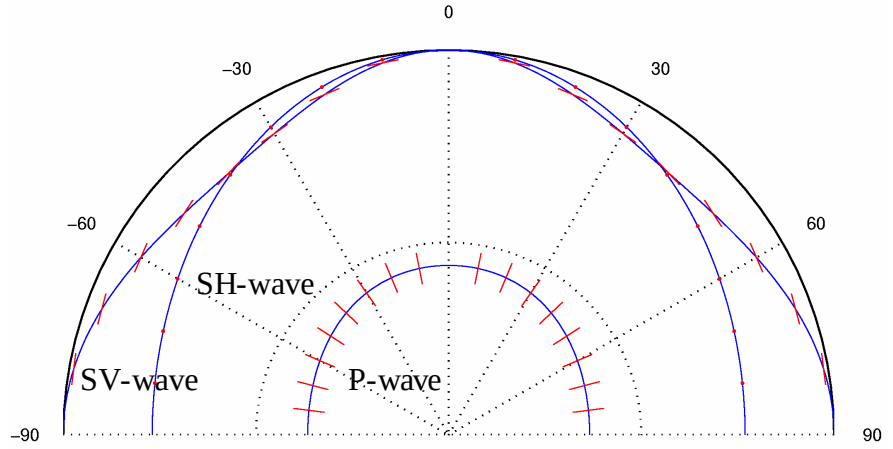

(b)

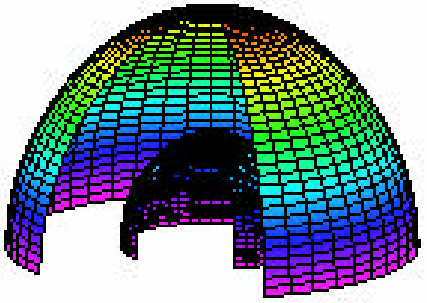

(c)

Figure 2.4 Characteristics of P, SV, and SH-waves for Dog Creek shale. (a) Phase velocity fields (red dashed curves) and group velocity fields (blue curves). (b) Slowness surfaces (blue curves) and the wave polarization directions (red lines). (c) Group velocity surfaces. The values of its anisotropic parameters are $e=0.225$, $d=0.100$, $g=0.345$ (parameters are from Thomsen, 1986).

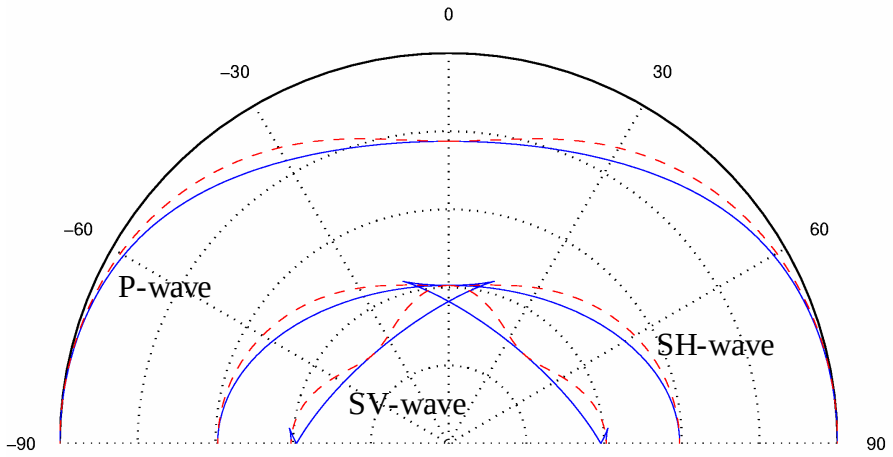

(a)

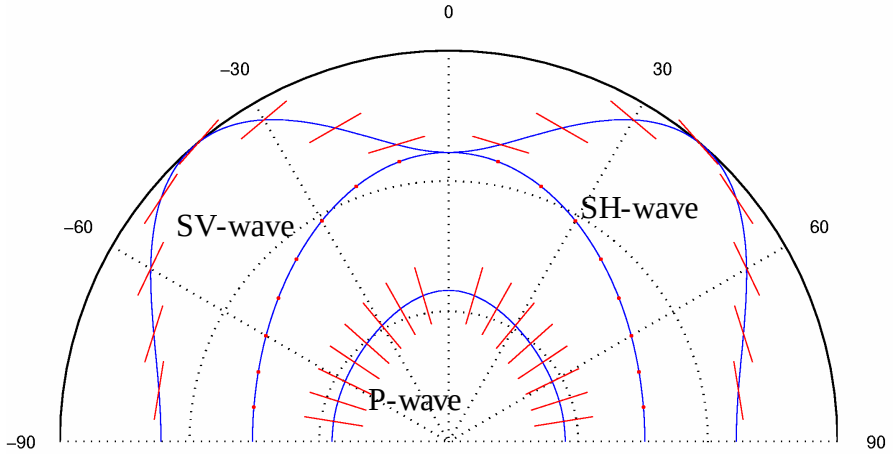

(b)

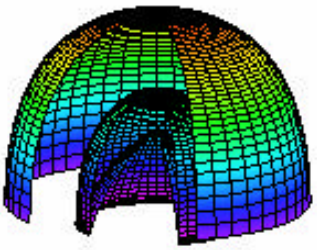

(c)

Figure 2.5 Characteristics of P, SV, and SH-waves for Mesaverde (5501) clayshale. (a) Phase velocity fields (red dashed curves) and group velocity fields (blue curves). (b) Slowness surfaces (blue curves) and the wave polarisation directions (red lines). (c) Group velocity surfaces. For the SV-waves, cusps (triplication effects) exist near the *0°* and *±90°* directions from the symmetry axis. The values of the anisotropic parameters are *e=0.334, d=0.730, g=0.575* (parameters are from Thomsen, 1986).

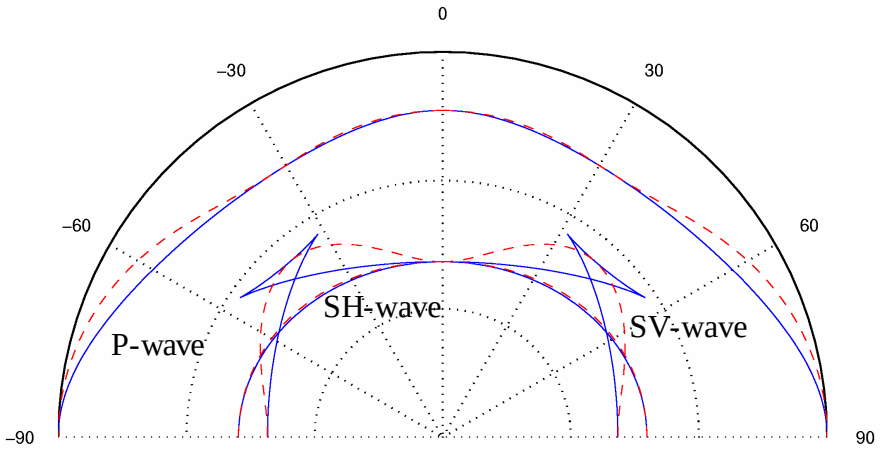

(a)

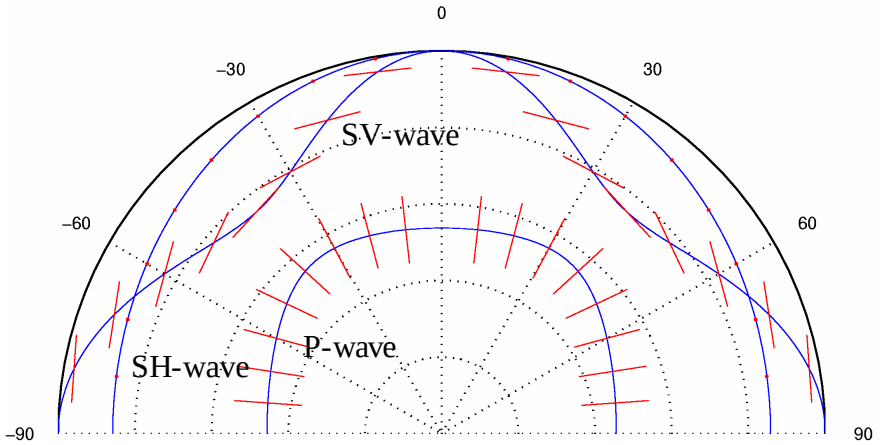

(b)

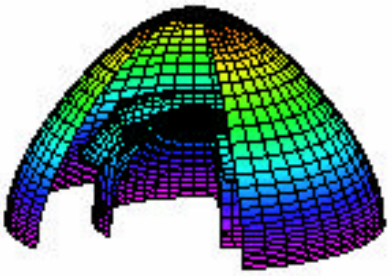

(c)

Figure 2.6 Characteristics of P, SV, and SH-waves for Green River shale. (a) Phase velocity fields (red dashed curves) and group velocity fields (blue curves). (b) Slowness surfaces (blue curves) and the wave polarisation directions (red lines). (c) Group velocity surfaces. For the SV-waves, cusps (triplication effects) exist near the $\pm 45°$ directions from the symmetry axis. The values of the anisotropic parameters are $e=0.195, d=-0.220, g=0.180$ (parameters are from Thomsen, 1986).

For Taylor sandstone, Figure 2.3a gives the phase velocity field (red dashed curves) and group velocity field (blue curves). These velocity fields are not the same because of the anisotropy present. The slowness surfaces (blue curves) and polarization directions (red lines) are shown in Figure 2.3b. Generally the polarization direction is not along the slowness direction for the P-wave, while for the SV-wave it is not perpendicular to the slowness direction. But for SH-waves, the polarization direction is always normal to the plane containing the symmetry axis and the raypath. The P and SV-waves are quasi-P and quasi-SV-waves. The SH-wave is a pure shear wave. Figure 2.3c shows the group velocity surface, which provides a three-dimensional wavefront image.

For Taylor sandstone and Dog Creek shale, the degrees of anisotropy are in the weak to moderate range. Their anisotropic parameters are ($e=0.110$, $d=-0.035$, $g=0.255$) and ($e=0.225$, $d=0.100$, $g=0.345$), respectively. The differences between their group velocities and phase velocities are consequently small. For a strongly anisotropic medium such as Mesaverde (5501) clayshale ($e=0.334$, $d=0.730$, $g=0.575$) and Green River shale ($e=0.195$, $d=-0.220$, $g=0.180$), wave characteristics are more complex as in Figure 2.5 and Figure 2.6. The differences between their group velocities and phase velocities become greater. For the SV-waves, cusps exist in the group velocity surfaces, which have three different velocity values in one direction. The cusps, so called triplication effects, occur near the $\pm 45°$ directions from the symmetry axis for Green River shale, and near the horizontal and vertical axes for Mesaverde (5501) clayshale. The existence of such cusps is expected to make inversion problems harder to solve because of this non-uniqueness. It is noticed that Mesaverde (5501) clayshale has such a negative anellipticity that it must be looked at critically (Schoenberg, personal communication and 1994). Nevertheless it was still chosen as a medium for the numerical experiments in this research, for more thorough testing. It was considered better to include media with differing characteristics in the numerical experiments in this research.

CHAPTER 3
INVERSION METHOD FOR APPARENT PARAMETERS

For a transversely isotropic (TI) medium, Thomsen (1986) gave a widely used model based on the vertical P and S-wave velocities (a_0, b_0); P-wave anisotropy (e); the near-vertical P-wave anisotropy (d or d^*); and SH-wave anisotropy (g). From these five elastic parameters and the density, the stiffness coefficients can be determined. The velocity field of seismic waves through this medium then can be computed.

For a single-layered transversely isotropic medium with a vertical symmetry axis (VTI), Okoye et al. (1996) developed a P-wave inversion method. This inversion method recovered the elastic parameters a_0 and d^*, while fixing the other parameters b_0 and e. The method recovered the elastic parameters from a large numbers of observations, thereby statistically reducing measurement errors. However, this inversion method is difficult to apply to walkaway VSP field survey data, because it requires horizontal velocity to be input. No single value for the horizontal velocity exists in layered TI media where each layer has a different velocity. No representative value may be found.

For a layered model, if the individual layer thickness is much less than the seismic wavelength (thin layers), a stratified medium behaves like a single transversely isotropic medium to those waves (Postma, 1955; Backus, 1962). The elastic moduli of such a medium can also be expressed in terms of the thickness-weighted average values of the constituents (Helbig and Schoenberg, 1987). However, for a layered model with thick layers, that is where individual layer thickness is greater than the seismic wavelength, we do not know whether we can treat it as a single-layered transversely isotropic medium. If the answer is "*yes*", a single set of elastic parameters — *apparent* parameters — could be used to describe wave propagation through such a layered model.

In this chapter, the overall velocity field of a layered model with thick layers will be studied. Based on the results of the forward modelling studies, a new inversion method will be developed suitable for field VSP surveys.

3.1 P-wave Inversion for a Single-Layered VTI Medium

Let us begin this research with P-wave propagation through a single-layered transversely isotropic medium with a vertical symmetry axis (VTI). This is a logical step before we extend the work to a multi-layered VTI medium.

a_0 and b_0 are the vertical P and S-wave velocities respectively. In actual field VSP surveys, they may be directly calculated from zero-offset VSP shooting (Urosevic, 2000). In this section, I consider an inversion method to recover the other parameters e and d. The parameter g, which relates to shear waves, cannot be recovered from P-wave propagation data. That will be left to a later section which will deal with inversion from combined wave modes.

3.1.1 Inversion Method

From field survey data or laboratory data, the seismic velocity of P-waves as a function of direction may be measured at various angles. Now the problem is to find the most suitable parameters e and d to describe the elastic property of the medium. The elastic parameters e and d *may be* computed using the velocity values measured in three specific directions (e.g. Dellinger and Vernik, 1994; Vestrum, 1994; Vernik and Nur, 1992; Lo et al., 1986; Jones and Wang, 1981). However, if redundant measurements are taken at a much larger range of angles, this should statistically reduce the effect of measurement errors. Elastic parameters inverted from such

massively over-determined data sets should be more accurate than those based on just three travel time measurements. This is the rationale that is chosen in this research.

The general approach

An iterative procedure was carried out to solve this inversion problem. The iteration started with an initial guess at the values of the unknown elastic parameters e and d. The group velocity field of P-waves through this medium was then calculated by using fundamental equations 2.24, 2.28, and 2.29 at those angles for which measurements existed. The calculated velocity field was then compared with the observation velocity field. The corrections to the guessed parameters e and d were found using the least-squares method as described below. They were then added to their original values. The process was then repeated. This iterative procedure was continued until the increment values of the parameters e and d differed from those in the previous iteration by less than 10^{-5}. The best-fit values of parameters e and d were thus determined, minimising the differences between the observed velocities and the calculated ones:

$$\sum_{i}^{n_{obs}} |v_{gobs}(i) - v_{gcal}(i)| \to \text{minimum.} \qquad (3.1)$$

A practical protection against non-convergence was built into this procedure. The iteration would be compulsorily stopped if the iteration occurred for *50* or more times to avoid ineffective long run times.

Figure 3.1 shows the flow chart of my inversion program "*para.f*" which follows the above procedures.

Basic principles of the least-squares method in the inversion

During the iteration, the least-squares method was employed to calculate the corrected value for each unknown parameter as follows.

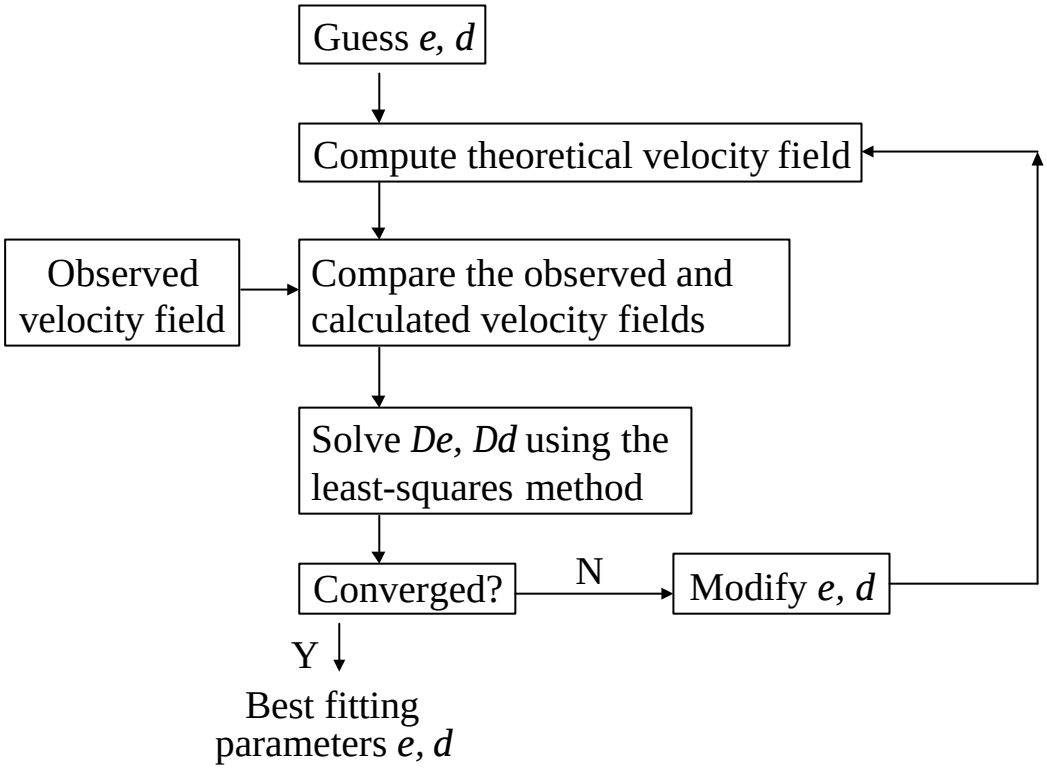

Figure 3.1 Flowchart of the inversion program "*para.f*". This program is designed to recover the parameter e and d for a VTI medium. The convergence is decided when the increment $\Delta e < 10^{-5}$, and $\Delta d < 10^{-5}$. If the number of iterations reaches *50*, the iteration circle will be stopped unconditionally.

The group velocity $v_g(f)$ is a non-linear function of parameters e and d. For the convenience of avoiding complex algebraic derivations, v_g^2 instead of v_g was chosen to be the function used to determine best fit. The values of parameters e and d were determined, minimising the differences between the squared velocities and the ones calculated with the current values of e and d.

In the first order approximation, the square of the i^{th} observed group velocity $v_g^2(i)$ was written as:

$$v_g^{\,2}(i) = v_{gcal}^2(i) + \frac{\partial v_{gcal}^{\,2}(i)}{\partial e}\Delta e + \frac{\partial v_{gcal}^{\,2}(i)}{\partial d}\Delta d \,. \tag{3.2}$$

Using matrix notation with:

$$\tilde{G} = \begin{bmatrix} v_g^{\,2}(1) - v_{gcal}^{\,2}(1) \\ \cdots \\ v_g^{\,2}(i) - v_{gcal}^{\,2}(i) \\ \cdots \end{bmatrix},$$

$$\tilde{D} = \begin{bmatrix} \dfrac{\partial v_{gcal}^2(1)}{\partial e} & \dfrac{\partial v_{gcal}^2(1)}{\partial d} \\ \cdots & \cdots \\ \dfrac{\partial v_{gcal}^2(i)}{\partial e} & \dfrac{\partial v_{gcal}^2(i)}{\partial d} \\ \cdots & \cdots \end{bmatrix}, \tag{3.3}$$

$$\tilde{\Delta} = \begin{bmatrix} \Delta e \\ \Delta d \end{bmatrix},$$

we wrote:

$$\tilde{G} = \tilde{D} \times \tilde{\Delta} \,. \tag{3.4}$$

After solving the above equation, the increment values of Δe and Δd were added to the initial guesses and the process was repeated. This iterative procedure was continued until only very small corrections ($<10^{-5}$) were made to the estimates of the parameters e and d. Effectively equation 3.1 was satisfied.

Calculation of the corresponding phase angle q_i in any observation direction f_i

When writing equation 3.4 for any set of trial parameters e and d, we need to compare the difference between the observed velocity field input to the inversion program and that calculated from the trial parameters e and d during the iteration process. We also needed to find the first derivatives of the velocity field with respect to parameters e and d in any observation direction f_i. In any specific observation direction f_i, the ray velocity $v_{gcal}(f_i)$ and its first derivatives cannot be calculated directly because no explicit equations exist for this. However, they can be calculated for a specific phase angle q. So, before we solved equation 3.4, we needed to find the corresponding phase angle q_i for an observed group velocity direction f_i.

For a given phase angle q, the phase velocity $v_{pcal}(q)$ was calculated using equation 2.24. From equations 2.28 and 2.29, the corresponding magnitude $v_{gcal}(f)$ and direction of the corresponding ray velocity f were determined numerically. The ray velocity in a specific direction needed to be found by searching over different phase angles. I adopted the commonly used "golden-ratio" search method (Gottfried and Weisman, 1973) to find the corresponding phase angle for each observed ray angle as follows.

According to the golden-ratio search method, if the phase angles q_1, q_2 corresponded to ray angles f_1, f_2 respectively, and the desired ray angle f_i lies within the range [f_1, f_2], the next search direction would be $q = q_1 + (q_2 - q_1) * 0.618$. The iterations would continue until the ray velocity was calculated in a direction that had an allowable deviation from the desired direction f_i. In my research, the allowable angle of deviation was chosen to be below 10^{-10} radian.

After finding the corresponding phase angle q_i for any observation direction f_i, the corresponding calculated ray velocity and its first derivatives with respect to parameters e and d were calculated analytically, using equations 2.24, 2.28 and 2.29. Then we were able to solve equation 3.4 to obtain the corrections to be made to the trial parameters e and d.

My inversion program *"para.f"* was developed using these concepts. In the following section, the testing of this inversion program to recover the parameters e and d from the synthetic velocity field of a numerical model will be described.

3.1.2 Numerical Results and Discussion

Initial tests were carried out on synthetic model data. The agreement between the recovered elastic parameters and the exact model values will show the success of the inversion program.

Synthetic model data

A single-layered VTI model was first established using the elastic parameters of real sedimentary rocks or laboratory materials. To simulate the velocity field that can be acquired from a field VSP survey, the velocities at different directions for the VTI model were calculated as follows:

For any phase angle q, the corresponding P-wave phase velocity $v_p(q)$ was found by equation 2.24. Then the corresponding ray velocity $v_g(f)$ and its direction f were calculated by equations 2.28, and 2.29. The calculation started from the phase angle q as $0°$, with an increment of $0.9°$ $(=90°/100)$ at the next calculation. Thus, the velocity field of P-waves propagating through this medium was obtained. This calculated velocity field was then used as the observation velocity field to be inverted. My

forward modelling program *"phiv.f"* was written to implement the above modelling procedures.

The model we considered was a VTI model. The synthetic data were in the range of *0°* to *90°*. However, the program could be changed to include negative offsets by beginning the calculation from a negative angle. The observation number was chosen as *100* in my synthetic data which is typical of the number of shots fired for each level of a marine petroleum walkaway VSP survey. The number of the observations was also adjustable in the program.

With the modelled observation velocity field as input, the inversion program *"para.f"* was then tested. The elastic parameters e and d were recovered. The success of the inversion program *"para.f"* was judged by the *"chi-by-eye"* approach. The calculated velocity field was compared with the modelled observation velocity field. A comparison was also made between the recovered values of parameters and their real values as used in the forward modelling program "*phiv.f*".

Program testing

The elastic parameters of real sedimentary rocks (Thomsen, 1986) and laboratory materials (Okoye et al., 1997) were used in building the single layered models used in the following tests. Three representative sets of parameters from Table 3.1 were chosen: Plexiglas which is an isotropic material with values of zero for anisotropic parameters, Pierre shale A which is weakly anisotropic, and Green River shale which is strongly anisotropic. An isotropic medium can be treated as a special case of a transversely isotropic medium with the values of its anisotropic parameters being zero.

The range of angles used in the modelled velocity fields was from *0°* to *90°*. With an initial input as zero for each guessed parameter, the inversion program converged

Table 3.1 The elastic parameters of the materials used in numerical modelling experiments in this thesis. The parameters are taken from Thomsen (1986) and Okoye et al. (1997).

Material	$a_0(ms^{-1})$	$b_0(ms^{-1})$	e	d
Phenolite A	3057	1538	0.300	0.404
Phenolite B	2229	1318	1.070	0.327
Plexiglas	2760	1404	0.000	0.000
Pierre shale A	2074	869	0.110	0.090
Pierre shale B	2106	887	0.195	0.175
Pierre shale C	2202	969	0.015	0.060
Mesaverde (5501) clayshale	3928	2055	0.334	0.730
Green River shale	3292	1768	0.195	-0.220

quickly for each model. The number of iterations was less than *15*. Table 3.2 shows the inverted parameters compared with their exact values used in the input data generated by forward modelling. The recovered values of the elastic parameters are very close to their exact values with the differences being less than *0.001*. The average velocity error *D* is less than *0.084 m/s.* The relative velocity error is generally less than *0.01%*. As a verification process, the velocity field computed using the exact parameter values and that from the inverted values were compared visually. Both sets of velocity fields overlap each other so well that there is no need to display the velocity field comparison. The inversion program "*para.f*" was considered to be successful.

Inversion of synthetic data with added noise

Some degree of noise will always be present in field or laboratory measurements. Hence, the inversion program "*para.f*" needs to be able to handle measurement data with noise. A single layered VTI model was used again. Assuming the thickness of the layer to be *2000 m*, random noise in travel time up to *±10 ms* was generated by computer. The travel time errors produced were less than *2%*. The velocity field generated in program "*phiv.f*" was then input to the inversion program "*para.f*". The inversion program "*para.f*" still gave good results, shown in Table 3.3. The differences between the recovered parameters and their exact values are no greater than *0.012*. The average velocity error *D* is less than *50 m/s*, and its relative error *W* is below *2%*. Figure 3.2 gives an example of the velocity fields for Pierre shale A. The velocity field calculated from the exact model data with random noise was compared with that from the recovered parameter values. We see that these velocity fields coincide quite well.

The inversion program "*para.f*" was successfully applied to the numerical models in the presence of random noise. It is ready to be tested on laboratory data and field data.

Table 3.2 Inversion results from program "*para.f*" for a single-layered model. $\Delta = \sum_{i=1}^{n} \frac{\left| v_g(i) - v_{g\,\mathrm{mod}}(i) \right|}{n}$ represents the average error between the input velocities calculated by forward modelling and the velocities calculated from the inverted parameter values.

		e	$\lvert e_{inv}\text{-}e_{exact}\rvert$	d	$\lvert d_{inv}\text{-}d_{exact}\rvert$	D(m/s)
Plexiglas	exact values	0.000		0.000		
	recovered values	0.000	0.000	0.000	0.000	0.03
Pierre shale	exact values	0.110		0.090		
A	recovered values	0.110	0.000	0.090	0.000	0.058
Green River	exact values	0.195		-0.220		
shale	recovered values	0.194	0.001	-0.220	0.000	0.084

Table 3.3 Inversion results for a single-layered model data set with added random travel time noise from program *"para.f"*. $\Delta = \sum_{i=1}^{n} \frac{\left| v_g(i) - v_{g\,\mathrm{mod}}(i) \right|}{n}$ represents the average error between the input velocities calculated by forward modelling and the velocities calculated from the inverted parameter values.

		e	$\lvert e_{inv}-e_{exact}\rvert$	d	$\lvert d_{inv}-d_{exact}\rvert$	$D(m/s)$
Plexiglas	exact values	0.000		0.0		
	recovered values	0.003	0.003	-0.003	0.003	31
Pierre shale A	exact values	0.11		0.090		
	recovered values	0.110	0.000	0.090	0.000	18
Green River	exact values	0.195		-0.220		
shale	recovered values	0.183	0.012	-0.214	0.006	50

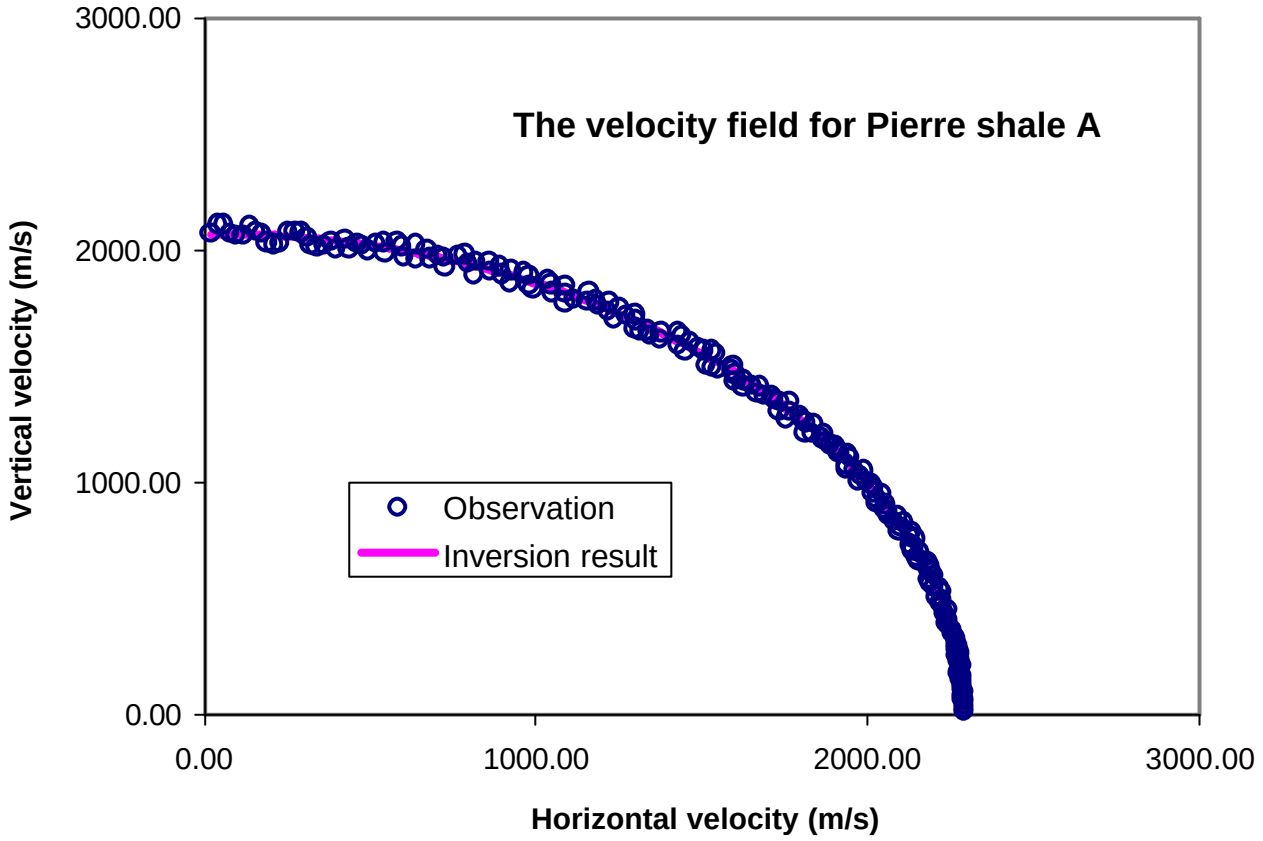

Figure 3.2 Velocity fields for a single layered Pierre shale A model in numerical modelling experiments. The circles represent the input velocity field generated by computer from given elastic parameters with random noise, and the curve represents the velocity field calculated from the anisotropic parameters recovered by inversion. The curve and the circles are in a good agreement.

3.2 P-wave Inversion for Multi-Layered VTI Media

Horizontally layered models comprising VTI media and isotropic media will be studied in this section. This section will begin with the simplest two-layered model. The results will then be generalized to a multi-layered model.

As the starting point in these trials, apparent velocity fields through layered models were generated for the geometrical arrangement in Figure 3.3. The two-layered model consisted of two isotropic components, or mixture of isotropic and VTI components, or two VTI components. The thicknesses of these two components were z_1, z_2 respectively. Using the approach outlined in Chapter 3.1, travel times from a source moved on the upper surface to a receiver on the lower surface were calculated. The corresponding offset was defined as the horizontal distance between the source and the receiver. The apparent ray path assuming the model to be a single layer, and the actual ray paths are shown in Figure 3.3.

The velocity of deeper geological structures normally increases as the depth of burial increases. Figure 3.3 shows such a case with the velocity of layer 2 greater than that of layer 1. If the velocity of layer 2 is less than that of layer 1, the ray path is refracted in the opposite direction.

Then an apparent velocity field as a function of apparent ray directions was generated. This apparent velocity field was input to the previously developed inversion program "*para.f*". If inversion were possible, apparent parameters *e* and *d* could be found. We would then be able to consider that this layered model was adequately represented by an equivalent single layer. If it were not possible, then either the multi-layered model might not be treated as a single equivalent layer, or the inversion program would need to be re-examined.

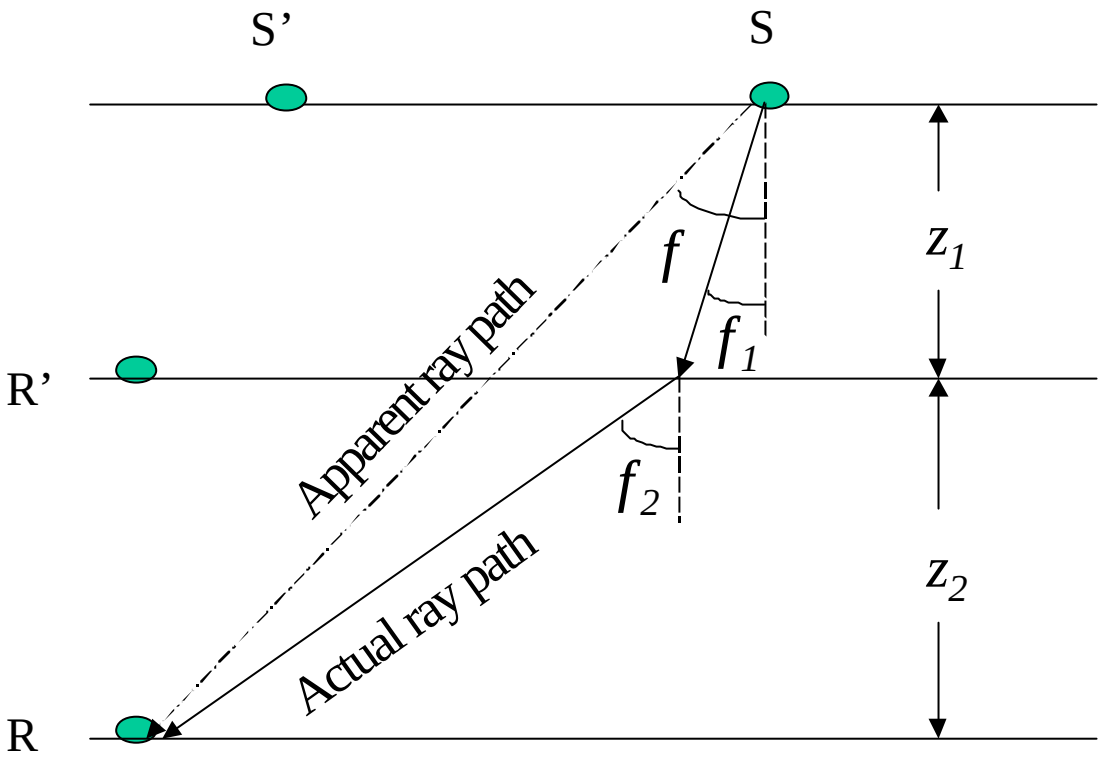

Figure 3.3 Ray path of a seismic wave through a two-layered model. Here, R and R' are receivers while S and S' are shot locations. Without knowledge of the layer structure, an apparent path from S to R must be assumed as shown. The actual ray path is shown here if the velocity of layer 2 is greater than that of layer 1. If the velocity of layer 2 is smaller than that of layer 1, the ray path will be bent the other way. Ray directions are given by angles f, f_1 and f_2.

The main test of equivalence of multi-layered models and single layered models is the comparison of the input apparent velocity field and the velocity field calculated using the elastic parameters obtained by inversion.

3.2.1 Calculation of the Apparent Velocity Field for a Two-layered Model

When a seismic wave propagates through a two-layered model, it will refract at the interface between the component layers. Figure 3.3 shows the apparent and actual ray paths of the seismic wave from a source *S* to a receiver *R*.

The ray path through the boundary between the two layers will follow Snell's law as stated in Chapter 2. If the incident ray angle is f_1, with a corresponding phase angle of incidence q_1, the phase velocity will be $v_{p1}(q_1)$ according to equations 2.24 — 2.29. If the refracted phase angle is q_2, the phase velocity will be $v_{p2}(q_2)$, and the corresponding refracted ray angle will be f_2 using the same equations 2.24 — 2.29. They will satisfy equation 2.11 (Snell's law). The value of q_2 will be obtained after numerically solving equation 2.11. Because the phase velocity $v_{p2}(q_2)$ is related to q_2, there is not any explicit solution to the refracted angle f_2.

If we ignore refraction at the interface, the overall effect of seismic ray propagation through this two-layered model will appear to be a ray going straight from source *S* to receiver *R*. The apparent ray path will be *SR*, and the apparent ray angle will be f, as shown in Figure 3.3. Here, the word "apparent" is used as a qualifier before the "ray path" and "ray angle", to indicate that they are not the real ray path and ray angle of the ray from a source to a receiver. The corresponding overall apparent velocity will be found by dividing the distance between *S* and *R* by the wave travel time. The overall velocity field $v_g(f)$ for the overall two-layered model can be found from the following relationships.

Referring to Figure 3.3, the distance between the source *S* and the receiver *R* is:

$$\overline{SR} = \sqrt{(z_1 + z_2)^2 + (z_1 \tan f_1 + z_2 \tan f_2)^2} \ . \tag{3.5}$$

Where, z_1, z_2 are the thicknesses of these two individual layers. The travel time of this ray through the model is

$$t = t_1 + t_2 = \frac{z_1}{\cos f_1 v_{g1}(f_1)} + \frac{z_2}{\cos f_2 v_{g2}(f_2)}. \tag{3.6}$$

Then the magnitude of this overall velocity field $v_g(f)$ is as follows:

$$v_g(f) = \frac{\overline{SR}}{t} = \frac{\sqrt{(z_1 + z_2)^2 + (z_1 \tan f_1 + z_2 \tan f_2)^2}}{\dfrac{z_1}{\cos f_1 v_{g1}(f_1)} + \dfrac{z_2}{\cos f_2 v_{g2}(f_2)}}. \tag{3.7}$$

Its apparent ray angle is found from:

$$\tan f = \frac{z_1 \tan f_1 + z_2 \tan f_2}{z_1 + z_2}. \tag{3.8}$$

In the vertical direction, the apparent velocities of P and S-waves in this two-layered model will be:

$$\begin{aligned} a_0 &= \frac{z_1 + z_2}{\dfrac{z_1}{a_{01}} + \dfrac{z_2}{a_{02}}}, \\ b_0 &= \frac{z_1 + z_2}{\dfrac{z_1}{b_{01}} + \dfrac{z_2}{b_{02}}}. \end{aligned} \tag{3.9}$$

The equations 3.7, 3.8 and 3.9 are based on the actual ray paths shown in Figure 3.3. If the velocity of layer 1 is less then the velocity of layer 1, the same equations still can be derived.

Apparent horizontal velocity

There is no physical meaning for the apparent horizontal velocity of a thick layered model. However, the apparent horizontal group velocity can still be obtained by finding the limiting value of equation 3.7 in the horizontal direction.

For a two-layered model shown in Figure 3.3, the phase velocity of layer 2 is greater than that of layer 1, which represents the most common geological situation. In this case, the apparent ray velocity in the limit of the horizontal direction is the same as the horizontal velocity of the second layer. This will also happen when the horizontal velocity of layer 2 is less than that of layer 1. The apparent ray velocity in such a situation, in the horizontal limit, will be the same as the horizontal ray velocity of the first layer, since most of the travel path will be in the upper layer. The above statement is demonstrated mathematically as follows.

Suppose a wave is incident on an interface at a critical phase angle of incidence q_1, and the corresponding refracted phase velocity of layer 2 is greater than the incident phase velocity of layer 1. The angle of refraction in the second layer is a phase angle $q_2=p/2$. The corresponding ray angle of refraction will be $f_2=p/2$ (see Section 2.3). By solving equation 3.8 in the limit of $f_2 \to p/2$, the apparent ray angle will be $f \to p/2$. The corresponding apparent ray velocity $v_g(f \to p/2)$ can be seen as the apparent ray velocity in the limit of horizontal direction.

According to Snell's law (equation 2.11), we have: $v_{p1}(q_1)<v_{p2}(p/2)$. The corresponding ray angle for the phase angle of refraction q_2 should be $f_2 \to p/2$. Thus, to find the limit of equation 3.7 with $f \to p/2$, we have:

$$v_g(f \to p/2) = \lim_{f_2 \to p/2} \frac{\sqrt{(z_1 + z_2)^2 + (z_1 \tan f_1 + z_2 \tan f_2)^2}}{\dfrac{z_1}{\cos f_1 v_{g1}(f_1)} + \dfrac{z_2}{\cos f_2 v_{g2}(f_2)}}$$

$$= \lim_{f_2 \to p/2} \frac{\sqrt{(z_1 + z_2)^2 \cos^2 f_1 \cos^2 f_2 + (z_1 \sin f_1 \cos f_2 + z_2 \sin f_2 \cos f_1)^2}}{\dfrac{z_1 \cos f_2}{v_{g1}(f_1)} + \dfrac{z_2 \cos f_1}{v_{g2}(f_2)}}$$

$$= \lim_{f_2 \to p/2} \frac{z_2 \sin f_2 \cos f_1}{\dfrac{z_2 \cos f_1}{v_{g2}(f_2)}} = v_{g2}(p/2).$$

(3.10)

If the velocity of the first layer is greater than that of the second layer, the above derivations still can be carried out. The only change is swapping indices 1 and 2.

Program "*twophiv.f*"

According to the principles described above, a program "*twophiv.f*" was written to numerically calculate the apparent velocity field of seismic waves through a two-layered model. The two components of the model may be either transversely isotropic media, or isotropic media, as isotropy is a special case of anisotropy.

If the incident phase angle on the interface was q_1, the corresponding refraction phase angle in layer 2 was assumed to be q_2. The fundamental equations 2.24, 2.28 and 2.29 were used to formulate the corresponding phase velocity, ray velocity and ray direction for these two individual layers. To find the phase angle of refraction q_2 for an incident phase angle q_1, we solved an equation based on equation 2.11 (Snell's law). The bisection method with subroutine *RTBIS* (Press et al., 1992b) was employed in my program to do this. Finally, by using equations 3.7 and 3.8, the apparent ray velocity and its apparent ray angle were found.

The incident phase angle q_1 was chosen to start from *0°* having an increment of *0.9°* (*=90°/100)* for successive angles. When the calculated apparent velocity approached the horizontal direction, the calculation was stopped. Thus, the number of the calculated apparent velocities was equal to or less than *100*. This normally was about *80~100* in my simulation models. The number of synthetic data pairs, which were generated as input to the inversion program, could be adjusted by changing the incremental step size in the incident phase angle q_1.

A series of numerical computer experiments was then designed to compute the apparent ray velocity field for a two-layered model. This apparent ray velocity field was then input to the inversion program "*para.f*". The apparent elastic parameters for this layered model were recovered. The inversion results for the models were then studied. These numerical computer experiments investigated the velocity properties of P-wave propagating through a two-layered model, and they are described below.

3.2.2 Two-layered Numerical Model Composed of Two Isotropic Media

The first two-layered model tested was composed of two *isotropic* materials. The velocities and thicknesses of the component layers were varied as follows. Figure 3.4 shows the two-layered model.

A two-layered model with velocity contrast as 0.4 and thickness ratio of unity

The first specific two-layered model was set up with the first layer velocities a_{01}*=2600 m/s,* b_{01}*=1300 m/s,* and the second layer velocities a_{02}*=3640 m/s,* b_{02}*=1820 m/s.* The

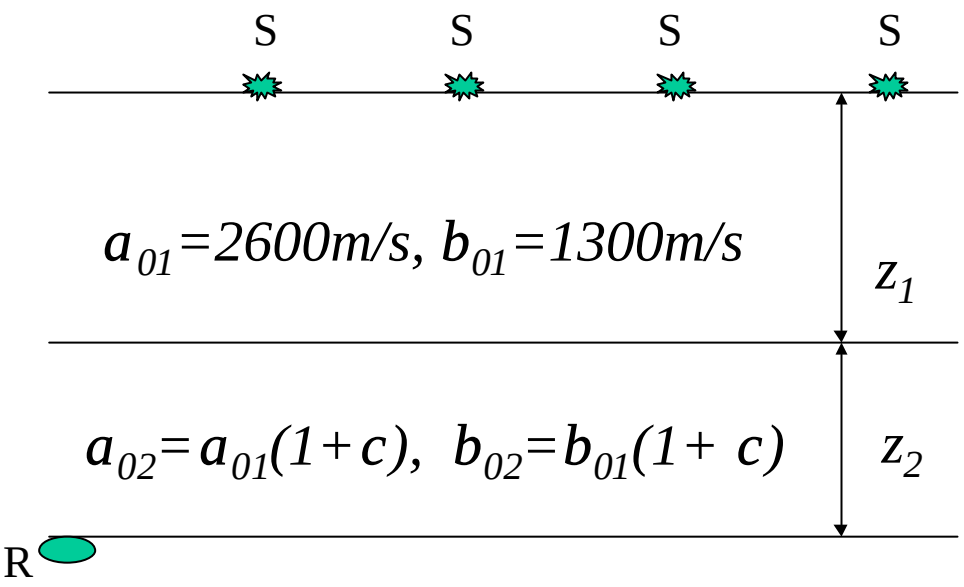

Figure 3.4 Two-layered isotropic model used in the numerical simulation experiments. Shot S moved along the upper surface while a receiver R was on the lower surface of the model. The materials were isotropic with a range of velocities and thickness ratios. Here, a_{01} and b_{01} were fixed, while a_{02} and b_{02} could be varied by changing the velocity contrast coefficient c. The velocity contrast coefficient c was chosen to be in the range *0.2* to *1*, and the thickness ratio z_1/z_2 in the range from *0.2* to *100*.

velocity contrast between these two layers was: $c = \frac{a_{02} - a_{01}}{a_{01}} = 0.4$. With the thickness ratio $z_1/z_2 = 1$, the apparent velocity field was computed using program "*twophiv.f*", shown as the red circles in Figure 3.5a. It was noticed that the limiting apparent velocity value in the horizontal direction was close to the faster velocity value of these two layers. The mathematical derivation in Section 3.2.1 for apparent horizontal velocity was verified.

This calculated apparent velocity field was used as "observations" and the inversion program "*para.f*" was used to recover the apparent parameters e and d from this apparent velocity field. Using the initial guesses of the parameters $e=0, d=0$ to start the iteration, the inversion program converged quickly and gave inversion results: $e=0.128, d=-0.057$. Comparing the apparent velocity field (red circles) with that calculated from the inverted apparent parameter values (blue line), we see that they are in good agreement except in the near horizontal direction, shown in Figure 3.5a. The apparent velocity field marked as green dots in Figure 3.5a represents the observation data that were input to the inversion program. A large discrepancy between the inverted velocity field and the apparent velocity field was found at large incident angles. This two-layered model does not behave like a completely single-layered VTI model. The fact that $e \neq 0, d \neq 0$ means that this pair of *isotropic* layers exhibits an *apparent transverse isotropy* within a large range of ray angles.

To examine this discrepancy further, more tests were carried out. Because a large discrepancy occurred in the near horizontal direction, the apparent velocity field data in the ranges of ray angle $f \leq f_{max}=80°, 70°, 60°$ were input to the inversion program "*para.f*" in turn. The apparent parameters of this two-layered model were recovered from each of these restricted input ranges of data. Table 3.4 gives the inversion results for the apparent parameters e and d of this two-layered model for each range of input.

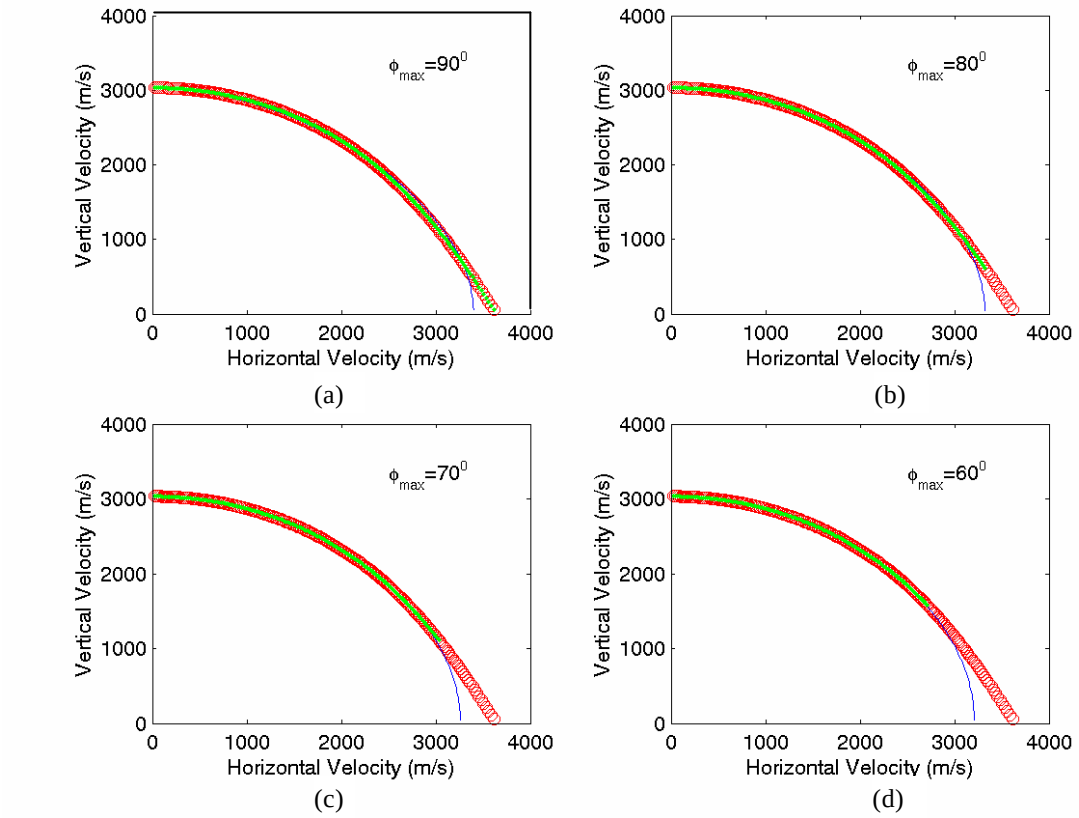

Figure 3.5 Velocity fields for a two-layered model with isotropic components. Velocity fields obtained from the inversion (blue curved lines) and input velocity fields computed by forward modelling (red circles) are illustrated. Different ranges of velocity data at transmission angles $f \le f_{\max}$ (green dots) were input to the inversion program for comparison. Here, the first layer velocities are a_{01}=2600 m/s, b_{01}=1300 m/s, and the second layer velocities a_{02}=3640 m/s, b_{02}=1820 m/s. The thickness ratio z_1/z_2 was assumed to be 1. Notice that the greatest discrepancy occurs in the near horizontal direction.

Table 3.4 Inversion results for the two-layered model composed of two isotropic media. Different ranges of velocity data ($f \le f_{\max}$) were input to the inversion program. Here, the true first layer velocities were a_{01}=2600 m/s, b_{01}=1300 m/s, and the true second layer velocities a_{02}=3640 m/s, b_{02}=1820 m/s. The thickness ratio z_1/z_2 was assumed to be 1. The mean relative error between the inverted velocity field and that from forward modelling is given by $W = \frac{1}{n}\sum_{i=1}^{n}\frac{\left|v_g(i) - v_{g\,mod}(i)\right|}{v_{g\,mod}(i)}$.

a_0(m/s)	b_0(m/s)	f_{max}(°)	e	d	W(%)
3033.33	1516.67	60	0.060	0.002	0.06
		70	0.078	-0.011	0.17
		80	0.100	-0.031	0.39
		90	0.128	-0.057	0.77

Here, $W = \frac{1}{n}\sum_{i=1}^{n}\frac{|v_g(i) - v_{g\,mod}(i)|}{v_{g\,mod}(i)}$, is the mean relative error between the velocity field v_g calculated by inversion and the input velocity field v_{gmod}. Table 3.4 clearly shows that when f_{max} increases, the relative error increases. This indicates that the main errors come from the near horizontal input data. Inputting model data at larger transmission angles to the inversion program will increase the relative errors in the inversion.

Figure 3.5 shows graphically three sets of data. One is the apparent velocity data computed by forward modelling (red circles). The green dots represent the ranges of the input velocity data to the inversion. The velocity fields obtained from the inverted parameters are shown as blue lines. The green and blue velocity fields coincide with each other fairly closely. They match with the red velocity data within the range of input data. When the range of the input velocity data at large transmission angles is decreased, Figure 3.5a to Figure 3.5d show an improvement in the coincidence of these three velocity fields within the range of $f \pounds f_{max}$=*90°*, *80°*, *70°*, *60°*, respectively. However, in the near horizontal transmission directions, large discrepancies occur. This two-layered model cannot be treated as a completely single-layered transversely isotropic medium for all ray angles.

Inputting velocity field data without the larger transmission angle data into the inversion program mainly affects the inverted value of e, as can be seen in Table 3.4. The anisotropic parameter e is defined by the P-wave velocity values both at the vertical and horizontal directions for a TI medium. For a two-layered model, the vertical P-wave velocity is defined by equation 3.9 while the velocity in the limiting horizontal direction is the velocity of the second layer. If the model were a completely TI medium, the value of the parameter e would be calculated by equation 2.20 as *0.220*. Actually, this layered model cannot be treated entirely as a single-layered model, especially in the near horizontal direction. This is the main reason why the

inverted value of e is farther away from *0.22* when we include less data at larger transmission angles in the inversion.

The practical offset limit in laboratory or field measurements is normally less than twice the model thickness, i.e., the transmission angle is $f£64°$. It is expected that no direct measurements would be made beyond such large transmission directions. These limited tests seem to indicate the following. This two-layered model comprising two *isotropic* media can be approximated as a single layered *transversely isotropic* medium, within the practical offset limit of field measurements. The inversion program *"para.f"* can be used to recover the apparent parameters of this two-layered model.

A two-layered isotropic model with different velocity contrasts

Next, the effect of the velocity contrast between these two isotropic layers was examined. When the thickness ratio (z_1/z_2) was fixed at unity, the velocities of the second layer were changed as follows:

$a_{02} = a_{01}(1+c)$, $b_{02} = b_{01}(1+c)$, and c=0.2, 0.4, 0.6, 0.8, 1.

The apparent velocity fields for the above models were generated and assumed to be "observations".

The apparent velocity data with angles $f£64°$ were chosen to input to the inversion program. The inversion results for these two-layered models composed of two isotropic media are given in Table 3.5. The velocity field calculated from the recovered parameters and the synthetic observations were then compared and found to be in good agreement. These two-layered models behave like a single-layered transversely isotropic medium within the range of the input data.

Table 3.5 Inversion results for the two-layered model composed of two isotropic media with different velocity contrasts between these two layers. Here, the thickness ratio (z_1/z_2) is set at 1. The first layer velocities are a_{01}=2600 m/s, b_{01}=1300 m/s, and the second layer velocities are given by $a_{02} = a_{01}(1+c)$, $b_{02} = b_{01}(1+c)$. $\Delta = \sum_{i=1}^{n} \frac{|v_g(i) - v_{g\,\mathrm{mod}}(i)|}{n}$ represents the average error, while $W = \frac{1}{n}\sum_{i=1}^{n} \frac{|v_g(i) - v_{g\,mod}(i)|}{v_{g\,mod}(i)}$ is the relative error between the velocity field from the inverted parameters and the input velocity field within the range of $f£64°$.

c	a_0(m/s)	b_0(m/s)	*e*	*d*	*D*(m/s)	*W*(%)
0.2	2836.36	1418.18	0.021	-0.002	1.2	0.04
0.4	3033.33	1516.67	0.067	-0.002	3	0.09
0.6	3200.00	1600.00	0.125	0.002	4.3	0.13
0.8	3342.86	1671.43	0.190	0.011	5.2	0.15
1	3466.67	1733.33	0.262	0.022	5.9	0.16

The recovered apparent anisotropic parameters e, d with different velocity contrasts c (*=0.2, 0.4, 0.6, 0.8, 1*) are shown in Figure 3.6. The greater the velocity contrasts between these two isotropic media, the greater the apparent parameters e and d for the two-layered model. That is, the more anisotropic it appears to be. However, when the velocity contrast is very small (e.g., c*=0.2*), the absolute values of the inverted apparent parameters e and d are very small (less than 0.022). When the velocity contrast is increased, the model behaves more like a single transversely isotropic layer.

A two-layered model with different thickness ratios

The following tests studied the effects of different thickness ratios (z_1/z_2) on the recovered apparent parameters e and d.

For a two-layered model, the first layer velocities were assumed to be a_{01}*=2600 m/s,* b_{01}*=1300 m/s,* and the second layer velocities were a_{02}*=5200 m/s,* b_{02}*=2600 m/s*. The corresponding velocity contrast for these two layers was c*=1*. The thickness ratio was chosen to be *0.2, 0.4, 0.6, 0.8, 1, 5, 10,* and *100*. The apparent velocity fields for these models were calculated from the program "*twophiv.f*", and these data within the angle range of f*£64°* were inputted to the inversion program.

Table 3.6 gives the recovered apparent parameters with different thickness ratios (z_1/z_2). Velocity fields were then compared to verify the inversion results. When the slower layer is far thinner than that of the faster layer, the recovered apparent parameters e and d are very small. The combination behaves like a single isotropic layer. When the travel times in these two layers are more nearly equal, the absolute values of the recovered apparent parameters e and d increase. Then this two-layered model behaves more like a transversely isotropic medium.

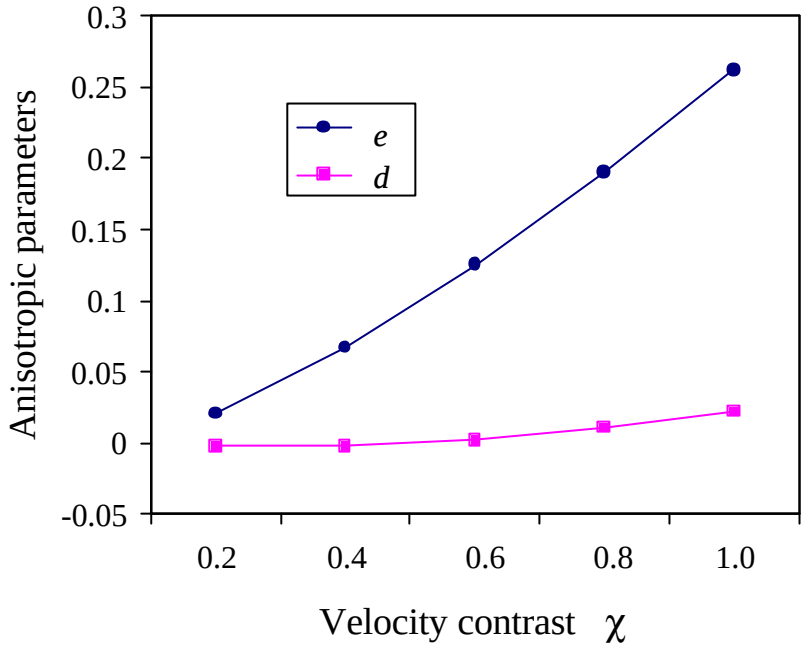

Figure 3.6 Recovered apparent anisotropic parameters e, d plotted against velocity contrast $c = (a_{02} - a_{01})/a_{01}$, or $c = (b_{02} - b_{01})/b_{01}$. The two-layered model is shown in Figure 3.4 with a thickness ratio $z_1/z_2 = 1$. As the velocity contrast increases, the isotropic two-layered model behaves more anisotropically.

Table 3.6 Inversion results for the apparent parameters of a two-layered model composed of two isotropic media with different thickness ratios. Here, the first layer velocities are a_{01}=2600 m/s, b_{01}=1300 m/s, and the second layer velocities are a_{021}=5200 m/s, b_{02}=2600 m/s. $\Delta = \sum_{i=1}^{n} \frac{\left| v_g(i) - v_{g\,\mathrm{mod}}(i) \right|}{n}$ represents the average error, while $W = \frac{1}{n} \sum_{i=1}^{n} \frac{\left| v_g(i) - v_{g\,mod}(i) \right|}{v_{g\,mod}(i)}$ is the relative error between the velocity field from the inverted parameters and the input velocity field within the range of f£64°.

z_1/z_2	a_0(m/s)	b_0(m/s)	e	d	J (%)	W(%)
0.2	4457.14	2228.57	0.090	0.023	2.7	0.06
0.4	4044.45	2022.22	0.154	0.029	4.1	0.1
0.6	3781.82	1890.91	0.199	0.030	4.8	0.12
0.8	3600.00	1800.00	0.235	0.026	5.5	0.15
1	3466.67	1733.33	0.262	0.022	5.9	0.16
5	2836.36	1418.18	0.402	-0.046	8.4	0.29
10	2723.81	1361.91	0.421	-0.070	9.1	0.33
100	2612.94	1306.47	0.412	-0.092	8.4	0.32

Discussion

A two-layered model composed of two *isotropic* media behaves like a single-layered *transversely isotropic* medium, within the offset range in a typical field survey. The inversion program *"para.f"* can recover the apparent anisotropic parameters for this two-layered model. The inverted apparent parameters e and d depend on the velocity contrast and thickness ratio between these two layers. The greater the velocity contrast or the more nearly equal the travel times for these two layers, the more anisotropic this two-layered structure becomes. If the velocity contrast is very small, the apparent parameters e and d will be very small, and the combination becomes more isotropic.

3.2.3 Two-layered Numerical Model Composed of Two VTI or VTI/isotropic Media

After examining the simple two-layered model with isotropic components, let us now examine the results from tests on a generalized two-layered model with both VTI and VTI/isotropic media. The elastic parameters of Plexiglas and Phenolite blocks (Okoye et al., 1997) with isotropic and transversely isotropic properties respectively were used in building a series of numerical models. Parameters for Pierre shale A, B, C, Mesaverde clayshale (5501) and Green River shale (Thomsen, 1986), for which the anisotropic parameters were quoted, were also used. The elastic parameters for each of the modelling materials are shown in Table 3.1. The six representative two-layered models studied are shown in Figure 3.7.

The apparent velocity fields for a set of two-layered models were computed numerically using the forward modelling program *"twophiv.f"*. The symmetry axis was assumed to be vertical in each case. Using the inversion program *"para.f"*, the apparent parameters e and d for each of these two-layered models were then recovered from the synthetic velocity field.

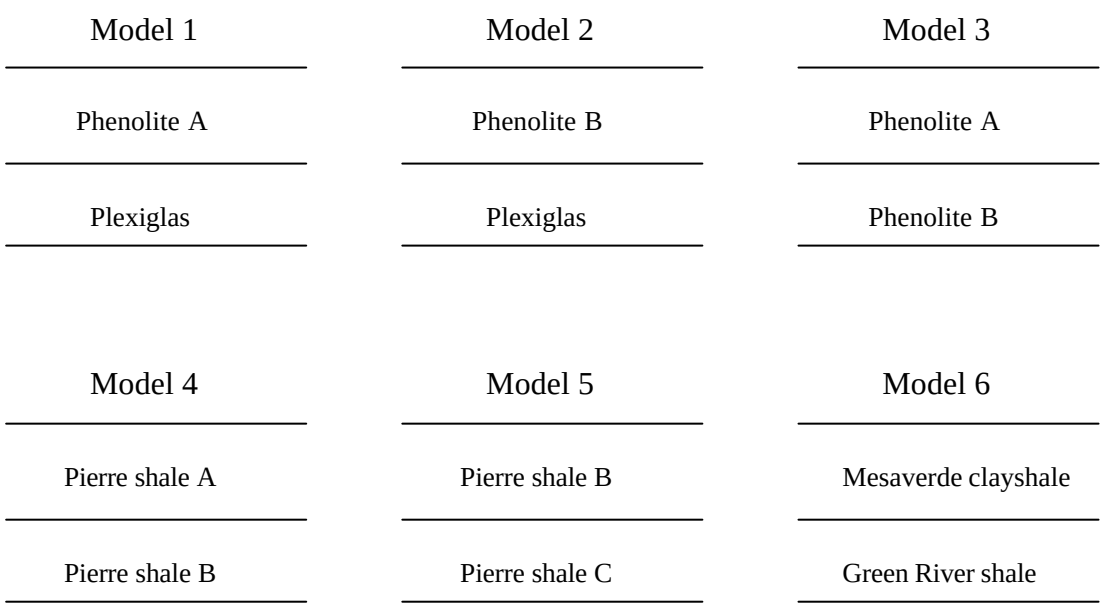

Figure 3.7 Six representative two-layered models. Modelling materials include components which are isotropic and anisotropic with positive and negative values of d. Elastic parameters for these media are given in Table 3.1.

Figure 3.8 gives some examples of the input apparent velocity fields of the two-layered models obtained by forward modelling and those calculated from the parameters recovered by inversion. These show that these two velocity fields are in good agreement except at near horizontal directions. The recovered apparent parameters are partly listed in Table 3.7. More results are shown in (Li et al., 1997). The average errors in velocity fields were less than *6.4 m/s*, and the corresponding relative errors in the inversion were less than *0.2%*. Hence, these two-layered models composed of VTI media or isotropic media can be treated as a single-layered VTI medium with apparent parameters e and d.

It is noticed that for different models, large divergences appear at different large transmission angles. Normally, large divergence between the model data and the velocity field calculated from the inverted parameters occurs when the ray angle exceeds *80°*. The corresponding offsets are well beyond twice the model thickness, which is outside the typical range of field survey geometry. However, for model 6 composing Mesaverde (5501) clayshale and Green River shale, the inversion program diverged. When only the data within the typical survey offset range ($f \pounds 64°$) were put into the inversion program, the inversion program did converge. The synthetic data and the calculated velocity field using the inverted parameters were then compared. Large divergences occurred when the ray angle exceeded *64°*. The components of Model 6 have strong and contrasting anisotropy. For Mesaverde (5501) clayshale $d=0.730$, while for Green River shale $d=-0.220$. This may be the reason why for model 6, the degree of similarity to a single-layered TI medium decreased.

Effects of noise

The presence of noise in travel time measurements in laboratory or field data is inevitable, so the inversion program needs to be able to handle measurement data with

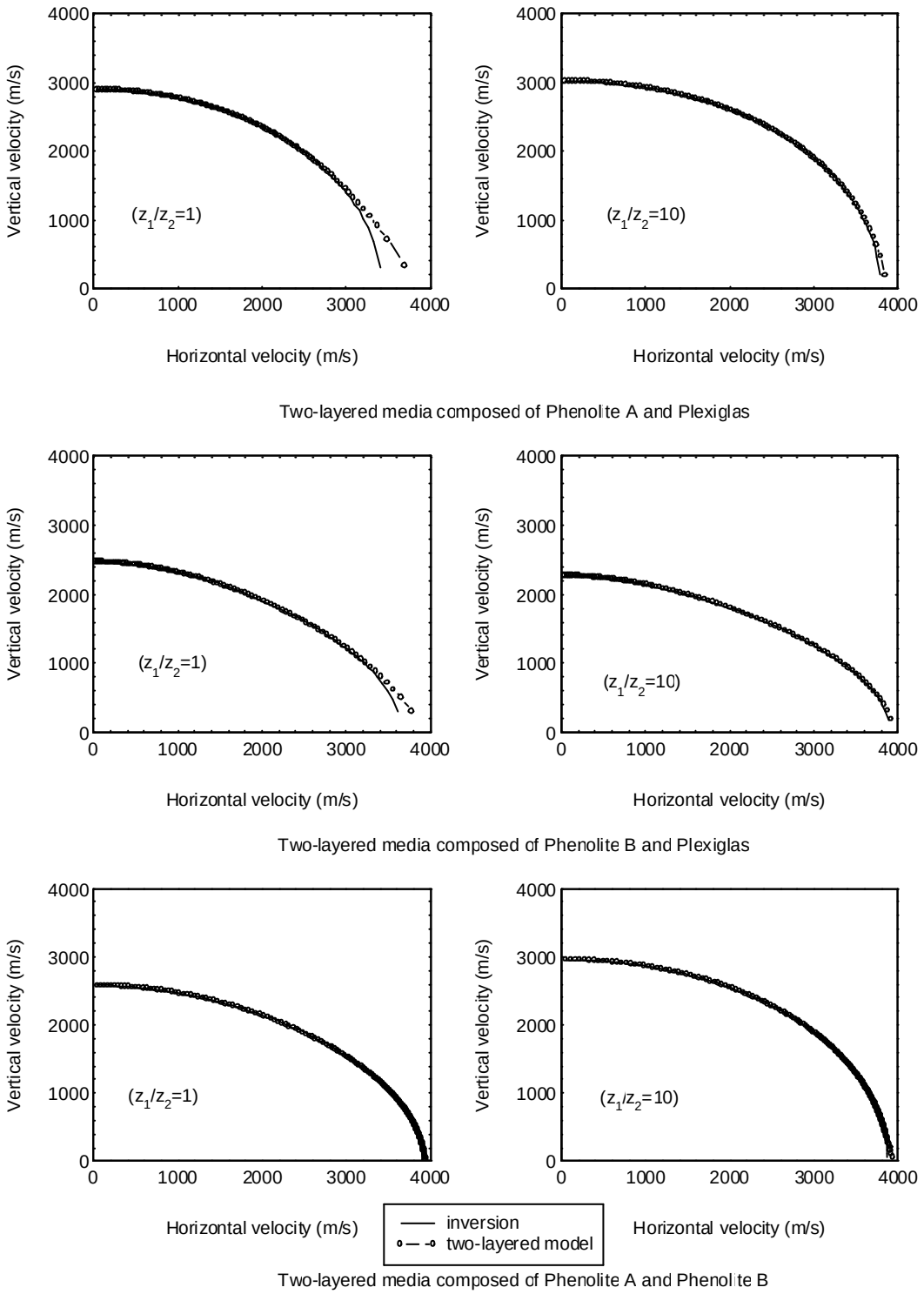

Figure 3.8 The apparent velocity fields for different two-layered models. The apparent velocity field from forward modelling with noise (circle dots), and the calculated velocity field from its recovered parameters determined by inversion (curve) are shown here. The greatest discrepancy occurs at the large transmission angle directions.

Table 3.7 Numerical inversion results for apparent parameters for a two-layered model ($z_1 = z_2$). $\Delta = \sum_{i=1}^{n} \frac{\left| v_g(i) - v_{g\,\mathrm{mod}}(i) \right|}{n}$ represents the average error between the velocity field calculated from the recovered apparent parameters and that from the forward modelling.

	a_0(m/s)	b_0(m/s)	e	d	D(m/s)
Model 1	2901	1468	0.196	0.202	1.3
Model 2	2466	1360	0.599	0.145	0.4
Model 3	2578	1419	0.640	0.379	0.5
Model 4	2089	878	0.156	0.132	0.08
Model 5	2152	926	0.110	0.115	0.2
Model 6	3582	1901	0.227	0.242	6.4

random noise. Assuming the thickness of each layer to be *1000 m*, random noise in travel time up to ±*10 ms*, which is the typical error in a field survey, was synthetically generated. The errors in the travel times produced were less than *2%* and were added to the model data.

After the addition of random noise to the input travel time data, convergence was still achieved by the inversion program. The differences in recovered apparent parameters e and d from travel times with noise and without noise are below *0.04*, as may be seen by comparing Table 3.8 with Table 3.7. The observations were then compared with the velocities calculated from the inverted parameter values. Figure 3.9 shows an example. In the figure, the apparent velocity field from forward modelling with noise is represented by circles, the sub-set of the apparent velocity field inputted to the inversion is marked by *, while the calculated velocity field from the recovered parameters determined by inversion is denoted by a curve. The results show that the inversion program can handle model data with a typical range of random noise. The inversion procedure has been found to be robust.

The apparent anisotropic parameters recovered from models with different thickness ratios

Now we examine the values of the apparent parameters recovered when thickness ratios (z_1/z_2) were varied. The thickness ratio was chosen from *0.1* to *10*.

The synthetic velocity data were generated first for each model. The inversion program was then run using the synthetic data as input. The apparent elastic parameters recovered from the two-layered numerical models with different thickness ratios are shown in Figure 3.10. Analysis of the results indicates that the apparent values of parameters e and d have values which are intermediate between those of the individual layers. How close these apparent values of parameters e and d are to the

Table 3.8 Numerical inversion results for apparent parameters for a two-layered model ($z_1 = z_2$) with random noise. $\Delta = \sum_{i=1}^{n} \frac{\left| v_g(i) - v_{g\,\mathrm{mod}}(i) \right|}{n}$ represents the average differrence between the velocity field calculated from the recovered apparent parameters and that from the forward modelling.

	a_0(m/s)	b_0(m/s)	e	d	D(m/s)
Model 1	2901	1468	0.193	0.206	20
Model 2	2466	1360	0.571	0.160	14
Model 3	2578	1419	0.648	0.380	16
Model 4	2089	878	0.157	0.131	10
Model 5	2152	926	0.107	0.117	10
Model 6	3582	1901	0.262	0.195	56

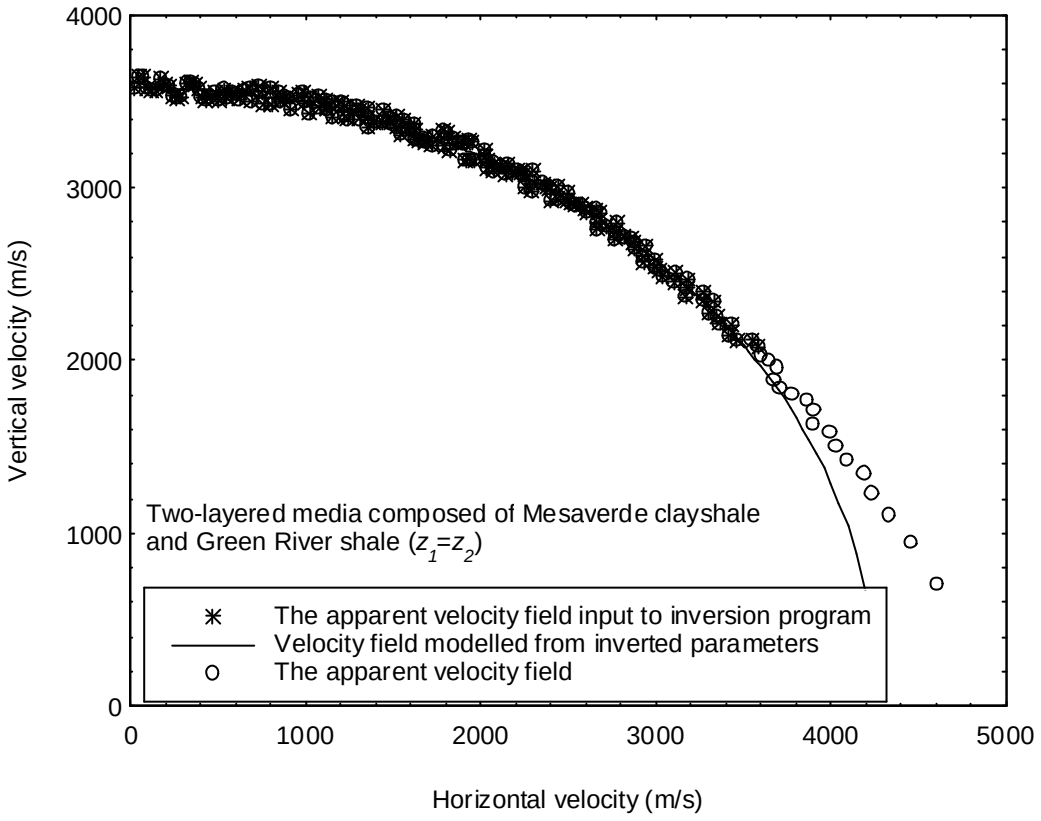

Figure 3.9 The apparent velocity fields for a two-layered model composed of Mesaverde clayshale and Green River shale with random noise. Circles represent the apparent velocity field from forward modelling with noise, stars are the input ranges of the apparent velocity field, while the calculated velocity field from its recovered parameters determined by inversion is denoted by a curve. The travel times had added noise generated by computer before inversion to simulate real measurements. The greater discrepancies occur at large transmission angles.

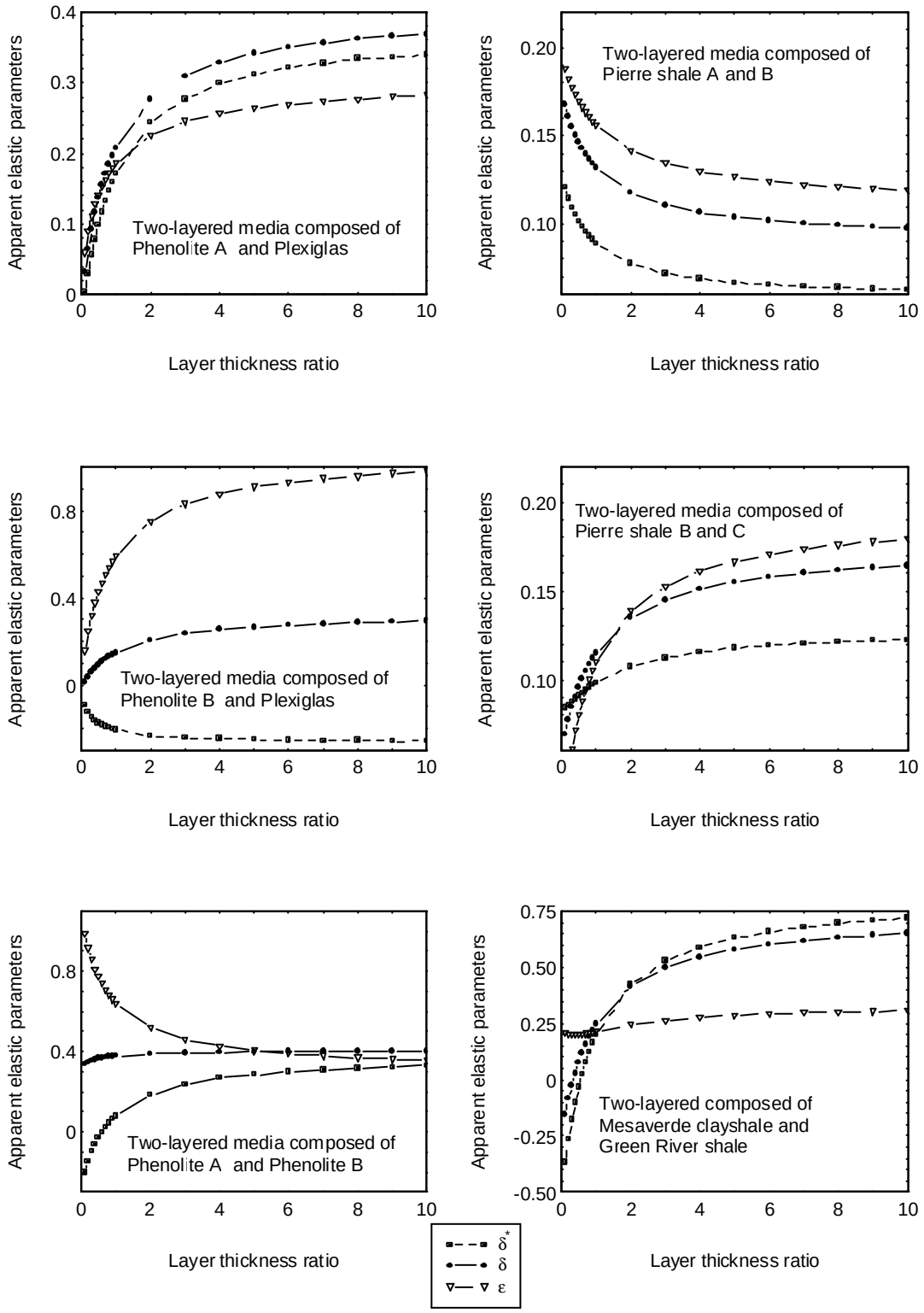

Figure 3.10 The recovered elastic parameters of two-layered models with different thickness ratios. The inverted apparent parameters are related to the layer thickness ratios.

values of any one component depends on the thickness ratio. For example, inversion of data from the two-layered model composed of Phenolite A and Phenolite B, when $z_1/z_2=0.1$, gave the apparent parameters $e=0.986$, $d=0.338$, which are close to the values of the elastic parameters for Phenolite B (thicker layer). When $z_1/z_2=10$, the recovered apparent parameters were $e=0.356$, $d=0.401$, which are close to the values for Phenolite A, which is the thicker layer in this case.

Using the curve-fitting function in "EasyPlot", a relationship between the apparent and the individual parameters was established. Simple formulas for the apparent parameters were then developed as follows:

$$e = \frac{e_1 z_{12}}{a_1 z_{12} + b_1} + \frac{e_2 z_{21}}{a_2 z_{21} + b_2} = \frac{e_1 z_1}{a_1 z_1 + b_1 z_2} + \frac{e_2 z_2}{a_2 z_2 + b_2 z_1}, \tag{3.11a}$$

$$d = \frac{d_1 z_{12}}{c_1 z_{12} + d_1} + \frac{d_2 z_{21}}{c_2 z_{21} + d_2} = \frac{d_1 z_1}{c_1 z_1 + d_1 z_2} + \frac{d_2 z_2}{c_2 z_2 + d_2 z_1}. \tag{3.11b}$$

Here $z_{12} = 1/z_{21} = z_1/z_2$ is the thickness ratio of these two layers. Empirical constants a_1, a_2, b_1, b_2, c_1, c_2, d_1, d_2 were obtained from curve fitting, and were different for different models. Mostly they have values around 1, but there are some exceptions. These results are shown in Table 3.9, while some examples of curve fitting are given in Figure 3.11.

Let us assume that a multi-level VSP survey is carried out in a region where two major formations exist. Let the lower layer be considerably thicker than the upper layer. Shots are recorded at various levels in the lower layer and at the interface. The following strategy may be used to deduce the apparent parameters for a combined layer to a depth where no geophone is located. The apparent velocity field for the total layer above any geophone can be inverted from the signals recorded by the geophone. The corresponding apparent parameters may then be recovered. The interval elastic parameters of the lower layer may also be recovered using the method to be developed in Chapter 4. For each geophone, the thickness ratio (z_1/z_2) is determined

Table 3.9 Empirical constants a_1, a_2, b_1, b_2, c_1, c_2, d_1, d_2 obtained from curve fitting procedures.

	a_1	b_1	a_2	b_2	c_1	d_1	c_2	d_2
Model 1	1.020	0.504			0.992	0.972		
Model 2	1.030	0.747			0.978	1.280		
Model 3	1.000	0.790	0.998	1.260	0.998	0.687	1.010	1.360
Model 4	1.000	1.210	1.000	0.830	1.000	1.230	0.998	0.911
Model 5	1.010	0.922	0.844	0.920	0.997	0.950	1.010	1.370
Model 6	0.994	1.250	0.847	2.050	0.982	0.988	0.880	0.874

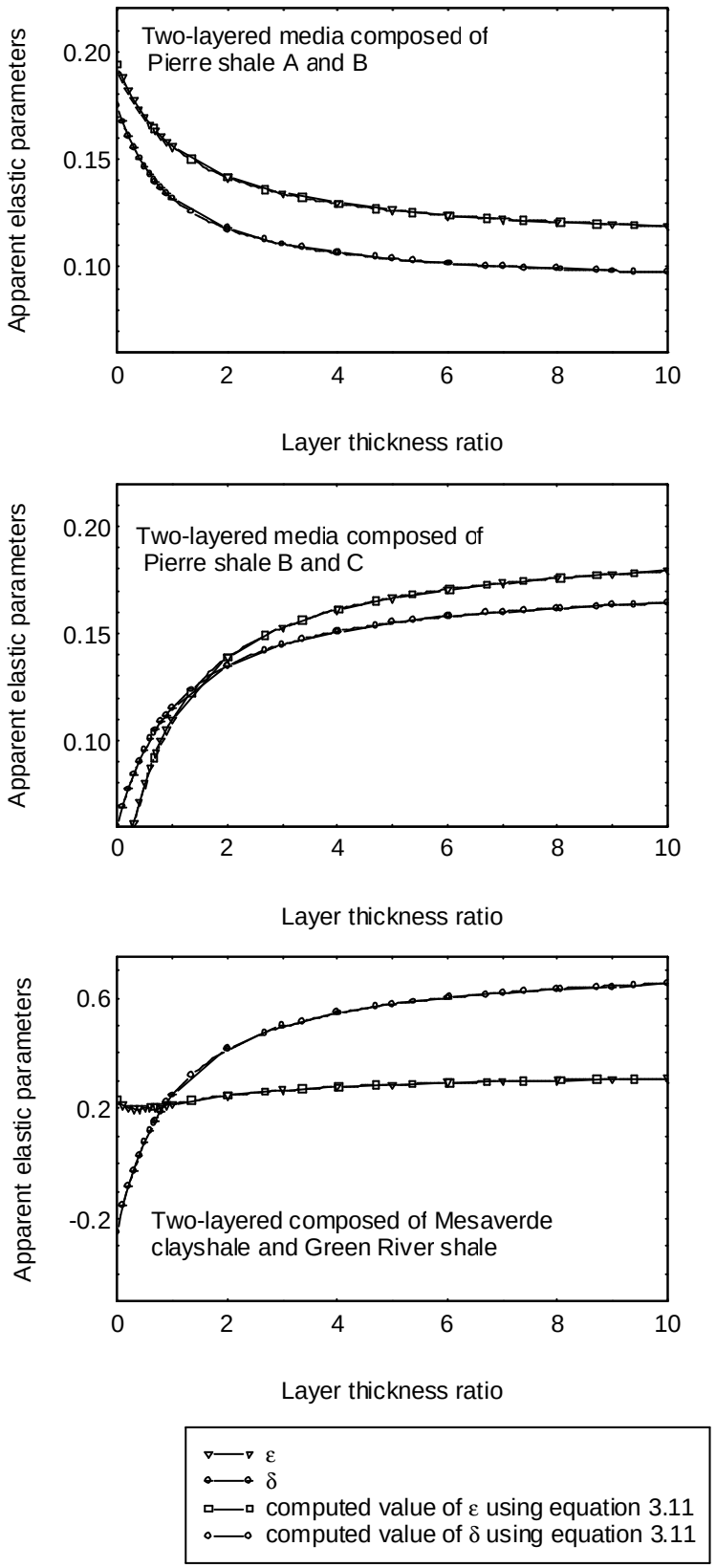

Figure 3.11 Curve-fitting for apparent parameters *e* and *d* with different model thickness ratios. Equation 3.11 was used to best fit the inverted apparent parameters. Empirical constants in equation 3.11 were then determined.

from the depths of the geophone and the upper layer thickness. The recovered parameters can then be plotted against the thickness ratios for these multi-level geophones. The empirical constants (a_1, a_2, b_1, b_2, c_1, c_2, d_1, d_2) in equation 3.11 may be obtained by a curve fitting technique applied to these graphs. Then for the layer to a depth beyond the deepest geophone, the apparent parameters may be inferred using equations 3.11 together with the known empirical constants. This information would be useful in imaging deeper reflectors.

The recovered apparent parameters related to different individual layer parameters

Fixing the layer thicknesses at $z_1 = z_2$, the changes in apparent elastic parameters were examined with the changes in individual layer parameters. Figure 3.12 shows the changes in apparent parameters e and d as a result of changes in the corresponding parameters in the first layer (e_1, d_1). The P-wave anisotropy e shows a quadratic increase, while d shows a linear relation with increasing e_1. Changes in e_1 have a greater influence on e rather than on d (refer to Figure 3.12a, 3.12b, 3.12c). When d_1 changes, both e and d are nearly linearly related to d_1, but the slope of the d curve is greater than the e curve (refer to Figure 3.12d, 3.12e, 3.12f). Hence, both e and d will be affected when e_1, or d_1 changes respectively, but e_1 has more impact on e than on d, while d_1 has more impact on d than on e.

Inversion program "*para.f*" may be used to recover the apparent anisotropy parameters of a two-layered model. A two-layered medium may be treated as a single transversely isotropic medium with apparent elastic parameters within the offset range

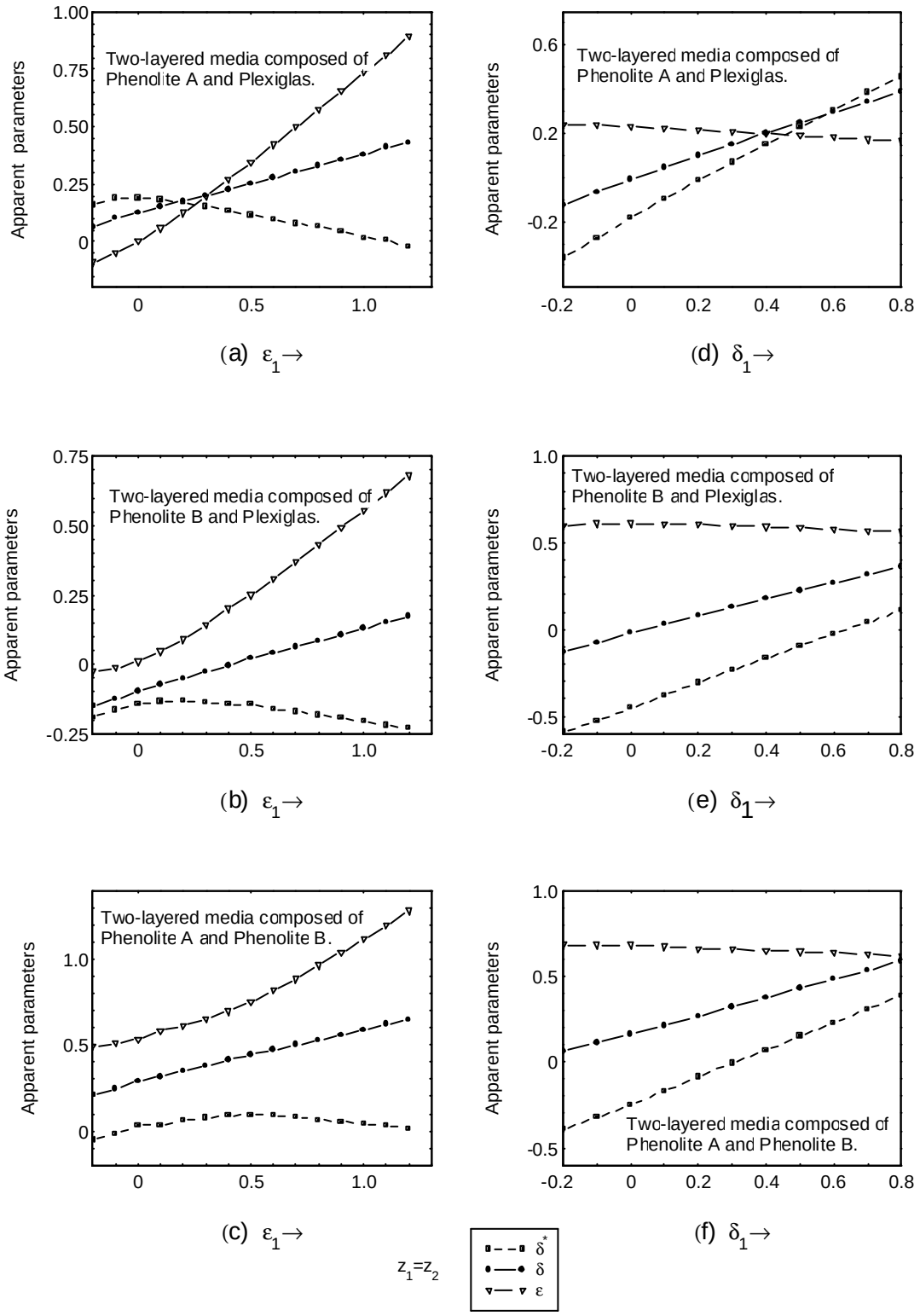

Figure 3.12 The effects of the individual layer's parameters e_1 and d_1 on the inverted apparent parameters e and d. Changes in e_1 have more impact on e than on d, while changes in d_1 have more impact on d than on e.

of a practical field survey. These depend in a generally non-linear fashion on the parameters and thicknesses of the individual layers.

3.2.4 Multi-layered Model

For a multi-layered model as shown in Figure 3.13, an inversion procedure is proposed to recover the apparent parameters of successive layers as described below.

The first layer may be treated as a single-layered medium as discussed in Section 3.1. The downhole receiver R_1 records the seismic signals travelling through the first layer from sources on the surface at varying distances from the well head. The apparent ray distance between a source *S* and the receiver R_1, and the apparent ray angle between a ray path SR_1 and the vertical direction may then be calculated. The first arrival times are converted to a velocity field. The elastic parameters of the first layer a_{01}, b_{01}, e_1 and d_1 may then determined using program "*para.f*", as was outlined in Section 3.1.

Next, the first two layers may then be treated like a two-layered model as discussed in Section 3.2.1. Downhole receiver R_2 records the seismic signal through these two layers. The apparent ray distances SR_2 may be calculated first for waves emitted from any source *S*. The corresponding apparent ray angles may also be calculated as the angles between SR_2 and the vertical direction. A velocity field for seismic waves propagated through the first two layers may be obtained. The apparent elastic parameters of the combined layers may then be obtained by using program "*para.f*" as before.

Similarly, travel times can be recorded from different receivers at the base of each successive layer in the same fashion. Downhole receiver R_i records the seismic signal through these upper i layers. After calculating the apparent ray distances and the

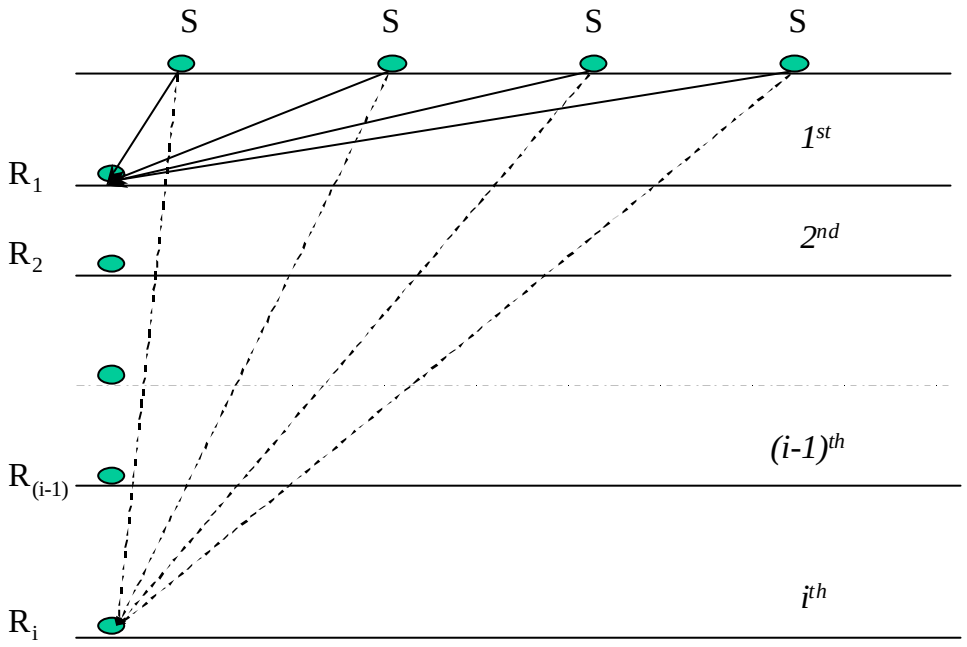

Figure 3.13 Seismic measurements in multi-layered media. A walkaway VSP survey is simulated by placing a receiver at the base of each successive layer, adding more layers as we go.

corresponding apparent ray angles, the effective velocity field of waves propagated through the first *i*-layers can be obtained. The apparent elastic parameters of the first *i*-layers may then determined by using program *"para.f"*, treating these layers as a single layer.

3.3 P-wave Inversion of Data from a Transversely Isotropic Medium with a Tilted Symmetry Axis

The inversion program *"para.f"* was developed to recover the apparent elastic parameters from the apparent velocity field observed in transversely isotropic media with a vertical symmetry axis (VTI). However, if the sedimentary beds are dipping, the symmetry axis of the layered VTI medium may not be vertical. For a layered transversely isotropic medium with a tilted symmetry axis (TTI), the recorded transmission travel times may be quite different from those for a VTI medium with the same elastic parameters as shown in the following example. For Mesaverde (5501) clayshale and Green River shale, Figure 3.14 shows some comparisons of synthetic VSP shot records for a single-layered medium with vertical and then tilted symmetry axes (Li et al., 1998b). The angle of tilt given to the symmetry axis is *45°*. It can be seen that a tilted axis of symmetry can have a significant effect on recorded VSP travel times.

In this section, the studies that follow are based on a layered transversely isotropic medium with a tilted symmetry axis (TTI medium). An inversion program will be developed to recover the tilt angle as well as the elastic parameters for a layered TTI medium. The research will be limited to the 2-D case where the survey line is along the dip direction as stated in Chapter 1.

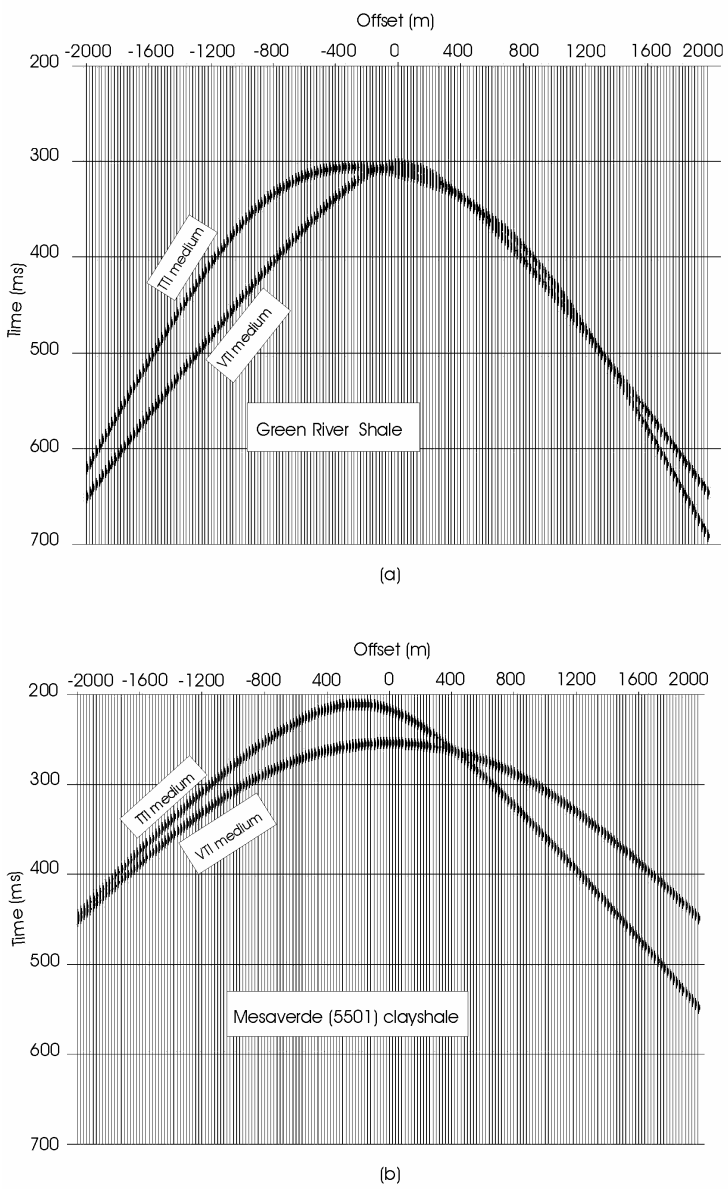

Figure 3.14 Two synthetic VSP data sets each for a VTI medium and a TTI medium with a *45°* tilt angle. The elastic parameters used are (a) Green River shale for which *d* is negative; and (b) Mesaverde (5501) clayshale for which *d* is positive. Here, the depth of the medium is assumed to be *1000 m.* A tilted axis of symmetry causes a significant change in recorded travel times.

3.3.1 Inversion Method

Consider a layered transversely isotropic medium with a symmetry axis tilted at an angle y from the vertical direction as shown in Figure 3.15. The survey line is in the dip direction. We start with the velocity equation for a VTI medium, re-written by Tsvankin (1996) from Thomsen (1986). Rotating the symmetry axis from the vertical to a tilt angle y, the phase velocity for P-waves in the direction of phase angle q measured from the vertical direction, is then re-written as (Li et al., 2000c):

$$\frac{v_p^2(q,y)}{a_0^{\,2}} = 1 + e\sin^2(q-y) - \frac{f}{2} + \frac{f}{2}\sqrt{1 + \frac{4\sin^2(q-y)}{f}(2d\cos^2(q-y) - e\cos 2(q-y)) + \frac{4e^2\sin^4(q-y)}{f^2}}, \quad (3.12)$$

where, $f = 1 - b_0^{\,2}/a_0^{\,2}$.

The group velocity $v_g(f,y)$ at ray angle f from the vertical direction can be re-written from equations 2.28 and 2.29 as:

$$v_g^2(f,y) = v_p^2(q,y) + \left(\frac{\partial v_p(q,y)}{\partial q}\right)^2, \quad (3.13)$$

$$\tan(f-y) = \frac{\tan(q-y) + \frac{1}{v_p(q,y)}\cdot\frac{\partial v_p(q,y)}{\partial q}}{1 - \tan(q-y)\cdot\frac{1}{v_p(q,y)}\cdot\frac{\partial v_p(q,y)}{\partial q}}. \quad (3.14)$$

Using the first arrival picks from a dip line walkaway VSP survey, one can obtain a set of observations (x — offset *vs* t — P-wave first arrival time). Hence, the effective group velocity over a range of directions can be obtained. Then, the problem is how to find estimated values of the apparent parameters (a_0, b_0, e, d and y) by fitting a calculated velocity field curve to these observations.

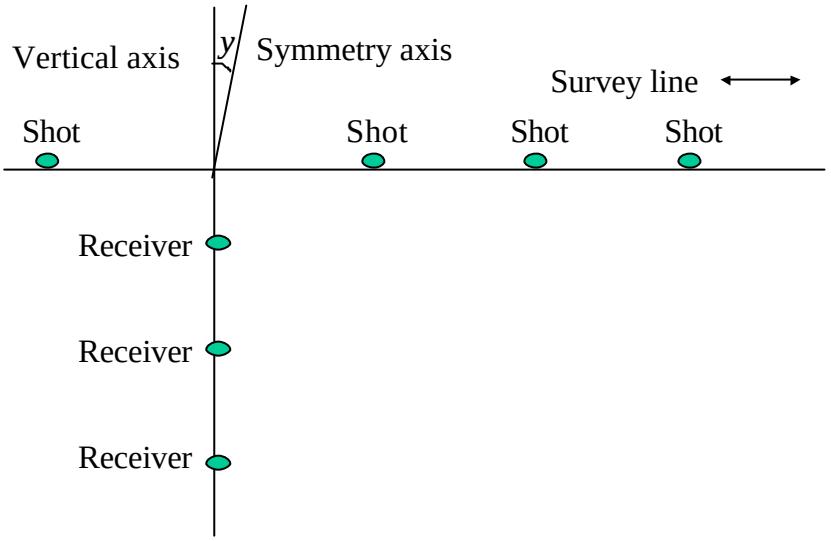

Figure 3.15 Model of a transversely isotropic medium with a tilted symmetry axis (TTI medium). The tilt angle is y. Shot and receiver locations for a walkaway VSP survey are shown on this dip section.

The velocity equations depend nonlinearly on the unknown parameters (a_0, b_0, e, d and y). To reduce the chances of divergence of the inversion process in what follows, the *ratio* of the P-wave and S-wave velocities perpendicular to the dip direction (a_0/b_0) was assumed to be obtained through direct measurement and inputted to the inversion. For example, given data sets like the TTI plots in Figure 3.14, velocities at different directions were inverted from travel times. The value of a_0 (similarly b_0) may be found as the minimum value in the velocity plot for most existing sedimentary rocks. Then the ratio (a_0/b_0) may be obtained. To increase the accuracy, the value of a_0 could be left for the inversion. The tilt angle y could also be found from the velocity plot. This will not necessarily be very accurate though due to the small change rate of velocity with direction near the symmetry axis. However, such a value could be used as the starting value in the following iteration procedure. That would leave four parameters — a_0, e_0, d and y to be inverted for.

The least-squares method, which was previously used in the program "*para.f*" in Section 3.1 and Section 3.2, generally failed to find suitable values for parameters a_0, e, d and y, due to a tendency for that iteration procedure to diverge. The Levenberg-Marquardt Method (Press et al., 1992a), instead of the least-squares method, was then chosen for a new inversion program "*paratilt.c*". The Levenberg-Marquardt method is described as follows:

The model to be fitted is:

$$v_{gcal}(f) = v_{gcal}(f, a_0, e, d, y). \tag{3.15}$$

The "chi-square" merit function is:

$$c^2(a_0, e, d, y) = \sum_{i=1}^{nobs} \frac{1}{s_i^2} \left[v_{gobs}(f_i) - v_{gcal}(f_i, a_0, e, d, y) \right]^2. \tag{3.16}$$

Here, s_i is the measurement error (standard deviation) of the i^{th} data point. The measurement errors may all be set to be a constant value of unity (Press et al., 1992a). In the following derivations, $s_i = 1$.

For the most suitable parameter set $\{a_0, e, d, y\}$, because c^2 will be a minimum, the gradient of c^2 with respect to the parameters a_0, e, d and y will be zero. Thus, we need to solve the following linear equations:

$$\sum_{l=1}^{4} a_{kl} da_l = b_k . \tag{3.17}$$

Where, a_l represents the variables a_0, e, d, y . The elements of the curvature matrix are defined as:

$$\begin{aligned} a_{kl} &= \sum_{i=1}^{nobs} \left[\frac{\partial v_{gcal}(f_i, a_0, e, d, y)}{\partial a_k} \frac{\partial v_{gcal}(f_i, a_0, e, d, y)}{\partial a_l} \right], \\ b_k &= \sum_{i=1}^{nobs} \left[v_{gobs}(f_i) - v_{gcal}(f_i, a_0, e, d, y) \right] \frac{\partial v_{gcal}(f_i, a_0, e, d, y)}{\partial a_k}. \end{aligned} \tag{3.18}$$

Then we find the increments da_l by solving equation 3.17, add them to the estimated values of the parameter a_l, to give the next approximation in the iteration process. Using the steepest descent method with an adjustable "fudge factor" l, we have:

$$l\, a_{ll} da_l = b_l . \tag{3.19}$$

I now define a new matrix a' by

$$a'_{lk} \equiv a_{lk}(1 + l\, d_{lk}), \text{ where, } d_{lk} = 0, \text{ when } l \neq k ;$$

$$d_{lk} = 1, \text{ when } l = k . \tag{3.20}$$

Equation 3.17 is then replaced by

$$\sum_{l=1}^{4} a'_{kl}\, da_l = b_k . \tag{3.21}$$

The constant l is automatically changed during the inversion process. When the chi-square function increases from the previous iteration, l is increased by a factor of

10. When the chi-square function decreases from the previous iteration, l is decreased by a factor of *10*. A very large l will force equation 3.21 to become equation 3.19, while a near zero value of l makes equation 3.21 identical to equation 3.17. The iteration program proceeds until 'chi-square' — the sum of the squared differences between observed and calculated velocity field — changes by less than an arbitrary *0.0001* from the previous iteration. The standard errors of the fitted parameters a_0, e, d and y are estimated by setting l to zero, and finding the relevant diagonal elements of the curvature matrix. The Levenberg-Marquardt Method works very well for this inversion problem.

Four subroutines *mrqmin.c, mrqcof.c, covsrt.c, gaussj.c*, implementing parts of the Levenberg-Marquardt Method, were included into the main program "*paratilt.c*".

3.3.2 Numerical Results and Discussions

A transversely isotropic model with a tilted axis of symmetry (TTI) was set up to carry out a series of numerical tests.

Shots were assumed on the top surface of the TTI model, with a receiver located at the bottom of the model, simulating a real field survey of the type illustrated in Figure 3.15. The synthetic velocities at different ray directions were then generated along a survey line, as follows.

My program "*phiv.f*" developed in Section 3.1.2 was modified using equations 3.12, 3.13, and 3.14 instead of equations 2.22, 2.28 and 2.29. The synthetic velocity data for a TTI model were then generated. Here, the offset was chosen to a maximum of twice the model thickness. It included positive and negative offsets. The number of the shots was *200*. The geometry followed the offset range and observation number of the

typical marine field VSP survey. Testing was carried out on various numerical model materials as described below.

The computer generated velocity data were used to test the inversion program "*paratilt.c*". If the velocity field calculated from the inverted results is in good agreement when plotted with the input velocity data, then the inversion program "*paratilt.c*" will be considered to have been successful.

Table 3.10 gives the elastic parameters of four rocks (Thomsen, 1986) in which the anisotropy varies from weak to strong, and with positive and negative d values. These parameters of real sedimentary rocks were used to generate synthetic data. The tilt angle y was selected as one of the following representative angles *-10°*, *0°*, *10°*, *45°*, and *90°*.

Numerical models with the parameters of Taylor sandstone

Using Taylor sandstone parameters with different tilt angles as an example, synthetic velocities at different ray directions were generated using program "*phiv.f*". To simulate real VSP surveys more closely, the thickness of the model was assumed to be *1000 m*, and the maximum noise in travel time to be *±10 ms*. The synthetic velocity data for each model were generated again with noise.

The elastic parameters and the tilt angles were then recovered by the TTI inversion method described in Section 3.3.1. Table 3.11 shows the initial input values of variables to the iteration and their inversion results. For the synthetic VSP data, the recovered elastic parameters and tilt angles from the inversion program "*paratilt.c*" converged to the correct model values within acceptable errors. The error in e, d and y was less than *0.001* without noise, and *0.03* with random noise. For each model, the calculated velocity field was compared with the synthetic data. Agreement was seen

Table 3.10 The elastic parameters (Thomsen, 1986) of the measured sedimentary rocks used in building the numerical single layer TTI models.

Sedimentary rock	$a_0(ms^{-1})$	$b_0(ms^{-1})$	e	d
Taylor sandstone	3368	1829	0.110	-0.035
Mesaverde clayshale (5501)	3928	2055	0.334	0.730
Dog Creek shale	1875	826	0.225	0.100
Green River shale	3292	1768	0.195	-0.220

Table 3.11 Inversion results for Taylor sandstone models with different tilt angles. The ratios of P-wave and S-wave vertical velocities (a_0/b_0) were input manually, and were held fixed when the inversion was executed.

Tilt angles			$a_0(ms^{-1})$	$b_0(ms^{-1})$	e	d	y (*radian*)
0 radian≈ 0°	Input parameters		3000		0	0	0
	Output parameters	No noise	3368	1829	0.110	-0.035	0.000
		With noise	3362	1826	0.102	-0.017	-0.014
0.15 radian≈ 10°	Input parameters		3000		0	0	0
	Output parameters	No noise	3368	1829	0.110	-0.035	0.150
		With noise	3364	1827	0.104	-0.021	0.147
0.78 radian≈ 45°	Input parameters		3000		0	0	0.4
	Output parameters	No noise	3368	1829	0.110	-0.035	0.780
		With noise	3376	1833	0.107	-0.053	0.793
1.57 radian≈ 90°	Input parameters		3000		0	0	1.5
	Output parameters	No noise	3368	1829	0.110	-0.035	1.570
		With noise	3377	1834	0.108	-0.045	1.566
-0.15 radian≈ -10°	Input parameters		3000		0	0	0
	Output parameters	No noise	3368	1829	0.110	-0.035	-0.150
		With noise	3364	1827	0.105	-0.025	-0.173

between these two velocity fields, same as that in Figure 3.2 for positive and negative offsets. The introduction of random noise affects the accuracy of the recovered elastic parameters, but the inversion program still provides satisfactory results. The inversion program *"paratilt.c"* was considered to be successful. It is expected that the inversion program *"paratilt.c"* may be reliably applied to field survey data.

It is noticed that from the results shown in Table 3.11, that the initial hypothetical input values of e, d and y may be chosen as zeros. However, when the tilt angle y increases, the initial hypothetical input values of y need to be non-zero for the inversion procedure to converge. For Taylor sandstone with a tilt angle of *0.78* radian (» *45*°), the input tilt angle was chosen as *0.4* radian. With the input tilt angle chosen to be *0*, the inversion program diverged. The initial hypothetical input values of e, d and y may also influence the inversion to yield unreasonable results. Hence, it is better to choose starting values for the elastic parameters and the tilt angle on geological grounds. Values of these parameters sufficiently close to the correct ones should be found for convergence to be assured.

Numerical models with parameters for different sedimentary rocks (same tilt angle)

In the following test, the tilt angle for the model was assumed to be *0.5* radian ≈ *30*°. Program *"phiv.f"* was used to generate synthetic velocity data for the four representative sedimentary rocks in Table 3.10. These synthetic velocity data were then input to the inversion program *"paratilt.c"*. Inversion results are shown in Table 3.12. The recovered elastic parameters and tilt angles agree very well with their real values. The differences between the parameters e, d and y obtained by inversion and those used to generate the input data are less than *0.001* with no random noise added. It is noticed that the non-zero initial input values of e, d and y are needed for the

Table 3.12 Inversion results for various sedimentary rocks with a tilt angle of 0.5 radian (~30°). The ratios of P-wave and S-wave vertical velocities (a_0/b_0) are fixed when the inversion is executed.

0.5 radian≈30°			$a_0(ms^{-1})$	$b_0(ms^{-1})$	e	d	y (radian)
Taylor sandstone	Exact values		3368	1829	0.110	-0.035	0.500
	Input parameters		3000		0	0	0
	Output parameters	No noise	3368	1829	0.110	-0.035	0.500
		With noise	3375	1833	0.104	-0.045	0.520
Mesaverde clayshale (5501)	Exact values		3928	2055	0.334	0.730	0.500
	Input parameters		3000		0	0	0
	Output parameters	No noise	3928	2055	0.334	0.730	0.500
		With noise	3933	2057	0.329	0.719	0.496
Dog Creek shale	Exact values		1875	826	0.225	0.100	0.500
	Input parameters		2000		0	0	0.2
	Output parameters	No noise	1875	826	0.225	0.100	0.500
		With noise	1876	827	0.222	0.097	0.500
Green River shale	Exact values		3292	1768	0.195	-0.220	0.500
	Input parameters		3000		0	-0.1	0.3
	Output parameters	No noise	3292	1768	0.195	-0.220	0.500
		With noise	3299	1772	0.187	-0.225	0.513

inversion program to converge for some cases, as that for Taylor sandstone model in Table 3.11.

Next, the thickness of the model was assumed to be *1000 m*, and the maximum noise in travel time to be *±10 ms*, the same as that for Taylor sandstone models in the above section. Random noise of *2% ~ 3%* in travel times was added to the synthetic data. The errors in the inversion results were found to be less than *0.02*, also shown in Table 3.12. The input velocity field, with added random noise generated by forward modelling, was compared with that computed from the inversion results. Figure 3.16 gives an example for a Dog Creek shale model with a tilt angle of *0.5 radian*. These two sets of velocity data are in good agreement. The inversion program was successful in recovering the elastic parameters and the tilt angle.

These numerical results so far indicate that my inversion program "*paratilt.c*" is capable of recovering the elastic parameters and angles of tilt in a single transversely isotropic medium with a tilted symmetry axis from a dip line walkaway VSP survey.

Further testing of the inversion (VTI) result for a TTI model

For the same synthetic data of Dog Creek shale model with a tilt angle of *0.5 radian*, the inversion program was run again with a VTI assumption (fixing tilt angle $y = 0$). The input synthetic velocity field and that from the inverted parameters were compared, and shown in Figure 3.17. The differences between the velocity field generated from the recovered parameters and synthetic data were substantial.

This is clearly a case where a minimum error function was found, yet the inversion result is not satisfactory! The use of an inappropriate model like this is expected to give a faulty result. As stated in Section 2.1, a verification procedure, like the "*chi-by-eye*" approach, needs to be carried out after we obtain an inversion result.

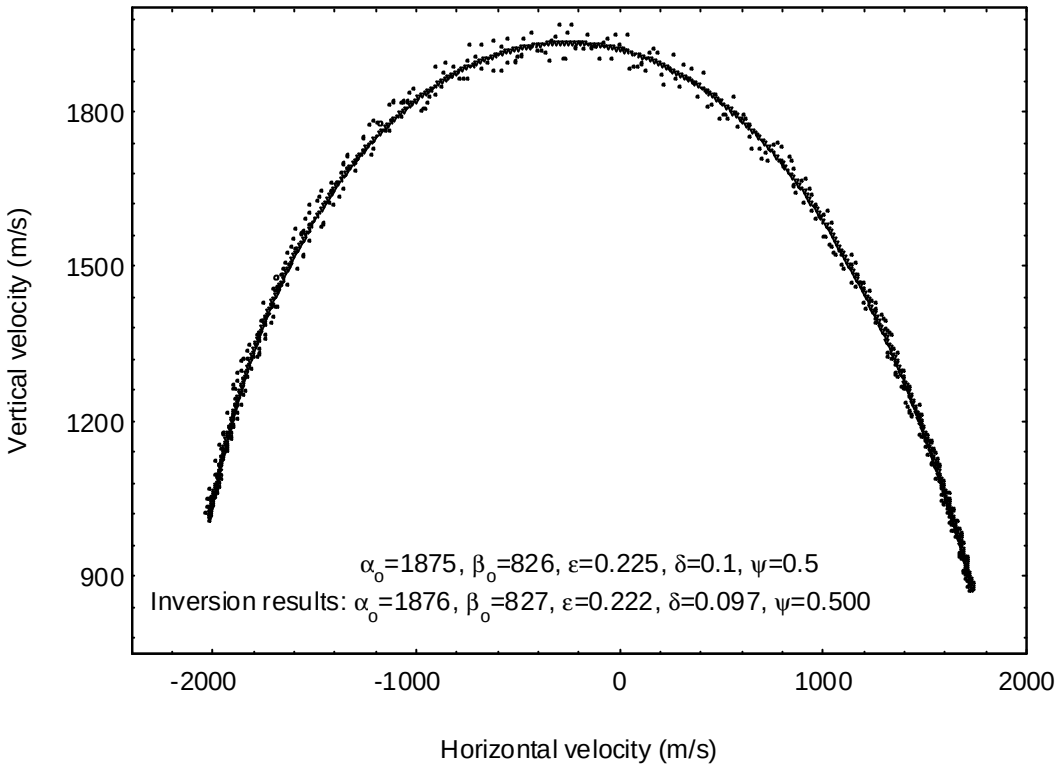

Figure 3.16 Comparison of the inversion result with the model data and the velocity fields for a TTI Dog Creek shale model. The circles represent the synthetic velocity field generated by forward modelling with stochastic noise, while the curve is the velocity field generated using the inverted elastic parameters. The values of the inverted parameters are close to the model values. These two velocity fields are in good agreement.

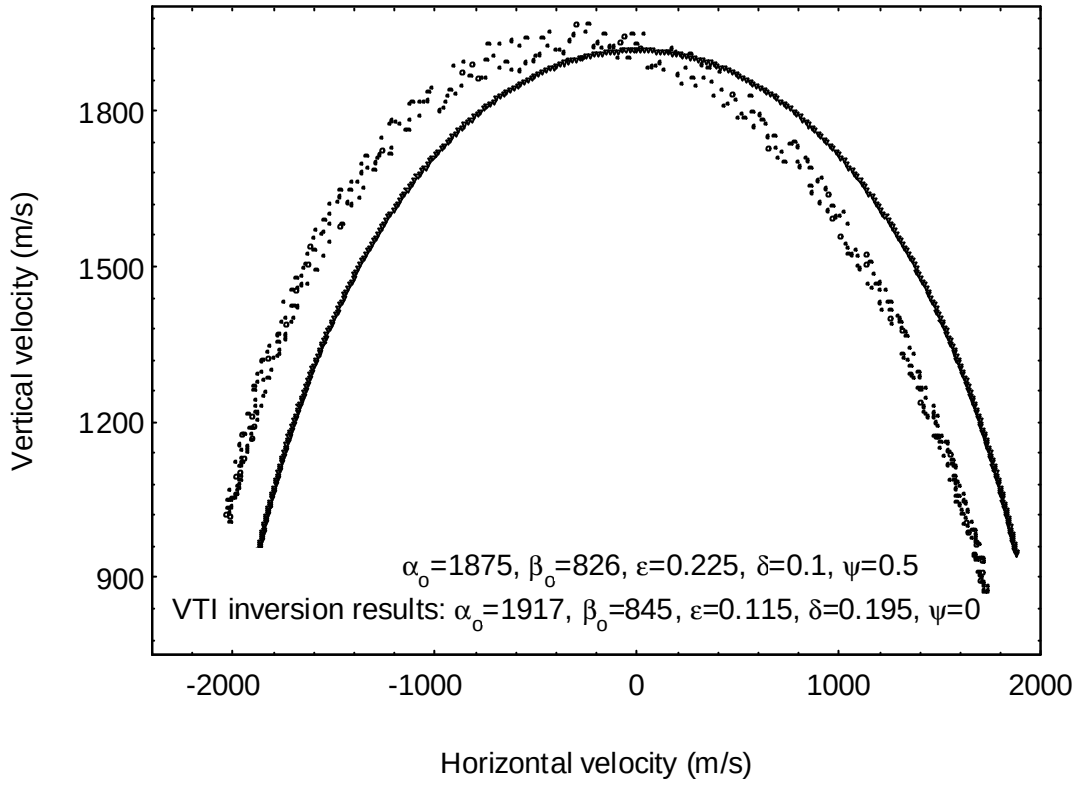

Figure 3.17 Comparison of the inversion result based on a VTI assumption with the model data and the velocity fields for a TTI Dog Creek shale model. The circles indicate the synthetic velocity field for a TTI model, and the curve is the velocity function generated using the inversion results assuming VTI. The inverted parameters differ substantially from their model values. A significant discrepancy exists between the synthetic velocity field and the velocity field calculated from the inverted parameters when an inappropriate model was chosen.

If the symmetry axis of the model is tilted with a non-negligible angle (e.g., close or larger than 30°), the inversion method based on the TTI assumption should be used.

Inversion results with different numbers of variables

The inversion procedure in program "*paratilt.c*" permits some parameter values to be fixed. If some parameters of the model are already known, this flexibility enables us to determine the unknown parameters while fixing the known parameters in the iteration. Constraining parameters may help to improve the accuracy of the inversion results as is shown in the following.

As a test, the same TTI model with random noise was established as that in the above numerical simulations. Synthetic VSP data were generated for Taylor sandstone tilted at *0.15* radian. The synthetic data were then input to the inversion program "*paratilt.c*". The inversion results were obtained separately when all variables were allowed to change, then when a_0 was fixed, and when a_0 and y were fixed. Table 3.13 lists these inversion results.

Reducing the number of variables, which are allowed to change in the inversion, appears to improve the accuracy of the inversion result. With well-logging data or other survey information, it is possible to have some parameters determined before the inversion. When some of the parameters are accurately determined and fixed in the inversion, the inversion program will provide more accurate estimates of the unknown parameters.

Table 3.13 Effects of fixing some values of variables in the inversion for the Taylor sandstone data set with a tilt angle of *0.78* radian (*~45°*) with random noise. Decreasing the number of variables increases the accuracy of the inversion results.

		$a_0(ms^{-1})$	$b_0(ms^{-1})$	e	d	y (radian)
	Input parameters	3000		0	0	0.1
	Output parameters	3376	1833	0.107	-0.053	0.790
Fix a_0	Input parameters	3368		0	0	0.1
	Output parameters	3368	1829	0.109	-0.041	0.790
Fix a_0 and y	Input parameters	3368		0	0	0.78
	Output parameters	3368	1829	0.109	-0.038	0.780
Correct values		3368	1829	0.110	-0.035	0.780

Synthetic data with different numbers of input measurements and different ranges of offsets

The effects of different numbers of input measurements and different ranges of offsets on the accuracy of the inversion results were next considered. The same TTI model with random noise in the previous sections was used to generate synthetic velocity data for Taylor sandstone with different tilt angles. The synthetic data with different numbers of observations and different offset ranges were input to the inversion program. The apparent parameters were recovered. The velocity field comparisons ("*chi-by-eye*") were carried out but are not plotted here to save space. The inversion results are discussed as follows.

- **Taylor sandstone model with tilt angle of *0.5* radian (*~30°*)**

Synthetic model velocity data were first calculated for positive and negative offsets, uniformly spread over the same offset range. The numbers of observations generated were *20, 40, 100, 200,* and *400,* respectively. These synthetic data sets were input to the inversion program. The inversion results are shown in Table 3.14. When the number of measurements was increased, a better inversion result was obtained. The inversion results were however still acceptable even when the number was decreased to *20*.

To examine the effect of a limited range of input data, the inversion program "*paratilt.c*" was run again using the above synthetic data but only with positive offsets from one side of the borehole. Table 3.14 shows the inversion results. When the number of input data was less than *50,* the inversion did not provide an acceptable result.

Table 3.14 Inversion results for Taylor sandstone with a tilt angle of *0.5* radian (*~30°*) with random noise (TTI model). The inversion results are slightly improved when the number of observations increases. Inversion results were less accurate when surveys were taken from one side of the borehole. An inversion, which only uses a small number of positive offset measurements, may not provide a satisfactory result.

No. of observations	offset range	$a_0(ms^{-1})$	$b_0(ms^{-1})$	*e*	*d*	*y*	*D(m/s)*
20	±	3378	1834	0.110	-0.033	0.440	12
40	±	3365	1827	0.108	-0.005	0.493	14
100	±	3374	1832	0.107	-0.04	0.528	17
200	±	3366	1828	0.112	-0.031	0.505	18
400	±	3366	1828	0.112	-0.033	0.494	19
10	+	3346	1817	0.259	0.125	0.445	41
20	+	3373	1832	0.436	-0.084	0.532	14
50	+	3373	1832	0.153	-0.045	0.669	19
100	+	3366	1828	0.056	-0.024	0.395	16
200	+	3367	1829	0.181	-0.048	0.524	19
Correct values		3368	1829	0.110	-0.035	0.500	

For a TTI model with a non-negligible tilt angle, the inversion program may produce an acceptable result from a set of input measurement data with diverse source offsets, even when the measurement number is very low (eg., *20* in this case). However, the inversion program may fail to provide a reasonable result if the source offsets are located only on one side of the bore hole, even when the number of measurements is not too low (eg., *50* in this case). Now let us look at the wavefront in the presence of elliptical anisotropy — a special case of transverse isotropy, as shown in Figure 3.18 modified from Uren (1989). When only one part of data — either positive offsets or negative offsets — is available, the characteristics of the wavefront are hard to predict. The inversion program needs to have a broad range of input data from both sides of the borehole, in the presence of TTI medium with a non-negligible tilt angle, in order to ensure that the velocity characteristics are adequately captured in acquisition.

- **Taylor sandstone model with tilt angle of *0.1* radian (~*6*°)**

Many sedimentary geology shows nearly horizontal layered structure. The next numerical simulations were then designed to study the Taylor sandstone model with a very small tilt angle of *0.1 radian* (~*6*°).

Measurement data with positive and negative offsets were input to the inversion program. Table 3.15 shows the inversion results. When measurements were carried out with a large number of observations, better inversion results were obtained. The inversion program provided reasonable estimates for the model even when the number of the input data was chosen to be as low as *20*.

The inversion program was run again using only the synthetic model data from one side of the borehole – e.g., positive offsets. There was no significant change in the inversion results. For this model with a very small tilt angle, the inversion still provides satisfactory results using positive offset data.

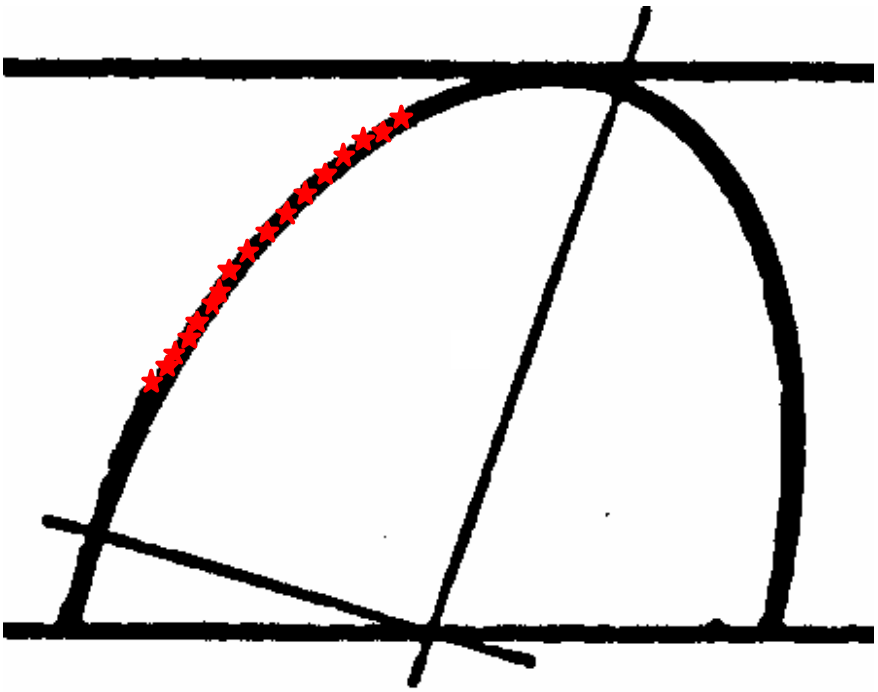

Figure 3.18 Wavefronts for tilted elliptical anisotropy (after Uren, 1989), which is a special case of TTI model. When only one side of data from the vertical direction are available, eg., the red stars are obtained from field surveys, the characteristics of the wavefront are still hard to predict, when the information does not sufficiently characterize the medium.

Table 3.15 Inversion results for Taylor sandstone with a tilt angle of *0.1* radian (~*6*°) with random noise (TTI model). The inversion results are slightly improved when the number of observations increases. No significant improvements were made when all range of data were input to the inversion instead of only one side of data from the vertical direction were used.

No. of observations	offset range	$a_0(ms^{-1})$	$b_0(ms^{-1})$	*e*	*d*	*y*	*D(m/s)*
20	±	3360	1824	0.124	-0.028	0.054	12
40	±	3382	1837	0.108	-0.046	0.080	14
100	±	3366	1828	0.101	-0.014	0.108	17
200	±	3366	1828	0.109	-0.028	0.106	17
400	±	3370	1830	0.113	-0.042	0.103	18
10	+	3355	1821	0.117	0.049	0.202	10
20	+	3382	1836	0.129	-0.065	0.080	14
50	+	3358	1823	0.090	0.000	0.097	18
100	+	3368	1829	0.112	-0.040	0.092	17
200	+	3370	1830	0.128	-0.045	0.126	19
Correct values		3368	1829	0.110	-0.035	0.100	

For most subsurface structures with a small tilt angle (several degrees), the offset data from one side of the bore hole may be enough for the inversion program providing the number of measurements is not too low (eg., more than 20 in this case). This is presumably due to the sufficient velocity characteristics having being sampled by the input data.

- **VTI model for Taylor sandstone**.

Because the symmetry axis of a VTI model is vertical, it is expected that whether the negative offset data is input should have no significant influence on the inversion results. The following numerical experiments were processed for a VTI model for Taylor sandstone.

The number of measurements for both positive and negative offsets was chosen to be *20*, *40*, *100*, *200*, and *400*, the same as that in the above TTI models. Synthetic velocity fields with random noise were simulated, as the above TTI models. The generated synthetic velocity data were then input to the inversion program "*paratilt.c*". The tilt angle was fixed at zero during the inversion. Table 3.16 shows the inversion results for this VTI model.

When the number of measurements was increased, the inversion result was improved. Inputting data with or without negative offsets to the inversion program was not found to change the accuracy of the inverted values of the elastic parameters very much. This should not surprise us because the velocity field is symmetric about the vertical direction.

The synthetic data which were generated for a VTI model in Section 3.1 and 3.2 included only the positive offset data. The inversion using these data sets provided reasonable estimates from the model data. For a VTI model, the offset data from one side of the borehole should be enough for the inversion progrom.

Table 3.16 Inversion results for Taylor sandstone with random noise (VTI model). The inversion results are slightly improved when the number of observations increases. The inversion, which used only positive offset measurements and the full range of measurements, yielded a satisfactory result.

No. of observations	offset range	$a_0(ms^{-1})$	$b_0(ms^{-1})$	e	d	$D(m/s)$
20	±	3353	1821	0.113	-0.012	16
40	±	3386	1839	0.109	-0.055	15
100	±	3366	1828	0.101	-0.015	17
200	±	3368	1828	0.110	-0.031	17
400	±	3370	1830	0.114	-0.042	18
10	+	3342	1815	0.115	0.025	11
20	+	3381	1836	0.128	-0.061	15
50	+	3356	1823	0.100	0	18
100	+	3369	1829	0.113	-0.039	17
200	+	3372	1831	0.113	-0.047	19
Correct values		3368	1829	0.110	-0.035	

3.3.3 Conclusions

A computer program *"paratilt.c"* has been developed to recover the elastic parameters and the tilt angle of the symmetry axis from walkaway VSP survey data for TTI media. If we assume a zero tilt to a TTI medium, where tilt is actually non-negligible, we may find significant errors in the recovered elastic parameters. This would lead to a misunderstanding of the bedding nature of the rocks, which is very important in reservoir estimations.

For a selection of sedimentary anisotropic rocks, a number of synthetic VSP data sets were inverted and the results were found to be in good agreement with their model values. The velocity fields generated using the inverted elastic parameters and the tilt angle of the symmetry axis were in close agreement with the input data.

We have the ability to fix any parameters for which we already know values, and invert for the remaining parameters. This capability makes the program *"paratilt.c"* useable in different situations, and may improve the accuracy of our inversion results. For known VTI media, we could fix the tilted angle y to be zero. Hence, the more general program *"paratilt.c"* now supersedes the program *"para.f"* developed in Section 3.1.

For a TTI model with a non-negligible tilt angle (e.g., close or larger than 30°), the numerical results suggest that the inversion always needs to be carried out on data with positive and negative offset ranges. However, for a VTI model or a TTI model with a negligible tilt angle, the inversion may be carried out satisfactorily on the measurements from one side of the bore hole. It is recommended that the number of measurements be more than *20*.

This inversion program was developed for the 2-D case, in which the survey line is in the dip direction. Extension to the general 3-D case may be done. However, more variables would need to be introduced, and this extension is considered to be beyond the scope of this thesis.

3.4 Inversion Using Combinations of P, SV, and SH-wave Data

In the earlier sections of this chapter, inversion procedures were developed for transversely isotropic media for P-waves only. Because of the limited information held in the P-wave travel time signature, it should be more beneficial to input the value of S-wave velocity along the symmetry axis (b_0), or to fix the ratio of P-wave and S-wave velocities along the symmetry axis (a_0/b_0), when running the inversion program *"paratilt.c"* (from the above section).

As mentioned in Chapter 1, S-waves contain a lot of information about rock properties. Because "shear waves should be more sensitive to anisotropy than P-waves" (Urosevic, 1985), the greater information content in shear waves should be used to improve the yield from travel time inversion methods. Nowadays, new technology is developing quickly and multi-component walkaway VSP surveys are being more widely used. Multi-component VSP surveys provide us with information not only from P-wave data, but also from SV and SH-wave data. Multi-component VSP surveys make the utilization of shear wave information possible. In this section, I propose to develop inversion methods using P, SV, and SH-wave velocity fields for multi-layered media.

As for the studies in Sections 3.1 and 3.2, an inversion program for a single-layered medium will be developed first. Then the apparent velocity field for two-layered

models will be examined. After developing an inversion procedure for a two-layered model, the result will be generalized to a multi-layered model.

3.4.1 Inversion for a Single-Layered Model

Consider a single-layered transversely isotropic medium with the symmetry axis, tilted at an angle y from the vertical direction, as shown in Figure 3.15. The survey line is assumed to be along a dip line in this initial study. A receiver down the borehole records the signals emitted from the shots. The velocity field is then obtained for the single-layered medium above the receiver as a function of direction.

In this section, I propose to develop an inversion program to recover the elastic parameters and the tilt angle from the observed P and S wave velocity fields for a TTI medium.

Inversion program *"parameter.c"*

The phase velocity $v_p(q)$ of P-waves can be calculated using equation 3.12. For SV, SH-wave, the phase velocities are:

$$\frac{v_{sv}^2(q,y)}{b_0^2} = 1 + \frac{a_0^2}{b_0^2} e \sin^2(q-y) + \frac{a_0^2}{b_0^2}\frac{f}{2} - \frac{a_0^2}{b_0^2}\frac{f}{2}\sqrt{1 + \frac{4\sin^2(q-y)}{f}(2d\cos^2(q-y) - e\cos 2(q-y)) + \frac{4e^2\sin^4(q-y)}{f^2}}, \tag{3.22}$$

$$\frac{v_{sh}^2(q,y)}{b_0^2} = 1 + 2g\sin^2(q-y). \tag{3.23}$$

From equations 3.13 and 3.14, the corresponding magnitude and direction of the group velocity $v_g(f)$ for P, SV, and SH-waves may be determined.

As previously stated in Section 3.1.1, the seismic group velocity depends on the elastic parameters of a medium, with a given set of elastic parameters a_0, b_0, e, b, g, and tilt angle y. The group velocity $v_g(f)$ could not be calculated explicitly in a given direction. No explicit expression existed. I again used the golden-ratio search method (Gottfried and Weisman, 1973) — the same as that in Section 3.1.1 — to find the phase angle in a specific observed ray direction. The calculated velocity field, as well as the first derivatives of the velocities with respect to the parameters a_0, b_0, e, d, g, and y were then analytically calculated.

This velocity field was then compared with the observed velocity field. The Levenberg-Marquardt method, which was described in Section 3.3.1, was then employed to calculate the updated trial parameters. Then the velocity field was calculated again with the new trial parameters. The iteration procedure was then run until the chi-square function reduced to a pre-determined value, e.g., less than *0.0001*. A set of parameters a_0, b_0, e, d, g, and tilt angle y were found which minimized the differences between the observed group velocity field and the calculated velocity field:

$$\sum_{i}^{n_{obs}} |v_{gobs}(i) - v_{gcal}(i)| \rightarrow minimum. \qquad (3.24)$$

The iteration was stopped unconditionally if the iteration had proceeded for *50* or more times to avoid ineffective long run times, the same as in Section 3.1.

My newly developed inversion program "*parameter.c*" was written to implement the above procedures.

Using the symbolic algebra package *Maple*, for an arbitrary phase angle, the corresponding group velocity and the first derivatives with respect to a_0, b_0, e, d, g, and tilt angle y were formulated for P, SV, and SH-waves, respectively. The *Maple* procedures were then converted to C subroutines. Using the golden-ratio search method combined with these C subroutines, three subroutines "*parameter_p6.c*",

"*parameter_sv6.c*" and "*parameter_sh6.c*" were written to calculate the velocity fields and the first derivatives for a set of trial parameters a_0, b_0, e, d, g for P, SV, and SH-waves, respectively.

These three subroutines were included in the main program "*parameter.c*", which uses the Levenberg-Marquardt method to find the best-fit parameters a_0, b_0, e, d, g, and y for observed velocity fields.

The inversion program "*parameter.c*" also permits arbitrary fixing of known parameters during inversion (Li et al., 1999). If only a P-wave velocity field is obtained from a survey, the program can be asked only to recover the elastic parameters a_0, e, d, and y associated with P-waves. Then the program is equivalent to program "*paratilt.c*". If a model is a VTI model, then the tilt angle of the symmetry axis can be fixed to be zero. The inversion program "*parameter.c*" can be used to substitute for the programs "*paratilt.c*" and "*para.f*". This feature makes the program "*parameter.c*" versatile in different situations.

According to Caldwell (1999), P and S-waves "can provide much more information about a reservoir than can be provided by either alone". It was hoped that the inversion program "*parameter.c*" would also provide more accurate values of the elastic parameters from the observed velocity fields of P, SV, and SH-waves than those inverted from the observed velocity field of one wave mode alone.

Numerical testing

To test the newly developed program "*parameter.c*", a series of computer simulation experiments were carried out first.

- **Synthetic data**

For a transversely isotropic medium with a set of model parameters a_0, b_0, e, d, g, and y, the velocity fields for P, SV, and SH-waves were generated as follows.

We assumed a phase angle ranging from *-90°* to *90°*. The corresponding phase velocity for a TTI medium was calculated using equations 3.12, 3.22, and 3.23. From equation 3.13 and equation 3.14, the corresponding ray velocity and ray angle were determined. Hence, the ray velocity fields of P, SV, and SH-waves for a TTI medium were obtained. A program *"forward.c"* was written to implement this procedure. As in Section 3.3.2, the number of calculated velocities was chosen to be *100*, and the range of the phase angle q was from *-90°* to *90°*. To stimulate real field data, the depth of this single layer was assumed to be *3000 m*, and the maximum travel time error was taken to be *±10 ms*. So around *1%* random noise in the velocity field was added.

The parameters of four representative rocks were chosen to carry out the numerical modelling experiments. These four representative rocks were Taylor sandstone, Mesaverde (5501) clayshale, Pierre shale A, and Green River shale. To save the reader time finding the elastic parameter values from the previous tables, Table 3.17 lists the elastic parameters for these four rocks for convenience.

- **Inversion results**

Using the elastic parameters of these four representative rocks, the velocity fields for each rock were computed using the forward modelling program *"forward.c"*. Here, the tilt angle of symmetry axis was chosen as *0°*, *30°*, and *-30°*, respectively. The calculated velocity fields were assumed to be the observed velocity fields for a TTI medium, and were input to the inversion program *"parameter.c"*. The inversion program converged quickly in less than *25* iterations. Table 3.18 shows the inversion results as well as the initial input values of the parameters used. The inverted elastic parameters and tilt angles are quite close to their model values, with errors less than *0.01* in e, *0.02* in d, *0.01* in g, *0.5°* in y. In order to examine the inversion results, Figure 3.19 (Taylor sandstone), Figure 3.20 (Pierre shale A), Figure 3.21 (Mesaverde

Table 3.17 The elastic parameters (Thomsen, 1986) of the four sedimentary rocks used to build the single layer numerical models for P, SV, and SH-waves.

Sedimentary Rocks	a_0(m/s)	b_0(m/s)	e	d	g	r
Taylor sandstone	3368	1829	0.110	-0.035	0.255	2.500
Pierre shale A	2074	869	0.110	0.090	0.165	2.250
Mesaverde (5501) clayshale	3928	2055	0.334	0.730	0.575	2.590
Green River shale	3292	1768	0.195	-0.220	0.180	2.075

Table 3.18 Inversion results for synthetic velocity data with about *1%* random noise added. Here, VTI represents a transversely isotropic model with a vertical symmetry axis, while TTI represents a transversely isotropic model with a tilted symmetry axis. Δ represents the average difference between the synthetic velocity data and the velocity data calculated from the recovered parameters.

	Initial input values						Inversion results or exact values						
	a_0(m/s)	b_0(m/s)	e	d	g	y (°)	a_0(m/s)	b_0(m/s)	e	d	g	y (°)	D(m/s)
* Taylor sandstone (exact values)							3368	1829	0.110	-0.035	0.255		
Taylor sandstone (VTI)	3000	1500	0	0	0	0	3374	1830	0.107	-0.035	0.252	0	13
Taylor sandstone (TTI, 30°)	3000	1500	0.1	0	0.2	25	3373	1829	0.109	-0.036	0.255	30.42	13
Taylor sandstone (TTI, -30°)	3000	1500	0.1	0	0.2	-25	3374	1829	0.109	-0.039	0.252	-30.11	13
* Pierre shale A (exact values)							2074	869	0.110	0.090	0.165		
Pierre shale A (VTI)	2000	1000	0	0	0	0	2078	869	0.108	0.089	0.162	0	7
Pierre shale A (TTI, 30°)	2000	1000	0.1	0.1	0.1	25	2077	869	0.109	0.089	0.165	30.55	7
Pierre shale A (TTI, -30°)	2000	1000	0.1	0.1	0.1	-25	2077	869	0.109	0.087	0.163	-30.27	7
* Mesaverde (5501) clayshale (exact values)							3928	2055	0.334	0.730	0.575		
Mesaverde (5501) clayshale (VTI)	4000	2000	0	0	0	0	3935	2057	0.331	0.727	0.567	0	15
Mesaverde (5501) clayshale (TTI, 30°)	4000	2000	0.2	0.5	0.5	25	3934	2053	0.333	0.726	0.578	30.08	15
Mesaverde (5501) clayshale (TTI, -30°)	4000	2000	0.2	0.5	0.5	-25	3934	2054	0.333	0.725	0.572	-30.04	16
* Green River shale (exact values)							3292	1768	0.195	-0.220	0.180		
Green River shale (VTI)	3000	1500	0	0	0	0	3288	1768	0.180	-0.204	0.178	0	13
Green River shale (TTI, 30°)	3000	1500	0.1	-0.1	0.1	25	3295	1767	0.194	-0.220	0.181	30.23	13
Green River shale (TTI, -30°)	3000	1500	0.1	-0.1	0.1	-25	3305	1769	0.192	-0.233	0.177	-30.28	13

*: See Table 3.17.

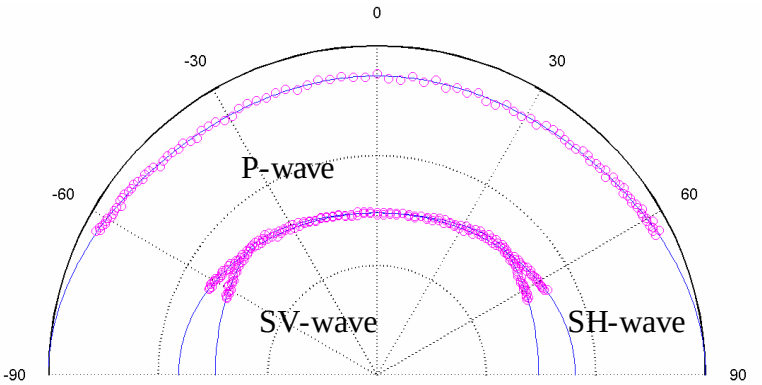

(a)

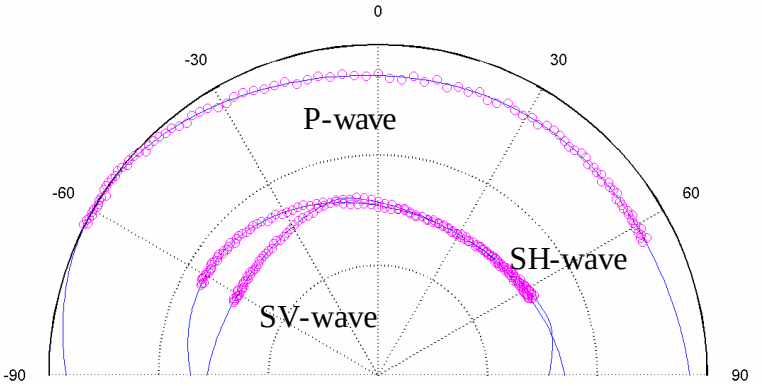

(b)

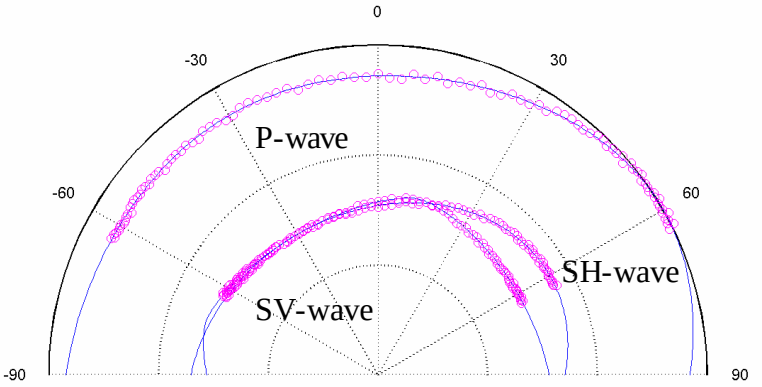

(c)

Figure 3.19 Velocity fields from the inversion result and the input model data for Taylor sandstone. The model is a single-layered transversely isotropic medium with (a) vertical symmetry axis, (b) 30° tilt symmetry axis, (c) -30° tilt symmetry axis. Here, the magenta dots are the input velocity fields given by numerical modelling experiments. The blue lines are the velocity fields calculated using the recovered parameters. The blue lines and magenta dots coincide quite well.

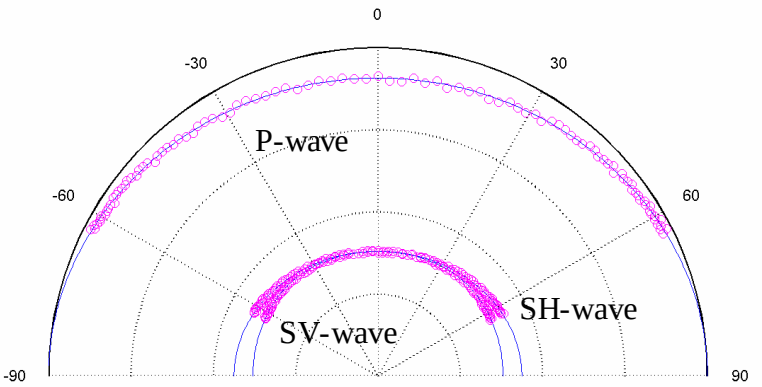

(a)

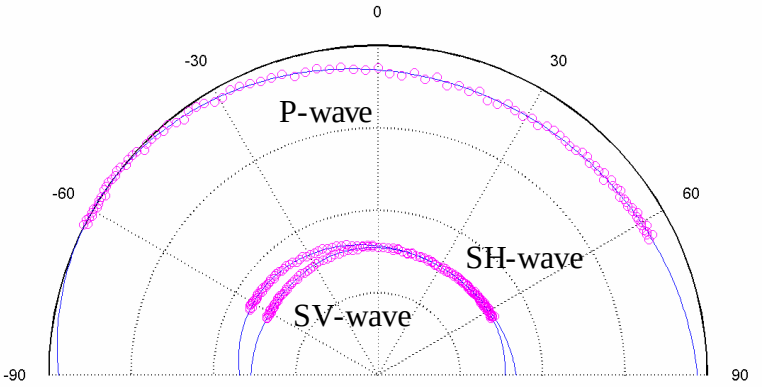

(b)

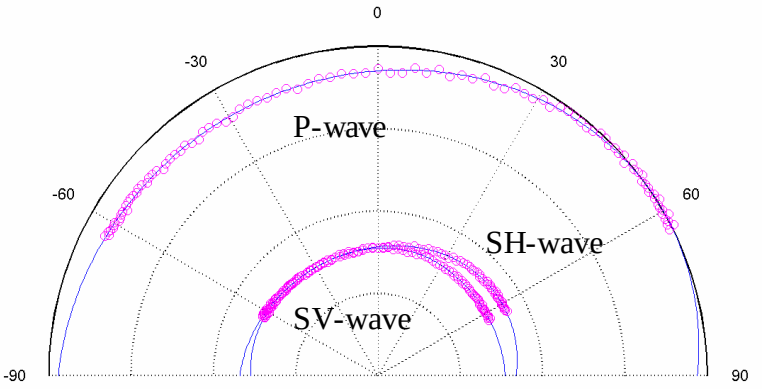

(c)

Figure 3.20 Velocity fields from the inversion result and the input model data for Pierre shale A. The model is a single-layered transversely isotropic medium with (a) vertical symmetry axis, (b) 30° tilt symmetry axis, (c) -30° tilt symmetry axis. Here, the magenta dots are the input velocity fields given by numerical modelling experiments. The blue lines are the velocity fields calculated using the recovered parameters. The blue lines and magenta dots coincide quite well.

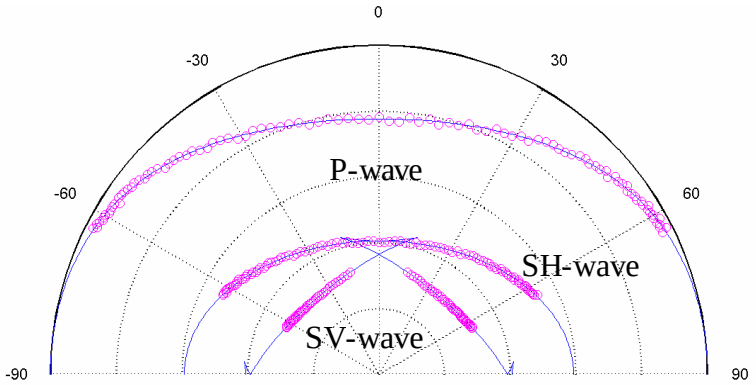

(a)

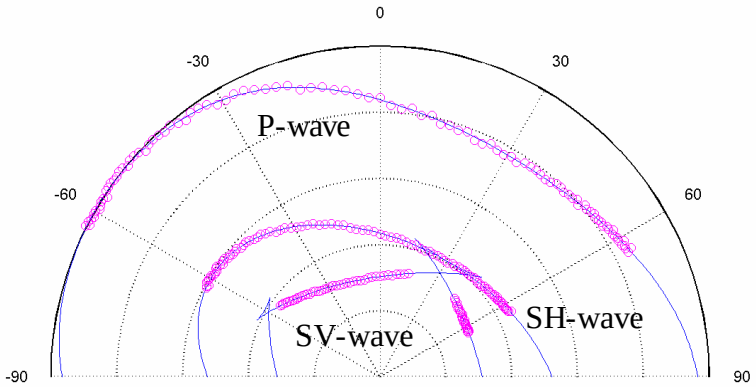

(b)

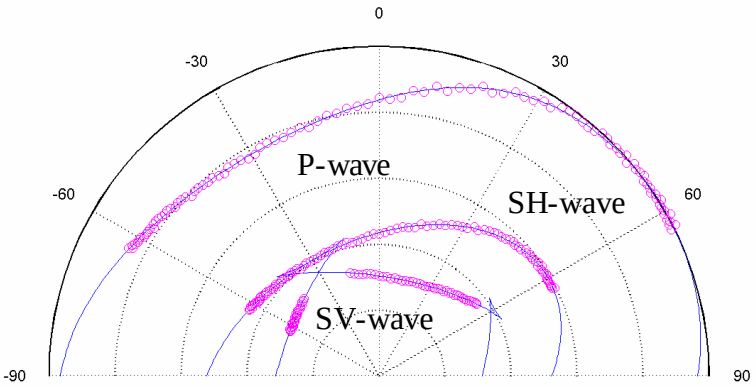

(c)

Figure 3.21 Velocity fields from the inversion result and the input model data for Mesaverde clayshale. The model is a single-layered transversely isotropic medium with (a) vertical symmetry axis, (b) 30° tilt symmetry axis, (c) -30° tilt symmetry axis. Here, the magenta dots are the input velocity fields given by numerical modelling experiments. The blue lines are the velocity fields calculated using the recovered parameters. The blue lines and magenta dots coincide quite well.

(5501) clayshale), Figure 3.22 (Green River shale) show the input velocity fields from the "observations" and those computed from the inverted parameters. It can be seen that both the velocity fields from the observations and from the inversion results coincide with each other. The inversion program "*parameter.c*" was considered successful in these numerical experiments.

It can be seen that cusps exist at directions near *0°* and *90°* from the symmetry axis for Mesaverde (5501) clayshale (shown in Figure 3.21), and near *45°* from the symmetry axis for Green River shale (shown in Figure 3.22). Figure 3.23 shows an example of a raw time section with cusps from a physical modelling experiment. If cusps exist, it is hard to obtain the first arrival picks for SV-waves near the cusps (Urosevic, 1985). For this reason it was found better to omit the numerical data near the cusps as inputs to the inversion program.

From the above numerical experiments, the inversion program "*parameter.c*" recovered the elastic parameters and tilt angle of these single layer models within acceptable errors.

3.4.2 Inversion Methods for a Two-layered Model

For a two-layered VTI model, we found in Section 3.2 from the overall apparent velocity field for P-waves propagated through it, that this model may be considered to be equivalent to a single-layered VTI medium, except in the near horizontal direction. In this section, it is proposed to examine the apparent velocity fields of a two-layered model not only for P-waves, but also for SV and SH-waves as well. The apparent velocity fields of these wave types will be input to the previously developed inversion program "*parameter.c*". If inversion is possible, and the apparent parameters a_0, b_0, e, b, g can be found, we will consider that such a layered model may be represented by an equivalent single layer. If it is not possible, then either the two-layered model may not

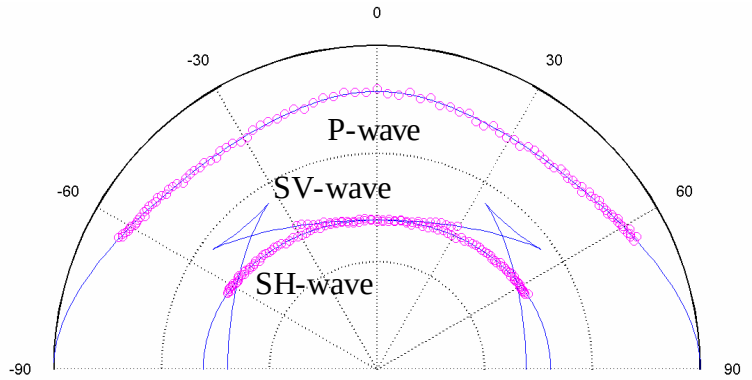

(a)

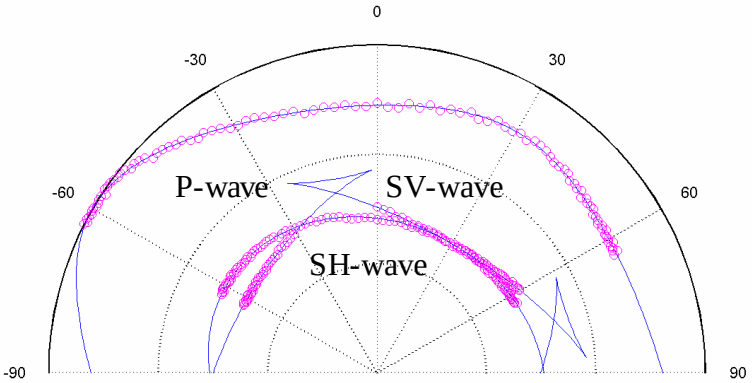

(b)

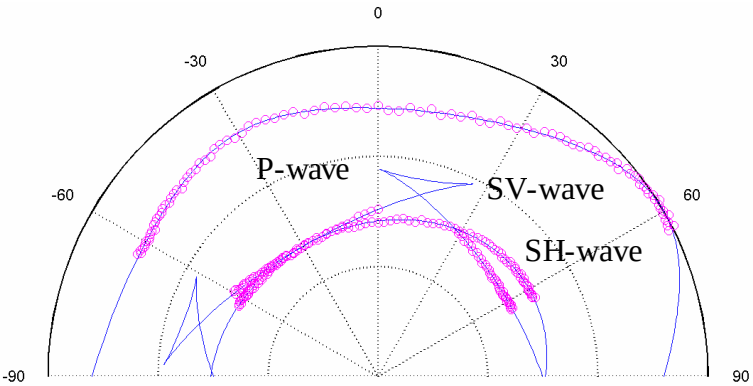

(c)

Figure 3.22 Velocity fields from the inversion result and the input model data for Green River shale. The model is a single-layered transversely isotropic medium with (a) vertical symmetry axis, (b) *30°* tilt symmetry axis, (c) *-30°* tilt symmetry axis. Here, the magenta dots are the input velocity fields given by numerical modelling experiments. The blue lines are the velocity fields calculated using the recovered parameters. The blue lines and magenta dots coincide quite well.

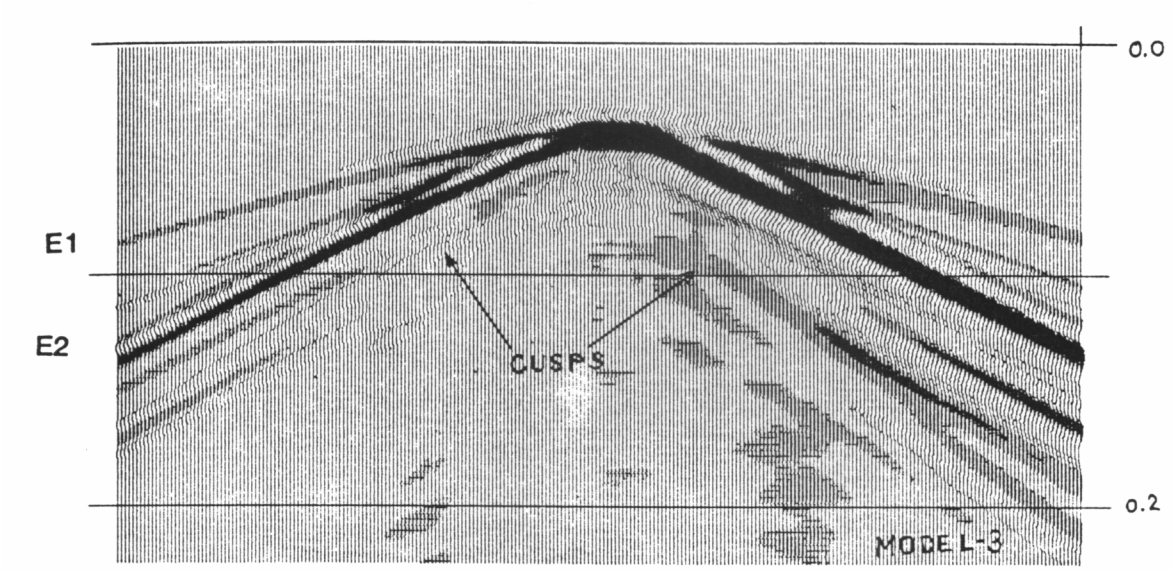

Figure 3.23 Raw time section from physical modelling experiment (Urosevic, 1985). The events labeled E1 and E2 correspond to P and SV waves. Possible cusps are indicated by arrows. It is hard to obtain the first arrival picks for SV-waves near the cusps.

be treated as a single equivalent layer, or the inversion program needs to be re-examined.

The geometrical arrangement in generating the numerical test data is the same as that in Section 3.2.1, shown in Figure 3.3. A receiver is situated on the lower surface of the two-layered model, while a source moves along the upper surface of the model. For each wave mode, either P, or SV, or SH-waves, the refracted phase angle was determined for an incident phase angle on the interface between these two layers using Snell's law. The corresponding group velocity and its ray angle were calculated for the incident wave and the refracted wave. Following the derivations in Section 3.2.1, apparent velocity fields for the model were calculated using equation 3.7 and equation 3.8 for P, SV, and SH-waves, respectively. To implement the above procedures, a forward modelling program "*twoforward.c*" was written to calculate apparent velocity fields for P, SV, and SH-waves in the two-layered model. As in Section 3.3.2, the number of the calculated velocities was chosen to be *100*, and the offset range was chosen to be the typical field survey range, i. e., to the maximum of twice the model thickness.

An example is shown here for a two-layered VTI model constructed using the elastic parameters for Taylor sandstone and Pierre shale A. The thickness ratio for the two components was varied between $0.1:1$, $1:1$, and $10:1$. To simulate real field data, around *1%* random noise was added to the synthetic data.

Using program "*twoforward.c*", the apparent velocity fields of P, SV, and SH-waves for the two-layered model were computed and used as observed velocity fields. When the observed velocity field was input to the inversion program "*parameter.c*" with the tilt angle of the symmetry axis being fixed as zero, the program converged. The inversion results are shown in Table 3.19, which gives the apparent elastic parameters for the two-layer combination.

Table 3.19 Inversion results for the apparent parameters for numerical synthetic data from a two-layered model. The first layer has the values of parameters for Taylor sandstone, while the second layer has the values of parameters for Pierre shale A. The (z_1/z_2) represents the thickness ratio of these two layers. *D* represents the average error in velocity field between the observations and that by inversion, while *W* is the relative error in percentage.

z_1/z_2	a_0(m/s)	b_0(m/s)	*e*	*d*	*g*	*D*(m/s)	*W*(%)
0.1	2147	908	0.251	0.113	0.472	31	2.7
1	2563	1175	0.245	0.067	0.468	25	1.7
10	3187	1660	0.144	-0.016	-0.128	15	0.7

In Figure 3.24, the velocity fields of the synthetic observations (magenta dots) were then compared with the velocity fields computed using the inverted elastic parameters (blue lines). It can be seen that these two sets of velocity fields generally are in a good agreement. But for Figure 3.24(a) and Figure 3.24(b), a large difference becomes apparent at offsets larger than 1.7 times the model depth ($f > 57°$).

This leads us to a result similar to that found by P-wave inversion in Section 3.2. The apparent velocity fields of P, SV, and SH-waves for a two-layered model composed of transversely isotropic media appear to be like the velocity fields for a single-layered transversely isotropic medium, within the typical offset range of a field survey. It was noticed that the offset range in some of the above examples needed to be limited to less than twice the model thickness for satisfactory results. This may have been a consequence of the greater number of constraints involved in multi-wave mode inversion than in single P-wave inversion.

3.4.3 Inversion Methods for a Multi-layered Model

Figure 3.13 shows a multi-layered model with a receiver array down a borehole and a source moving along the upper surface. As in Section 3.2.4, the inversion program "*parameter.c*" can be applied to the P, SV, and SH-wave data for this multi-layered model.

With a receiver at R_1, the seismic signals travelling through the first layer are recorded. By picking the first arrival times for every shot position, the observed velocity fields can be computed for P, SV, and SH-waves. By inputting these observed velocity fields into the inversion program "*parameter.c*", the elastic parameters of the first layer a_{01}, b_{01}, e_1, d_1, and g_1 can be determined.

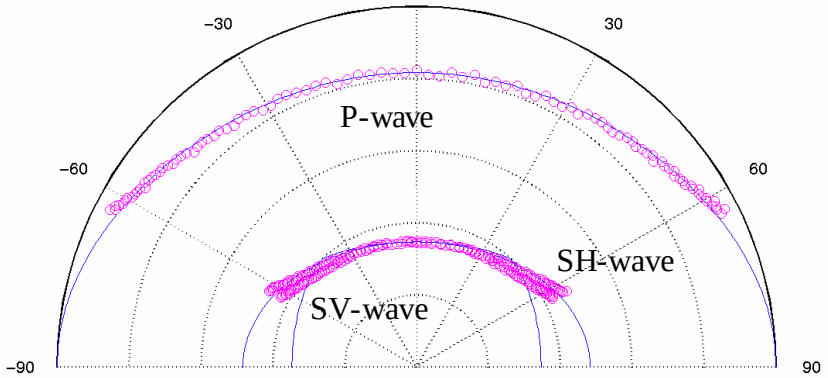

(a)

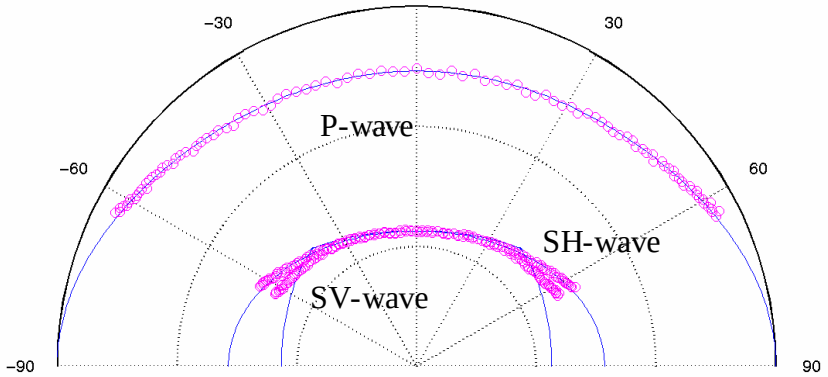

(b)

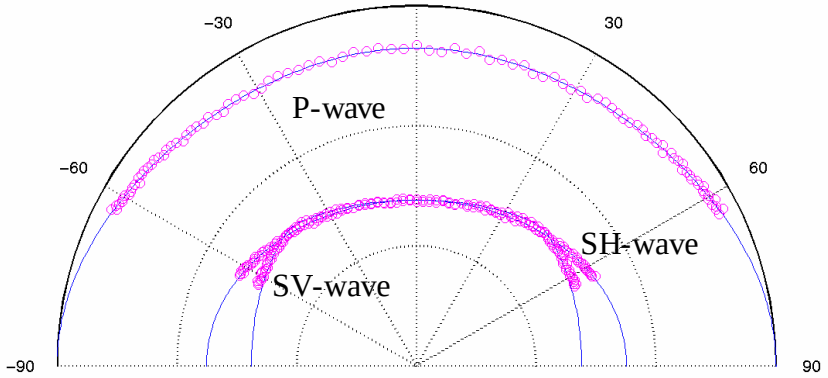

(c)

Figure 3.24 Velocity fields for a synthetic two-layered model composed of Taylor sandstone and Pierre shale A. The thickness ratio for Taylor sandstone and Pierre shale is (a) *0.1*, (b) *1*, (c) *10*, respectively. The synthetic data are marked with magenta dots. The velocity fields calculated using the inverted parameters from inversion (blue lines) coincide with the synthetic data. In (a) and (b), the coincidence in velocity fields deteriorates at large ray angles from the symmetry axis.

Similarly, with signals recorded by receiver R_2, the travel times for a ray from a shot S for P, SV, and SH-waves may be obtained. The apparent ray distances are then determined by finding the length of the straight line SR_2 between the receiver and the shot, and the apparent velocity for the ray is obtained with dividing the apparent length by the travel time. The apparent ray angle is also measured as the angle between the straight line SR_2 and the vertical direction. Thus, the apparent velocity fields of P, SV, and SH-waves for this two-layered medium can be determined. By inputting the observed velocity fields to the inversion program "*parameter.c*", the apparent elastic parameters of the combined two layers may be obtained.

Working downwards, the combined apparent elastic parameters of the first i-layered media may be determined analyzing the signals recorded by receiver R_i. Examples of applying this procedure to field data will be given in Chapter 6.

3.5 Conclusions

An inversion method has been developed to recover the elastic parameters for horizontally layered VTI media. If the symmetry axis is tilted, it can also recover the tilt angle, when the survey line is along the dip direction.

For two-layered VTI media within a practical offset range (i.e., less than twice the depth of the layers), it has been numerically demonstrated that these media may be treated as a single layer with apparent parameters recovered by my inversion program. The offset limitation depends in a generally non-linear fashion on the parameters and thickness ratio of the individual layers. For multi-layered media, the inversion method still can be applied to the apparent velocity data acquired from the signals recorded by a downhole receiver.

For various models, a number of inversion programs were developed in this chapter. Of all these programs, the versatile inversion program *"parameter.c"* generated for multi-component VSP survey can be used for the other specific inversion cases too. When this program "*parameter.c*" is run, the computer asks the user to input the parameters that are already known, and it will recover the parameters that are requested. For example, if the media are VTI, then one needs to simply fix the tilt angle as *0*.

In this chapter, an inversion method has been developed to recover the apparent parameters of various media. It was successfully tested by computer simulation experiments. Further tests on physical laboratory experiments will be shown in Chapter 5. In Chapter 6 this method will also be applied to real field VSP survey data.

In the next chapter, an inversion method for the interval elastic parameters of an individual layer of interest will be established.

CHAPTER 4
INVERSION FOR THE ELASTIC PARAMETERS OF A LAYER OF INTEREST

The velocity fields of waves propagating both through multi-layered transversely isotropic (TI) media and isotropic media has been numerically studied in Chapter 3. Within practical offset limits that are normally less than twice the depth to the receivers, such media may be treated as an equivalent single-layered transversely isotropic medium. From a walkaway VSP survey, the *apparent* ray path from a shot to a receiver can be determined as the straight line between the shot to the receiver. The travel time of seismic wave propagation from each shot to a receiver can also be determined from the seismic record. Hence, the overall apparent velocity field of the layers above the receiver can be found. The apparent values of the elastic parameters for this multi-layered medium may then be recovered by the inversion methods developed in Chapter 3.

In practice, one may also wish to determine the elastic parameters of an interval layer of interest between two receivers. The term *"interval"* parameter is used in this thesis to represent the elastic parameter of an interval layer of interest. Because rocks are heterogeneous at all scales, the word "interval" may be replaced by "apparent" or "average" in a strict sense. The degree of anisotropy of an interval layer of interest may contain information about bedding structures within it. A good knowledge of the elastic parameters of interval layers would help us to improve seismic data processing, such as anisotropic depth migration.

Previous researchers have shown that we can measure the elastic parameters of core samples from ultrasonic experiments in the physical modelling laboratory (e.g., Vernik and Nur, 1992; Lo et al., 1986; Jones and Wang, 1981). Because a core sample needs to be cut and its heterogeneity becomes significant, errors in measurement could be great in such small samples.

Another method to invert for elastic parameters is through slowness surfaces and polarization directions (e.g., Hsu and Schoenberg, 1991; Horne and Leaney 2000). By measuring the travel time differences between adjacent sources and receivers, the slowness surfaces and polarization directions may be determined. The elastic parameters for the interval layer between two downhole receivers are then inverted from the slowness surface and polarization directions. The method is successful and can be used for field surveys (Horne and Leaney, 2000). However, according to Kebaili et al. (1996), the existence of a heterogeneous layer between receivers may produce errors in slowness surface determination. The deviation of the borehole or topography of the surface also make the calculation of slowness surfaces more complex for careful correction. Because errors in slowness are in inverse proportion to the layer's thickness, errors for a thin interval layer will be larger due to the small time differences involved.

In this chapter, a new inversion method will be developed to recover the elastic parameters of an interval layer of interest from recorded velocity fields. According to the proposal stated in Chapter 1, only a horizontally layered VTI model will be dealt with in this chapter. The research will begin with P-wave inversion for a two-layered model. It will then be extended to develop a combined inversion method for P, SV, and SH-waves. A multi-layered application will be discussed at the end of this chapter.

4.1 P-wave Inversion for a Two-layered Model

Consider a model consisting of two horizontal layers, the components of which are either isotropic or transversely isotropic media, as shown in Figure 4.1. Simulating physical laboratory experiments or walkaway VSP field surveys, signals emitted from shots S on the upper surface of the model are recorded at receiver R_1 for the first layer,

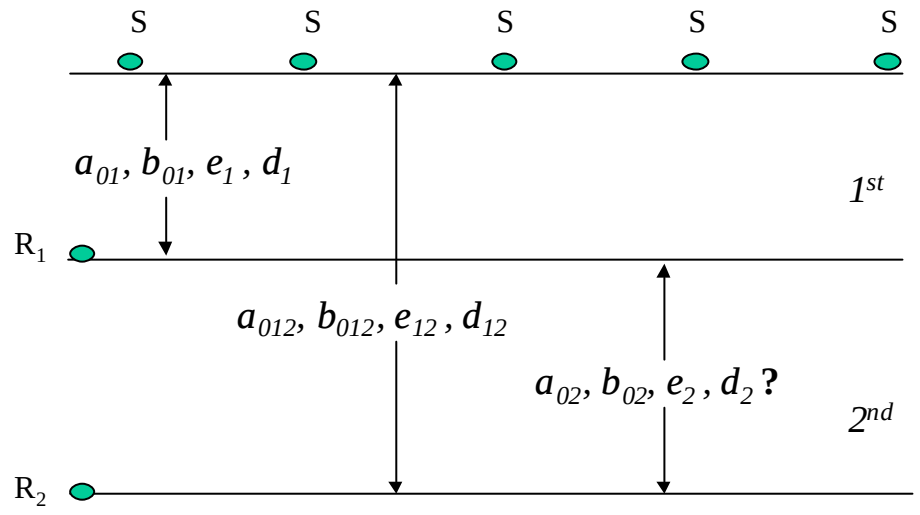

Figure 4.1 Two-layered model simulating a walkaway VSP survey.

and by receiver R_2 for the combined layers. The P-wave velocity field of the first layer $v_{g1}(f)$ and the overall apparent P-wave velocity field of the two layers $v_g(f)$ can thus be acquired. As shown in Chapter 3, we may obtain, by inversion of these P-wave velocity fields, the elastic parameters a_{01}, b_{01}, e_1, d_1 of the top layer, and the apparent parameters a_0, b_0, e, d of the combined layer.

In this section, a method of recovering the elastic parameters of the second layer will be developed once the parameters of the first layer and the combined layer are all known.

4.1.1 Inversion Method

From equation 3.9, the vertical velocities of the second layer for P-waves and S-waves were derived directly as:

$$a_{02} = z_2 \Big/ \left(\frac{z_1 + z_2}{a_0} - \frac{z_1}{a_{01}}\right), \tag{4.1}$$

$$b_{02} = z_2 \Big/ \left(\frac{z_1 + z_2}{b_0} - \frac{z_1}{b_{01}}\right). \tag{4.2}$$

The following iteration procedure was designed to find the best-fit parameters e_2, d_2 from the apparent velocity field of the combined layer.

Iteration procedures

In commencing the iterative inversion process, initial guesses for parameters e_2 and d_2 were used. To avoid complex algebraic derivations, v_g^2 instead of v_g was chosen to be the best fitting function.

With this set of trial parameters e_2, d_2, the apparent group velocity $v_{gcal}(f)$ with an incident phase angle q_1 for the combined layer was calculated using the same method as that in Section 3.2.1. Then the calculated group velocity $v_{gcal}(f)$ in a specific observed apparent ray direction f was found using the same approach as that in Section 3.1.1.

In the first order approximation, the square of the i^{th} observed group velocity $v_g^2(i)$ can be written as:

$$v_g{}^2(i) = v_{gcal}{}^2(i) + \frac{\partial v_{gcal}^2(i)}{\partial e_2} De_2 + \frac{\partial v_{gcal}^2(i)}{\partial d_2} Dd_2 . \tag{4.3}$$

For the combined layer, the calculated velocity field was compared with the observation velocity field. The corrections for trial parameters were obtained by solving the following equations:

$$\begin{bmatrix} v_g{}^2(1) - v_{gcal}^2(1) \\ \cdots \\ v_g{}^2(i) - v_{gcal}^2(i) \\ \cdots \end{bmatrix} = \begin{bmatrix} \frac{\partial v_{gcal}^2(1)}{\partial e_2} & \frac{\partial v_{gcal}^2(1)}{\partial d_2} \\ \cdots & \cdots \\ \frac{\partial v_{gcal}^2(i)}{\partial e_2} & \frac{\partial v_{gcal}^2(i)}{\partial d_2} \\ \cdots & \cdots \end{bmatrix} \cdot \begin{bmatrix} De_2 \\ Dd_2 \end{bmatrix}. \tag{4.4}$$

The values of Δe_2 and Δd_2 were then added to the initial guesses. Following this, the iteration process was repeated. This iterative calculation was continued until only very small increment values ($<10^{-5}$) needed to be made to update the estimates of the parameters e_2 and d_2. The inverted ray velocity field was then assumed to be the best-fit velocity field to the observations.

$$\sum_i^{n_{obs}} | v_{gobs}(f_i) - v_{gcal}(f_i) | \rightarrow minimum. \tag{4.5}$$

As in program "*para.f*" in Section 3.1.1, the iteration would be compulsorily stopped if the iteration had processed for *50* or more times to avoid ineffective long run times.

The first derivatives of function $v_g^2(f)$ with respect to unknown parameters e_2, d_2

During the above iterative calculations, the first derivatives of the best fitting function needed to be computed. Because of the complexity of the $v_g^2(f)$ calculation, it was hard to compute its first derivatives with respect to unknown parameters e_2, d_2. Hence, numerical approximations were used in the program as follows:

$$\frac{\partial v_g{}^2(f)}{\partial e_2} \approx \frac{v_g^2(f;e_2+se)-v_g^2(f;e_2)}{se},$$
$$\frac{\partial v_g{}^2(f)}{\partial d_2} \approx \frac{v_g^2(f;d_2+sd)-v_g^2(f;d_2)}{sd}. \qquad (4.6)$$

The values of constant *se*, *sd* were adjustable, and were chosen as very small values (10^{-12}) in my programs.

Inversion program "*separa.f*"

My inversion program "*separa.f*" was developed to implement the above procedures. It can be used to recover the parameters of the second layer from the velocity fields of the combined layer. Figure 4.2 shows the flowchart of the inversion program "*separa.f*".

From the signals recorded by receivers located on the bottoms of the first and the second layers, the apparent velocity fields of the first layer and the combined layer may be obtained. The elastic parameters a_{01}, b_{01}, e_1 and d_1 of the first layer and a_{012}, b_{012}, e_{12} and d_{12} of the overall combined layer may be found by using the inversion program "*para.f*" developed in Chapter 3. Subsequently, the recovered parameters a_{01}, b_{01}, e_1 and d_1 of the first layer and a_{012}, b_{012} of the combined layer can be used as input

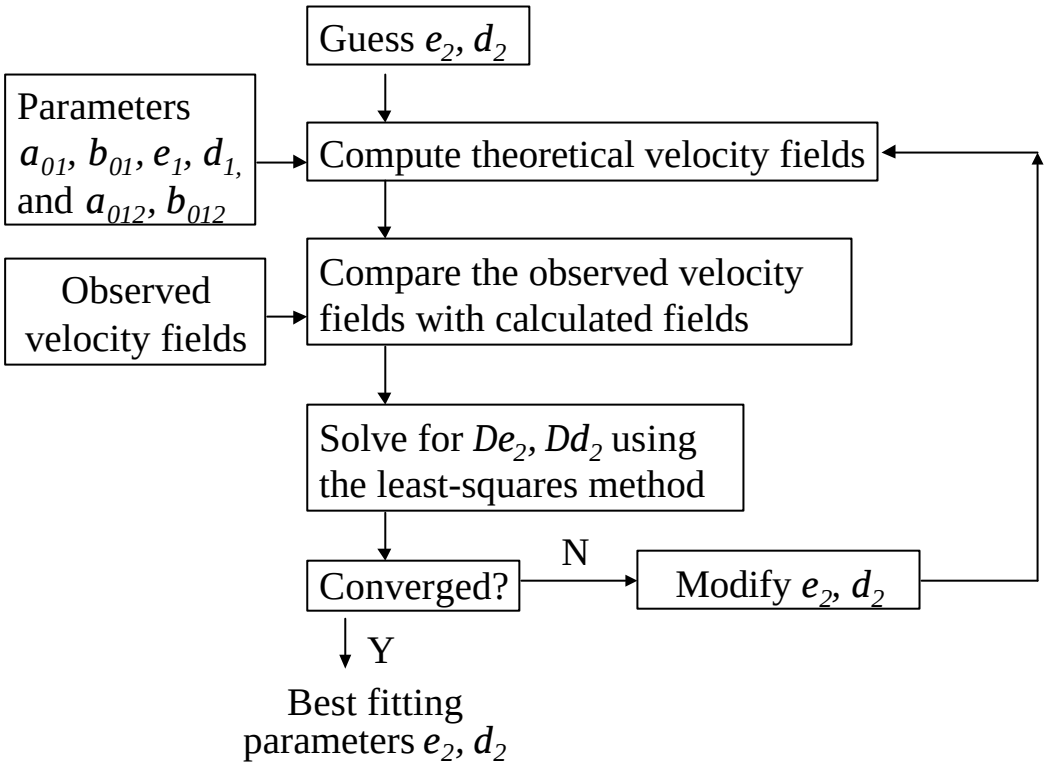

Figure 4.2 The flowchart of the inversion program "*separa.f*". This iterative calculation continues until only very small increment values ($<10^{-5}$) need to be made to the estimates of the parameters e_2 and d_2. The iteration will be compulsorily stopped if the iteration continues for *50* or more times.

to the inversion program *"separa.f"*. The parameters of the second interval layer may be then recovered.

4.1.2 Numerical Results

In this section, numerical modelling experiments are reported which were carried out to test the performance of my inversion program *"separa.f"*.

Synthetic forward modelling data

The six representative two-layered models in Chapter 3.2.3, as shown in Figure 3.7, were used again. Table 3.1 lists the values of the elastic parameters for each material. The thickness ratio z_{12} of these two components was chosen in the range *0.1* to *10*, the same as that in Chapter 3.

Programs *"phiv.f"* and *"twophiv.f"* developed in Chapter 3 were employed again. The velocity fields of P-waves transmitted through the top layer and the combined layer of the models were calculated. These two velocity fields were then assumed to be the observed velocity fields from real field surveys. Since the presence of noise in practical measurement is inevitable, further models were rebuilt by adding random noise, the same as in Chapter 3. Assuming the thickness of each layer to be *1000 m*, random noise less than ± 10 *ms* was added to the travel times. The travel time errors generated by computer were around *2%*. The velocity fields for the top layer and the combined layer were generated again.

The inversion program *"para.f"* developed in Chapter 3 was then used to recover the apparent elastic parameters of each two-layered model. For each model, the parameters of the top layer were determined by the inversion of the velocity field of the top layer. The apparent parameters of these two-layered models were then recovered as before. The results are listed in Table 3.7 and Table 3.8.

Inversion results for interval parameters

The elastic parameters for each top layer and each combined layer were input to the inversion program "*separa.f*". The interval parameters for each second layer were then recovered from the apparent velocity field of the combined layer. Table 4.1 gives the inversion results when the thickness ratio $z_{12}=1$. The differences in interval parameters e_2, d_2 between the inversion results and the model values in each model are well below *0.001* without noise, and *0.03* with noise. The average errors in the velocity fields($\Delta = \sum_{i=1}^{n} \frac{\left| v_g(i) - v_{g\,\mathrm{mod}}(i) \right|}{n}$) from the recovered parameters and from the model data are also very small, less than *1 m/s* without noise, and *30 m/s* with noise.

To verify the inversion results for interval parameters, the apparent velocity field of the combined layer calculated from the inverted interval parameters was compared with the corresponding synthetic velocity data. Figure 4.3 shows an example of the P-wave apparent velocity fields for the fourth model comprising Pierre shale A and Pierre shale B with thickness ratio $z_1/z_2=1$. In the figure, magenta circles represent the synthetic "observation" data. The inverted parameters for the second layer were then input with the known parameters of the first layer to compute an overall apparent velocity field, marked as cyan dots. These two velocity fields (magenta circles and cyan dots) match each other quite well. This enables us to conclude that the inverted interval parameters were good estimations for the second layer of Pierre shale B.

According to Chapter 3, the combined layer may not behave as a completely transversely isotropic single layer for all ray directions. However, the inversion method for the interval parameters still can be used no matter what the property of the combined layer might be. The inversion program only demands transverse isotropy or isotropy for the top layer within survey offset limit.

Table 4.1 Numerical inversion results for interval (the second layer) parameters from two-layered models ($z_1 = z_2$). $\Delta = \sum_{i=1}^{n} \frac{\left| v_g(i) - v_{g\,\mathrm{mod}}(i) \right|}{n}$ represents the average error between the velocity field calculated from the recovered interval parameters and that computed from the model data.

		a_{02}(m/s)	b_{02}(m/s)	e_2	d_2	D(m/s)
	Exact values	2760	1404	0.0	0.0	
Model 1	Inverted parameters(+noise)			0.02	0.01	20
	(no noise)			0.000006	-0.000003	0.8
Model 2	Exact values	2760	1404	0.0	0.0	
	Inverted parameters(+noise)			0.06	-0.02	15
	(no noise)			0.00002	0.000002	0.0006
Model 3	Exact values	2229	1318	1.07	0.327	
	Inverted parameters(+noise)			1.075	0.321	16
	(no noise)			1.070	0.327	0.0012
Model 4	Exact values	2106	887	0.195	0.175	
	Inverted parameters(+noise)			0.195	0.173	14
	(no noise)			0.195	0.175	0.002
Model 5	Exact values	2202	969	0.015	0.060	
	Inverted parameters(+noise)			0.022	0.057	10
	(no noise)			0.015	0.060	0.0004
Model 6	Exact values	3292	1768	0.195	-0.22	
	Inverted parameters(+noise)			0.220	-0.227	30
	(no noise)			0.195	-0.219	0.0004

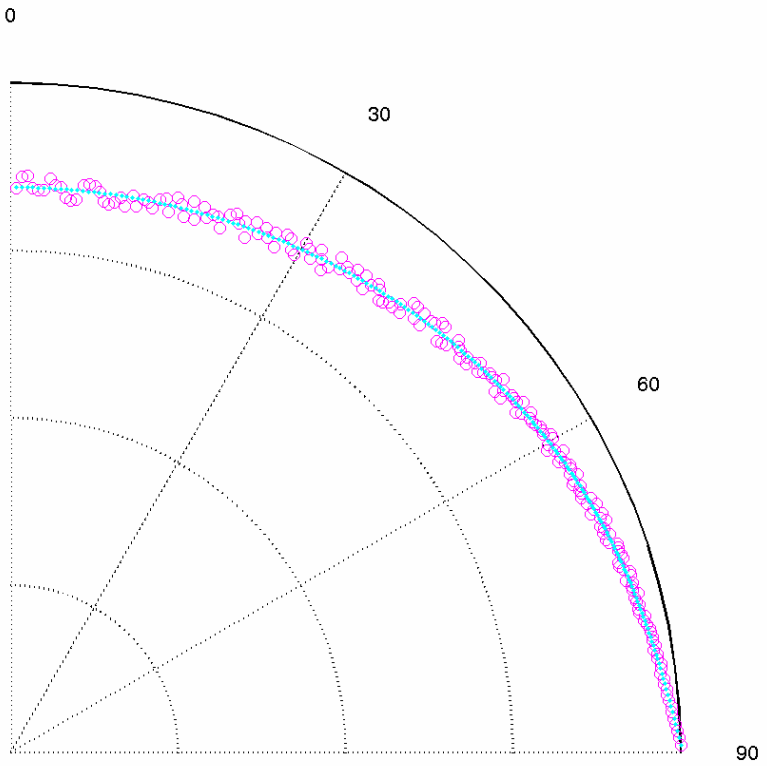

Figure 4.3 The apparent P-wave velocity fields for a two-layered model composing Pierre shale A and Pierre shale B (thickness ratio $z_1/z_2=1$). The magenta circles are synthetic model data with random noise, input as "observations". The inverted parameters for the second layer were then input with the known parameters of the first layer to compute an overall apparent velocity field, marked as cyan dots. These two velocity fields match each other very well.

More results with these same six models but with different thickness ratios were obtained. The recovered interval parameters of the second layer were close to the input model values in each case. Further discussion of these results may be found in Li et al. (1997).

Thus it has been demonstrated that the inversion program *"separa.f"* can recover the interval parameters of the second layer of a two-layered model. It is not affected badly by a reasonable level of random noise, and it is expected to be able handle field data with a typical range of random noise. The application of the inversion program to field data will be left to Chapter 6.

4.2 Joint Inversion of P, SV, and SH-wave VSP Survey Data

A multi-component walkaway VSP survey data set will provide not only P-wave information, but also SV and SH-wave information. It is expected that using the additional information obtained from such survey data should lead to a more accurate and stable result from an inversion process. There is a need to develop an inversion method to recover the interval elastic parameters using P, SV, and SH-wave data from multi-component walkaway VSP surveys.

4.2.1 Inversion for Interval Parameters for a Two-layered Model

The following is an account of the strategy which was developed for the recovery of interval parameters e_2, d_2, g_2 from multi-component measurements on a two-layered model. The steps outlined were incorporated into a computer program.

The two-layered model was considered to have the same acquisition geometry shown in Figure 3.3. The observation velocity fields were taken to include not only the P-wave velocity field, but also the SH, and SV-wave velocity fields.

First we measured the velocity fields for the top layer $v_{g1}(f)$ and for the combined layer $v_g(f)$ from travel time data. From these velocity fields, the corresponding parameters (a_{01}, b_{01}, e_1, d_1, g_1) for the top layer and apparent parameters (a_{012}, b_{012}, e_{12}, d_{12}, and g_{12}) for the combined layer were obtained separately using the inversion program "*parameter.c*" as in Section 3.4.

The elastic parameters a_{02}, b_{02} for the second layer were obtained directly from transmission data using equations 4.1 and 4.2. We now need to develop a new program to recover the anisotropic parameters e_2, d_2, and g_2 of the second layer.

Inversion program

For a set of trial parameters e_2, d_2, and g_2, a ray meeting the interface between these two layers with an incident phase angle q_1 in the top layer was considered first. The ray was assumed to refract into the second layer with a refracted phase angle q_2. The corresponding phase velocity for the incident and refracted rays was calculated using equations 2.24, 2.25, or 2.26. The refraction at the interface satisfied equation 2.11 (Snell's law). The refracted phase angle q_2 was then found using the bisection subroutine *RTBIS* (Press et al., 1992b), as in Section 3.2.1. Then the corresponding group velocities for the top layer $v_{g1}(f_1)$ and for the second layer $v_{g2}(f_2)$ were computed using equations 2.28 and 2.29. Thus, the apparent group velocity $v_{gcal}(f)$ for the combined layer with an incident phase angle q_1 in the top layer was calculated using equations 3.7 and 3.8 in Section 3.2.1.

The ray velocity $v_{gcal}(f)$ in a specific observed ray direction f was then calculated using the golden-ratio search method (Gottfried and Weisman, 1973) as in Section 3.1.1.

Using the above simulations, we obtained the calculated velocity fields for the combined layer with a set of trial parameters e_2, d_2, and g_2. We compared the

calculated velocity data for the combined layer with the observations. The iterative procedure using the Levenberg-Marquardt method (Press et al., 1992) was then implemented to find the best-fitting interval parameters e_2, d_2, and g_2.

The model to be fitted is:

$$v_{gcal}(f) = v_{gcal}(f, e_2, d_2, g_2) . \tag{4.7}$$

The "chi-square" merit function is:

$$c^2(e_2, d_2, g_2) = \sum_{i=1}^{nobs} \left[v_{gobs}(f_i) - v_{gcal}(f_i, e_2, d_2, g_2) \right]^2 . \tag{4.8}$$

Using Levenberg-Marquardt method described in Section 3.3.1, the increments in each variable De_2, Dd_2, and Dg_2 were calculated. These increments were added to their initial values and the iteration went back and ran again. The iteration proceeded until 'chi-square' — the sum of the squared differences between observed and calculated velocity fields — changed by less than *0.0001* from the previous iteration. The iteration would be compulsorily stopped if the iteration had processed for *50* or more times to avoid ineffective long run times.

Because of the complexity of the group velocity $v_g(f)$ calculation, it is hard to compute its first derivatives with respect to parameters e_2, d_2, and g_2. Hence, similar to equation 4.6, the following approximations were used in the programs:

$$\begin{aligned} \frac{\partial v_g(f)}{\partial e_2} &\approx \frac{v_g(f, e_2 + se) - v_g(f, e_2)}{se}, \\ \frac{\partial v_g(f)}{\partial d_2} &\approx \frac{v_g(f, d_2 + sd) - v_g(f, d_2)}{sd}, \\ \frac{\partial v_g(f)}{\partial g_2} &\approx \frac{v_g(f, g_2 + sg) - v_g(f, g_2)}{sg}. \end{aligned} \tag{4.9}$$

The values of constants *se, sd* and *sg* are adjustable. They must be chosen as very small values, and in my programs they were 10^{-12}.

The recovered parameters a_{01}, b_{01}, e_1, d_1, and g_1 of the first layer and a_{012}, b_{012} of the overall combined layer were used as input to this newly developed inversion program "*interval.c*". The interval parameters e_2, d_2, and g_2 of the second interval layer were then recovered from the apparent velocity fields of the combined layer.

4.2.2 Numerical Model Results

To test the program "*interval.c*", numerical simulation experiments were carried out.

Synthetic data

Using the elastic parameters in Table 3.17, a two-layered model was established consisting of Taylor sandstone and Pierre shale A. The thickness ratio z_{12} was chosen to have values *0.1, 1,* and *10*. To simulate real field data, random noise was added to the velocity field. The thickness of each layer was assumed to be *1000 m*, the errors in travel time picks were chosen to be no greater than *±10 ms*, which gave less than *2%* random noise in the velocity field.

Using programs "*forward.c*" and "*twoforward.c*", the velocity fields for P, SV, and SH-waves were calculated for the top layer and the combined layer. These apparent velocity fields were used as the "observations", and the number of the shots was set to be *100*.

The parameters for the top layer and the apparent elastic parameters for the combined layer were then recovered by the program "*parameter.c*" for various thickness ratios as listed in Table 3.19.

Inversion results for the interval parameters

Using these recovered elastic parameters as inputs, the inversion program "*interval.c*" was run to recover the interval parameters of layer two from the velocity fields of the combined layer. Table 4.2 gives the inversion results of interval parameters e_2, d_2, and g_2 for this synthetic two-layered model with different layer thickness ratios. The interval parameters e_2, d_2, and g_2 found by inversion coincide very well with their exact values, even when random noise was added to the travel time data. The

Table 4.2 Inversion results of interval parameters for synthetic multi-component VSP data for two-layered models. $\Delta = \sum_{i=1}^{n} \frac{\left| v_g(i) - v_{g\,\mathrm{mod}}(i) \right|}{n}$ represents the average difference between the velocity fields computed from the recovered interval parameters and the synthetic observed velocity fields, while W is the mean relative error. Here, z_1/z_2 represents the thickness ratio for the two-layered models.

	a_{02}(m/s)	b_{02}(m/s)	e_2	d_2	g_2	D(m/s)	W(%)
exact values	2074	869	0.110	0.090	0.165		
$z_1/z_2=0.1$			0.113	0.092	0.174	16	1.4
$z_1/z_2=1$			0.118	0.098	0.184	19	1.3
$z_1/z_2=10$			0.102	0.088	0.200	22	1.1

differences between the recovered interval parameters e_2, d_2, and g_2, and the actual layer two parameters are less than *0.04*.

The calculated apparent velocity fields for the *combined layer* were then obtained using the inverted interval parameters of layer two with the known parameters of the top layer. They were compared with the original synthetic data input to the inversion program for the combined layer. Figure 4.4 shows an example of this two-layered model with a thickness ratio $z_1/z_2=1$. The magenta circles represent the synthetic model data assumed to be "observations". The inverted parameters for the second layer were then input with the known parameters of the first layer to compute the overall apparent velocity field, marked as cyan dots. It can be seen that the two velocity fields match each other very well. This is a demonstration that the inversion program was successful.

The inversion program *"interval.c"* for interval parameters was demonstrated to be able to handle data with random noise. More numerical models were built to successfully test the program (not reported here), and further studies on the application to field data will be discussed in Chapter 6.

4.2.3 Multi-layered Application

Now consider a multi-layered model, where a source moves along the upper surface, and travel times are recorded at different 3-component receivers, as shown in Figure 3.13. This geometry simulates a multi-level multi-component VSP field survey. It is proposed to obtain the interval parameters of a layer of interest as follows.

With a 3-component receiver at R_1, the P, SV, and SH-wave signals travelling through the first layer are recorded. We pick the first arrival times for every shot position, and the observed velocity fields are calculated for P, SV, and SH-waves. By inputting these observed velocity fields into the inversion program *"parameter.c"*, the elastic parameters of the first layer a_{01}, b_{01}, e_1, d_1, and g_1 can be determined. Similarly, by analysing walkaway VSP signals at a 3-component receiver R_2, the

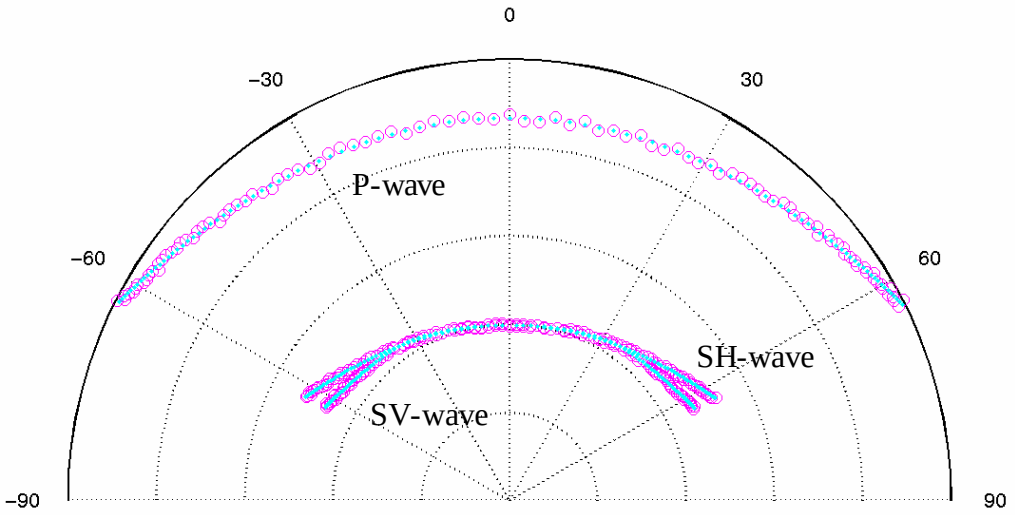

Figure 4.4 The apparent P-wave velocity fields of three wave modes for a two-layered model composing Taylor sandstone and Pierre shale A (thickness ratio $z_1/z_2=1$). The magenta circles are synthetic model data with random noise, assumed as "observations". The inverted parameters for the second layer were then input with the known parameters of the first layer to compute an overall apparent velocity field, marked as cyan dots. These two velocity fields match each other very well.

apparent elastic parameters a_{012}, b_{012}, e_{12}, d_{12}, and g_{12} of the first two layers overall are obtained. Then, the recovered elastic parameters for the top layer and the first two layers combined as well as the apparent velocity field for the first two layers combined are input to the inversion program *"interval.c"*. We obtain the recovered interval parameters a_{02}, b_{02}, e_2, d_2, and g_2 for the second layer.

Working downwards through successive levels, the apparent elastic parameters of the first *(i-1)*th, and *i*th layers may be determined from measurements at receivers R_{i-1} and R_i. From these two sets of measurements, the interval parameters of layer *i* may be determined as a generalisation of the two-layered case, discussed above. Hence, the interval parameters and velocity field of each individual layer may be readily determined. This concept will be tested on field survey data in Chapter 6.

4.3 Discussions and Conclusions

An inversion method has been developed to recover the interval anisotropic parameters of any layer of interest from walkaway VSP survey data. For a given layer of interest, receivers are used on the upper and lower surfaces of the layer of interest to record seismic travel times. The apparent elastic parameters of the combined media above the upper and lower surfaces of this layer are then obtained separately, by using inversion program *"parameter.c"* developed in Chapter 3. Then, the anisotropic properties of this individual layer may be determined, by using the inversion program "*interval.c*" developed in this chapter.

The interval parameters are also known as apparent interval parameters, because the inversion program is based on a two-layered model. The overall effect of seismic wave propagation through this interval layer is identical to that of a single layer with the inverted interval parameters. The assumption of homogeneity in the layer of interest is not required.

Computer simulation experiments were used to study horizontally layered VTI models. The inversion results satisfactorily agreed with the assumed model values even after

the addition of random noise to the input travel time data. The inversion method has been found to be successful with a typical range of random noise. Further application of this inversion method to field data will be studied later in Chapter 6.

The inversion program "*interval.c*" developed in Section 4.2 can now be used to replace program "*separa.f*" developed in Section 4.1. If only P-waves are acquired, the inversion program "*interval.c*" can still be run to recover the unknown parameters e_2 and d_2, without g_2.

CHAPTER 5

APPLICATION TO PHYSICAL MODELLING EXPERIMENTS

An inversion method for recovering the apparent elastic parameters of transversely isotropic media was developed in Chapter 3. The method was tested successfully on computer synthetic data. In this chapter, physical model tests will be implemented before the inversion method is tested on real field data in Chapter 6.

In the physical modelling laboratory, the experimental setting is designed to study seismic wave propagation through rocks on a laboratory scale. It is inexpensive compared to real field measurements. Because of the easy control over the structure and properties of an experimental model, physical modelling experiments make the study of wave propagation simpler and easier to verify. Physical modelling experiments provide a convenient way to study the acoustic properties of rocks, especially when complex models are involved, because the actual physical properties of the components in these models are known. Physical modelling experiments also simulate real field data with measurement errors. Thus they provide good means of testing these inversion procedures.

The inversion program will be applied to recover the elastic parameters of Plexiglas and Phenolite blocks from physical modelling data obtained in our Departmental Seismic Physical Modelling Laboratory.

The experiments reported in this chapter will be limited to P-wave inversion only, because difficulty was encountered in obtaining suitable shear wave data with the modelling system.

5.1 Introduction

As pointed out in Chapter 1, the elastic parameters of a transversely isotropic medium are often measured in the physical modelling laboratory using transmission experiments. Conventionally, the width and height of core samples are normally several centimeters. Measurements may be made on the cores cut at angles of *0°*, *45°* and *90°* to the symmetry axis. (e.g., Vernik and Nur, 1992; Lo et al., 1986; Jones and Wang, 1981). The elastic parameters are then obtained from the travel times in these three directions as follows.

Thomsen (1986) derived equations to determine e and d directly from a single set of measurements at $q=0°$, $45°$ and $90°$:

$$\begin{aligned} e &= \frac{v_h^{\,2}}{2a_0^{\,2}} - \frac{1}{2}, \\ d &= 4\left[v_p(p/4)/v_p(0) - 1\right] - \left[v_p(p/2)/v_p(0) - 1\right]. \end{aligned} \tag{5.1}$$

Note that the second expression in equation 5.1 is limited to the case of weak anisotropy. He also pointed out that the errors in measuring velocity would result in cumulative errors in the determination of elastic parameters. For example, if the relative error in velocity measurement is *2%*, the absolute standard error in d is of the order of *0.12*, which is of a similar magnitude to d itself. A small relative error in velocity measurement will introduce a large relative error in d, because of the nature of the equations from which d is derived.

Using numerical simulation methods, Dellinger and Vernik (1994) showed that whether experiments of this kind are more likely to measure phase or group velocity depends on the critical ratio of core-sample height to transducer width. The design of experiments should be carefully done to avoid mistakenly measuring the wrong velocities. In addition, as pointed out by Thomsen (1986), errors in measuring velocity will be great, because the sample needs to be cut and the heterogeneity (as distinct from anisotropy) of small samples becomes significant.

An inversion method was developed to recover the elastic parameters a_0 and d^* (Okoye et al., 1996), using group velocities at a range of offsets obtained from

laboratory transmission experiments. Subsequently, with real field surveys in mind, a new method was developed in Chapter 3. It recovers the elastic parameters a_0, b_0, e, d, and the angle of tilt y, from P-wave transmission times in a transversely isotropic medium. Using best-fit methods for a set of observations at many different ray angles ranging from $0°$ to $90°$, instead of only three directions ($0°$, $45°$ and $90°$) to symmetry axis, the method increases the statistical accuracy of the parameters recovered. My software has been successfully tested on computer simulated data (Li et al., 1998b). However, when applying this method to laboratory data for P-waves, Gyngell (1999) discovered the existence of a flat zone of equal traveltimes at near offsets. This observation suggests a measurement problem. Data of this kind does not appear to be characteristic of any real velocity functions. Further study of the physical modelling method is warranted.

5.2 Physical Modelling Experiments

5.2.1 Laboratory Setting

Figure 5.1 is a photo of the physical modelling laboratory in the Department of Exploration Geophysics, where the following research was conducted.

The physical modelling system

In the physical modelling laboratory, as we can see from Figure 5.1, steel scaffolding supports two independent mobile indexers. Each mobile indexer can be moved in three-dimensions manually or automatically according to the instruction from the software *SAM* in a personal computer. The accuracy of each of the mobile indexer positioning is ± 0.25 *mm*. A source or receiver can be fixed to the mobile indexers and moved with them.

The sources and receivers used are ultrasonic transducers. An ultrasonic transducer converts electrical energy to mechanic energy, in the form of sound, and vice versa.

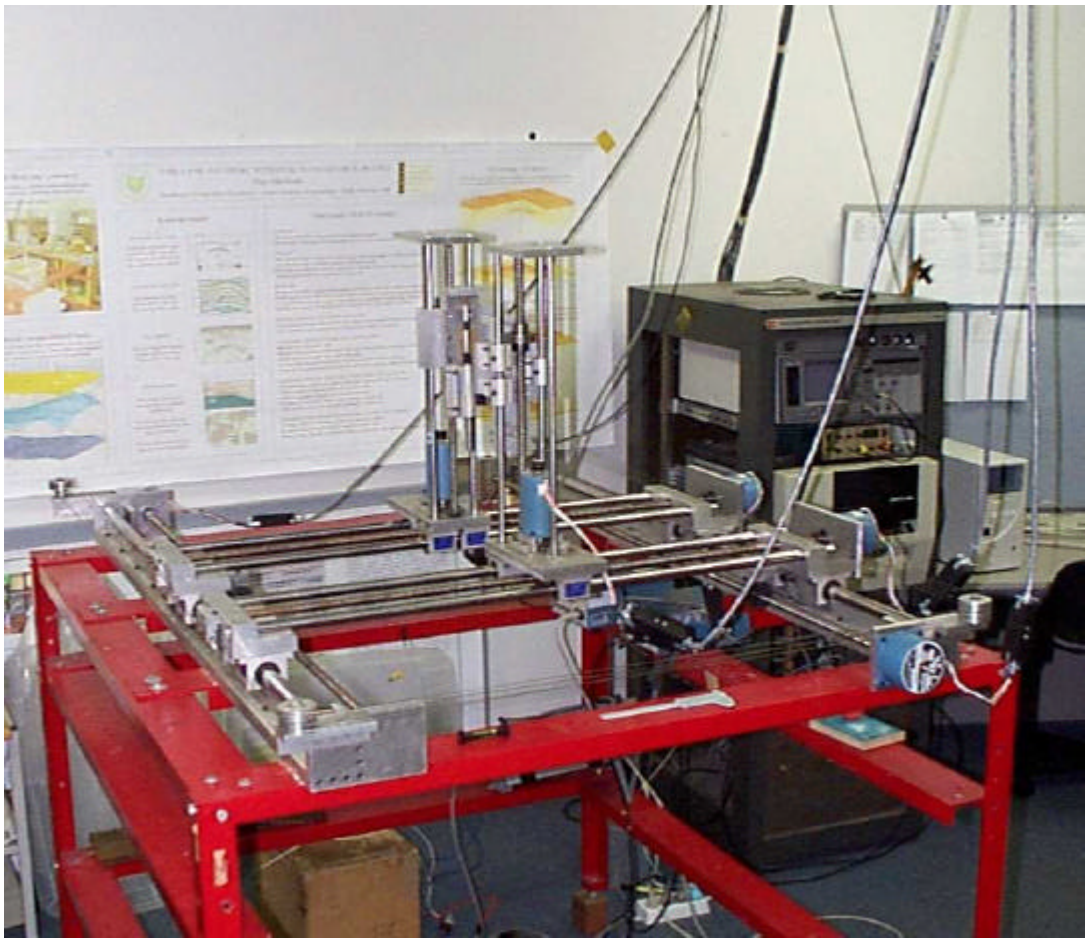

Figure 5.1 Photo of the Physical Modelling Laboratory. The physical modelling experiments in this thesis were carried out using these laboratory facilities. Ultrasonic sound waves were generated and detected with computer controlled transducers.

The main components of an ultrasonic transducer are the active element, the backing, and the wear plate, shown in Figure 5.2 (Panametrics Inc, 1999).

The basic equipment in the physical modelling laboratory is shown in Figure 5.3. As in a real field survey, there is a source, a receiver and recording instruments. More detailed descriptions of the Physical Modelling System have been given by Walton (1996) and Peyrière (1998).

In an ultrasonic experiment, a source transducer generates an impulsive wave from an oscilloscope through a source amplifier following a command from the controlling PC. The impulse wave travels through an experimental model and is received by a receiver transducer. Via a receiver amplifier, the signal is recorded by a computer in SEGY format (IRIS PASSCAL Instrument Center, 2002). PROMAX software (Landmark Graphics Co.) is then used to process the recorded data.

Laboratory experiment setting in this research

For this research, the laboratory experiments were designed to simulate walkaway VSP field surveys with a single receiver level. A sketch of the experimental laboratory setting is illustrated in Figure 5.4. A source transducer, which was fixed on the bottom surface of an experiment block, emitted an ultrasonic wave with a central frequency of *1.0 MHz*. After being transmitted through the experimental block, the seismic wave was recorded by a receiver transducer on the upper surface of the block. The receiver transducer was moved along the survey line in *2 mm* increments. The time sample interval used in seismic trace recording was chosen to be *0.1 ms*. The source was fired 10 times for every receiver position. These 10-fold traces were then stacked in order to reduce random noise. There were 120 receiver positions.

The scale factor in distance and time was chosen to be *10 000* in the experiment. This meant that the receiver transducer moving *2 mm* each time corresponded to a *20 m* receiver interval in the field, and the sample interval used in the recording which was chosen to *0.1 ms* corresponded to *1 ms* in field data.

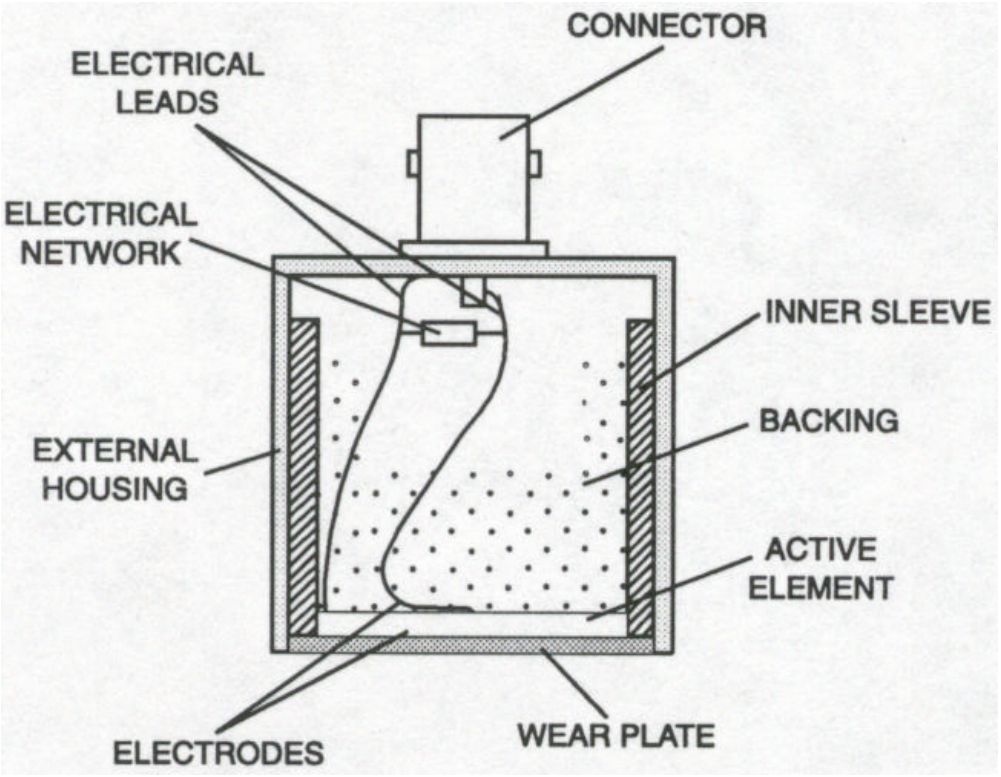

Figure 5.2 Illustration of the structure of an ultrasonic transducer. Ultrasonic transducers were used as sources and receivers in this study. The main components of an ultrasonic transducer are the active element, the backing, and the wear plate (Panametrics Inc, 1999).

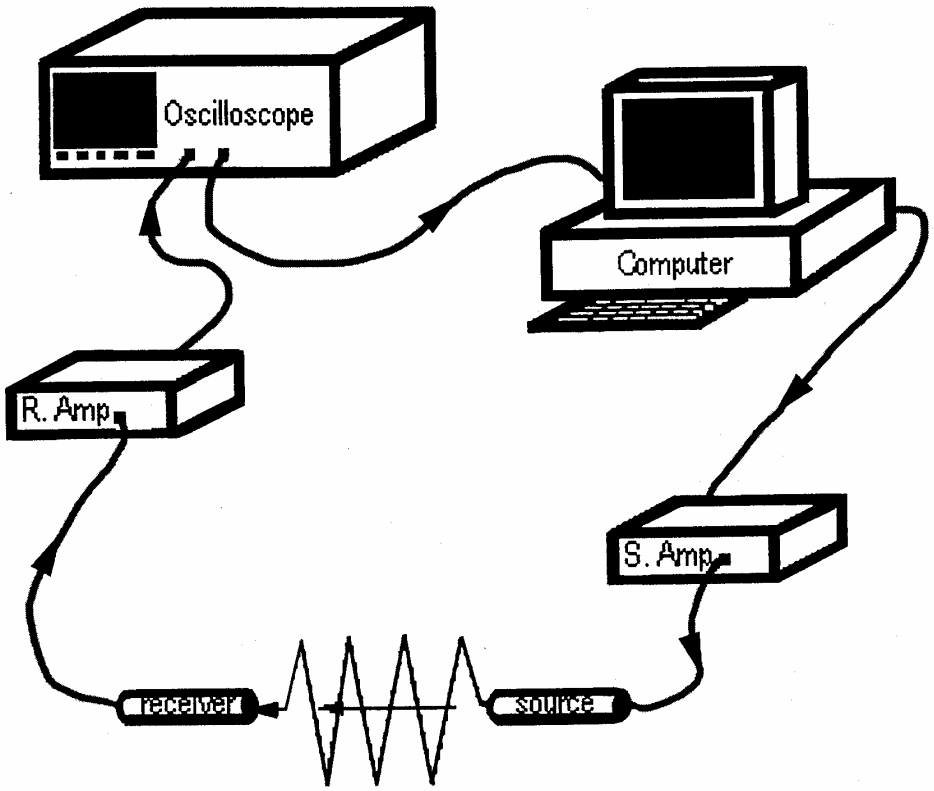

Figure 5.3 Setting of the Physical Modelling System. The physical modelling experiments in this thesis were carried out using the laboratory facilities in the Department of Exploration Geophysics at Curtin University. Here, S. Amp is a source amplifier, R. Amp is a receiver amplifier. The arrowheads show the direction of the "data flow". (after Peyrière, 1998)

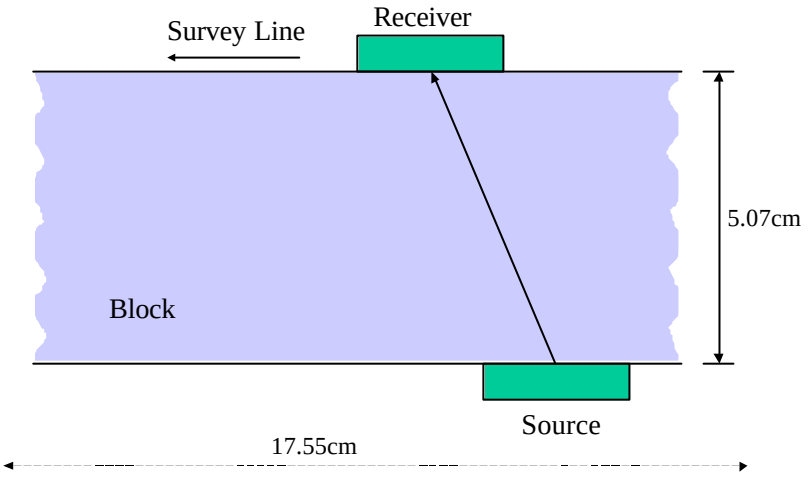

Figure 5.4 The experimental transmission setting in the physical modelling laboratory (not drawn to scale). The source transducer is located beneath the block, while the receiver transducer moves along the survey line on the other side.

Laboratory materials used in this research

The experimental materials used in this research were Phenolite and Plexiglas.

Phenolite is an electrical insulating material, which consists of layers of paper, pressed and packed together, and set in Phenolic resin. This thin-layer microstructure exhibits the property of transverse isotropy (Okoye, 1994). In my physical modelling experiments, the dimensions of the Phenolite block used were *39.35´17.55´5.07 (cm) (length´width´height)*, shown photographically in Figure 5.5. Its mass was *4.974 kg*, thus the density of this block was $1.43´10^3$ kg/m^3.

A block of Plexiglas, which is known to be an isotropic material, was also used. Figure 5.6 shows the experimental block of Plexiglas. The dimensions of the block are *30.05´18.05´4.88 (cm) (length´width´height)*, which were of the same order as those of the Phenolite block.

Types of transducers used in this research

"Large" transducers used by the previous researchers in our department (Okoye, 1994; Walton, 1996) were used in my laboratory experiments. The "large" transducers for P or S-waves were 1.46 *cm* wide. The recorded signals from the experiments using "large" transducers were strong.

"Point" size transducers for P-waves were available in the later stage of this research. They were used for comparison purposes. "Point" size transducers for P-waves were *0.14 cm* wide. They also provided signals of good quality.

Figure 5.7 shows the two kinds of transducers used. The results obtained using these two types of transducer will be examined next.

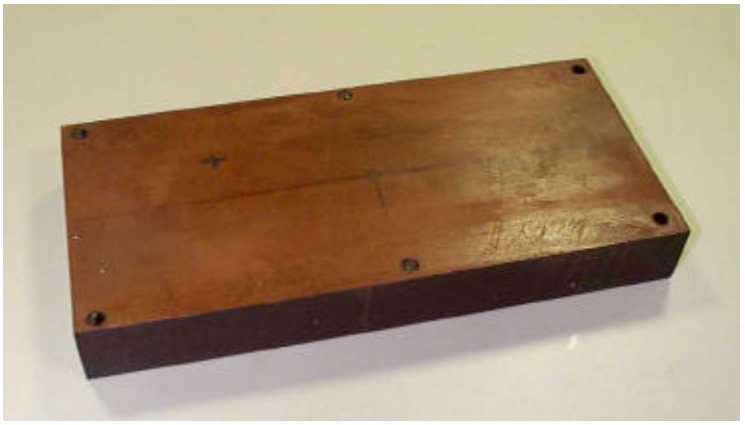

Figure 5.5 Phenolite block used in the laboratory experiments. The dimensions of the Phenolite block were *39.35´17.55´5.07 (cm) (length´width´height).*

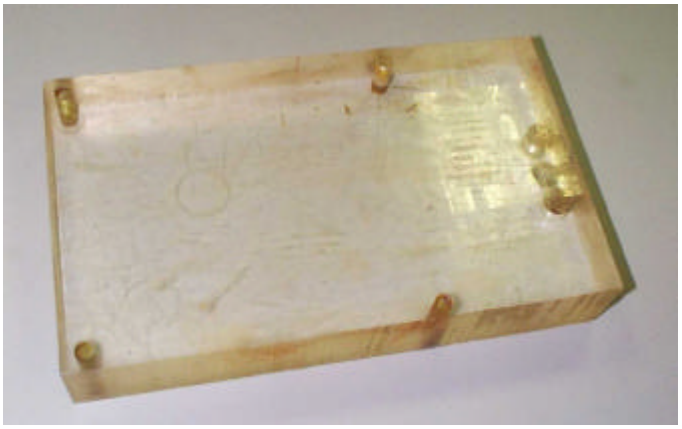

Figure 5.6 Plexiglas block used in the laboratory experiments. The dimensions of the Plexiglas block were *30.05´18.05´4.88 (cm) (length´width´height)*, of the same order as those of the Phenolite block.

- Point transducer:
  diameter is 0.14cm

- Large transducer:
  diameter is 1.46cm

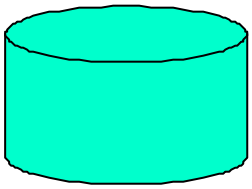

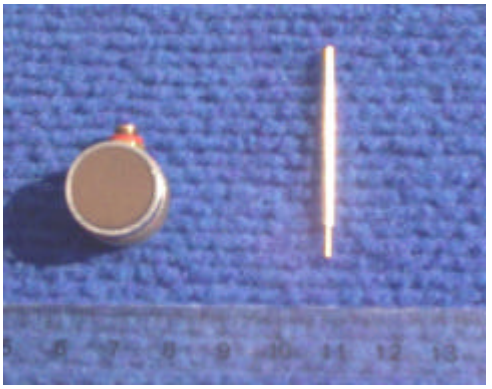

Figure 5.7 Comparison of “point” transducer and “large” transducer. The width of the “large” transducer was 10 times bigger than that of the “point” transducer.

Time picking and time correction

The physical modelling system produced data in SEGY format. Then the data were input to *Promax*. Ten traces for every receiver position were stacked, then the first break travel times were picked. The first break travel times $t_{recorded}$ were output as ASCII files.

If the source and receiver are placed in direct contact with each other without any medium between them, the first arrival travel times recorded should be zero. Any observed time delays could then be considered to be due to an "instrumental delay" arising from the amplifier or transducer characteristics. The recorded delay time was noted as t_{delay}.

Hence, using the same source and receiver in an experiment, a recorded first break travel time $t_{recorded}$ was considered to be composed of two travel time components. One was the travel time through the experimental block t_{block}. The other was the instrumental delay t_{delay}. So, the travel times through the experimental block t_{block} were then corrected as follows:

$$t_{block} = t_{recorded} - t_{delay}\,. \tag{5.2}$$

These travel times t_{block} through the experimental block were then converted to the velocities in the directions from the centre of the source to the centre of the receiver. The velocity field through this experiment block was obtained in this way for a range of directions through the block.

5.2.2 Experimental Results

Using the block of Phenolite, a transmission experiment, illustrated in Figure 5.4, was carried out to simulate single level walkaway VSP shot records. Both "point" and "large" transducers were used separately for comparison purposes. The experimental records obtained are shown in Figure 5.8.

When "large" transducers were used, the first break event at near offsets was flattened. At intermediate and far offsets, the first break event precedes the

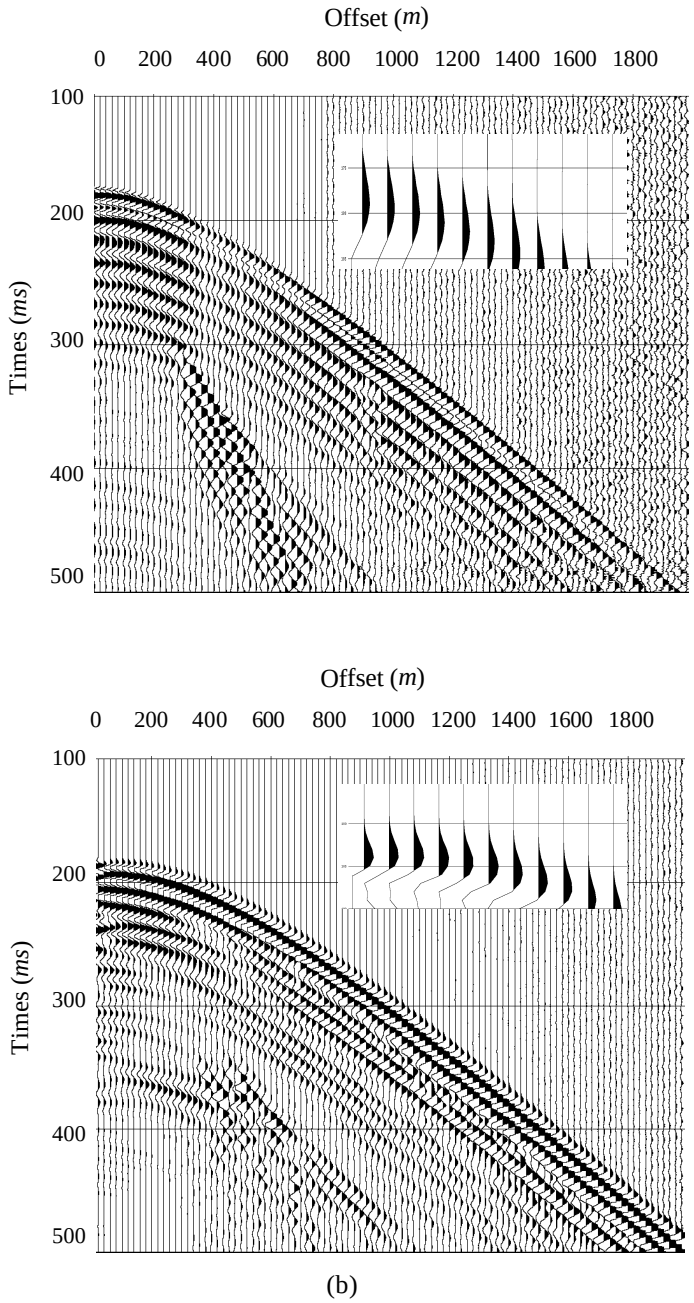

Figure 5.8 Simulated single level walkaway VSP shot records from physical modelling experiments using the Phenolite block. The top panel (a) was obtained with "point" transducers. The bottom one (b) was generated using "large" transducers. The near offset parts of each record are enlarged at the upper right corner for each panel. The first break event on the bottom panel is flattened at near offsets. At intermediate and far offsets, the first arrival times precede those on the top panel.

corresponding event observed when "point" size transducers were used by around *15 ms* in travel times. By picking the first arrival times for P-waves at different offsets, the velocities at different transmission angles were derived. Here, an offset was defined as the horizontal distance between the centre of the source and the centre of the receiver, a transmission angle was defined as the angle between the vertical direction and the straight line from the centre of the source to the centre of the receiver. Then using the inversion method developed in Chapter 3, the elastic parameters of this block were recovered. With *point* transducers, the parameter values recovered were a_0*=3089 m/s,* b_0*=1580 m/s,* e*=0.513,* d*=0.135,* and d^**=-0.179.* With *large* transducers, the parameters values recovered were a_0*=2988 m/s,* b_0*=1528 m/s,* e*=0.592,* d*=0.725,* and d^**=0.633*. The difference between these two inversion results for parameter e was *0.079,* for d was *0.59,* while d^* even changed its sign! These differences are unacceptable and need further investigation.

Horizontal velocity of SH-waves

For the purpose of verifying the stability conditions, the horizontal SH-wave first arrival time was also measured directly as shown in Figure 5.9, using "large" transducers. The first arrival time in the horizontal propagation direction for SH-waves was *1762 ms.* The horizontal velocity was then obtained as $v_h(SH)$*=2246 m/s.* From equation 8b in Thomsen's paper (1986), the Shear wave anisotropic parameter g was calculated to be:

$$g = \frac{v_h^2(SH)}{2b_0^2} - \frac{1}{2} = 0.51, \tag{5.3}$$

and C_{66} was 7.2×10^9 $N \cdot m^{-2}$ using equation 2.30.

Stability conditions

After examining the recovered stiffness coefficients of the Phenolite block from data sets using "point" and "large" transducers, all the stability conditions (stated in equation 2.31) for a transversely isotropic medium were found to be satisfied. Both sets of recovered elastic parameters are possible properties for a transversely isotropic medium.

Figure 5.9 The laboratory setting for the measurement of horizontal velocity. The source and receiver transducers were fixed on the opposite sides of the Phenolite block to record direct horizontal travel time.

For the same experimental block, inconsistent parameter values were recovered from different experimental records using the two transducer types. Further studies were needed to examine the experiments with different transducers.

5.2.3 Parameters Obtained From Direct Measurements

The horizontal P-wave first arrival time was measured directly on the Phenolite block, as shown in Figure 5.9, using the "large" transducers. The first arrival time in the horizontal propagation direction for P was *894 ms.* The horizontal velocity was then computed to be $v_h(P)=4402$ *m/s*. Using the exact expression from equation 5.1, the value of e was calculated to be

$$e = \frac{v_P^2(\frac{p}{2})}{2a_0^2} - \frac{1}{2} = 0.52 . \tag{5.4}$$

The block thickness in the experiments was measured and found to be not completely uniform. The measured thickness of the block was $d=(5.07\pm0.02)$ *cm*. So the relative error in the vertical seismic travel path was estimated to be: $\frac{Dd}{d} = \frac{0.02}{5.07} \approx 0.4\%$. Assuming the errors in the first break picking to be *1 ms*, the smallest travel time through this block was measured as *168 ms.* So the relative error in traveltimes will be less than $\frac{Dt}{t} = \frac{1}{168} \approx 0.6\%$. Hence the relative errors in the determined velocity field were estimated to be *1%*. Subsequently, we have:

$$\frac{D\left(\frac{v_P^2(\frac{p}{2})}{2a_0^2}\right)}{\left(\frac{v_P^2(\frac{p}{2})}{2a_0^2}\right)} = 2\frac{D\left(v_p(\frac{p}{2})\right)}{v_p(\frac{p}{2})} + 2\frac{D(a_0)}{a_0} \approx 4\times 1\% = 4\% . \tag{5.5}$$

So,

$$De = D\left(\frac{v_P^2 (\frac{p}{2})}{2a_0^2} \right) \approx 4\% \times (0.52 + 0.5) \approx 0.04 , \quad (5.6)$$

giving $e=(0.52\pm0.04)$. This result from the direct measurement with large transducers is close to the inverted value of e using "point" transducers.

5.2.4 Calibration Experiments

Subsequently, calibration experiments using "large" and "point" size transducers were conducted on a Plexiglas block, which is a known isotropic material. The dimensions of the Plexiglas block are of the same order as those for the Phenolite block. The calibration experiments were carried out in the same way as those for the Phenolite block in Section 5.2.2.

As in Section 5.2.2, P-wave transmission velocities in the Plexiglas block at different transmission directions were calculated from the recorded transmission times. The inversion program was then run to recover the elastic parameters. For "large" transducers, the elastic parameters for Plexiglas block were found to be $a_0=2761$ m/s, $b_0=1412$ m/s, $e=0.054$, and $d=0.686$, and for "point" transducers, $a_0=2773$ m/s, $b_0=1418$ m/s, $e=-0.007$, and $d=0.02$. For isotropic materials, the values of e and d should be zero. The recovered anisotropic parameters using "point" transducers $e=-0.007$, and $d=0.02$, were very small, and can be regarded as good estimates for the Plexiglas block. But the recovered anisotropic parameters using "large" transducers were $e=0.054$, and $d=0.686$. These differences from zero values cannot be ignored.

It is evident from the above inversion results that the errors in the recovered parameters using "point" transducers are quite small. This indicates that "point" transducers should be suitable for carrying out physical modelling experiments intending to recover the elastic parameters of anisotropic core samples. Using "large" transducers in the experiment may introduce appreciable errors in the inverted parameters.

5.2.5 Further Experiments

The parameters recovered from the measurements using "point" transducers were a_0*=3089 m/s*, b_0*=1580 m/s*, e*=0.513*, d*=0.135*, and d^**=-0.179*. These were used as the accepted standard values for the Phenolite block used in the physical modelling laboratory (Li et al., 2000d).

Using a "large" transducer as a source, and a "point" transducer as a receiver, and vice versa, two further sets of physical modelling experiments were conducted. Results obtained with various combinations of "large" and "point" transducers are tabulated in Table 5.1. Stability conditions (equation 2.31) were satisfied for each set of recovered parameters.

Examining the inversion results, we see that the experiments using one "large" transducer and one "point" transducer give better results than using "large" transducers only. The inversion results were considered better still when using two "point" transducers as a source and a receiver, instead of using combinations of one "point" and one "large" transducer. Figure 5.10 shows the inversion results for the elastic parameters for the Phenolite block with different combinations of "large" and "point" transducers.

5.2.6 Discussions of the Experiment Results

The large size of transducers appears to affect the accuracy of the inversion results. The width of "large" transducers in my experiments, i.e., *1.46 cm*, corresponds to a full scale field width of *146 m*. However, in a real field survey, a source or a receiver can be treated as a "point" source or receiver due to the width of a source or a receiver being much less than this dimension. The size effects of sources or receivers on the recovered parameters in field data would be too small to be considered.

Table 5.1 Inversion results from travel times using different size transducers on a Phenolite block. *D* represents the error in velocity field inversion, and *W* represents the percentage relative error in velocity field inversion. The recovered stiffness coefficients are listed here in order to verify the stability conditions for TI media.

Trial number	1	2	Average of 1 and 2	3	4	5
Source transducer	point	point	point	large	point	large
Receiver transducer	point	point	point	large	large	point
a_0(m/s)	3089	3089	3089	2989	3068	3064
b_0(m/s)	1580	1580	1580	1528	1569	1567
e	0.514	0.512	0.513	0.592	0.519	0.538
d	0.124	0.146	0.135	0.725	0.344	0.297
d^*	-0.197	-0.162	-0.179	0.633	0.125	0.041
C_{33}(´10^9 N× m^{-2})	13.65	13.64	13.65	12.77	13.46	13.43
C_{44}(´10^9 N× m^{-2})	3.57	3.57	3.57	3.34	3.52	3.51
C_{11}(´10^9 N× m^{-2})	27.66	27.63	27.64	27.88	27.43	27.88
C_{13}(´10^9 N× m^{-2})	8.07	8.34	8.21	12.89	10.29	9.81
D(m/s)	4.5	10	8	12	4.6	4.5
W(%)	0.12	0.25	0.21	0.32	0.13	0.12

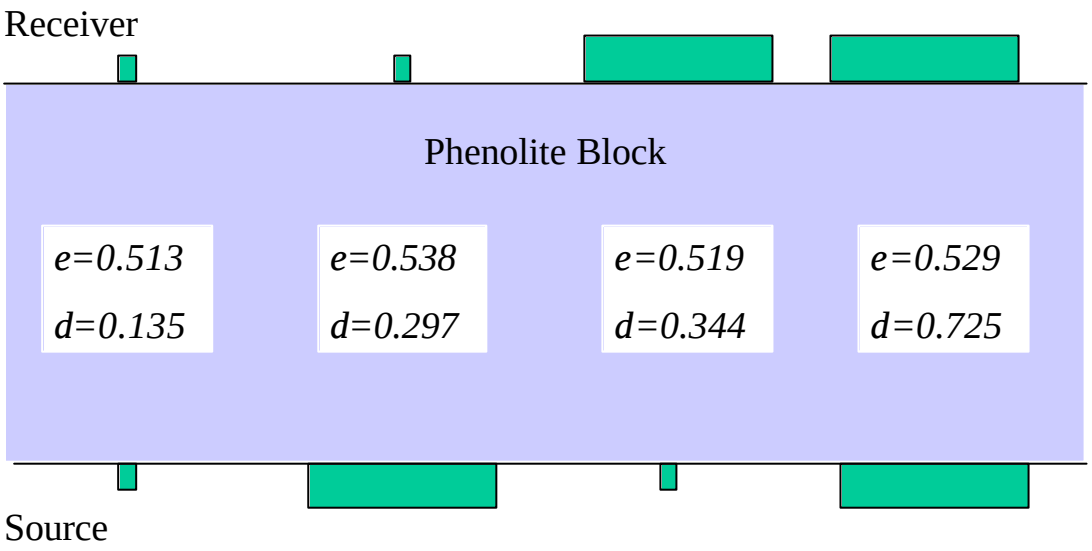

Figure 5.10 The inversion results from the experiments using different combinations of “large” and “point” transducers. The relative errors of the recovered parameters are high when “large” transducers are involved.

In the conduct of the above experiments, measurement errors were inevitable. The thicknesses of the experimental blocks were not completely uniform, the position of the mobile indexer holding the receiver transducers had a degree of uncertainty, and the first break picking may show a slight shift from its real travel time value, etc. However, for laboratory data with measurement errors, the inversion method developed in Chapter 3 still provided inversion results. The inversion method is expected to be applicable to field data.

5.3 Numerical Modelling Experiments

A series of numerical modelling experiments was carried out to study the size effect of transducers, as this clearly influences the outcomes of physical modelling experiments.

5.3.1 Synthetic Shot records for the Phenolite Block

Numerical simulations were carried out to calculate the first arrival transmission travel times. The synthetic shot records were examined for blocks with different recovered values of e and d from the laboratory experiments.

For the purpose of numerical analysis it was assumed that there were *two* Phenolite blocks with same dimensions as the experimental block. Their vertical velocities were assumed to be $a_0=3089$ *m/s*, $b_0=1580$ *m/s*. They were however assumed to have different elastic parameters e and d. One block designated as Phenolite P was assigned the values of $e=0.513$, and $d=0.135$. These values corresponded to the values previously obtained with "point" transducers. The other block (designated Phenolite L) was assigned the values of $e=0.592$, and $d=0.725$, corresponding to the values previously obtained with the "large" transducers.

The first arrival travel times of P-waves through these hypothetical Phenolite blocks were numerically calculated using the program "*phiv.f*" (developed in Section 3.1.2).

The forward modelling results are displayed in Figure 5.11 by software SU (Seismic Unix, Stockwell et al., 1998). The lower event was simulated using the elastic parameters of Phenolite P. The upper event was simulated using the values of elastic parameters for Phenolite L. These results suggest that travel times recorded by the "large" transducers would be smaller than the corresponding travel times recorded with the "point" transducers at intermediate and far offsets.

Let's go back to re-examine Figure 5.8. VSP shot records using different types of transducer display the same phenomenon. For the same Phenolite block, the travel times using the "large" transducers are shorter than the travel time using the "point" transducers at intermediate and far offsets. Thus, the different inversion results using "point" or "large" transducers probably mainly arise from the nature of the measurement transducers. Using "large" transducers in this type of experiment may introduce large measurement errors. The inversion program can recover the elastic parameters from the measured travel times. However, the inversion program cannot correct the measurement errors. When conducting laboratory experiments, the measurement errors should be carefully examined and minimized before running the inversion program.

The size effects of "large" transducers should be carefully considered, when conducting laboratory experiments to recover the elastic parameters of a core sample.

5.3.2 Simulation of the Laboratory Experiment with "Large" Transducers

Next, numerical modelling experiments were carried out to investigate the reason for the different shot records obtained with "point" transducers and "large" transducers.

Using the standard values of elastic parameters for the Phenolite block which were recovered from the "point" transducer measurements, a simulation was carried out to investigate the effect on shot records when using the "large" transducers. The block thickness, survey geometry, and the diameter of transducers was the same as that in the laboratory experiments on the Phenolite block.

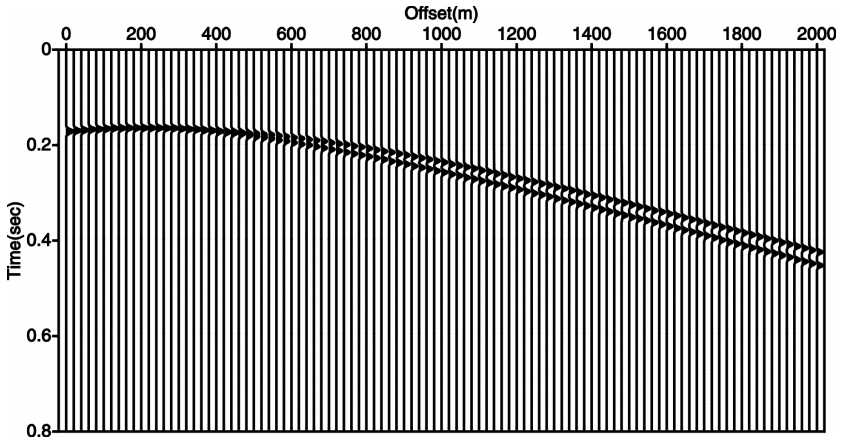

Figure 5.11 Computer simulation of VSP data for a VTI medium with different e and d values. Here, the elastic parameters were chosen to be $a_0=3089$ m/s, $b_0=1580$ m/s. The lower event was generated by assuming $e=0.513$, $d=0.135$, as would have been obtained using "point" transducers. The upper event was generated by assuming $e=0.592$, $d=0.725$ as would have been obtained using "large" transducers.

It had been assumed that a direct wave propagates from the centre of a source transducer to the centre of a receiver transducer. But actually the waves received by the receiver transducer probably also include those waves emitted from the edges of the source transducer and received by the edges of the receiver transducer as shown in Figure 5.12. At any specific offset R'S, the signal received by the "large" receiver will come from a small range of directions, instead of from only one nominal direction. The signals received by the transducer will include rays whose offsets are within the range of D'A and C'B, instead of one ray with offset R'S. The receiver station interval is *2 mm*, and the diameter of the "large" transducer is *7* times larger. From the lower event in Figure 5.11, for any offset position, if we sum *7* traces to the left and *7* traces to the right of the central trace, we may simulate the signals recorded with "large" transducers. Figure 5.13 shows the results obtained on this assumption.

The event has been flattened at near offsets. At far offsets, the first arrivals come in ahead of the time observed with "point" transducers. The first arrival event on the synthetic shot records created in this way behaves similarly to that from the physical modelling experiment with "large" transducers. This simulation explains the laboratory results obtained with the "large" transducers.

It was noticed that pulse broadening exists especially at far offsets in Figure 5.13. It is not clearly observed from the P-wave event in Figure 5.8b. However, for the SH-waves, which are much slower than P-waves, Uren's experiment (1989) showed clear evidence of pulse broadening (Figure 5.14). It is believed that pulse broadening occurs with "large" transducers, especially at far offsets for experiments of this type generally.

5.3.3 Offset Correction

Waves emitted from the edges of the source transducer will also be received by the edges of the receiver transducer. The shortest ray path of the signal from the source to the receiver will be AD instead of SR in Figure 5.12. AD is the distance between the neighbouring edges of the source and receiver transducers. Because the velocity

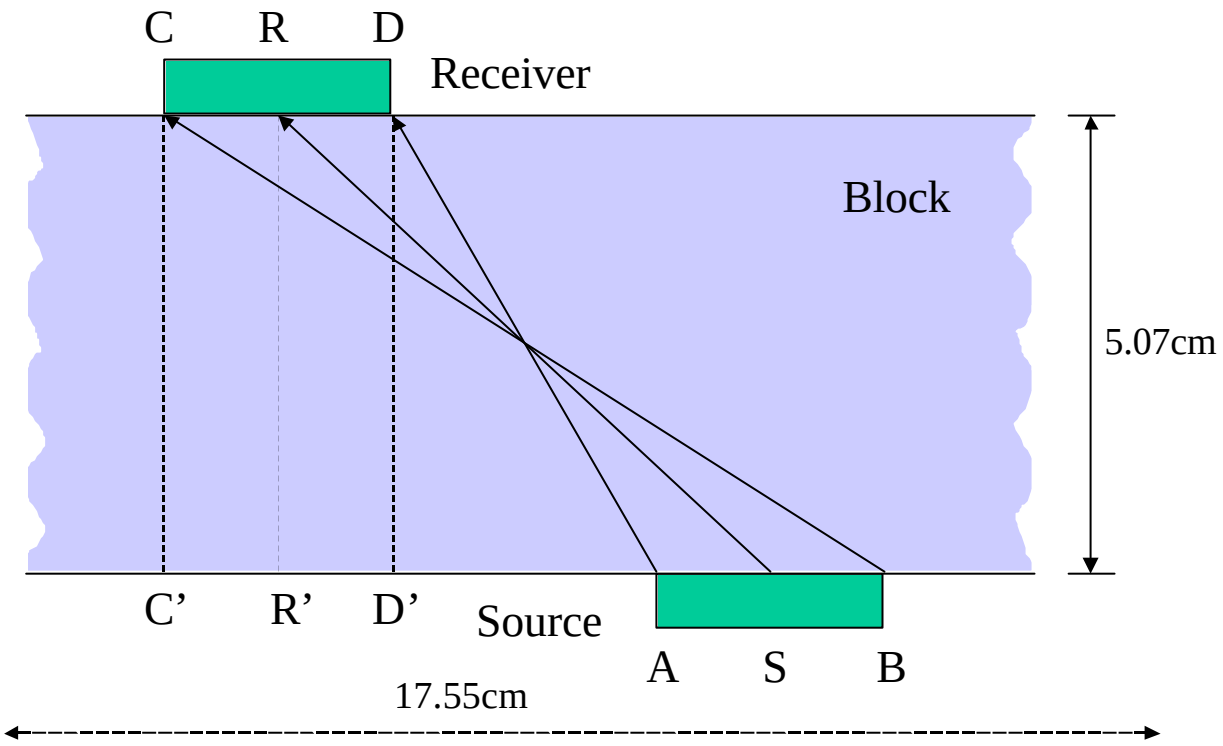

Figure 5.12 Sketch of the possible ray paths with "large" transducers. The nominal direction of source to receiver is SR. The receiver transducer will not only detect the wave propagating along SR, but it will also detect the waves propagating in the range of AD to BC.

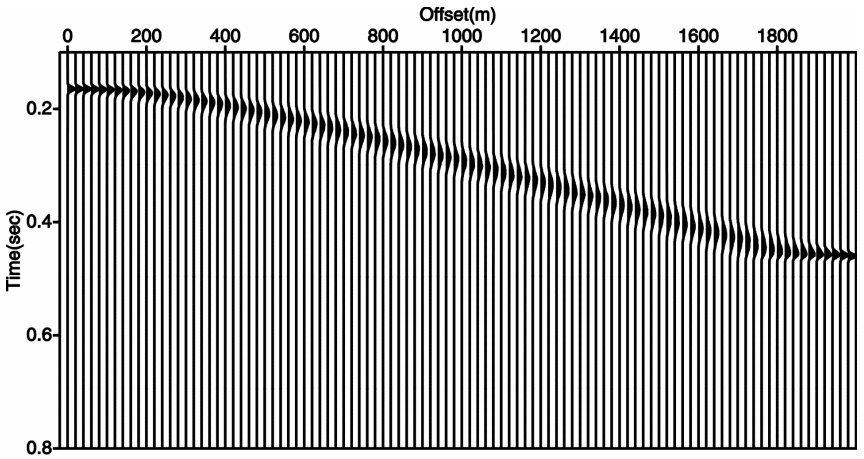

Figure 5.13 Numerical simulation of VSP data taking into consideration all the possible ray paths for "large" transducers. At any one specific offset, ray energy received comes from a small range of directions instead of one single direction. The event has been flattened at near offsets. At far offsets, the first arrivals come in ahead of the time observed with "point" transducers. Pulse broadening is clearly showed especially in the far offset.

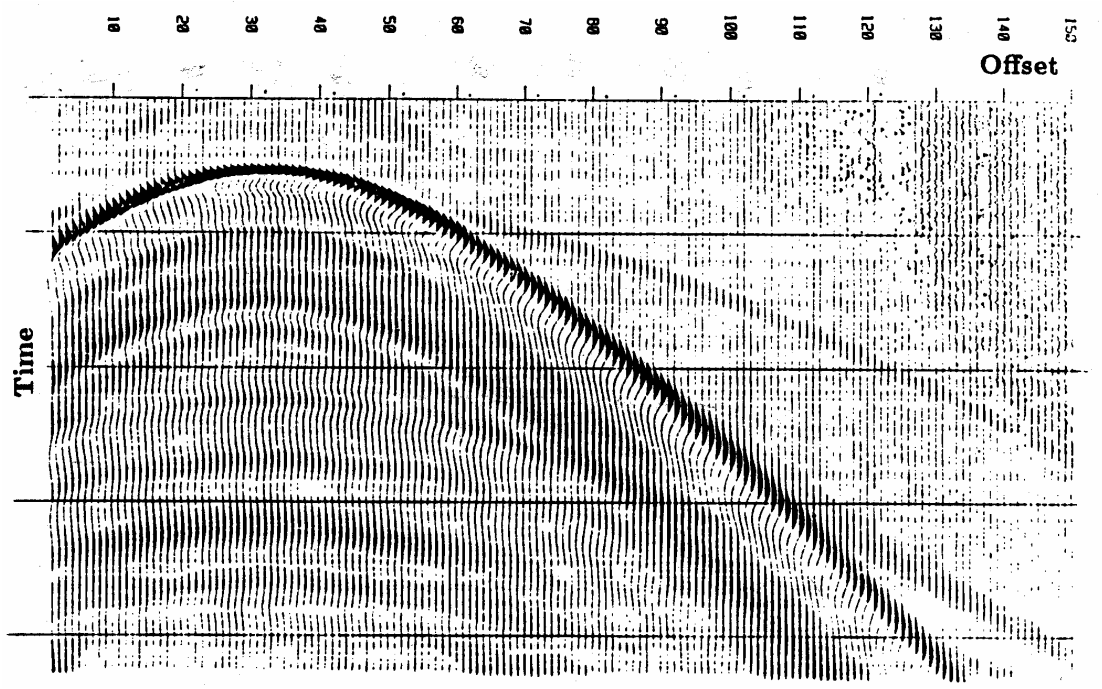

Figure 5.14 SH-wave transmission time records for a Phenolite block from Uren's experiment (Uren, 1989). It showed clear evidence of pulse broadening especially in the far offset. However, pulse broadening is not clearly observed from the P-wave event in Figure 5.8b, which is much faster than SH-waves.

is a function of the direction, it is complicated to make a travel time correction for each offset measurement. An offset correction method was proposed (Li, et al., 2000a) and is described as follows.

As shown in Figure 5.12, the corresponding offset should be D'A for the raypath AD, which is the ordinary offset R'S minus the average of the widths of the source and receiver transducers. Corrections for each measurement with "large" transducers were made in this way. We assumed that the real offset of the first arrival is the apparent offset minus the average of the source and receiver transducer widths.

Testing this method using Plexiglas experimental data with "large" transducers first, gave $e=0.016$, $d=-0.032$. The recovered values of the elastic parameters e and d are very small, and are acceptable estimated values of the true zero values. The results coincide with zero values of anisotropic parameters for isotropy. The inversion results with offset correction made a good improvement compared with that ($e=0.054$, $d=0.686$) without offset correction.

The offset correction method was applied to the measurement data using a "point" transducer as a source, a "large" transducer as a receiver, and vice versa. The corresponding offset correction value was the half the value for the experiment using "large" transducers. Table 5.2 gives the inversion results for the Phenolite block with and without offset correction for the experiments using different combinations of the transducers.

Using this method for Phenolite, the results show good improvements in the inverted d values, but little change in the inverted e values. The offset correction improves velocity measurement for Phenolite at each observation position. For the same amount of offset correction, a relatively large change in velocity was made at short offsets, due to the relatively large change in the ray path. Because parameter d is the near vertical anisotropic parameter (Thomsen, 1986), an improvement in the accuracy of the inverted d value is to be expected and is shown in Table 5.2.

Table 5.2 Comparisons of inversion results for the physical modelling experiments, with and without corrections for ray path directions, using different size transducers on a Phenolite block. *D* represents the error in velocity field inversion, and *W* represents the percentage relative error in velocity field inversion.

Trial number	3	4	5	3'	4'	5'
Source transducer	large	point	large	large	point	large
Receiver transducer	large	large	point	large	large	point
Offset correction (*m*)				*140*	*70*	*70*
a_0*(m/s)*	*2989*	*3068*	*3064*	*2936*	*3035*	*3077*
b_0*(m/s)*	*1528*	*1569*	*1567*	*1502*	*1552*	*1574*
e	*0.592*	*0.519*	*0.538*	*0.588*	*0.530*	*0.512*
d	*0.725*	*0.344*	*0.297*	*0.169*	*0.163*	*0.140*
d^*	*0.633*	*0.125*	*0.041*	*-0.185*	*-0.150*	*-0.171*
C_{33}*(´*10^9 $N \times m^{-2}$*)*	*12.77*	*13.46*	*13.43*	*12.33*	*13.17*	*13.54*
C_{44}*(´*10^9 $N \times m^{-2}$*)*	*3.34*	*3.52*	*3.51*	*3.23*	*3.45*	*3.54*
C_{11}*(´*10^9 $N \times m^{-2}$*)*	*27.88*	*27.43*	*27.88*	*26.84*	*27.13*	*27.41*
C_{13}*(´*10^9 $N \times m^{-2}$*)*	*12.89*	*10.29*	*9.81*	*7.77*	*8.24*	*8.18*
D(m/s)	*12*	*4.6*	*4.5*	*5.1*	*4.4*	*10*
W(%)	*0.32*	*0.13*	*0.12*	*0.14*	*0.13*	*0.27*

Offset correction may improve the data to a certain degree. It is suggested that "point" transducers should be used in laboratory experiments for the best results.

5.4 Discussions and Conclusions

The inversion method developed in Chapter 3 successfully recovers the elastic parameters of the blocks in the Physical Modelling Laboratory. These velocity measurements will include random noise from first break picking, positional errors of the mobile indexer holding the receiver transducers, uneven thickness of the experimental block, etc. The inversion method was demonstrated to provide satisfactory estimates of elastic parameters providing suitable "point" transducers were used.

However, when processing laboratory transmission data, the effect of transducer dimensions should be carefully considered. When using this inversion method on laboratory data, we normally assume that the transducers only detect signals in the nominal direction. If the ratio of the sample thickness to the transducer width is not sufficiently large (e.g., less than *4:1* for "large" transducers in my laboratory experiments), the effect of transducer size needs to be considered.

Actually, the receiver transducer will detect not only the wave from the centre of a source to the centre of a receiver, but also all the waves emitted from every point on the source transducer to every point on the receiver transducer. The raypath for the first break for an observation may not correspond to the nominal measurement offset. Since offsets from the laboratory are utilized to calculate the velocity field for an experiment block, the observed velocity field may not be the appropriate one if "large" transducers are used. In this case, systematic errors would exist in the laboratory observations, which cannot be eliminated by the inversion program. If the effects of transducer dimensions are not taken into consideration, the recovered elastic parameters of experiment blocks may not be reliable.

To solve this problem in laboratory tests, we need to decrease the size of the transducers as much as we can. If the ratio of the sample thickness to the transducer

width is sufficiently large (e.g., around *36:1* in my experiments with "point" transducers), the inversion results probably would be satisfactory. The correction of offset data in this chapter may be another effective way of reducing the measurement error resulting from the use of "large" size transducers in the laboratory.

The above problem of the size effect of transducer dimensions on recovered parameters is not likely to be a problem in the field. The ratio of the rock depth to the width of the source or the receiver in a field survey normally will be sufficiently larger than in the laboratory experiments using "point" transducers. There is no need to discuss the size effects of sources and receivers for field survey data. However, laboratory testing is a necessary step in the validation of my inversion software. The laboratory tests confirm the validity of my inversion program when applied to suitable data.

The shear wave signals in the experiments were not clear and mixed with the reflected wave from the side face of the experimental block. Thus, the inversion program from combined wave modes could not be tested on the laboratory data. The inversion program for apparent parameters was also not applied to a multi-layered model. The signals in the laboratory from such a model were weak, together with spurious effects from multiples, air bubbles between the layers etc. The dimensions of the experimental blocks also prevented us from recording the signals to the limiting offset range of twice the depth of the receiver. Hence, the inversion program for the interval parameters developed in Chapter 4 could not be tested on multi-layered models. However, my inversion programs will be applied to the real field surveys in the next chapter.

CHAPTER 6
APPLICATION TO FIELD VSP DATA

The inversion methods for apparent and interval parameters were successfully tested on numerical simulation data in Chapters 3 and 4. The inversion method for apparent parameters was successfully used on physical modelling laboratory experiment data in Chapter 5. Now, the issue becomes:

- *Are these two developed inversion methods applicable to real field VSP survey data?*

In this chapter, my inversion methods for apparent and interval parameters will be applied to two sets of real field VSP survey data. One set is coal data from the southern Sydney Basin, Australia. The other is offshore petroleum data from the Timor Sea.

6.1 Application to Coal Field Data

In the southern Sydney Basin, Australia, the stratigraphy "has been considered for years as an ideal seismic medium with its characteristic near constant seismic velocity down to the mining targets" (Urosevic, 2000). It exhibits gently dipping strata and uniform lithology. Normally panels of coal are *200-250 m* in width and *1.5 km* in length, and coal mining takes place to a depth of *500 m.* However, seismic methods "have not always been completely successful in predicting fine structural detail" (Urosevic, 2000). Further study is needed to improve the seismic images.

A multi-component VSP survey was conducted for coal exploration in the Sydney Basin, Australia (Urosevic, 2000). The shots were fired in the sub-weathering. Figure 6.1 shows the survey acquisition geometry. Six receivers were located at *45 m, 141 m, 237 m, 333 m, 429 m,* and *525 m* down the borehole. Table 6.1 gives the offset range and the number of the observations for each wave mode at each receiver level.

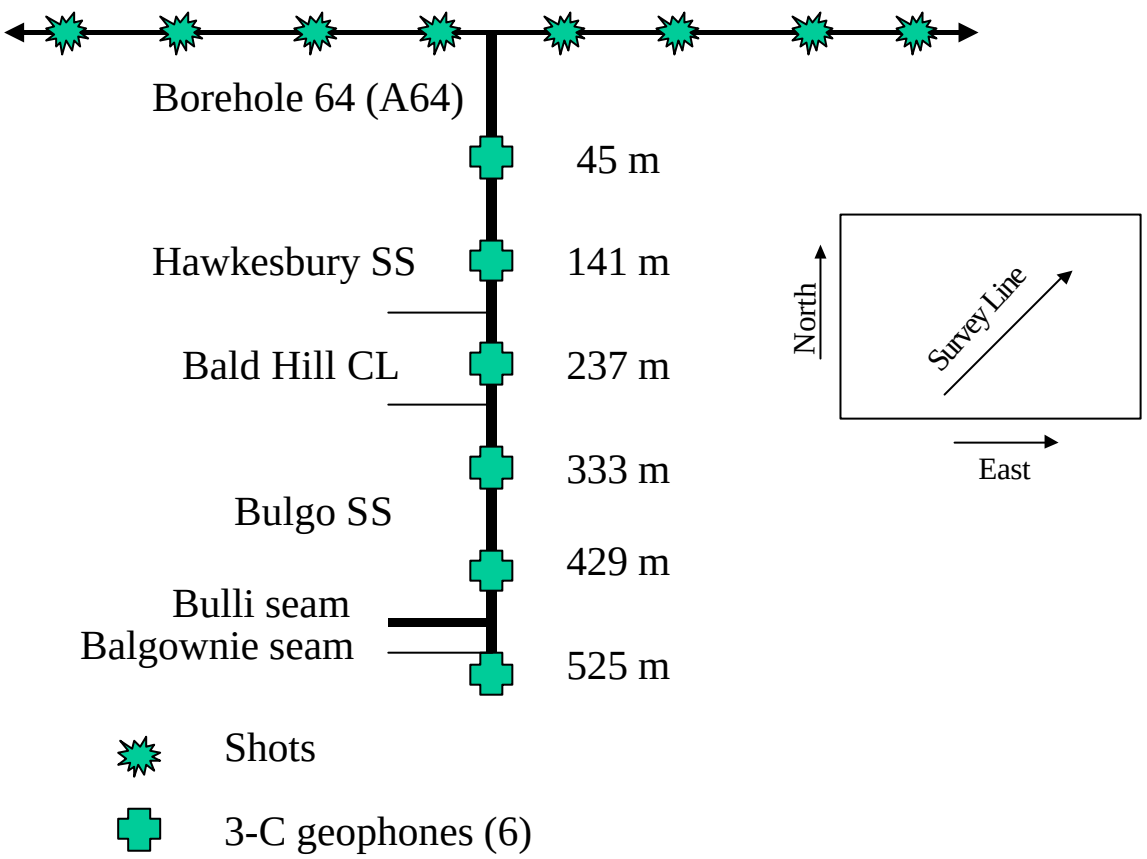

Figure 6.1 The relative location and geometry of the coal VSP data. The data were recorded in borehole 64 (A64). The receiver interval is 96 m (modified from Urosevic, 2000).

Table 6.1 The offset range and the number of observations for each wave mode at every receiver level. Data were supplied by Urosevic (personal communication).

Receiver Depth (*m*)	*Angle range of the survey*	*Number of observations*			
		Total	*P*	*SV*	*SH*
45	*-85°, 87°*	*96*	*42*	*12*	*42*
141	*-67, 76°*	*112*	*42*	*35*	*35*
237	*-54°, 66°*	*126*	*42*	*42*	*42*
333	*0°, 58°*	*81*	*27*	*27*	*27*
429	*0°, 51°*	*80*	*27*	*26*	*27*
525	*0°, 45°*	*81*	*27*	*27*	*27*

For P, SV, and SH-waves, the travel times from each source to each receiver were picked from the seismic records and supplied by Urosevic (personal communication). The apparent velocity was determined by dividing the direct distance between the source and the receiver by the travel time. The apparent ray angle was obtained as being the angle between the vertical direction and the straight line from the source to the receiver. Thus, for the layer above a given receiver depth, the velocity fields with different apparent ray paths from each source to each receiver were obtained for P, SV, and SH-waves, respectively.

6.1.1 P-wave Inversion for Apparent Parameters

Inversion based on a VTI model

Using the P-wave velocity field measured above each receiver, the inversion program "*para.f*" developed in Section 3.2 was run assuming a layered VTI medium (transversely isotropic medium with a vertical symmetry axis). Table 6.2 shows the inversion results for apparent elastic parameters for the regions above the stated receiver depths. The velocity field calculated from the inverted apparent parameters was compared with the observations. Figure 6.2 gives an example of the velocity field comparison for the layer above the receiver at a depth of *141 m.* The velocity field calculated from the inverted parameters and the velocity field obtained from the field data match each other.

The various layers above each receiver depth behave like a single-layered transversely isotropic medium. We see that the anisotropic parameters e and d are especially high for the layer to a depth of *45 m*. Strong anisotropy exists in the shallow region.

The approach "*chi-by-eye*" was used again to examine the velocity fields. In Figure 6.2, the observation data also shows slightly symmetrical departures. It is noticed that

Table 6.2 Inversion results for apparent parameters using the inversion program under a VTI assumption for the coal VSP data. *D* represents the mean difference between the velocity field from the field data and that calculated from the inverted parameters. Data were supplied by Urosevic (personal communication)

Receiver Depth (*m*)	a_0(m/s)	b_0(m/s)	*e*	*d*	*D*(m/s)
45	*1756*	*974*	*1.46*	*0.964*	*63*
141	*2765*	*1760*	*0.359*	*0.221*	*54*
237	*3183*	*1863*	*0.184*	*0.104*	*50*
333	*3400*	*1990*	*0.079*	*0.066*	*17*
429	*3446*	*2029*	*0.074*	*0.035*	*13*
525	*3530*	*2019*	*0.155*	*-0.048*	*13*

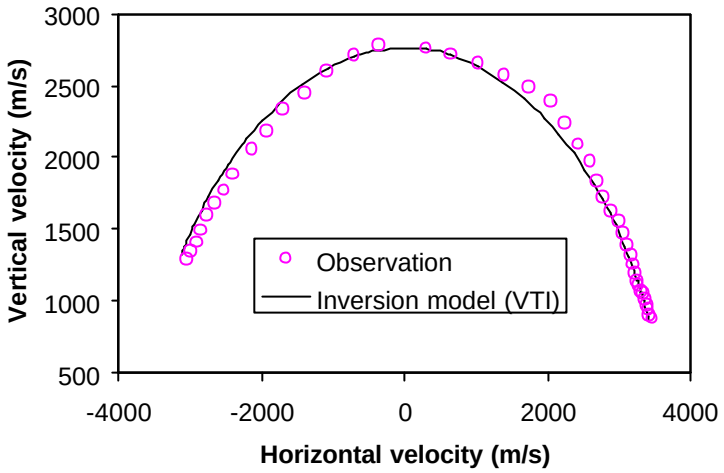

Figure 6.2 Comparison of the velocity field computed from recovered elastic parameters (under VTI assumption) with the measured field data for the receiver at *141 m*. The velocity field from the field data is marked with circles. The continuous curve is the plot of velocity function generated using the inverted apparent elastic parameters found assuming a VTI medium. The velocity fields match each other reasonably well. The observation data shows slightly symmetrical departures. It is noticed that the curve is normally above the circles on the left side, while the curve is generally below the circles on the right side.

the curve is normally above the circles on the left side, while the curve is generally below the circles on the right side. It suggests that the symmetry axis is not strictly vertical, but tilted at a small angle. A TTI model was then assumed for the inversion procedure as follows.

Inversion based on a TTI model

The inversion program "*paratilt.c*" developed in Section 3.3 for a TTI medium (transversely isotropic medium with a tilted symmetry axis) was then run with the same P-wave survey data (Li, et al., 2000b). Table 6.3 shows the inversion results for the apparent elastic parameters for the regions above each stated receiver depth. The differences *D* between the velocity field measured directly from the field data and that computed from the inverted parameters are smaller than those listed in Table 6.2. The "*chi-by-eye*" approach was again used as the final test of the goodness of fit of the velocity fields. Figure 6.3 shows the velocity field comparison for the layer above the receiver at a depth of *141 m.* The velocity field plotted from the field data and that computed from the inverted parameters is a better match than those under the VTI assumption in Figure 6.2.

The results suggested that the regions investigated are transversely isotropic media with tilted symmetry axes. The small angles of tilt from the inversion results indicate that the layers are slightly dipping. The survey line is from the southwest to northeast direction (see in Figure 6.1). A negative tilt angle indicates that the layer dips towards the southwest, while a positive tilt angle represents a dip towards the northeast. Of course, the significance of "average" apparent dip values needs further geological study.

The initial parameter input to the inversion influenced the recovered parameters, under both the VTI and the TTI assumptions. This may be due to having only a small

Table 6.3 Inversion results for apparent parameters of the coal VSP data using inversion program "*paratilt.c*" which is based on a TTI assumption. *D* represents the mean difference between the velocity field from the field data and that calculated from the inverted parameters, which is smaller than that in Table 6.2. Data were supplied by Urosevic (personal communication).

Receiver Depth (*m*)	a_0(*m/s*)	b_0(*m/s*)	*e*	*d*	*y* (°)	*D*(*m/s*)
45	*1756*	*974*	*1.420*	*0.920*	*-2.68*	*32*
141	*2765*	*1760*	*0.320*	*0.250*	*-6.19*	*22*
237	*3183*	*1863*	*0.130*	*0.140*	*-12.20*	*23*
333	*3396*	*1988*	*0.078*	*0.086*	*2.00*	*17*
429	*3445*	*2028*	*0.076*	*0.046*	*2.08*	*12*
525	*3533*	*2021*	*0.069*	*-0.044*	*-9.70*	*11*

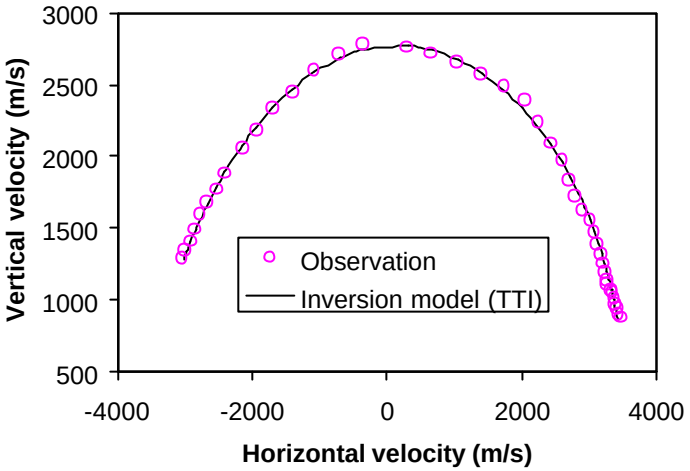

Figure 6.3 The velocity field comparison with a TTI model for the overall layer to the depth of *141 m* for coal VSP data. The observed velocity field from the field data is marked with circles. The continuous curve is the velocity plot generated using the inverted apparent elastic parameters assuming a TTI medium. The layer to the depth of *141 m* is equivalent to a transversely isotropic medium with the symmetry axis tilted at *6.9°* to the vertical.

number of P-wave field data (eg., *27* for the receiver depths at *333 m*, *429 m*, and *525 m*) involved in the inversion. After the inversion results were obtained, the "*chi-by-eye*" approach was used to determine the suitability of the values of the elastic parameters obtained. The velocity fields both from the field data and that calculated from the inverted parameters were compared. If these two velocity fields match sufficiently, the inverted parameters were then taken to be the best estimations for that survey layer.

6.1.2 Inversion Using Three Body Waves

The VSP data sets from the southern Sydney Basin actually included multi-component measurements. The additional data enabled shear wave analysis to be carried out also. Including information from all types seismic waves into the inversion programs should provide better inversion results.

Apparent parameters

The observed velocity fields for P, SV, and SH-waves were input to the inversion program "*parameter.c*" developed in Section 3.4. The apparent parameters and the tilt angles of the symmetry axis for the layer to the various receiver depths were then recovered. The inversion results for the layers to the depths of each receiver are listed in Table 6.4. The results were evaluated by the "*chi-by-eye*" approach that compared the velocity fields computed using the recovered parameters with the initial observations. Figure 6.4 shows the velocity fields from the field data (the magenta circles) and those calculated from the recovered parameters using a TTI model (the blue curves) for the layer to the depth of each receiver. They coincide very well. The layer to the depth of each receiver behaves like a transversely isotropic medium with a tilted symmetry axis. The tilt angles are only a few degrees.

Table 6.4 Recovered apparent parameters and tilt angle of symmetry axis by assuming a TTI model for the coal multi-component VSP data. *D* represents the mean difference between the velocity field from the field data and that calculated from the inverted parameters. Data were supplied by Urosevic (personal communication).

Receiver Depth (*m*)	a_0(m/s)	b_0(m/s)	*e*	*d*	*g*	*y* (°)	*D*(m/s)
45	*1750*	*970*	*1.430*	*1.030*	*1.220*	*-3.32*	*39*
141	*2740*	*1745*	*0.320*	*0.370*	*0.200*	*-6.33*	*23*
237	*3173*	*1857*	*0.140*	*0.180*	*0.135*	*-8.50*	*23*
333	*3390*	*1984*	*0.057*	*0.127*	*0.222*	*2.89*	*13*
429	*3436*	*2023*	*0.032*	*0.093*	*0.157*	*2.08*	*10*
525	*3496*	*2000*	*0.022*	*0.049*	*0.102*	*-9.70*	*11*

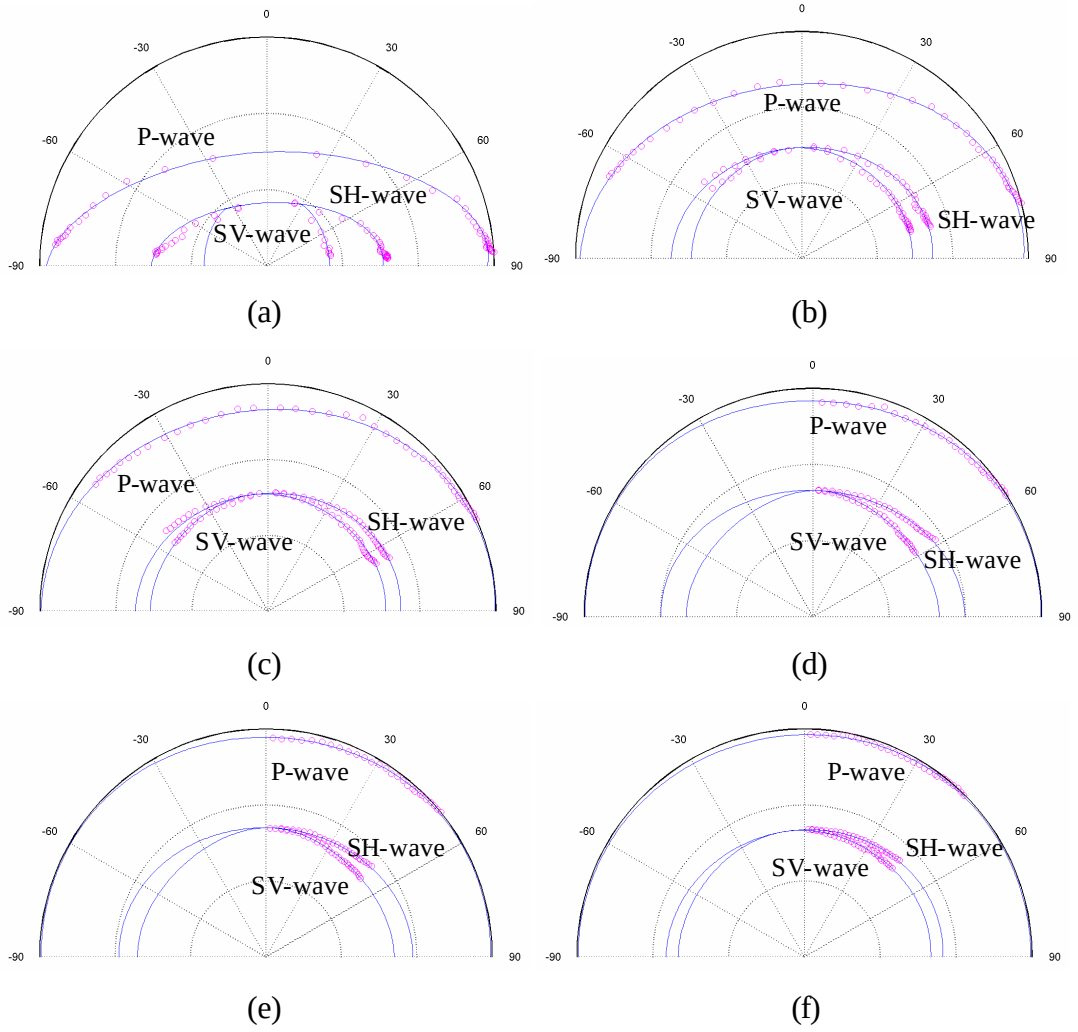

Figure 6.4 The apparent velocity fields of P, SV, and SH-waves for the coal VSP data. The magenta circles are the velocity fields from the field data. The blue curves are the velocity fields calculated from the inverted apparent parameters and the tilt angles. The layers are to the depths of (a) *45 m*, (b) *141 m*, (c) *237 m*, (d) *333 m*, (e) *429 m*, and (f) *525 m*. Both velocity fields are in a good agreement for each panel.

The inversion results were verified by seismic sections of the survey region which showed near horizontally layered geometry (Urosevic, 2000). It was noticed that the anisotropic parameter values decreased quickly from the depth of *45 m* to *141 m.* It suggested a large stratigraphy change within this depth region.

We could have assumed that the layers were VTI media, ignoring the very small tilt angles. When a VTI model is assumed, the tilt angle is zero and fixed in the inversion procedure. The inversion program "*parameter.c*" was run again and those inversion results are given in Table 6.5.

- **Comparison of the inversion results under the TTI or the VTI assumptions**

The velocity differences *D* in Table 6.4 under a TTI assumption were compared with those in Table 6.5 under a VTI assumption. The velocity differences *D* based on a TTI model are smaller. Hence, the inversion results based on a TTI assumption are believed to be better than those based on a VTI assumption. It is necessary to use a suitable model in the inversion in order to obtain good estimates of apparent parameters. It is noticed that the recovered values of tilted angles y are very small (only several degrees), and the differences between the inversion results using either the VTI or the TTI model are very small. These regions above each receiver can be treated approximately as VTI media.

- **Comparison of the inversion results from multi-wave modes and P-waves only**

Under the VTI assumption, the velocity differences *D* in the inversion from multi-wave modes in Table 6.4 were compared with those in Table 6.2 which were obtained from P-wave data only. The velocity differences *D* in Table 6.4 are smaller or equivalent. A similar comparison was made under the VTI assumption between Table 6.5 and Table 6.3. The velocity differences *D* in Table 6.5 are smaller or equivalent to those in Table 6.3.

When P, SV, and SH-waves instead of P-waves only were used, the differences between the velocity fields calculated from the inverted parameters and the observation velocity fields from the field data are smaller. The implementation of the

Table 6.5 Recovered apparent parameters assuming a VTI model for the coal multi-component VSP data. *D* represents the mean difference between the velocity field from the field data and that calculated from the inverted parameters. Data were supplied by Urosevic (personal communication).

Receiver Depth (*m*)	a_0(m/s)	b_0(m/s)	*e*	*d*	*g*	*D*(m/s)
45	*1732*	*976*	*1.490*	*1.210*	*1.200*	*68*
141	*2744*	*1742*	*0.340*	*0.370*	*0.230*	*38*
237	*3183*	*1853*	*0.142*	*0.180*	*0.164*	*30*
333	*3382*	*1982*	*0.057*	*0.125*	*0.198*	*14*
429	*3433*	*2023*	*0.032*	*0.091*	*0.140*	*10*
525	*3508*	*2001*	*0.023*	*0.054*	*0.161*	*12*

"*chi-by-eye*" approach demonstrated that including all wave modes in the inversion program provided better inversion results than those using only P-wave data in the inversion program.

- **Discussion of velocity field comparisons**

The "*chi-by-eye*" approach was used to compare the velocity fields calculated from the inverted parameters with the observation velocity fields from the field data. During the above comparisons, it was hard to find a perfect match for these two sets of velocity fields. This was assumed to be due to measurement error and local geological variability.

Interval parameters

If we make a VTI assumption for this survey region, we should be able to recover the parameters of an interval layer between any two receivers using the inversion program "*interval.c*" presented in Section 4.3.

The velocity fields from the field data measured for each receiver located at *45 m, 141 m, 237 m, 333 m, 429 m,* and *525 m* down the borehole were input to the inversion program "*parameter.c*" separately. The apparent parameters of the layers to those receiver depths were recovered and listed in Table 6.5. Then, the inversion program "*interval.c*" was used to recover the interval parameters of the layers of interest between successive receivers. Table 6.6 gives the inversion results for these interval parameters for these field VSP data sets.

The apparent velocity fields to the bottom of each layer of interest were then examined. For example, Figure 6.5 shows the apparent velocity fields to the depth of *237 m*. The magenta circles are the observation velocity fields from the field data recorded by the receiver at *237 m*. The layer to the depth of *237 m* was then assumed to be a two-layered model with the interface between the two layers at a depth of *141 m*. The elastic parameters for the layer to the depth of *237 m* were shown in Table 6.5. The interval layer between *141 m* and *237 m* was assumed to have the parameter values found by the inversion program in Table 6.6. The apparent velocity fields for this two-layer model were then calculated using the program "*twoforward.c*" developed in

Table 6.6 Inversion results for interval parameters for the coal VSP data. *D* represents the mean difference between the velocity field from the field data and that calculated using the inverted parameters. Results of the interval parameters suggest complex anisotropy exists in the survey region (possibly orthorhombic).

	a_0(m/s)	b_0(m/s)	*e*	*d*	*g*	*D*(m/s)
Layer between *45m* and *141m*	*3779*	*2754*	*-0.200*	*-0.020*	*-0.220*	*46*
Layer between *141m* and *237m*	*4161*	*2044*	*-0.085*	*-0.044*	*0.066*	*60*
Layer between *237m* and *333m*	*4000*	*2394*	*-0.145*	*0.006*	*0.189*	*55*
Layer between *333m* and *429m*	*3622*	*2179*	*-0.056*	*-0.021*	*-0.051*	*9.5*
Layer between *429m* and *525m*	*3888*	*1908*	*-0.020*	*-0.072*	*0.208*	*13*

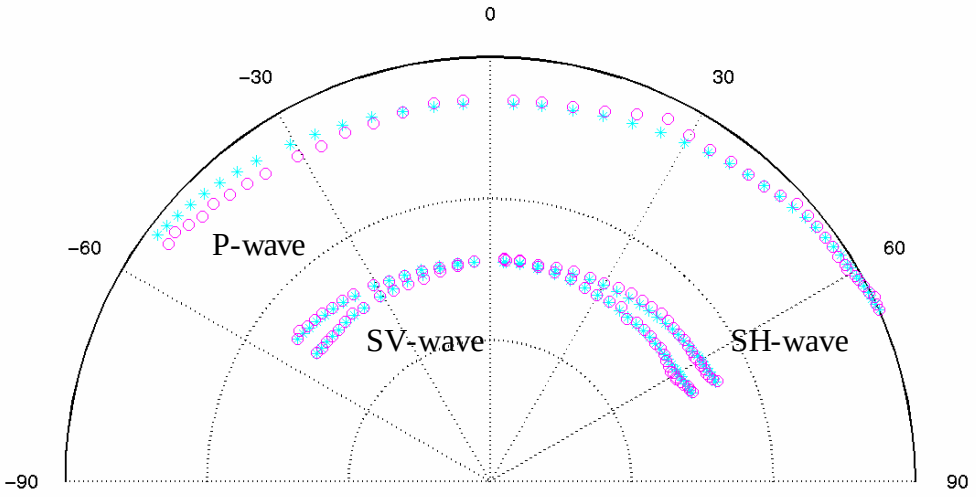

Figure 6.5 Velocity fields for the layer to the depth of *237 m* for the coal VSP data. The magenta circles represent the observations from the field data to *237 m*. The inverted parameters for the layer between *141 m* and *237 m* were then input with the known parameters for the layer to *141 m* to compute the apparent velocity field to the depth of *237 m*, marked with cyan stars. These sets of velocity fields match each other. The inverted interval parameters can well describe the elastic property of the interval layer between the depth of *141 m* and *237 m*.

Section 3.4.2, shown with the cyan stars (*) in Figure 6.5. The magenta circles and the cyan stars are in good agreement. The mean difference D between the observation velocity fields (magenta circles) and those calculated from the inverted interval parameters (cyan stars) is very small and listed in Table 6.6. Generally the relative error in velocity field is less than *2%*. It is demonstrated that the inverted interval parameters are suitable estimates of elastic parameters of the interval layer.

Results of the interval parameters suggest complex anisotropy exists in the survey region (possibly orthorhombic). Actually, the first layer behaves like a VTI medium, while vertical fractures dominate the other interval layers which behave like HTI (transverse isotropy with a horizontal symmetry axis) media (Urosevic, 2000).

During the iteration procedure, cusps may be computed for the SV-wave velocity field of the interval layer for some trial sets of interval parameters. Because there are three values of SV-wave velocity in the same direction around the cusps, they are also called triplications. Examples of cusps can be seen in Figures 2.5 and 2.6. In the inversion, we need to compare an observation velocity with the calculated velocity from a set of trial parameters. If a cusp exists, the inversion program may not choose the right velocity value from these three values of velocity. For this reason the inversion program may fail to yield results. A further modification to the inversion program was needed to account for this eventuality. An example is described below.

When inverting for the interval parameters of the layer between *45 m* and *141 m* from the field data recorded at *141 m*, the program initially failed to find the interval parameters. The observation data *excluding* the SV-wave data at larger transmission angles ($f \geq 48.7°$) from the vertical were then input to the inversion program again. This inversion gave the following parameters for this interval layer: $a_0=3779$ *m/s*, $b_0=2754$ *m/s*, $e=-0.086$, $d=0.259$, and $g=-0.144$. For verification purposes, the apparent velocity fields to the depth of *141 m* were examined. The above inverted parameters for the layer between *45 m* and *141 m* and the known elastic parameters for the layer to *45 m* were then input to program "*twoforward.c*" to calculate the overall velocity field to the depth of *141 m*. These calculated velocity fields for the layer to the depth of *141m* are then plotted as cyan stars in Figure 6.6. The observations from

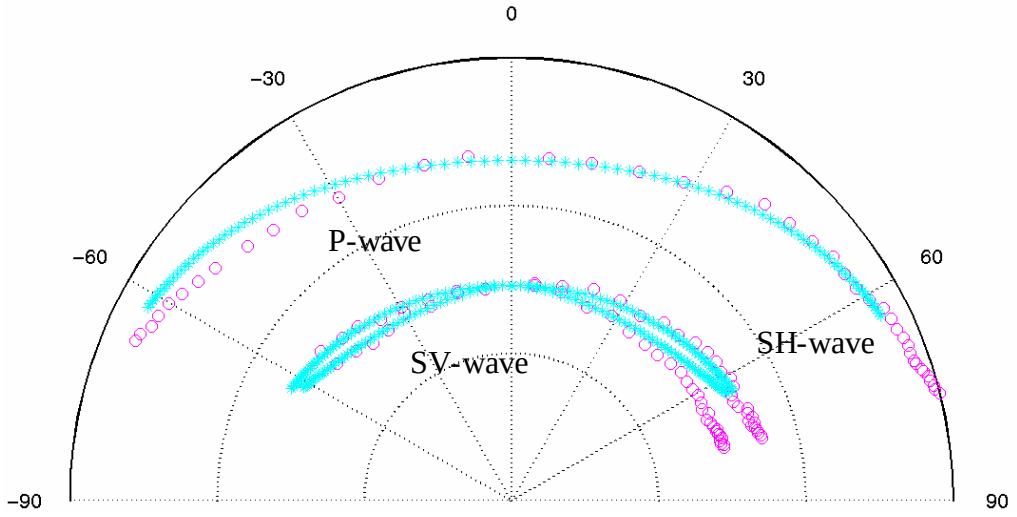

Figure 6.6 Velocity fields for the layer to the depth of *141 m* without part of SV-wave ($f > 48.7°$) field data for the coal VSP data. The magenta circles represent the observations from the field data. The inverted parameters for the layer between *45 m* and *141 m* were then input with the known parameters for the layer to *45 m*, to program "*twoforward.c*" to compute the apparent velocity field to the depth of *141 m*, marked with cyan stars. Both velocity fields match each other for P, and SH-waves. But for SV-waves, the cyan stars deviate from the magenta circles at a large incident angle. The inverted interval parameters for the interval layer between the depth of *45m* and *141m* are not acceptable.

the field data are represented as magenta circles. Both sets of velocity fields match each other for P and SH-waves. However, for SV-waves, a deviation occurs when the incidence angle increases. The "*chi-by-eye*" approach demonstrated that this inversion solution was not acceptable. Ignoring some SV-wave data at larger transmission angles in the inversion may lose some useful wave information and lead the inversion to a wrong result.

So the inversion program was modified again. When cusps exist in the SV velocity function of the interval layer with the trial parameters, a calculated ray angle in the second layer for a larger phase angle may be smaller than the ray angle with a smaller phase angle. When this happened, the corresponding SV-wave field data for the combined layer were ignored in this iteration. The increments for the trial parameters were calculated and the iteration was carried out again. After the modification of the inversion program, a reasonable result was obtained: a_0*=3779 m/s,* b_0*=2754 m/s,* e*=-0.200,* d*=0.020,* and g*=-0.220*. Figure 6.7 shows the comparison of the velocity fields to the depth of *141 m*. The magenta circles are the observations. The velocity fields calculated using the inverted interval parameters for the layer between *45 m* and *141 m* and the known parameter for the layer to *45 m* are marked as cyan stars. Both sets of velocity fields now show a better coincidence than that in Figure 6.6. This inversion result was chosen as the interval parameters for the layer between *45 m* and *141 m*.

It is noticed that the range of cyan stars on the right side of Figure 6.7 for SV-wave is limited. The missing cyan stars would have resulted from the cusps in the interval layer between depths of *45 m* and *141 m*. The velocity fields for this interval layer with the recovered elastic parameters were then plotted for verification purposes, shown in Figure 6.8. Cusps occur at large ray angles for the SV-waves in this interval layer. The vertical velocity is larger than the horizontal velocity. The velocity characteristics of this interval layer suggest possible presence of vertical fractures. This was subsequently confirmed by mining (Urosevic, 2000).

The inversion programs for apparent elastic parameters and interval elastic parameters have been tested and demonstrated on field coal data from the southern Sydney Basin,

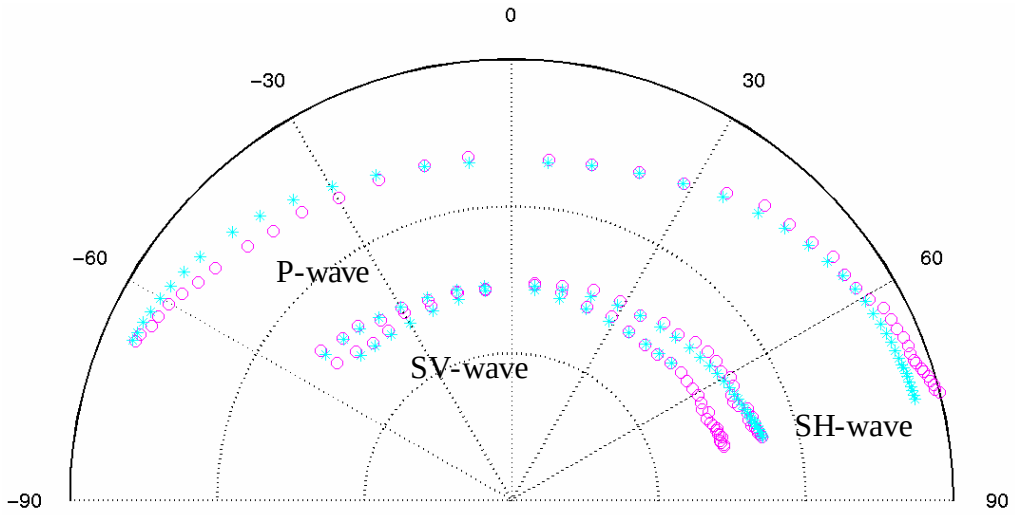

Figure 6.7 Velocity fields for the layer to the depth of *141 m* for the coal VSP data. The magenta circles represent the observations from the field data to *141 m*. The inverted parameters for the layer between *45 m* and *141 m* were then input with the known parameters for the layer to *45 m* to compute the apparent velocity field to the depth of *141 m*, marked with cyan stars. These sets of velocity fields match each other. The inverted interval parameters can well describe the elastic property of the interval layer between the depth of *45 m* and *141 m*.

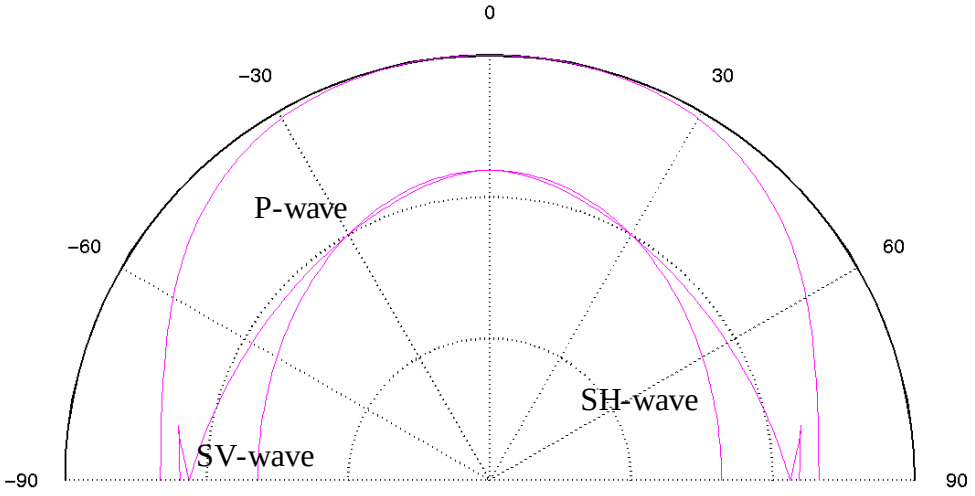

Figure 6.8 Velocity fields for the interval layer between the depths of *45 m* and *141 m* for the coal VSP data. Cusps occur at large ray angles for SV-waves. The vertical velocity is larger than the horizontal velocity. The velocity characteristics of this interval layer suggest possible presence of vertical fractures. This was subsequently confirmed by mining (Urosevic, 2000).

Australia. Further examples of the application of my inversion programs can be seen in Urosevic (2000).

6.2 Application to Petroleum Field Data

A 3-component multi-level multi-offset VSP survey was acquired offshore from a well in the Timor Sea. These petroleum VSP field data, provided by Woodside Petroleum Ltd., were used to test the inversion methods that were developed in Chapter 3 and Chapter 4. The well name is not given here, and is kept confidential for commercial reasons.

6.2.1 Walkaway VSP Acquisition

The acquisition geometry of this survey is sketched in Figure 6.9. A 4-gun source sled was suspended from a crane *5 m* below Mean Sea Level. An MLR (Multi-Level Receiver) tool, which has *5* three-component geophones, was lowered into the well to record the data. These five in-line geophones have a *15 m* interval between any two successive geophones. When the source was sailed along the first survey line, the MLR tool was at the bottom of the well. Shots were fired at shot points *25 m* apart. Then the MLR tool was pulled up to two other positions, and shots were fired along the second and third survey lines, in turn. Thus, with the MLR tool firmly locked at three different positions, walkaway VSP data were acquired from three survey lines. This resulted in *15* sets of VSP data, which had three mutually orthogonal components. Table 6.7 gives the geometry details of the shooting.

The depths to each receiver were: *2732 m, 2747 m, 2762 m, 2777 m, 2792 m, 2806 m, 2821m, 2836 m, 2851 m, 2866 m, 2882 m, 2897 m, 2912 m, 2927 m,* and *2942 m*. They are denoted as receiver 1, to receiver 15, respectively. The first survey line recorded *271* shots at locations from *172660.1E, 8816621.2N* to *172647.9E, 8823627.2N*. The second survey line was from *172640.8E, 8823614.5N* to *172644.3E, 8816606.7N* with *266* shots recorded. The third survey line was recorded from *172644.5E, 8816621.9N* to *172647E, 8823627.6N* and *256* shots were recorded. These three survey lines were

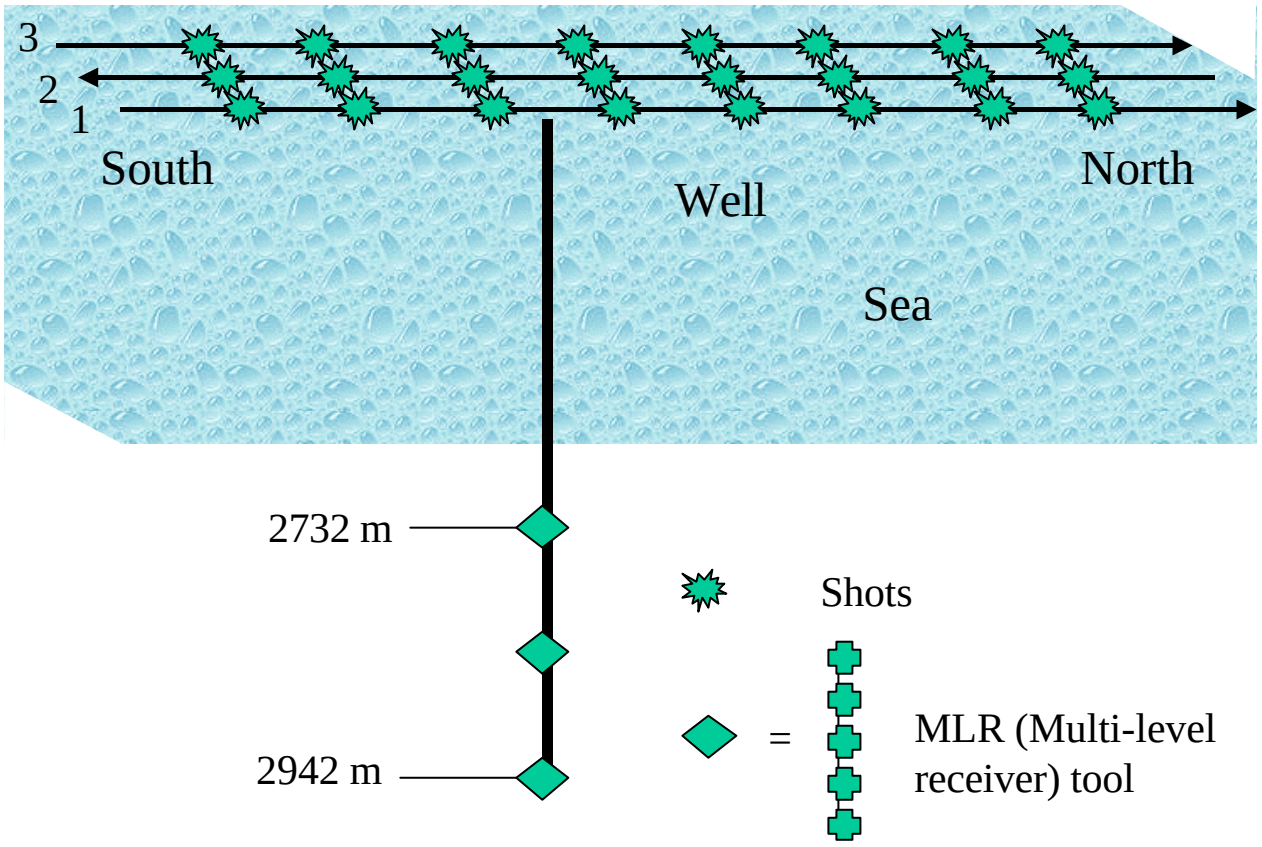

Figure 6.9 Geometry of the petroleum VSP survey recorded offshore in the Timor Sea. While the source sailed along the first survey line, the MLR tool was located at the bottom of the well. The MLR tool was then pulled up to two other positions, while shots were fired along the second and third survey lines, separately. These three survey lines were very close to each other and were treated as the same line. Shot points in each line were *25 m* apart.

Table 6.7 The survey location and geometry of the VSP survey in the offshore Timor Sea.

Receiver level number	Receiver depth (m)	Survey line number	Survey Line
11,12,13,14,15	2882, 2897, 2912, 2927, 2942	1	172660.1E, 8816621.2N to 172647.9E, 8823627.2N
6,7,8,9,10	2806, 2821, 2836, 2851, 2866,	2	172640.8E, 8823614.5N to 172644.3E, 8816606.7N
1,2,3,4,5	2732, 2747, 2762, 2777, 2792	3	172644.5E, 8816621.9N to 172647.0E, 8823627.6N

close to each other, and were treated as a single survey line in the subsequent inversion procedures.

6.2.2 Data Processing

The software package *"Promax"* (by Landmark Graphics Corporation) was used to process the VSP data.

The first step in data processing was to determine the orientations of the geophones on the well wall. The "3-Component Hodogram Analysis" module in *"Promax"* was used. For each receiver and shot position, the "vertical component" from the field survey was computer-rotated to an angle which gave a maximum P-wave response. The angle was found to be approximately the apparent ray angle, especially for the far-offset data. Thus, the vertical components of the geophones were verified as being vertically fixed on the well wall.

Then, the "Apply 2-C Rotation" Promax module was used to rotate the geophone components to obtain maximum P-wave amplitude. The P-wave first arrival times were picked from the rotated components in the shot-receiver directions. It was found that the first arrival time only slightly changed from the time picking without rotation by less than *0.1%*. Hence, the P-wave first arrival times were picked directly from the vertical components without using "Apply 2-C Rotation".

Figure 6.10 shows the raw data for receiver No. *15* displayed using *"Promax"*, as an example. The P-wave first break arrival times to each receiver position were picked as indicated by the red dots in the figure. By assuming a straight ray path between a shot and a receiver, the first break arrival times were converted to apparent velocities. The corresponding apparent ray angles were taken to be the angles between the vertical direction and the straight lines from sources to receivers. The velocity field for P-waves was found to be a function of offset. The region of the survey was clearly anisotropic.

In the absence of sonic log data, the strictly vertical velocities of P and S-waves were unknown. The ratio of vertical velocity of S-wave to P-wave was needed to run the

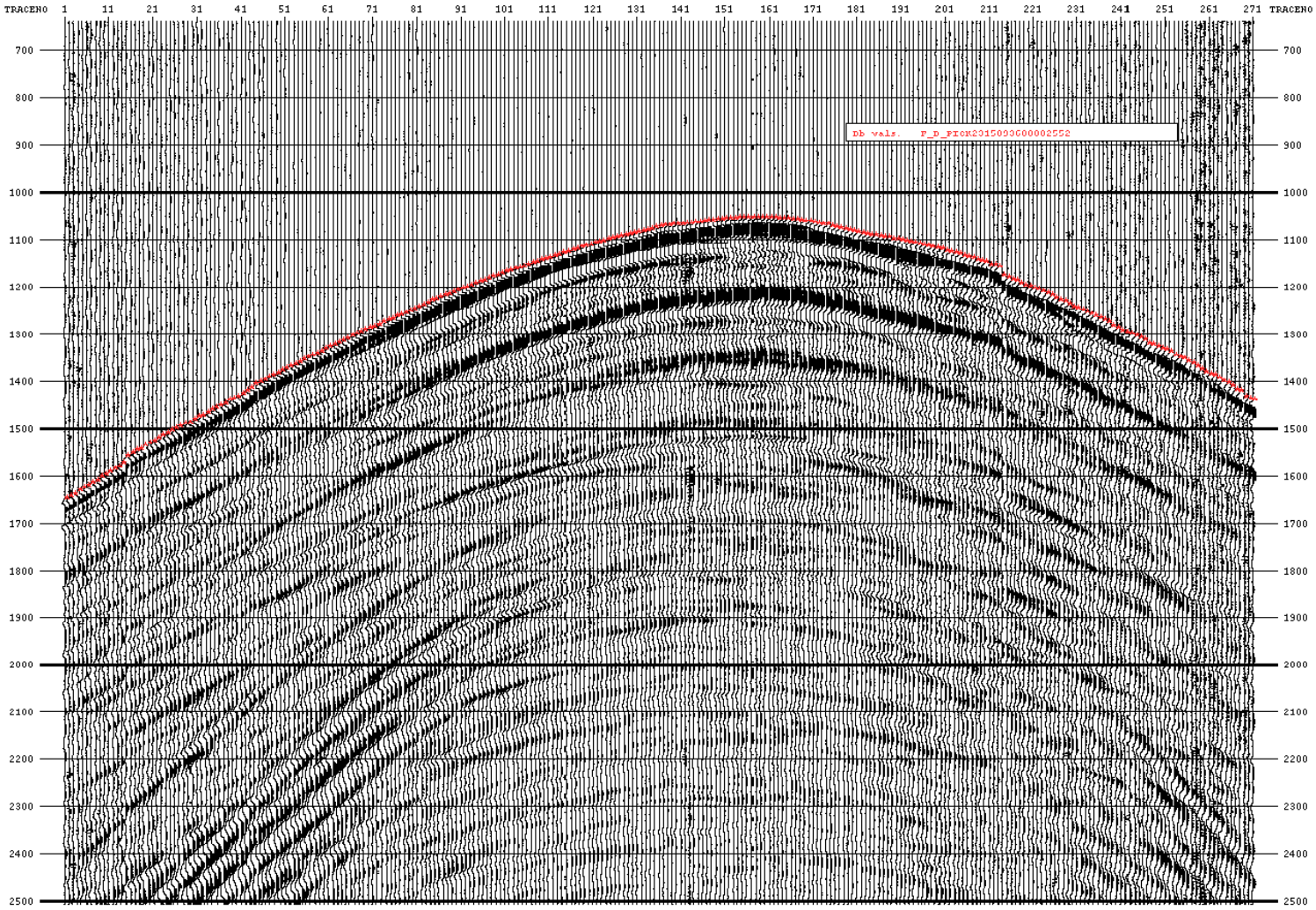

Figure 6.10 The P-wave signal recorded by receiver *15* at a depth of *2942 m*. The record is of good quality for picking the first arrival times. The vertical axis is time in milliseconds. First break picking was carried out and is shown with the red dots. The discontinuities in the record resulted from the missing shot positions.

inversion program developed in Section 3.3.1. The vertical velocity ratio for S and P-waves was first assumed to be *0.700* in the following trial inversion procedures.

6.2.3 Recovery of Apparent Elastic Parameters

For the total thickness to the depth of each receiver position, the apparent P-wave velocity field was calculated from the first arrival times. By applying the inversion program *"parameter.c"* to this apparent P-wave velocity field, the apparent parameters of each "layer" were recovered.

Total thickness to the depth of *2732 m* (the first receiver position)

Firstly, the velocity field was computed for the "layer" to the depth of *2732 m* from the signals recorded by the shallowest receiver. The circles in Figure 6.11a show the velocity field computed from this field data. The central area of the plot with ray angles ranging from *-10°* to *20°*, is obviously an abnormal area that departs from transverse isotropy. The basic assumption of my inversion software is transverse isotropy. Hence, in the following inversion procedures, the field data located in the central area of this record between *-10°* to *20°* were not input to the inversion program.

Field data in the southern and northern areas

Field data in the southern and northern areas with the shooting direction less than *-10°* and larger than *20°* from the vertical were input to the inversion program.

It was first assumed that the "layer" to the depth of *2732 m* was a VTI medium. The inversion program was run with a fixed tilt angle of zero. This inversion result is shown in Figure 6.11a. The velocity field calculated from the inverted apparent parameters (red curve) is also plotted for comparison with the field velocity data (blue circles). These velocity fields show some obvious differences.

Then the inversion program was run again under a TTI assumption. Figure 6.11b gives these inversion results and the input velocity field for the "layer". The field velocity data (red curve) and that calculated from the inverted apparent parameters

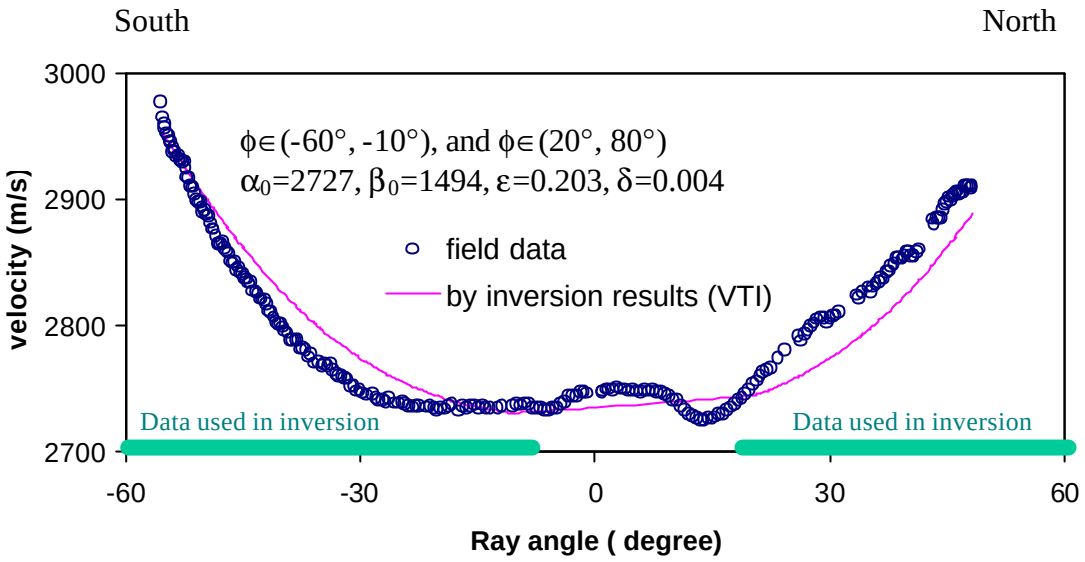

(a)

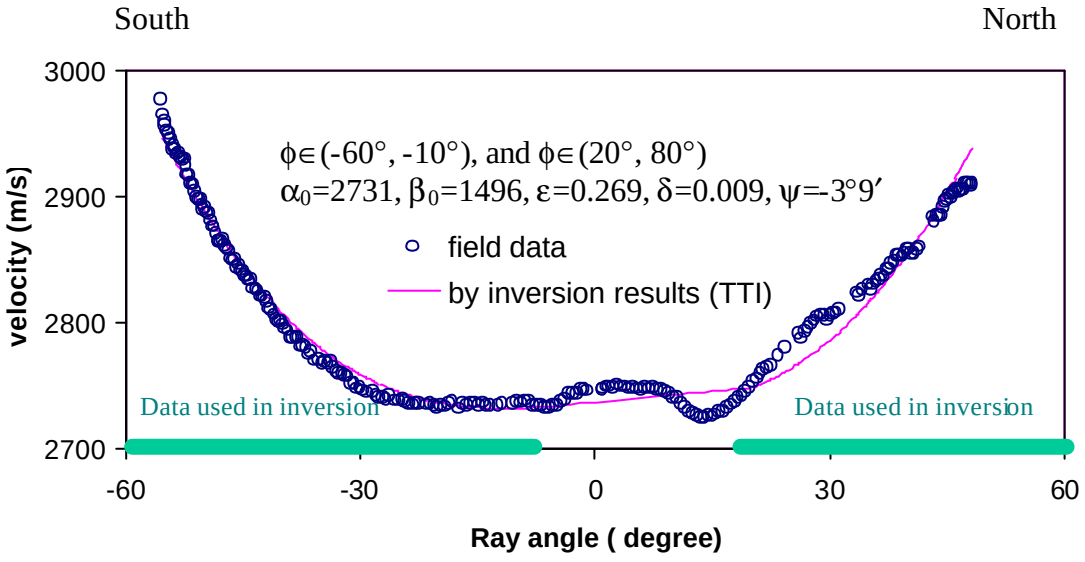

(b)

Figure 6.11 The inversion results for apparent parameters for the layer above the first receiver at *2732 m.* Field data except for the central part were used to invert for the elastic parameters. The velocity fields of the field data and that computed from the inverted parameters show noticeable differences for (a) inversion result based on a VTI assumption, and (b) inversion result based on a TTI assumption.

(blue circles) still do not match well. However, in the southern area, the coincidence of correlation between these two velocity fields is improved.

These inversion results imply that we cannot treat the southern and northern survey areas as a transversely isotropic medium with uniform properties. The data set was then divided into three sub-areas — the southern area with ray angles lying between *–60°* and *–10°*, the central area with ray angles ranging between *-10°* and *20°*, and the northern area with the ray angles ranging between *20°* and *60°*.

Field data from the southern area

Firstly, we assumed that the southern region was a VTI medium. By applying the inversion program *"parameter.c"* to the field data in the southern area, the apparent parameters of the total layer to the depth of *2732 m* were recovered. The recovered apparent parameters were $e=0.295$ and $d=-0.0784$. Figure 6.12a provides a comparison of the recorded and the reconstructed velocity fields at different ray angles. The blue circles represent the velocity field from the field data (observations), and the red curve represents the velocity field calculated from the inverted apparent parameters. These velocity fields coincide fairly well in the southern area. We can conclude that the southern area can be treated as a transversely isotropic medium with a vertical symmetry axis.

The same inversion program was run again assuming the layer was a TTI medium with the same field data from the southern area as input. Figure 6.12b shows the resulting velocity fields. The velocity field from the field data (circles) and that calculated from the inverted apparent parameters (curve) show a better match in the southern area than that in Figure 6.12a. The recovered tilt angle of the symmetry axis was determined to be $y = -5.44°$. The recovered elastic parameters e and d ($e=0.409$ and $d=-0.037$) are somewhat different from the former inversion results ($e=0.295$ and $d=-0.078$) when a VTI medium was assumed.

In the southern area, the layer to the depth of *2732 m* behaves like a transversely isotropic medium. The negative small tilt angle suggests that the bedding of the total layer is nearly horizontal and dipping slightly towards the south.

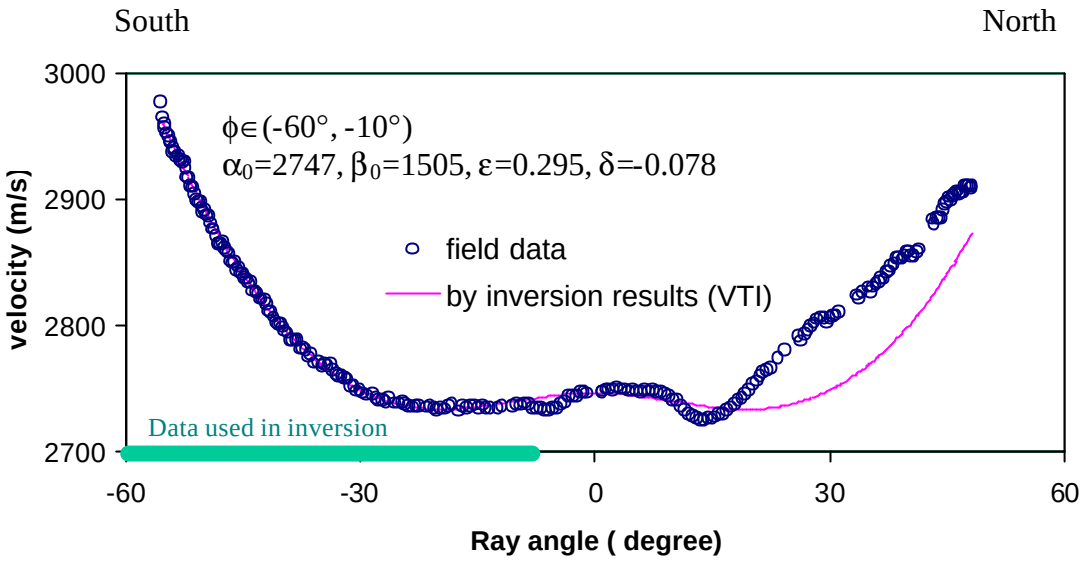

(a)

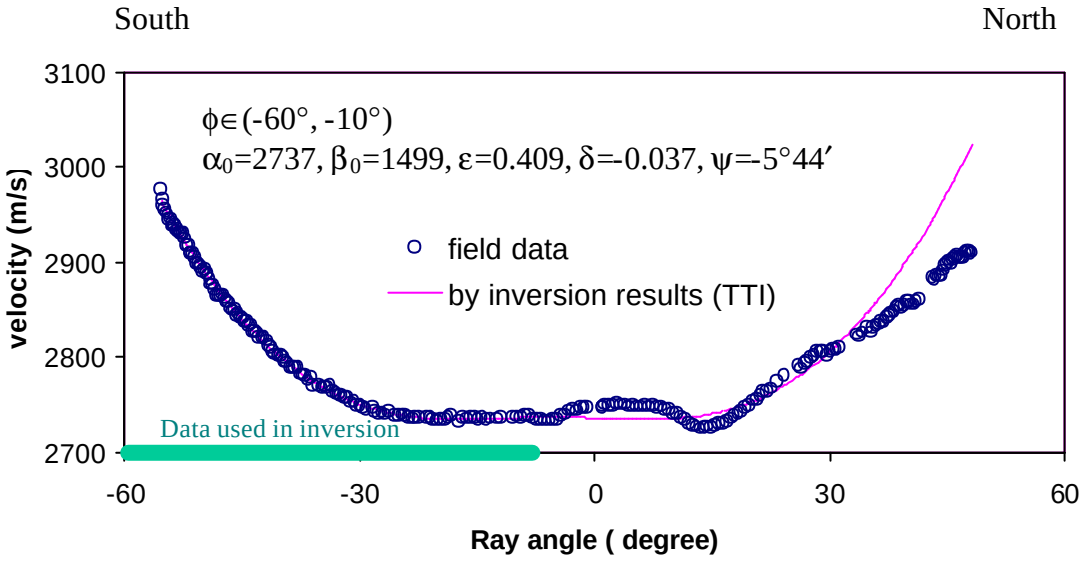

(b)

Figure 6.12 The inversion results of apparent parameters for the layer above the first receiver in the southern area. Field data from the southern part were used to invert for the elastic parameters. The velocity fields from the field data and from the inverted parameters are in good agreement for (a) inversion result based on a VTI assumption, and (b) inversion result based on a TTI assumption.

The angle of tilt of the symmetry axis was quite small, being only several degrees. As a consequence, there are only small differences between the inverted anisotropic parameters under a VTI assumption and a TTI assumption. For this reason, in the following inversion procedures, a VTI assumption was considered to be quite adequate.

Field data from the northern area

Field data from the northern area collected at an angle larger than $20°$ from the vertical were input to the inversion program. The inverted apparent elastic parameters for ray angles between $20°$ and $60°$ were then obtained. The anisotropic parameters were found to be $e=0.156$ and $d=0.133$, different from those of the southern part. The velocity field input from the field data and that re-constructed from the inverted apparent parameters are shown in Figure 6.13. These velocity fields match each other fairly well in the northern area. So we conclude that the northern area behaves mainly like a transversely isotropic medium. However, there are differences in anisotropic parameters between the northern and the southern areas.

Because of the lack of sonic log and water depth data, the inversion procedures were carried out only for testing the inversion programs. In the following, only the field data from the southern area were studied further.

.

Analysis of data to different receiver positions in the southern area

Under the assumption of VTI, my inversion procedures were implemented on the VSP data recorded at each receiver station from sources in the southern region. For the southern area between ray angles $-60°$ and $-10°$, the inversion results for each overall layer above the receivers were obtained and are shown in Table 6.8. The field velocity data and the velocity field calculated from the recovered parameters were then compared (Li and Okoye, 1999), similar to that in Figure 6.12. Both velocity fields match each other very closely.

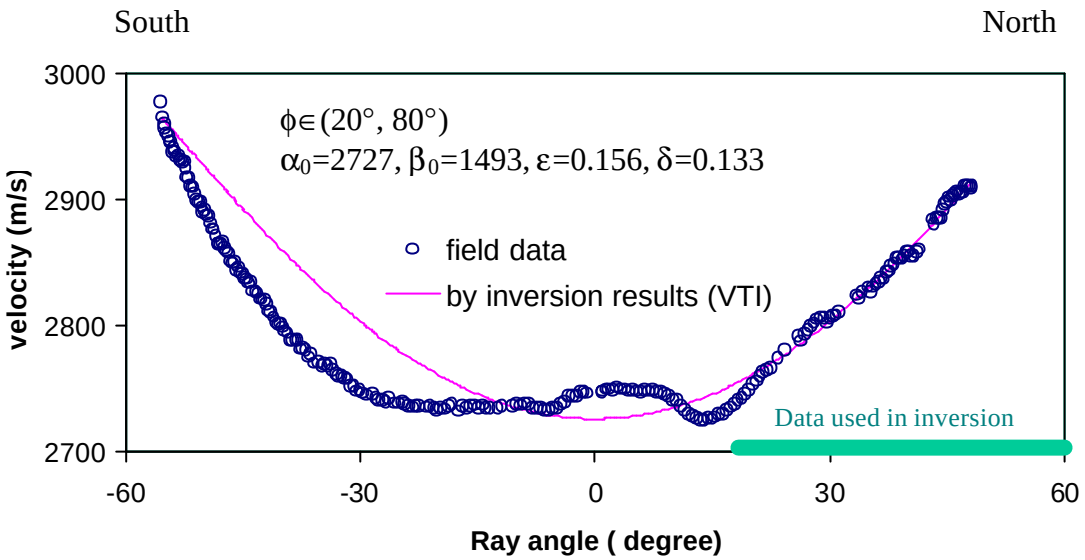

Figure 6.13 The inversion results for apparent parameters using the northern data for the layer above the depth of *2732 m.* Field data from the northern region indicated were used to invert for the elastic parameters. A VTI medium was assumed. In this northern area, the velocity fields from the field data and from the inverted parameters are in reasonably good agreement.

Table 6.8 Inversion results for the southern area for apparent parameters of the total layer above each receiver using the inversion program assuming a VTI medium. The vertical velocity ratio for P and S-wave was assumed to be *0.700* due to the absence of field log data. *D* represents the mean difference between the velocity field from the field data and that calculated from the inverted parameters. Data were supplied by Woodside Petroleum Ltd.

Receiver number	Receiver depth (*m*)	a_0(*m/s*)	b_0(*m/s*)	*e*	*d*	*D*(*m/s*)
1	*2732*	*2747*	*1505*	*0.295*	*-0.078*	*1.8*
2	*2747*	*2747*	*1504*	*0.287*	*-0.071*	*1.6*
3	*2762*	*2747*	*1505*	*0.292*	*-0.069*	*2.1*
4	*2777*	*2751*	*1506*	*0.292*	*-0.066*	*2.2*
5	*2792*	*2755*	*1509*	*0.289*	*-0.059*	*2.0*
6	*2806*	*2758*	*1511*	*0.299*	*-0.063*	*2.2*
7	*2821*	*2759*	*1511*	*0.291*	*-0.052*	*2.3*
8	*2836*	*2764*	*1514*	*0.292*	*-0.048*	*2.5*
9	*2851*	*2771*	*1518*	*0.302*	*-0.053*	*2.4*
10	*2866*	*2771*	*1518*	*0.301*	*-0.044*	*2.6*
11	*2882*	*2763*	*1514*	*0.286*	*-0.025*	*3.5*
12	*2897*	*2761*	*1512*	*0.287*	*-0.020*	*4.2*
13	*2912*	*2764*	*1514*	*0.291*	*-0.024*	*3.9*
14	*2927*	*2762*	*1513*	*0.307*	*-0.032*	*4.5*
15	*2942*	*2762*	*1513*	*0.288*	*-0.010*	*3.9*

The inversion results obtained suggest that in the southern areas, the total layer above each receiver is an equivalent VTI media. The apparent P-wave vertical velocity from inversion increases from receiver No. 1 to receiver No. 9 monotonically, but only slightly increases or decreases by less than *10 m/s* thereafter. The value of e is around *0.29* and d has a value of approximately *–0.08* for the region. The degree of anisotropy of the southern area is in the weak to moderate range.

6.2.4 Recovery of Interval Elastic Parameters

The apparent elastic parameters for the various layers to different receiver depths in the southern area were recovered in Section 6.2.3. In this section, the elastic parameters of the interval layer between any two receivers in the southern area are recovered by using inversion program "*interval.c*".

The interval layer between depths of *2732 m* and *2942 m* was examined first. The inversion program was run using the field velocity data recorded by receiver 15 at the depth of *2942 m*. The inverted apparent parameters listed in Table 6.8 for the layers to the depths of *2732 m* and *2942 m* were also input to the inversion program "*interval.c*". The inversion result was given as $e=0.174$, and $d=1.204$, shown in Figure 6.14a.

To verify the inversion result, the velocity fields for the layer to the depth *2942 m* were examined in Figure 6.14a. The field velocity data were marked as blue circles. The inverted interval parameter values for the layer between *2732 m* and *2942 m*, and the known parameter values for the layer to the depth of *2732 m* were then used to calculate the apparent velocity field to the depth of *2942 m*, shown with the red curve. Both these velocity fields are well matched in the southern area. The interval layer between depths of *2732 m* and *2942 m* in the southern area can be treated as a VTI medium with the inverted interval parameters obtained.

For the interval layer between depths of *2732 m* and *2806 m*, the recovered parameters were $e=0.071$, and $d=0.434$ (Figure 6.14b). For the interval layer between depths of *2806 m* and *2942 m*, the recovered parameters were found to be $e=0.246$, and $d=1.258$ (Figure 6.14c). In Figure 6.14b and 6.14c, the field velocity data recorded by the

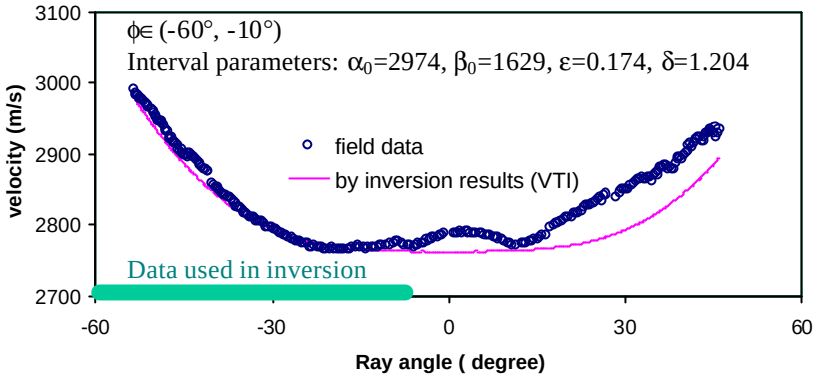

(a)

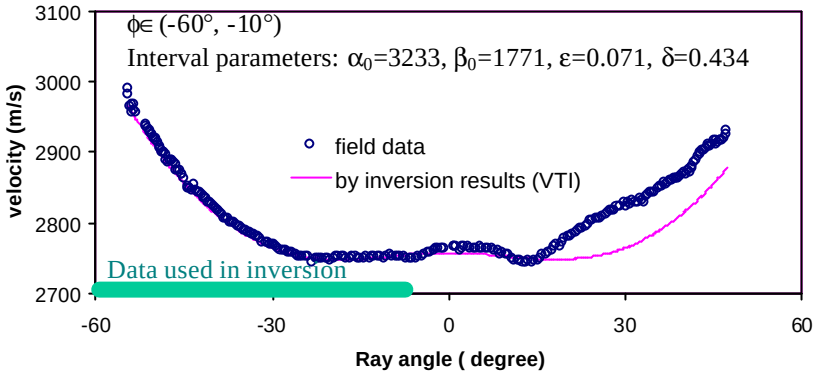

(b)

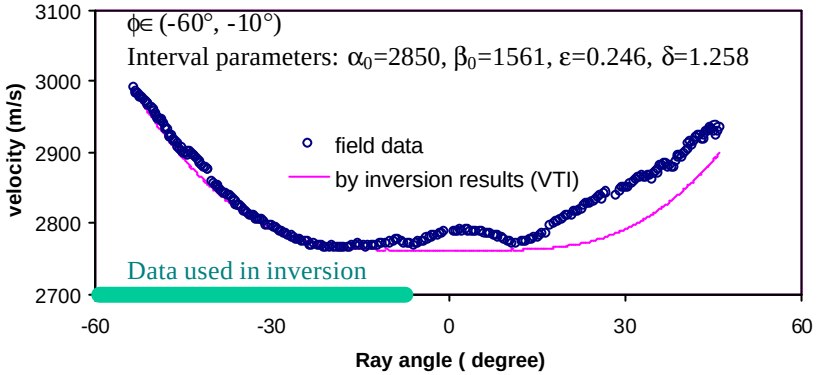

(c)

Figure 6.14 The velocity fields for the layer to the depth of (a) *2942 m*, (b) *2806 m*, and (c) *2942 m*. The interval layers studied are between depths of (a) *2732 m* and *2942 m*, (b) *2732 m* and *2806 m*, and (c) *2806 m* and *2942 m*. The field velocity data recorded by the receiver located at the lower surface of each interval layer are denoted as blue circles. The recovered parameters for each interval layer and the known parameters for the layer to the upper surface of this interval layer were then used to re-construct the apparent velocity fields to the lower surface of the interval layer, marked as red curves. In the southern area, the blue circles and the red curves are in good agreement for each panel.

receiver located at the lower surface of each interval layer are denoted as blue circles. The recovered parameters for each interval layer and the known parameters for the layer to the upper surface of this interval layer were then used to calculate the apparent velocity fields to the lower surface of the interval layer, marked as red curves. The blue circles and the red curves in the southern area are in good agreement in Figures 6.14b and 6.14c. These interval layers behave like a VTI medium with the recovered interval parameters.

The recovered anisotropic parameters d for the interval layer between depths of *2806 m* and *2942 m* ($d=1.2578$), the interval layer between depths of *2732 m* and *2942 m* ($d=1.2037$), were found to be unreasonably large. This prompted the inversion steps to be re-examined.

To improve the inversion results, sonic logging data are needed to confirm the assumed ratio of vertical velocities for P, and S-waves. Due to the large velocity differences between the water and the rocks, the water effects need further examination. Information about the depth of water bottom is needed.

We may apply the inversion method to any layer between any two receivers. Because of the lack of water depth and the well log data when I processed the field data, only the parameters of the above three interval layers were recovered to test the inversion program.

6.2.5 Conclusions and Discussions

The inversion programs developed in Chapter 3 and Chapter 4 were satisfactorily tested on petroleum VSP field data. For a transversely isotropic medium, the inversion programs can determine the elastic parameters from the field velocity data.

The southern part and the northern part of the survey region are transversely isotropic media with different values of the elastic parameters, while the central part cannot be modelled as a transversely isotropic medium. The southern part of the survey area above any receiver depth can be treated as transversely isotropic media with a tilted

symmetry axis. The tilted angles of the symmetry axes were found to be very small, and the beddings dip slightly towards the south. There were no great differences between the inversion results under a VTI assumption and those under a TTI assumption.

The interval layers in the southern area between receivers 1 and 15, 1 and 6, 6 and 15 behave like VTI media. The inversion showed interval layers in this TI region with anisotropy parameters that are representative of a clay/sand sequence which was subsequently verified by the seismic section referred to in a later paragraph.

If we had more information about the well-logging data and the water depth data, the ratio of vertical velocity for P to S-waves could have been more accurately determined, and the travel times in water could have been removed from the recorded data. Then, the inversion programs may have provided more precise results.

Post Script

After the research reported in this chapter was completed, Woodside Petroleum Ltd. released a stacked seismic section through the well, shown in Figure 6.15. The stacked section reveals immediately the heterogeneous structural geology around the well. It indicated a layered medium to the south and far north of the well, while the central parts of the line show complex fracturing and heterogeneity. To the bottom of the bore hole there is a domal structure. The contents of this structure are of key interest for exploration in this area. It was considered beyond the scope of this thesis to examine the geology further.

An honours student carried out a further study with my encouragement on the applications of my inversion programs to this petroleum VSP field data. With well-logging data and water depth data released by Woodside Petroleum Ltd., she used my modified inversion programs to study the anisotropic property of the survey region. Her research provided more successful examples of my inversion programs (Nguyen, 2000).

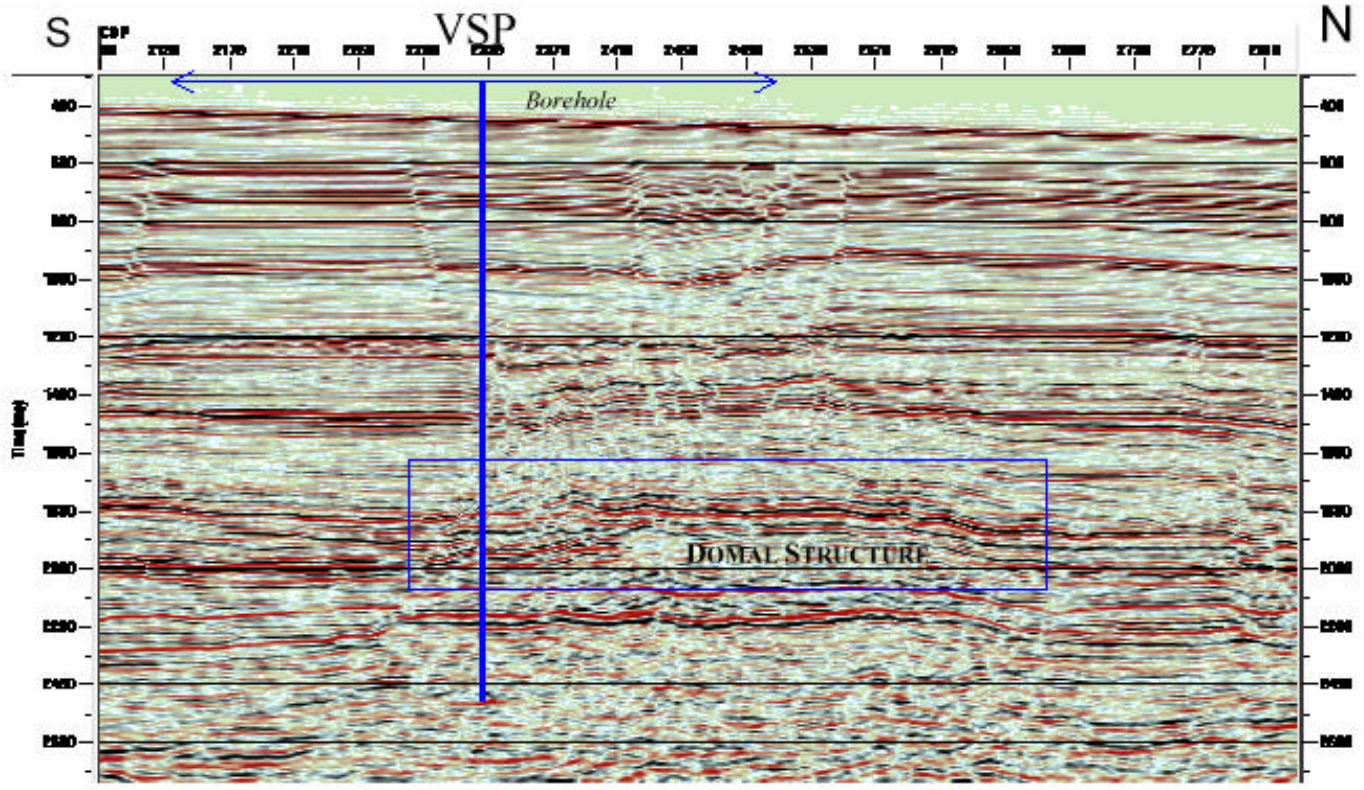

Figure 6.15 The seismic stacked section. The stacked section reveals immediately the heterogeneous structural geology of the subsurface. It indicates a layered medium to the south and far north of the well, while the central parts of the line show complex fracturing and heterogeneity. To the bottom of the borehole there is a domal structure. The contents of this structure are of key interest for exploration in this area. (after Nguyen, 2000).

CHAPTER 7
APPLICATIONS OF RECOVERED ANISOTROPIC PARAMETERS TO MOVEOUT CORRECTIONS

Inversion methods for the recovery of elastic parameters of transversely isotropic media from walkaway VSP surveys have been successfully developed in the previous chapters. One of the possible applications for the recovered elastic parameters is making moveout corrections in seismic data processing.

For elliptical anisotropy, a specific case of transverse isotropy where $e=d$, Uren et al. (1990b) developed an explicit general expression for normal moveout velocity (NMO). When the elastic parameters a_0, b_0, $e=d$, and tilt angle y are recovered, the moveout velocity independent of offset can be calculated, using the equation 6 in the paper by Uren et al. (1990b).

For the general case of transverse isotropy, NMO velocity is a function of offset (Uren et al., 1990b). For zero-offset, an equation for NMO velocity has previously been derived (Thomsen, 1986). This equation has been used as the short offset NMO velocity, and it was believed to be valid for any degree of anisotropy (Tsvankin, 1996; Alkhalifah et al., 1996). It is however an approximation to use it in this way and the accuracy of this equation for short offsets needs to be examined. Okoye et al. (1998) showed experimentally that the accuracy and validity of this NMO equation for short offsets depends on the nature and degree of anisotropy prevailing in a given sedimentary area. The possibility of a more suitable analytical expression for moveout velocity for short offsets needs to be investigated.

In this chapter, the effects of elastic parameters on P-wave moveout at short offsets will be studied. Analytical derivations and numerical modelling experiments will be

used in this research. *Maple* (Waterloo Maple Inc.), which is a comprehensive computer package for advanced mathematics, will be used to carry out the complex algebraic derivations. Numerical simulations will be conducted using the measured elastic parameters for sedimentary anisotropic rocks.

As stated in Chapter 1, these studies will be limited to short offsets and horizontally layered transversely isotropic media with a vertical symmetry axis (VTI media), which is the most common case that reflection surveys encounter.

7.1 Theoretical Background

The phase velocity for P-waves at phase angle q, measured from the symmetry axis, can be re-stated from equation 2.24 as follows (Schoenberg, personal communication):

$$\frac{v_p^{\,2}(q)}{a_0^{\,2}} = 1 + e\sin^2 q - \frac{f}{2} + \frac{f}{2}\sqrt{(1+\frac{2e}{f}\sin^2 q)^2 - 2\frac{e-d}{f}\sin^2 2q}\,, \qquad (7.1)$$

where, a_0, b_0, are the P wave and S wave velocities along the symmetry axis; e is P-wave anisotropy and d represents the critical anisotropy for near-vertical P-wave propagation (Thomsen, 1986). The factor f is defined by $f = 1 - b_0^{\,2}/a_0^{\,2}$. In terms of the stiffness coefficients c_{ij}, the elastic parameters are defined in equations 2.18 — 2.21. When $e = d$, the wave surface is an ellipsoid. Such a medium is said to be elliptically anisotropic (Tsvankin, 1996).

The relationships between group velocity $v_g(f)$ and phase velocity $v_p(q)$ are written as equations 2.28 and 2.29. Here, the ray angle f is defined by conventional geometry, and differs from the phase angle q for a transversely isotropic medium, except at $f = q = 90°$, and $f = q = 0°$.

The exact zero-offset normal moveout velocity is given by Thomsen (1986) as:

$$v_{nmo}(0) = a_0\sqrt{1+2d}\ . \tag{7.2}$$

Firstly, from the definition of the elastic parameters,

$$e \equiv \frac{c_{11}}{2c_{33}} - \frac{1}{2} > -\frac{1}{2}, \tag{7.3}$$

$$d \equiv \frac{(c_{13}+c_{44})^2}{2c_{33}(c_{33}-c_{44})} - \frac{(c_{33}-c_{44})}{2c_{33}} > -\frac{1}{2} + \frac{c_{44}}{2c_{33}} > -\frac{1}{2}. \tag{7.4}$$

The values of e and d are not less than *–0.5*. Typically, for earth materials with $\frac{c_{44}}{c_{33}} = \frac{b_0^2}{a_0^2} = 1 - f \sim 1/3$, this requires $d > -\frac{1}{2} + \frac{c_{44}}{2c_{33}} \sim -\frac{1}{2} + \frac{1}{2}\cdot\frac{1}{3} = -\frac{1}{3}$. From Thomsen's paper (1986), the values of d for measured sedimentary rocks are in the range from *–0.264* to *0.730*, e are in the range from *–0.026* to *0.334*. Most of the sedimentary rocks have anisotropy in the weak to moderate range, i.e., values of anisotropic parameters e and d are small in absolute magnitude (*<0.2*). But there are some exceptions. Some media may show a strong degree of anisotropy with large values of anisotropic parameters e and d.

For a TI medium equivalent to isotropic fine layering, Schoenberg (1994) stated that its elastic moduli must satisfy the following conditions:

$$\begin{aligned} &c_{11}/c_{33} > 1/4, \\ &E^2 \equiv (c_{11}-c_{44})(c_{33}-c_{44}) - (c_{13}+c_{44})^2 > 0. \end{aligned} \tag{7.5}$$

Thus, we strictly have the condition for this isotropic fine layering medium:

$$d < \frac{(c_{11}-c_{44})(c_{33}-c_{44}) - (c_{33}-c_{44})^2}{2c_{33}(c_{33}-c_{44})} = \frac{1}{2c_{33}}(c_{11}-c_{33}) = e\ . \tag{7.6}$$

That is: $d < e$.

7.2 Small Phase Angle Approximations

Small phase angle approximations were derived below at a small offset or ray angle. Equations 7.1, 2.28 and 2.29 were expanded as functions of a small phase angle q using the advanced mathematical software package *Maple*. Taylor series expansions were obtained for the phase velocity v_p, the ray velocity v_g and the ray angle f, up to the third order of q. These can be written as (Appendix A):

$$v_p(f) \approx v_{pa}(f), \text{ and } \frac{v_{pa}(f)}{a_0} = 1 + \frac{d}{(1+2d)^2} f^2, \tag{7.7}$$

$$v_g(f) \approx v_{ga}(f), \text{ and } \frac{v_{ga}(f)}{a_0} = 1 + \frac{d}{1+2d} f^2, \tag{7.8}$$

and

$f(q) \approx f_a(q)$, and

$$f_a(q) = q\{(1+2d) + [-\frac{16}{3}d - 4d^2 - \frac{8}{3}d^3 + 4e + \frac{8}{f}d(e-d)]q^2\}. \tag{7.9}$$

Here, the lower subscript "*a*" means "approximation".

For the case of a horizontal reflector in a VTI medium, the incident and reflected rays will be at the same angle f to the vertical direction (Figure 7.1). Following a complex algebraic derivation (Appendix B), the gradient of a t^2 vs x^2 curve for small values of phase angle q was found to be:

$$\frac{d(t^2)}{d(x^2)} \approx \frac{1}{a_0^2(1+2d)}[1 - \frac{4}{(1+2d)^3}(e-d)(1+\frac{2d}{f})f^2]. \tag{7.10}$$

The gradients of t^2 vs x^2 plots are not a constant for a transversely isotropic medium (except for the case of elliptical anisotropy when $e=d$). The corresponding gradient of a t^2 vs x^2 curve is a function of ray angle f, or offset.

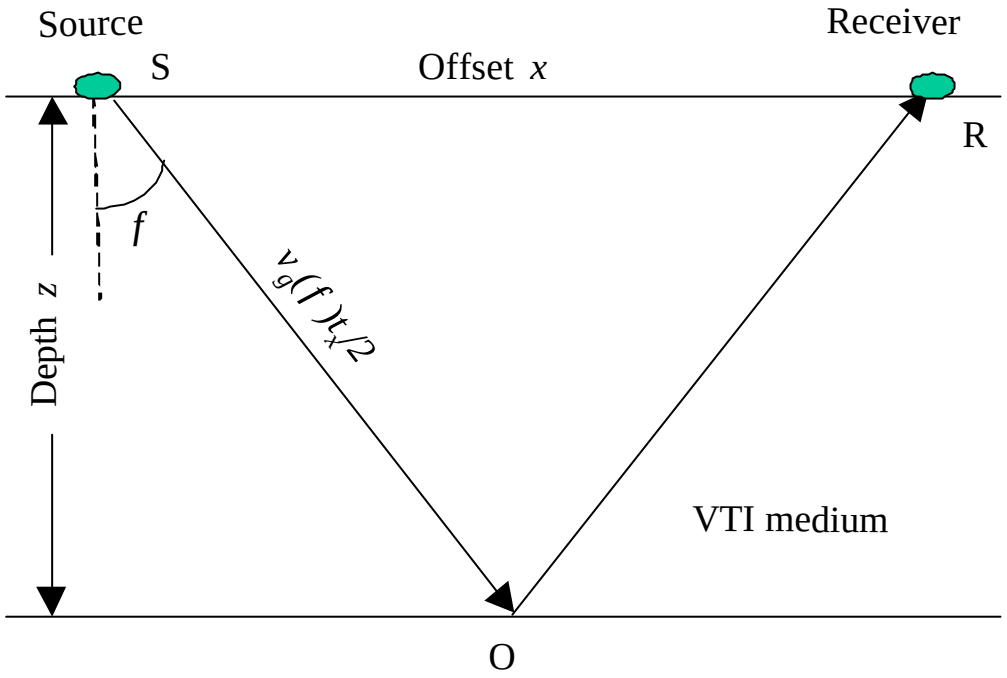

Figure 7.1 A sketch of a seismic ray reflecting from a horizontal reflector in a VTI medium. Here, the ray velocity along SO is represented as $v_g(f)$, and the travel time for the ray from S to R via O is t_x. The distance SO is $v_g(f)t_x/2$. This ray path symmetry is lost when the axis of symmetry is tilted, or when the reflector is dipping.

According to the conventional definition of moveout velocity in isotropic media, the moveout velocity v_{mo}, at offset x for VTI media (horizontal reflector) can be found from:

$$t_x^2 = t_0^2 + \frac{x^2}{v_{mo}^2(x)}. \tag{7.11}$$

In the case of transverse isotropy, the P-wave moveout velocity v_{mo} will not generally be a constant now, as it is a function of the offset x or the ray angle f. The exact moveout velocity expression at a ray angle f for VTI media and horizontal reflectors is (derived in Appendix B):

$$v_{mo}(f) = \frac{v_g(f)\sin f}{\sqrt{1-(\frac{v_g(f)}{a_0})^2 \cos^2 f}}. \tag{7.12}$$

By inserting equations 7.1, 2.28 and 2.29 into equation 7.12, and using a Taylor series expansion to the third order of q, a new equation was developed which describes the behaviour of P-wave moveout velocity $v_{mo}(f)$ for small phase angles:

$v_{mo}(f) \approx v_{moa}(f)$, and

$$\begin{aligned} v_{moa}(f) &= \sqrt{1+2d}\, a_0 \left(1 + \frac{1}{(1+2d)^3}(e-d)(1+\frac{2d}{f})f^2 \right) \\ &= v_{nmo}(0) \left(1 + \frac{1}{(1+2d)^3}(e-d)(1+\frac{2d}{f})f^2 \right) \end{aligned} \tag{7.13}$$

When q is small, f will also be small. The mathematical derivations of equations 7.10, 7.12 and 7.13 were obtained using the mathematics software package *Maple.* These derivations are given in Appendix B.

In terms of the anisotropic parameter η, defined by Alkhalifah and Tsvankin (1995),

$$h = \frac{e-d}{1+2d}, \tag{7.14}$$

the above expression then can be rewritten as:

$$v_{moa} = v_{nmo}(0) \left(1 + \frac{1}{(1+2d)^2} h (1+\frac{2d}{f}) f^2 \right) \tag{7.15}$$

When $f=0$, equations 7.13 and 7.15 reduce to Thomsen's equation 7.2. For elliptical anisotropy, $(e=d)$, a constant moveout velocity is obtained which is equal to the horizontal velocity, and the reflection moveout is purely hyperbolic. This result is consistent with those of Levin (1978) and Uren (1989).

At small phase angles, the deviation of the exact moveout velocity $v_{mo}(f)$ from Thomsen's normal moveout velocity $v_{nmo}(0)$ depends on the degree of anisotropy of the sedimentary rocks involved. Examining the second term on the right-hand side of equation 7.13, it is clear that the deviation mainly depends on the near-vertical anisotropy coefficient d. When d has a negative value, especially when d approaches -0.5, the denominator in the second term of equation 7.13 will become very small, and the difference between these two moveout velocities $v_{mo}(f)$ and $v_{nmo}(0)$ becomes very significant and cannot be ignored. This result coincided with the experimental results by Okoye et al. (1998).

7.3 Numerical analysis

The accuracy of the approximations made in the last section now needs to be assessed. Comparisons are needed between the derived approximation equations and their exact values. Because of the difficulty in obtaining explicit expressions for phase velocity $v_p(f)$ at ray angle f, ray velocity $v_g(f)$, ray angle $f(q)$, and moveout velocity $v_{mo}(f)$, numerical analyses for some specific materials were carried out as a way of investigating the validity of my derivations.

Three representative anisotropic rocks (Thomsen, 1986) and one typical $TISO_2$ (Thin ISOtropic layer equivalent with two constituents) medium (Schoenberg, 1994) were chosen. The materials chosen were Taylor sandstone, Dog Creek shale, Green River shale, and $TISO_2$. The degrees of anisotropy vary from very weak to strong, and have

different positive and negative values of near vertical P-wave anisotropy (d). Table 7.1 gives the parameters for these sedimentary rocks and $TISO_2$ material. The depth of the reflector was set arbitrarily at $z = 1000m$. The source-receiver offset at short offsets used here did not exceed the reflector depth, i.e., $x £ 1000\,m$, which conforms to the conventional definition of short offsets.

The small phase angle approximations in equations 7.7 — 7.9 for phase velocity $v_{pa}(f)$, ray velocity $v_{ga}(f)$ and ray angle $f_a(q)$ were numerically compared with their exact numerical values directly calculated from equations 7.1, 2.28 and 2.29. The moveout velocity values derived from equations 7.13 and 7.2, and the exact values numerically calculated from equation 7.12 were also compared. The phase angles q in the range of short offsets were examined, to verify the conditions of the approximations. The results and their analysis are given below and the subscript "a" represents the small phase angle approximation of a function.

7.3.1 Velocity and Travel Direction

Figure 7.2 compares the exact phase velocity v_p with its short offset approximations v_{pa}. The exact ray velocity v_g with its short offset approximation v_{ga}, are compared in Figure 7.3. The comparison of the exact ray angle f with its short offset approximations f_a is shown in Figure 7.4. Results in Figures 7.2 — 7.4 are shown for each of the materials in Table 7.2.

As can be seen from Figures 7.2 — 7.4, the percentage differences between the exact expressions and their approximations increase with offset. The accuracy of the approximations deteriorates as the offset increases.

It also can be seen that the percentage differences vary with the elastic parameters of rocks. For example, in Figure 7.2, a *2%* difference in phase velocity v_p occurs around

Table 7.1 The parameters of the measured sedimentary rocks and a typical material used in the moveout velocity study (Thomsen, 1986; Schoenberg, 1994).

Material	$a_0(ms^{-1})$	$b_0(ms^{-1})$	e	d
Taylor sandstone	3368	1829	0.110	-0.035
Dog Creek shale	1875	826	0.225	0.100
Green River shale	3292	1768	0.195	-0.220
$TISO_2$	2449	1414	0.333	0.089

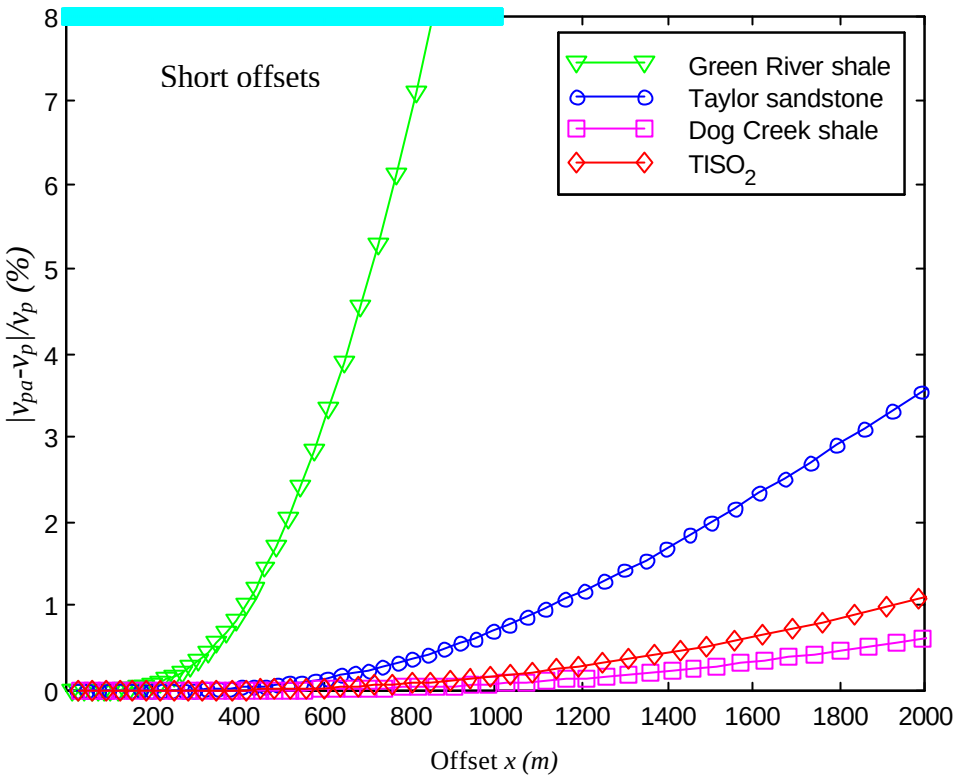

Figure 7.2 Percentage difference between phase velocity v_{pa}, and its exact value v_p, for different sedimentary rocks and $TISO_2$ material. Here, the depth of the reflector was arbitrarily chosen to be *1000 m*, and x is the source-receiver offset. $x \pounds$ *1000 m* is within the range of "short offsets".

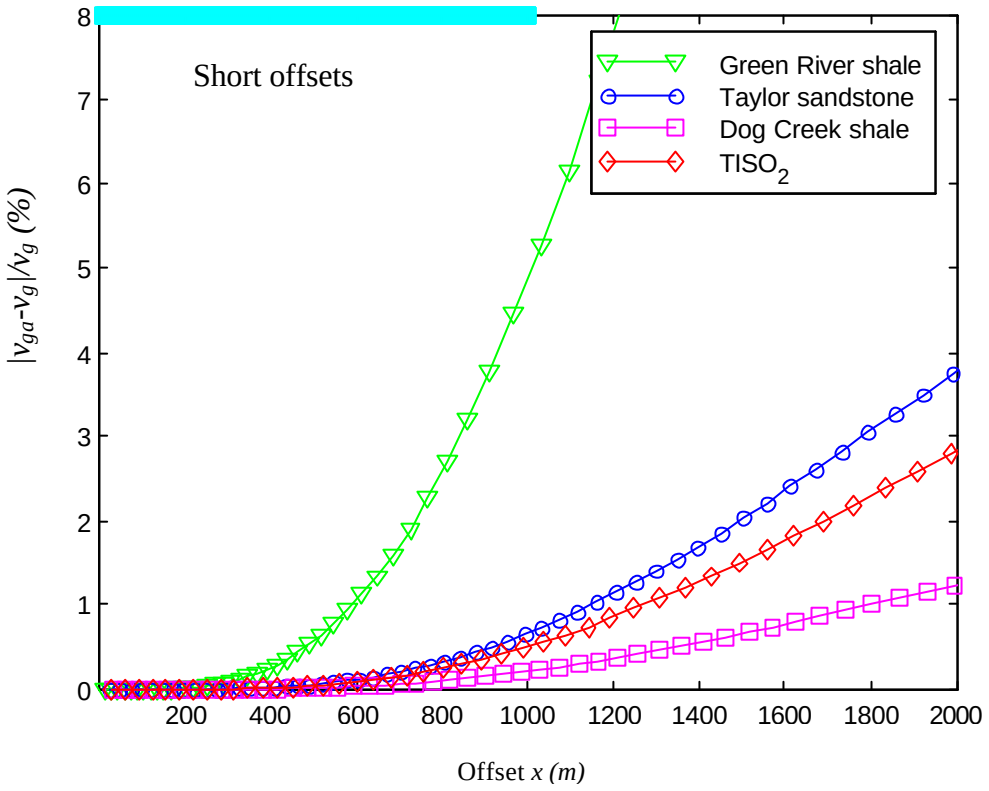

Figure 7.3 Percentage difference between ray velocity v_{ga}, and its exact value v_g, for different sedimentary rocks and $TISO_2$ material. Here, the depth of the reflector was arbitrarily chosen to be $1000\ m$, and x is the source-receiver offset. $x \pounds\ 1000\ m$ is within the range of "short offsets".

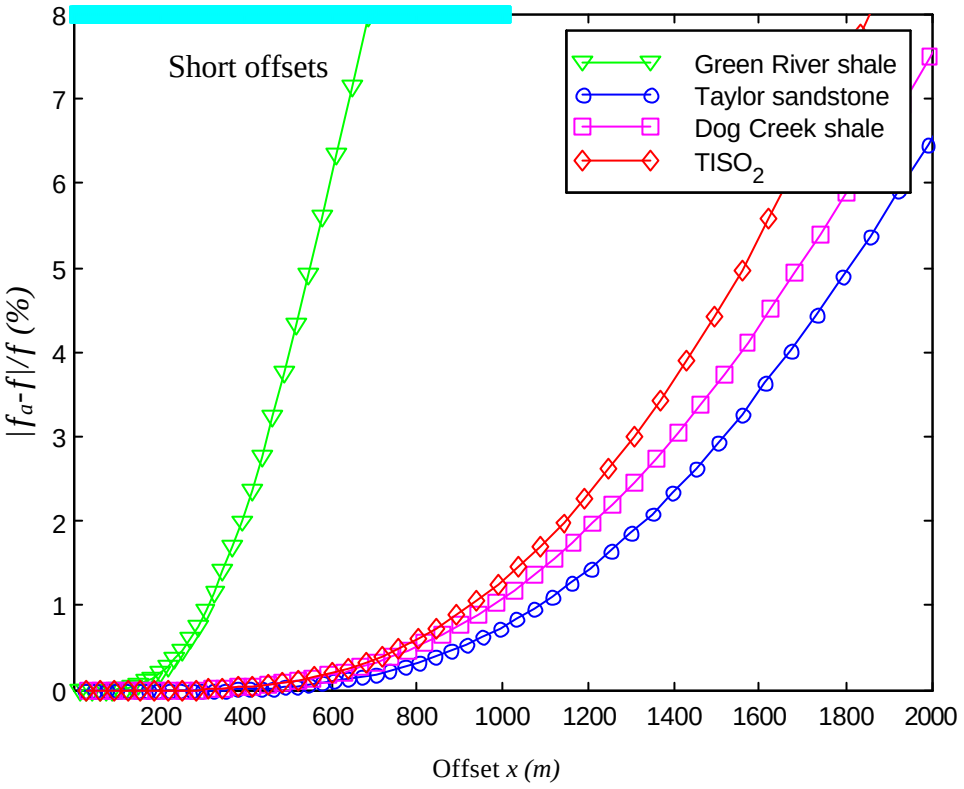

Figure 7.4 Percentage difference between ray angle f_a and its exact value f, for different sedimentary rocks and $TISO_2$ material. Here, the depth of the reflector was arbitrarily chosen to be $1000\ m$, and x is the source-receiver offset. $x \pounds\ 1000\ m$ is within the range of "short offsets".

the offset $x = 1500m$ for Taylor sandstone. But a similar difference occurs at $x = 500m$ for Green River shale. However, for Dog Creek shale and $TISO_2$, a *2%* difference occurs for $x > 2000m$. For ray velocity v_g in Figure 7.3, a *2%* difference occurs at an offset of $x = 700m$ for Green River shale, at $x = 1500m$ for Taylor sandstone, at $x = 1700m$ for $TISO_2$, and at $x > 2000m$ for Dog Creek shale. For different degrees of anisotropy, the acceptable range of offsets for these small phase angle approximations will be different. It should be noted that d has a negative but relatively large value for Green River shale, a small negative value for Taylor sandstone, and a small positive value for Dog Creek shale and $TISO_2$.

At any given offset, the error in v_{pa} is a little different from that of v_{ga}, due to the contribution of dv_p/dq in v_g.

When we examine the percentage differences in ray angle f shown in Figure 7.4, a *2%* difference occurs at $x = 400m$ for Green River shale, but at around $x = 1200m$ for Taylor sandstone, Dog Creek shale and $TISO_2$. It can be seen that the value of d for Green River shale is negative, and its absolute value is greater than those of Taylor sandstone, Dog Creek shale and $TISO_2$.

The above results lead us to believe that the absolute value of d will influence the accuracy of the approximations in equations 7.7 — 7.9, but the sign of d will have a greater impact on accuracy.

In an approximation to the first order of q, equation 7.9 reduces to: $f(q) = q(1 + 2d)$, neglecting higher order terms. Then, at a small phase angle, we have $f < q$ for negative d media, and $f > q$ for positive d media. Assuming that the depth of the reflector is fixed, we can see that for the same offset x, the corresponding phase angle q will be greater for media with negative d value, and smaller for media with positive d value. As the errors in v_{pa} and v_{ga} were introduced by Taylor expansion truncations, v_{pa} and v_{ga} at a large phase angle q will clearly contain large errors. Thus, larger errors will probably occur for media with negative d values, and smaller errors for media with positive d values.

In Figures 7.2, 7.3 and 7.4, the percentage differences between the approximations and their exact values are less than *2%* for Taylor sandstone, Dog Creek shale and $TISO_2$ when the offset is less than *1000 m*. The only exception is for Green River shale whose degree of anisotropy is very strong. Most sedimentary rocks have anisotropy in the weak-to-moderate range with the absolute values of anisotropic parameters (e, d) being less than 0.2 (Thomsen, 1986). Hence, the approximation equations 7.7 — 7.9, should be acceptable for most anisotropic media within the short offset limit. The acceptability of these equations will depend on the anisotropic degree of rocks, mainly on the value of d.

7.3.2 Curvature of the Moveout

It is necessary to examine the influence of anisotropic parameters on t^2 *vs* x^2 plots. For a CMP gather collected across a single isotropic layer, the t^2 *vs* x^2 curve (t being the reflection traveltime, x the offset) is a straight line, the slope of which is the inverse of the squared velocity. In the presence of non-elliptical anisotropy, the straight line will become curved, either concave or convex upwards depending on the nature of the anisotropy (Uren et al., 1990b; Okoye and Uren, 1995).

For VTI media, the concave or convex traveltime curve at short offsets can be theoretically explained in terms of the second order derivative of the curve, which is derived from equation 7.10 as follows:

$$\frac{d}{d(x^2)}\left(\frac{d(t^2)}{d(x^2)}\right) \approx -\frac{4}{a_0^4(1+2d)^4 t_0^2}(e-d)(1+\frac{2d}{f}). \tag{7.16}$$

That is, when

$$(e-d)(1+\frac{2d}{f})>0,\ \frac{d}{d(x^2)}\left(\frac{d(t^2)}{d(x^2)}\right)<0, \tag{7.17}$$

the moveout curve is convex upwards. When

$$(e-d)(1+\frac{2d}{f})<0,\ \frac{d}{d(x^2)}\left(\frac{d(t^2)}{d(x^2)}\right)>0, \tag{7.18}$$

the moveout curve is concave upwards. When

$$(e-d)(1+\frac{2d}{f})=0,\ \frac{d}{d(x^2)}\left(\frac{d(t^2)}{d(x^2)}\right)=0, \tag{7.19}$$

the moveout curve is a straight line. When $e=d$, the moveout is hyperbolic which corresponds to the case of elliptical anisotropy. This provides another description of the occurrence of elliptical anisotropy. Normally, $(1+\frac{2d}{f})>0$, for the measured anisotropy data published in Thomsen's (1986) paper. When $(1+\frac{2d}{f})>0$, $e>d$ and $e<d$ correspond to the convex upwards and concave upwards moveout curves, respectively (Li et al., 1998a).

The degree of curvature for the t^2 *vs* x^2 curve is related to the absolute value of $\frac{d}{d(x^2)}(\frac{d(t^2)}{d(x^2)})$. In other words, the curvature of the t^2 *vs* x^2 curve depends on the properties of the medium, namely the parameters a_0, b_0, e, d, and its depth *z*.

Okoye and Uren (1995) examined the t^2 *vs* x^2 plots for different anisotropic media. With $(e-d)(1+\frac{2d}{f})>0$, the traveltime plots for an aluminium-lucite composite, Green River shale, and Taylor sandstone clearly show that the traveltime curves are convex upwards. However, for $(e-d)(1+\frac{2d}{f})<0$, the traveltime plots for Mesaverde (5501) clayshale, Mesaverde (5566.3) laminated siltstone, and Mesaverde (4903) mudshale, the traveltime curves are concave upwards. These results are explained mathematically by equation 7.16.

7.3.3 Reflection Moveout Velocity

Many studies have used Thomsen's equation 7.2 as the short offset moveout velocity expression (e.g., Tsvankin, 1996; Tsvankin and Thomsen, 1994; Alkhalifah et al., 1996). However, physical modelling experiments have shown that while equation 7.2 is valid for some anisotropic sedimentary rocks, it will introduce serious errors for

other materials (Okoye et. al., 1998). The problem is that the zero offset equation 7.2 is only an approximation when used for finite offsets.

Thomsen's NMO equation 7.2 and moveout velocity equation 7.13 were then compared with the exact numerical values of moveout velocity calculated from equation 7.12 for short offsets as follows.

Figure 7.5 shows the percentage differences between normal moveout velocity v_{nmo} from Thomsen's equation 7.2, and the exact moveout velocity (v_{mo}). It also shows the percentage differences between the moveout velocity (v_{moa}) using equation 7.13 and the exact moveout velocity (v_{mo}). The percentage differences are functions of offsets, and increase rapidly when offsets increase. For different materials, the rate of increase is different, and depends on the anisotropic properties of the rocks. Thus, it is necessary to study the moveout velocity at short offsets rather than at zero-offset. From Figure 7.5, we can see that the value of v_{moa} obtained from equation 7.13 is closer to the exact moveout velocity given by equation 7.12, than the value of v_{nmo} obtained from Thomsen's equation 7.2.

Figure 7.5 also shows that the differences in normal moveout velocity v_{nmo} or small phase angle approximation v_{moa} from the exact value v_{mo} for Taylor sandstone, Dog Creek shale, and $TISO_2$ are smaller than that for Green River shale. For different materials, large negative values of d will substantially decrease the accuracy of v_{nmo}, as obtained from Thomsen's equation 7.2 and v_{moa}, as obtained from our equation 7.13. The more negative the value of d, the greater is the difference.

These results quantify the limitations of equation 7.2 as an estimate of the short offset moveout velocity, v_{mo} for anisotropic sedimentary rocks. For those sedimentary rocks with large negative values of d, Thomsen's normal moveout velocity equation 7.2 may not be suitable for removing moveout. We can see that equation 7.13 would be a better replacement for Thomsen's equation at short offsets.

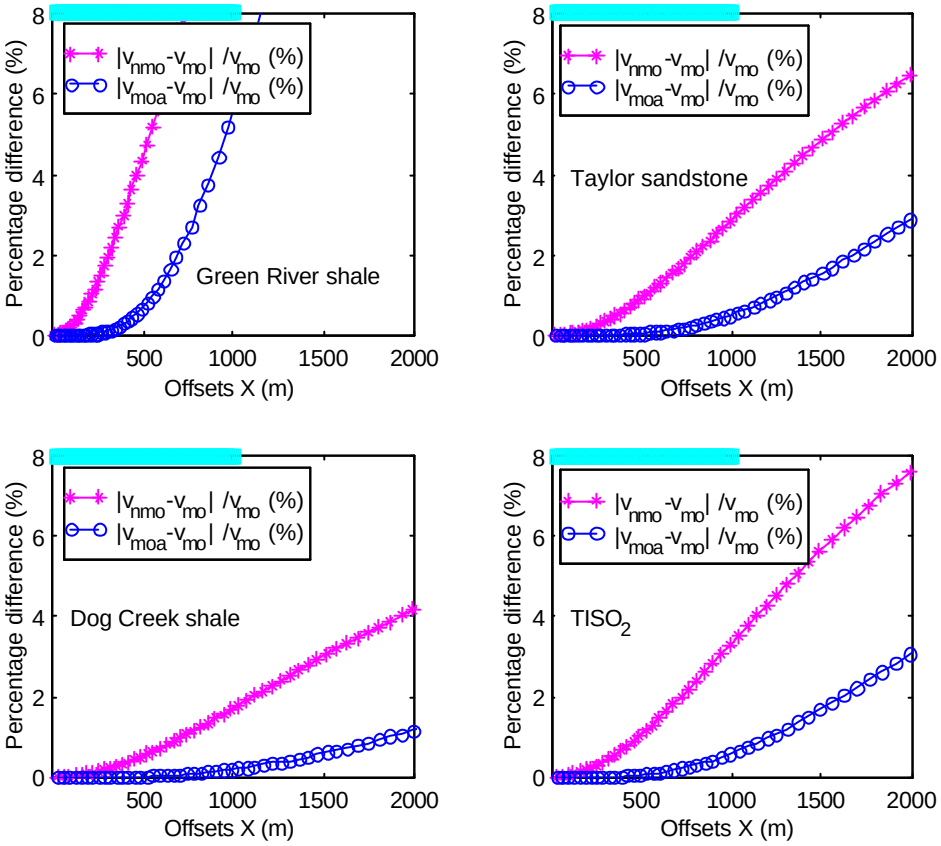

Figure 7.5 Numerical comparison of moveout velocity expressions. For different sedimentary rocks and $TISO_2$ medium, the percentage difference between moveout velocity v_{moa}, obtained from equation 7.13, normal moveout velocity v_{nmo}, obtained from equation 7.2, and their exact value v_{mo}. The depth of the reflector was arbitrarily chosen to be *1000 m*, and x is the source-receiver offset. $x \leq 1000$ *m* is within the range of "short offsets", marked with a cyan line.

Furthermore, if the maximum allowable error is set as *2%*, v_{moa} derived from equation 7.13 is a good approximation for moveout velocity, provided $x < 1700m$ for Taylor sandstone. However, for Green River shale $x < 700m$, for $TISO_2$ $x < 1600m$, and for Dog Creek shale x can exceed *2000m*. The applicability of equation 7.13 varies for different degrees of anisotropy. Increasingly negative values of d makes equation 7.13 unusable.

Using the measured anisotropic data published by Thomsen (1986), the percentage difference between v_{moa} from equation 7.13 and v_{nmo} from Thomsen's equation 7.2 was calculated for each sedimentary rock. Here, the offset was assumed to be *500 m*. Figure 7.6 shows the percentage differences *vs* the values of d for different sedimentary rocks. When d is positive, the difference is small. Conversely, when d is negative, the difference increases, especially as d becomes more negative. The near vertical anisotropic parameter d plays an important role in the deviation of v_{nmo} from v_{mo}, while other parameters a_0, b_0 and e still have some effect on it.

For comparison purposes, Figure 7.7 shows synthetic shot records before and after moveout correction. Figure 7.7a shows that the use of equation 7.2 results in overcorrection, which is noticeable to some extent in the short offset range, but quite noticeable at long offsets. Figure 7.7b shows that when correcting moveout with equation 7.13, a good flattening of the record occurs in the short offset range.

7.3.4 The Short Offset Approximation

Equations 7.7-7.10, and 7.13 were derived under the small phase angle approximation. These equations can only be used for offsets such that the corresponding phase angle is less than *1 radian*, according to the convergence condition of Taylor series expansions. The corresponding phase angles for short offsets were then numerically examined for the four representative sedimentary rocks and material listed in Table 7.1.

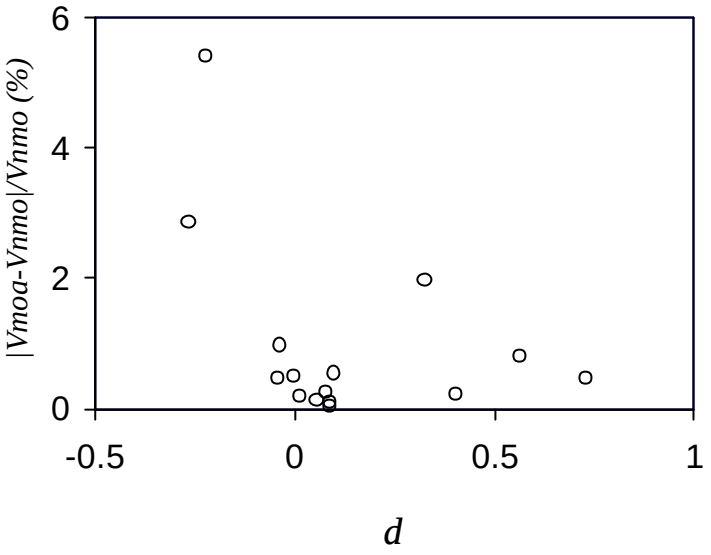

Figure 7.6 The percentage difference between the normal moveout velocities v_{nmo} and the short offset approximation v_{moa} for different sedimentary rocks with different values of d. Here, the depth was arbitrarily chosen to be *1000 m*, and the offset was chosen to be *500 m*.

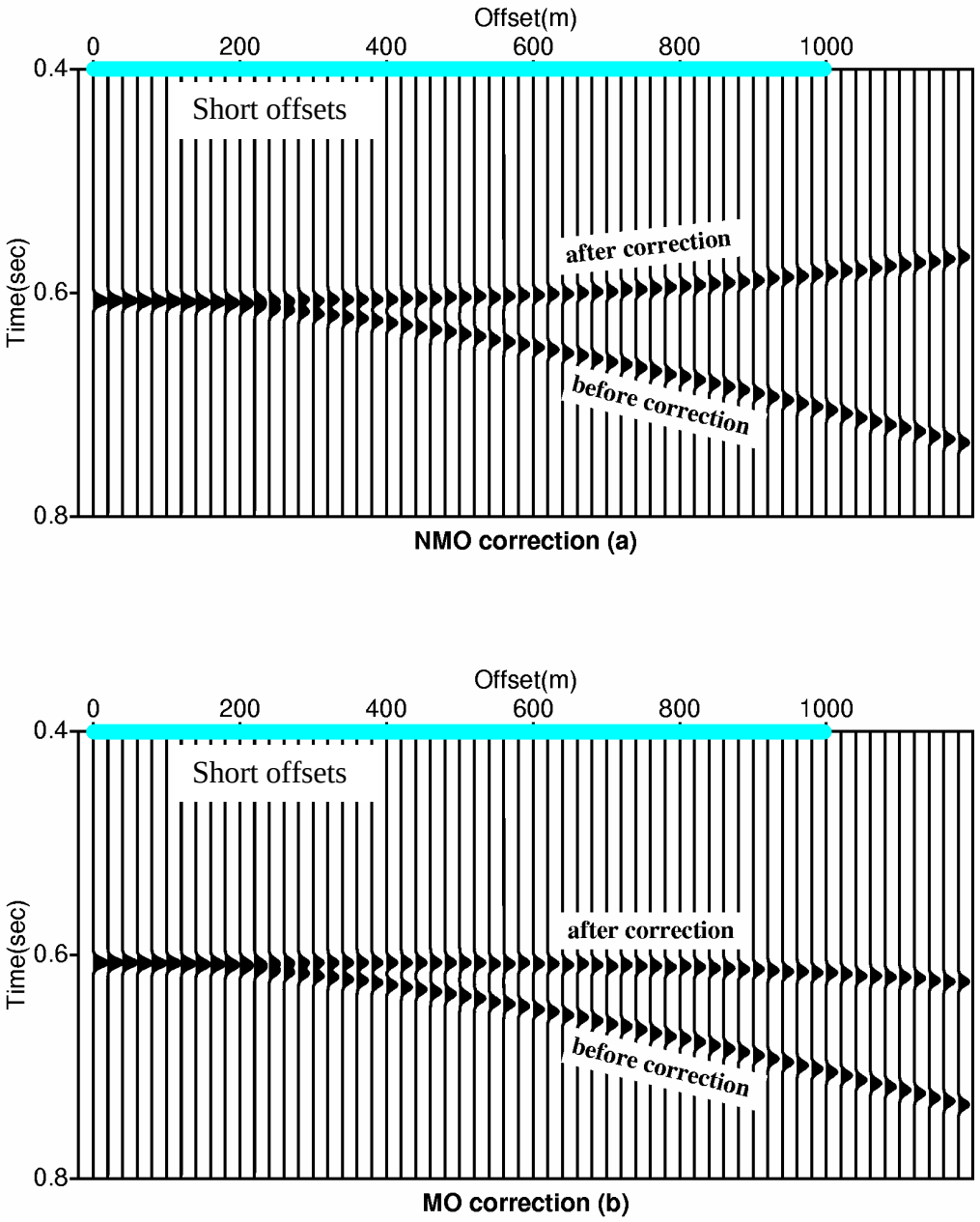

Figure 7.7 For Green River shale, correction of shot records using moveout velocity with (a) equation 7.2, and (b) equation 7.13. The depth of the reflector was arbitrarily chosen to be *1000 m*, and offset *x£ 1000 m* is within the range of "short offsets". It clearly shows that in this "worst case scenario", the use of equation 7.2 results in over-correction, while equation 7.13 gives good results within the short offset limit. For the offset range beyond "short offsets", equation 7.13 probably needs to be modified further by including higher order terms in the Taylor series expression to flatten the event.

Using the exact equations 7.1, 2.28 and 2.29, for different phase angles q, the corresponding offset x was calculated. The results for short offsets are shown in Figure 7.8. At short offsets, the phase angle will not exceed *30° » 0.52 radian* for these four representative materials. Thus, equations 7.7 — 7.9, and 7.13 can be used as approximations for short offsets.

From Figure 7.8, we can see that the same phase angle occurs at different short offsets for different sedimentary rocks. Thus, for different sedimentary rocks, the errors in the approximation, at the same offset, will be different. At the same short offset, for those rocks with a positive d value (Dog Creek shale and $TISO_2$), the phase angle is smaller than that for those rocks with negative d values (Green River shale and Taylor sandstone). This explains why we need to pay more attention to those rocks with a negative d value, when using Thomsen's NMO equation 7.2 at short offsets.

7.4 Discussions and Conclusions

The equations 7.7, 7.8, and 7.13 for the P-wave phase velocity v_p, ray velocity v_g and moveout velocity v_{mo} were derived as functions of ray angle f, for offsets less than or equal to the depth of the reflector. So was equation 3.9, the relationship between the phase angle q and the ray angle f. The expressions for phase velocity, ray velocity and moveout velocity give us an intuitive understanding of the behaviour of P-wave propagation at short offsets. The value of the anisotropic parameter d is the major factor controlling this behaviour.

For selected anisotropic sedimentary rocks, the results from equations 7.7 — 7.9 and equation 7.13 were numerically compared to their values from exact equations, and v_{mo} from equation 7.13 was also compared to v_{nmo} from equation 7.2. The numerical results show that Thomsen's NMO equation may be used at short offsets for most sedimentary rocks. But for those rocks with negative values of d, especially with a large negative value, significant errors may occur. The above results were also demonstrated by the experimental results from Okoye et al. (1998). Thus, there is a need to consider the significance of these errors on the formation of seismic images.

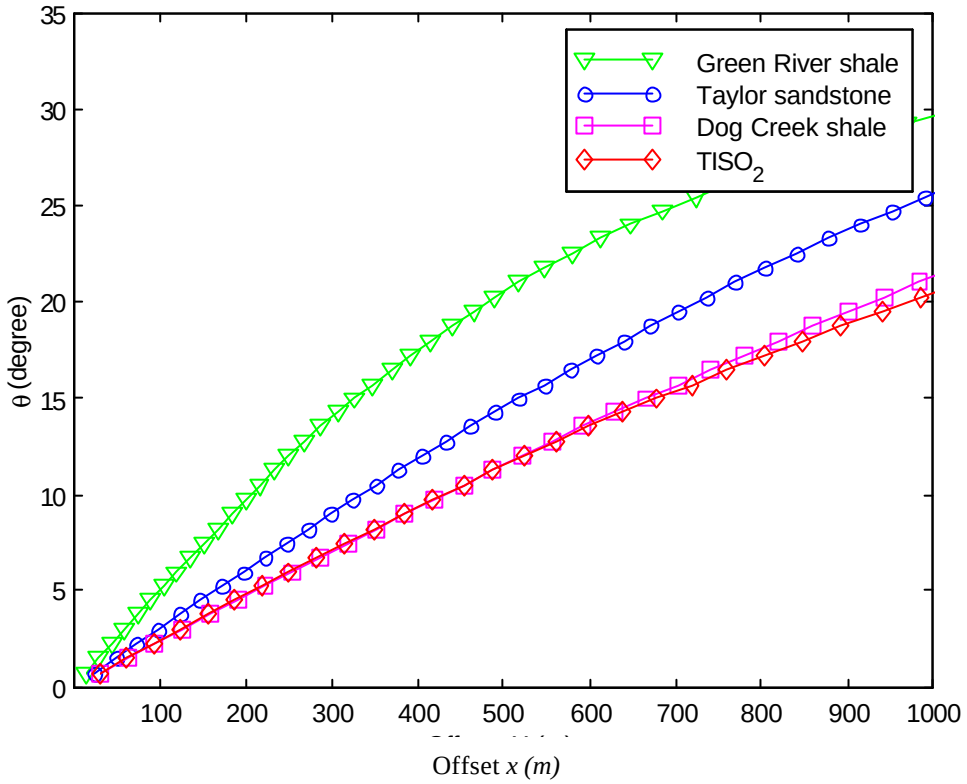

Figure 7.8 The corresponding phase angles q at different short offsets, for different sedimentary rocks and $TISO_2$ medium. The depth of the reflector was arbitrarily chosen to be *1000 m*, and x is the source-receiver offset. $x \pounds$ *1000 m* is within the range of "short offsets".

When dealing with sedimentary rocks, which have negative values of d, equation 7.13 will be a good approximation to the exact equation at short offsets.

Equation 7.2 has been used to estimate the short offset P-wave NMO velocity for field data (Alkhalifah et al., 1996; and Ball, 1995). The equation worked very well for those rocks with positive values of d. For rocks with a negative value d, equation 7.13 should be used.

It needs to be emphasised that equations 7.7 — 7.9 and equation 7.13 are valid at short offsets. When the offset x is greater than the reflector depth, further study is needed. Possibly, the equations may be modified to include the contribution of the higher order terms in $f^n (n \geq 4)$, or else some other approach entirely is needed (Zhang, personal communication).

CHAPTER 8

CONCLUSIONS AND RECOMMENDATIONS

8.1 Conclusions

The research in this thesis was directed at the development of new inversion techniques for the elastic parameters that quantify the degree of velocity anisotropy in multi-layered transversely isotropic media.

One major contribution of this research is a greater understanding of the apparent velocity fields of layered structures with thick components. A multi-layered Earth composed of transversely isotropic media and/or isotropic media behaves like a single-layered transversely isotropic medium except for rays travelling in near horizontal directions. Since a field survey normally lies within the offset range of less than twice the layer depth, the above statement is applicable to both reflection and VSP field surveys. For a thick layered model composed of transversely isotropic media or isotropic media, apparent elastic parameters *will not* be those thickness-weighted average values of elastic parameters of individual components, as stated for thin layers by Helbig and Schoenberg (1987). These elastic parameters can, however, be recovered by the inversion methods developed in this thesis.

Another important contribution is the development of inversion methods for apparent elastic parameters. The inversion programs developed recovered elastic parameters from the velocity fields obtained by VSP surveys. They were found to be robust and can be applied to field data with random noise. They have been successfully used on data from numerical simulation experiments, physical modelling experiments, and real field survey data. Especially, the inversion programs can recover parameters for P, SV, and SH-waves jointly, as well as the tilt angle of a symmetry axis. This feature, using data from all wave modes with an appropriate model, was

demonstrated to provide more accurate estimates for elastic parameters than from P-wave data alone.

The inversion programs for interval parameter recovery were developed based on a two-layered model. The velocity field of a layer of interest is hard to measure directly through field surveys. However, we can locate geophones on the upper and lower surface of the interval layer in question. The combined apparent velocity fields to the upper and lower subsurfaces of this interval layer may then be obtained. Using the developed inversion programs, the elastic parameters and the velocity fields for the interval layer of interest can be efficiently determined from these. The inversion programs provide a useful tool in understanding the anisotropic properties of a layer of interest from walkaway VSP surveys. It is noticed that a layer of interest may show some degree of local heterogeneity, but the inversion program may still be applied to find a representative result. The inversion result is regarded as the apparent or average properties for this interval layer.

The *"chi-by-eye"* test was used to judge the final acceptability of inversion results. If the measured field and that computed from the recovered parameters agree visually, the recovered parameters were accepted as suitable estimates.

System errors in physical modelling experiments have also been examined. It was shown that the size of source and receiver transducers should be far smaller than the thickness of the models used. When large transducers are used in laboratory experiments, the offset correction method developed in this thesis can be introduced to decrease measurement errors. An accurate measurement enables the inversion methods to provide more accurate estimates of elastic parameters for experimental models.

The recovered elastic parameters can then be used to study the anisotropic effect on the moveout velocity. Thomsen's NMO equation may be used at short offsets for most sedimentary rocks. But for those rocks with negative values of d, especially with a *large* negative value, significant errors will be introduced. A new analytical equation for moveout velocity at short offsets has been derived which is more accurate than the widely used Thomsen's NMO equation.

The inversion methods developed in this thesis are based on the exact wave propagation equations for transversely isotropic media. Because of the complexity of subsurface rocks, they may or may not behave like transversely isotropic media. It is important to be aware of the possible influence of lateral inhomogeneities before one runs the inversion programs.

The basis of the inversion programs developed here was the assumption of transverse isotropy and finding best-fit parameters to make a close agreement between the observations and the calculated data. Observations are normally not absolutely accurate but subject to measurement errors. So the TI assumption may not exactly fit the observations, and the key issue is:

Is the TI assumption correct for observations or not?

To answer this question in this research, the observations were compared with those calculated from the recovered parameters to see if they were acceptable. Coincidence indicates that the rock property can be described as a transversely isotropic medium with the recovered parameters. If there is a big difference, it may indicate that the assumption of transverse isotropy was not suitable for the structure from which the data were derived.

It is possible that the inversion programs developed in this thesis may fail to converge to a solution because the rock property is not faithfully represented by a transversely isotropic medium. Since the inversion problems in this research are non-linear, it is not unusual that the initial input guesses may affect the inversion result, and an unreasonable solution may be obtained consequently from the inversion programs. The important thing is to find the most reasonable solution, for which the calculated data using the recovered parameters *does* agree with the observations. The "*chi-by-eye*" approach is the final test.

8.2 Recommendations

My inversion techniques for transversely isotropic media could also be adapted for orthorhombic anisotropy. By applying inversion programs to multi-azimuth surveys

within three symmetry planes, the stiffness of rocks (Cheadle et al., 1991) may be recovered.

The inversion method for apparent elastic parameters of a TTI medium is limited in this thesis to a 2-D case, with a dip line survey. However, the inversion method may be developed to 3-D cases with further research. This is beyond the scope of my research as stated in Chapter 1.

For marine walkaway VSP surveys, the effect of water needs further study. Because of the large velocity differences between water and the rocks below, the recovered parameters for the rocks will be affected by the water above them. Further modification to my inversion programs may be necessary to exclude the water effect and carry out inversion from the velocity field of subsea rocks.

REFERENCES

Achenbach, J. D., 1973, Wave propagation in elastic solids: North-Holland Publishing Co.

Alkhalifah, T. and Tsvankin, I., 1995, Velocity analysis for transversely isotropic media: Geophysics, **60**, 1550-1566.

Alkhalifah, T., Tsvankin, I., Larner, K., and Toldi, J., 1996,Velocity analysis and imaging in transversely isotropic media: methodology and a case study: The Leading Edge, **15**, 371-378.

Alkhalifah, T., 1997, Velocity analysis using non-hyperbolic moveout in transversely isotropic media: Geophysics, **62,** 1839-1854.

Backus, G. E., 1962, Long-wave elastic anisotropy produced by horizontal layering: Journal of Geophysical Research, **67**, 4427-4440.

Ball, G., 1995, Estimation of anisotropy and anisotropic 3-D prestack depth migration, offshore Zaire: Geophysics, **60,** 1495-1513.

Banik, N. C., 1984, Velocity anisotropy of shales and depth estimation in the North Sea basin: Geophysics, **49**, 1411-1419.

Berryman, J. G., 1979, Long-wave elastic anisotropy in transversely isotropic media: Geophysics, **44**, 896-917.

Bevington, P. R., 1969, Data reduction and error analysis for the physical sciences: McGraw-Hill, New York.

Caldwell, J., 1999, Marine multicomponent seismology: The Leading Edge, **18**, 1274-1282.

Cheadle, S. P., Brown, R. J. and Lawton, D. C., 1991, Orthorhombic anisotropy: A physical seismic modeling study: Geophysics, **56**, 1603-1613.

Crampin, S., and Radovich, B. J., 1982, Interpretation of sythetic common-depth-point gathers for a single anisotropic layer: Geophysics, **47**, 323-335.

Crampin, S., Chesnokov, E. M., and Hipkin, R. A., 1984, Seismic anisotropy — the state of the art: First Break, **02**, 9-18.

Crampin, S., 1986, Anisotropy and transverse isotropy: Geophysical. Prospecting, **34,** 94-99.

Dellinger, J., and Vernik, L., 1994, Do traveltimes in pulse-transmission experiments yield anisotropic group or phase velocities?: Geophysics, **59**, 1774-1779.

Ebrom, D. and Sheriff, R. E., 1992, Anisotropy and reservoir development, *in* Sheriff, R. E., Ed., Reservoir geophysics: Soc. of Expl. Geophys., 355-361.

Ensley, R. A., 1989, Analysis of compressional- and shear-wave seismic data from the Prudhoe Bay Field: The Leading Edge, **8**, 10-13.

Geoltrain, S., 1988, Propagation of elastic waves in transversely isotropic media: CPW-074R, Center for Wave Phenomena, Colorado School of Mines.

Gottfried, B. S. and Weisman, J., 1973, Introduction to optimization theory: Prentice-Hall Inc.

Grechka, V., Tsvankin, I. and Cohen, J. K., 1999, Generalized Dix equation and analytic treatment of normal-moveout velocity for anisotropic media: Geophysical Prospecting, **47,** 117-148.

Gyngell, N., 1999, Determination of the average and interval elastic parameters in multi-layered transversely isotropic media: Physical modelling approach: M.Sc. thesis, Curtin University of Technology.

Helbig, K., 1984, Transverse isotropy in exploration seismics: Geophys. J. R. Astr. Soc. **76**, 79-88.

Helbig, K., and Schoenberg, M., 1987, Anomalous polarization of elastic waves in transversely isotropic media: J. of the Acoustical Society of America, **81**, 1235-1245.

Helbig, K., 1994, Foundations of anisotropy for exploration seismics: Pergamon.

Horne, S. and Leaney, S., 2000, Polarization and slowness component inversion for TI anisotropy: Geophysical Prospecting, **48,** 779-788.

Hsu, K., Schoenberg, M. and Walsh, J. J., 1991, Anisotropy from polarization and moveout: 61st Ann. Internat. Mtg., Soc. of Expl. Geophys., 1526-1529.

IRIS PASSCAL Instrument Center, 2002, SEG Y FORMAT [online]: from http://www.passcal.nmt.edu/NMT_pages/Software/segy.html.

Jakobsen, M., and Johansen, T. A., 2000, Anisotropic approximations for mudrocks: a seismic laboratory study: Geophysics, **65**, 1711-1725.

Jolly, R. N., 1956, Investigation of shear waves: Geophysics: **21**, 905-938.

Jones, E. A., and Wang, H. F., 1981, Ultrasonic velocities in Cretaceous shales from the Williston Basin: Geophysics, **21** 905-938.

Kebaili, A., Le, L. H. and Schmitt, D. R., 1996, Slowness surface determination from slant stack curves, *in* Rathore, J. S., Ed., Seismic anisotropy: Soc. of Expl. Geophys., 518-555.

Larner, K. and Cohen, J. K., 1993, Migration error in transversely isotropic media with linear velocity variation in depth: Geophysics, **58,** 1454-1467.

Levin, F. K., 1978, The reflection, refraction, and diffraction of waves in media with elliptical velocity dependence: Geophysics, **43**, 528-537.

Levin, F. K., 1979, Seismic velocities in transversely isotropic media: Geophysics, **44**, 918-936.

Levin, F. K., 1990, Reflection from a dipping plane — transversely isotropic solid: Geophysics, **55**, 851-855.

Li, R., Okoye P. and Uren N., 1997, Inversion of velocity field and anisotropic elastic parameters for layered transversely isotropic media with a vertical symmetric axis: Internal Report, SPS 694/1997/EG 76, Curtin University of Technology.

Li, R., Okoye P., Uren N. and McDonald J. A., 1998a, Analytic study of the short-spread moveout velocity estimation in a transversely isotropic medium: 68th SEG Annual Internal. Mtg., Expanded Abstracts, **98**, 1472-1474 (2 pages missing in printed volume).

Li, R., Okoye P. and Uren N., 1998b, Inversion of velocity field and anisotropic elastic parameters for layered VTI media: Exploration Geophysics, **29**, 477-483.

Li, R., Uren N., and Okoye P., 1999, Inversion Techniques for transverse isotropy using P, SV, and SH-wave first break picks: Internal Report, SPS 709/1999/EG 79, Curtin University of Technology.

Li, R., and Okoye P., 1999, Preliminary report on the recovery of elastic parameters from Woodside VSP walkaway survey: unpublished confidential report for Woodside Ltd.

Li, R., Okoye P. and Uren N., 2000a, A study of the effects of transducer size on physical modeling experiments for recovering anisotropic elastic parameters: Geophysical Research Letters, **27**, 3643-3646.

Li, R., Okoye P. and Uren N., 2000b, Inversion techniques for P-wave anisotropic parameters from VSP surveys: 70th Ann. Internat. Mtg., Soc. of Expl. Geophys., 1739-1742.

Li, R., Okoye P. and Uren N., 2000c, Inversion technique for transverse isotropy with a tilted symmetry axis: Exploration Geophysics, **31**, 337-342.

Li, R., Okoye P. and Uren N., 2000d, The effects of transducer size on recovered anisotropic parameters in physical modelling laboratory: Internal report, SPS 712/2000/EG 80, Curtin University of Technology.

Lo, T. W., Coyner, K. B., and Toksöz, M. N., 1986, Experimental determination of elastic anisotropy of Berea Sandstone, Chicopee Shale, and Chelmsford Granite: Geophysics, **51**, 164-171.

Love, A. E. H., 1927, A treatise on the mathematical theory of elasticity: Cambridge Press.

Menke, W., 1989, Geophysical data analysis: discrete inverse theory: Academic Press.

Musgrave, M. J. P., 1970, Crystal acoustics: introduction to the study of elastic waves and vibrations in crystals: Holden-Day.

Nguyen, T., 2000, The recovery of anisotropic elastic parameters for rock properties from 3-component multi-offset VSP: B.Sc. thesis (Hons), Curtin University of Technology.

Nye, J. F., 1993, Physical properties of crystals: their representation by tensors and matrices: Clarendon Press, Oxford.

Okoye, P. N., 1994, Seismic reflection process in anisotropic media: PhD dissertation, Department of Exploration Geophysics, Curtin University of Technology.

Okoye, P. N., and Uren, N. F., 1995, Influence of anisotropy on depth conversion: Minerals and Energy Research Institute of Western Australia (MERIWA), Report No. 152.

Okoye, P. N., Zhao, P. and Uren, N. F., 1996, Inversion technique for recovering the elastic constants of transversely isotropic materials: Geophysics, **61,** 1247-1257.

Okoye, P., Walton, C. and Uren, N., 1997, Recovery of elastic parameters in multi-layered transversely isotropic media: 67th Ann. Internat. Mtg., Soc. of Expl. Geophys., 1689-1692.

Okoye, P. N., Uren, N. F. and McDonald, J. A., 1998, Accuracy and limitations of the near-offset P-wave NMO velocity estimation in transversely isotropic media: 13th Ann. Internat. Mtg., Austr. Soc. Expl. Geophys., **29,** 550-553.

Panametrics Inc., 1999, Ultrasonic transducers [online]: from http://www.panametrics.com, USA.

Peyrière, J., 1998, Laboratory analysis of anisotropy on models of horizontal layered sub-surface: M.Sc. thesis, Curtin University of Technology.

Postma, G. W., 1955, Wave propagation in a stratified medium: Geophysics, **20**, 780-906.

Press, W. H., Teulolsky, S. A., Vetterling, W. T., and Flannery, B. P., 1992a, Numerical Recipes in C: The Art of Scientific Computing: Second Edition, Cambridge University Press, Cambridge, 1992

Press, W. H., Teulolsky, S. A., Vetterling, W. T., and Flannery, B. P., 1992b, Numerical Recipes in Fortran: The Art of Scientific Computing: Second Edition, Cambridge University Press, Cambridge, 1992.

Scales, J. A. and Snieder, R., 2000, The Anatomy of Inverse Problems: Geophysics, **65,** 1708-1710.

Schoenberg, M., 1994, Transversely isotropic media equivalent to thin isotropic layers: Geophysical Prospecting, **42,** 885-915.

Sheriff, R. E., 1991, Encyclopedic Dictionary of Exploration Geophysics: Soc. of Expl. Geophys., USA.

Stockwell, J. W., Cohen, J., and Cohen, J. K., 1998, The *New* SU User's Manual [online]: from http://www.cwp.mines.edu/sututor/sututor.html, Center for Wave Phenomena, the Colorado School of Mines.

Tarantola, A., 1987, Inverse problem theory — methods for data fitting and model parameter estimation: Elsevier.

Thomsen, L., 1986, Weak elastic anisotropy: Geophysics, **51**, 1954-1966.

Thomsen, L., 1993, Weak anisotropic reflections, *in* Backus, M. M., Ed., Offset-dependent reflectivity - theory and practice of AVO analysis: Soc. of Expl. Geophys., 103-111.

Tsvankin, I., and Thomsen, L., 1994, Nonhyperbolic reflection moveout in anisotropic media: Geophysics, **59**, 1290-1304.

Tsvankin, I. and Thomsen, L., 1995, Inversion of reflection traveltimes for transverse isotropy: Geophysics, **60,** 1095-1107.

Tsvankin, I., 1996, P-wave signatures and notation for transversely isotropic media: An overview: Geophysics, **61**, 467-483.

Tsvankin, I., 1997, Reflection moveout and parameter estimation for horizontal transverse isotropy: Geophysics, **62,** 614-629.

Uren, N. F., 1989, Processing of seismic data in the presence of elliptical anisotropy: PhD dissertation, Department of Geosciences, University of Houston, Texas.

Uren, N. F., Gardner, G. H. F., and McDonald, J. A., 1990a, Dip moveout in anisotropic media: Geophysics, **55**, 863-867.

Uren, N. F., Gardner, G. H. F., and McDonald, J. A., 1990b, Normal moveout in anisotropic media: Geophysics, **55**, 1634-1636.

Uren, N. F., Gardner, G. H. F., and McDonald, J. A., 1991, Anisotropic wave propagation and zero-offset migration: Exploration Geophysics, **22**, 405-410.

Urosevic, M., 1985, Some effects of an anisotropic medium on P and SV waves: A physical modelling study: M.Sc. thesis, University of Houston, USA.

Urosevic, M., 2000, A study of seismic wave propagation as applied to seismic imaging in the southern Sydney basin: PhD dissertation, Department of Exploration Geophysics, Curtin University of Technology.

Vernik, L., and Nur, A., 1992, Ultrasonic velocity and anisotropy of hydrocarbon source-rocks: Geophysics, **57**, 727-735.

Vestrum, R. W., 1994, Group- and Phase-velocity inversion for the general anisotropic stiffness tensor: M.Sc. thesis, Univ. of Calgary.

Walton, C., 1996, Recovering the elastic parameters of multi-layered transversely isotropic media: B.Sc (Hons) thesis, Department of Exploration Geophysics, Curtin University of Technology.

White, J. E., 1965, Seismic waves: radiation, transmission, and attenuation: McGraw-Hill, N.Y.

Winterstein, D. F., 1990, Velocity anisotropy terminology for geophysicists: Geophysics, **55**, 1070-1088.

Appendix A

Explicit Expressions for Phase Velocity, Ray velocity and Ray Angle at Small Phase Angles

In a transversely isotropic medium with a vertical symmetry axis (VTI), seismic wave propagation can be described using equations 7.1, 2.28 and 2.29. At a small phase angle q, the phase velocity, ray velocity and ray angle can be expressed as functions of phase angle q, in terms of a Taylor series expansion to the third order in q. Thus, at a small offset or a small ray angle f, the phase and ray velocities can be described as explicit approximations.

For the convenience of derivations, the following substitutions were made:

$$
\begin{aligned}
X &= (1+\frac{2e}{f}\sin^2 q)^2 - 2\frac{e-d}{f}\sin^2 2q, \\
P &= 1+e\sin^2 q - \frac{f}{2} + \frac{f}{2}\sqrt{X}, \\
L &= \frac{d(P)}{dq} = e\sin(2q) + \frac{1}{\sqrt{X}}\left((1+\frac{2e}{f}\sin^2 q)e\cdot\sin(2q) - (e-d)\sin(4q)\right).
\end{aligned}
\tag{A-1}
$$

For small values of q, using a Taylor series expansion to the third order in q, then we have:

$$
\begin{aligned}
X &= 1+\frac{4}{f}(2d-e)q^2 - \frac{4}{3f}(8d-7e-3\frac{e^2}{f})q^4 + O(q^6), \\
P &= 1+2dq^2 - \frac{2}{3}\left(4d-3e-\frac{6d}{f}(e-d)\right)q^4 + O(q^6), \\
L &= \frac{d(P)}{dq} = 4dq - \frac{8}{3}\left(4d-3e-\frac{6d}{f}(e-d)\right)q^3 + O(q^5).
\end{aligned}
\tag{A-2}
$$

Thus, from equation 7.1, there have

$$
\frac{v_p^2}{a_0^2} = P = 1+2dq^2 + \left(-\frac{8}{3}d+2e+\frac{4d}{f}(e-d)\right)q^4 + O(q^6). \tag{A-3}
$$

The phase velocity at small phase angles then can be represented as:

$$\frac{v_p}{a_0} = 1 + dq^2 + \left(-\frac{d^2}{2} - \frac{4d}{3} + e + \frac{2d}{f}(e-d) \right) q^4 + O(q^6). \tag{A-4}$$

According to equation 2.28, the ray velocity can be derived using

$$\begin{aligned} \frac{v_g^2}{a_0^2} &= \frac{v_p^2}{a_0^2} + \frac{1}{4\frac{v_p^2}{a_0^2}} \left(\frac{d\left(\frac{v_p^2}{a_0^2}\right)}{dq} \right)^2 \\ &= 1 + 2d(1+2d)q^2 + \left((1+8d)\left(-\frac{8}{3}d + 2e + \frac{4d}{f}(e-d) \right) - 8d^3 \right) q^4 + O(q^6), \end{aligned} \tag{A-5}$$

and,

$$\begin{aligned} \frac{v_g}{a_0} &= 1 + d(1+2d)q^2 \\ &+ \left(-\frac{4}{3}d + e - \frac{67}{6}d^2 + 8de - 6d^3 - 2d^4 + \frac{2d}{f}(e-d)(1+8d) \right) q^4 + O(q^6). \end{aligned} \tag{A-6}$$

For small values of the phase angle q, the ray angle f, given by equation 2.29, can be written as:

$$\begin{aligned} f &= q + \tan^{-1}\left(\frac{L}{2P} \right) \\ &= (1+2d)q + \left(-\frac{16}{3}d - 4d^2 - \frac{8}{3}d^3 + 4e + \frac{8d}{f}(e-d) \right) q^3 + O(q^5). \end{aligned} \tag{A-7}$$

Squaring both side of the above equation,

$$f^2 = (1+2d)^2 q^2 + 2(1+2d)\left(-\frac{16}{3}d - 4d^2 - \frac{8}{3}d^3 + 4e + \frac{8d}{f}(e-d) \right) q^4 + O(q^5). \tag{A-8}$$

Ignoring the higher order terms in $q^n (n > 3)$, then have the expression of q in terms of f:

$$q^2 = \frac{1}{(1+2d)^2} f^2 + O(q^4). \tag{A-9}$$

Thus, for small values of q, using a Taylor series expansion to the third order in q, the phase velocity, ray velocity takes the following forms:

$$\frac{v_p(f)}{a_0} = 1 + \frac{d}{(1+2d)^2} f^2 + O(q^4), \tag{A-10}$$

$$\frac{v_g}{a_0} = 1 + \frac{d}{(1+2d)} f^2 + O(q^4). \tag{A-11}$$

Appendix B

Curvature of t^2 *vs* x^2 Plots and Moveout Velocity for Small Ray Angles

For a transversely isotropic medium with a vertical symmetry axis (VTI), the t^2 *vs* x^2 plot may lose its straight-line character. The moveout velocity may not be a constant, but a function of offset. Using equation 24 in Thomsen's paper (Thomsen, 1986) and equation 7.12, we may calculate the exact values of the curvature of t^2 *vs* x^2 plots and moveout velocity for a small phase angle q. However, for a small offset or a small ray angle, explicit expressions for the curvature of the t^2 *vs* x^2 plots and moveout velocity cannot be obtained. In this appendix, the approximations to the curvature of the t^2 *vs* x^2 plots and moveout velocity at small ray angles will be derived using Taylor's series expansions.

According to equation 24 in Thomsen's paper (Thomsen, 1986), we have:

$$\begin{aligned}\frac{d(t^2)}{d(x^2)} &= \frac{1}{v_g^2}\left(1-\frac{2\cos^2 f}{v_g}\frac{dv_g/dq}{\sin(2f)df/dq}\right)\\ &= \frac{1}{v_g^2}\left(1-\frac{\cos^2 f}{v_g^2}\frac{dv_g^2/dq}{\sin(2f)df/dq}\right)\end{aligned} \tag{B-1}$$

From equations A-7 and A-5, we have:

$$
\begin{aligned}
\cos^2 f &= 1-(1+2d)^2 q^2 \\
&\quad -\frac{1}{3}(1+2d)\left(-1-38d-36d^2-24d^3+24e+\frac{48}{f}d(e-d)\right)q^4+O(q^6), \\
\sin(2f) &= 2(1+2d)q \\
&\quad +\left(-\frac{4}{3}+8e-\frac{56}{3}d-24d^2-16d^3+\frac{16}{f}d(e-d)\right)q^3+O(q^5), \\
\frac{df}{dq} &= (1+2d) \\
&\quad +\left(-16d-12d^2-8d^3+12e+\frac{24}{f}d(e-d)\right)q^2+O(q^4), \\
\frac{1}{a_0^2}\frac{dv_g^2}{dq} &= 4d(1+2d)q \\
&\quad +4\left((1+8d)(-\frac{8}{3}d+2e+\frac{4}{f}d(e-d))-8d^3\right)q^3+O(q^5).
\end{aligned}
\tag{B-2}
$$

Insert equations A-5, B-2 into equation B-1, using a Taylor's series expansion to the third order of q. The tangent to the reflection moveout curve for short offsets is then obtained as:

$$
\frac{d(t^2)}{d(x^2)} = \frac{1}{(1+2d)a_0^2} - \frac{4}{(1+2d)^2 a_0^2}(e-d)(1+\frac{2d}{f})q^2+O(q^4). \tag{B-3}
$$

If we substitute f for q, using equation A-9, equation B-3 can be re-written as:

$$
\frac{d(t^2)}{d(x^2)} = \frac{1}{(1+2d)a_0^2}\left(1-\frac{4}{(1+2d)^3}(e-d)(1+\frac{2d}{f})f^2\right)+O(q^4). \tag{B-4}
$$

According to the definition of moveout velocity (equation 7.11), for the case of a horizontal reflector in a VTI medium, $v_{mo}(f)$ is not a constant, and can be re-written as (shown in Figure 7.1):

$$
v_{mo}^2 = \frac{x^2}{t_x^2 - t_0^2} = \frac{(2z\tan f)^2}{\left(\frac{2z}{\cos f \cdot v_g}\right)^2 - \left(\frac{2z}{a_0}\right)^2}, \tag{B-5}
$$

where, z is the depth of the reflector. Then, the exact moveout velocity expression at offset x is:

$$
v_{mo} = \frac{v_g \sin f}{\sqrt{1-\frac{v_g^2}{a_0^2}\cos^2 f}}. \tag{B-6}
$$

When $x = 0$, $f = 0$, we must evaluate equations B-5 and B-6 as:

$$v_{mo}^2 = \lim_{x \to 0} \frac{x^2}{t_x^2 - t_0^2}, \tag{B-7}$$

$$v_{mo} = \lim_{x \to 0} \frac{v_g \sin f}{\sqrt{1 - \frac{v_g^2}{a_0^2} \cos^2 f}}. \tag{B-8}$$

From equation A-7, we have:

$$\sin f = (1 + 2d)q + \left(-\frac{1}{6} - \frac{19}{3}d - 6d^2 - 4d^3 + 4e + \frac{8}{f}d(e - d) \right) q^3 + O(q^5). \tag{B-9}$$

Using equations A-6, B-9, and B-2, then we have:

$$\frac{v_g}{a_0} \sin f = (1 + 2d)q + \left(-\frac{1}{6} - \frac{16}{3}d - 2d^2 + 4e + \frac{8}{f}d(e - d) \right) q^3 + O(q^5),$$

$$\left(\frac{v_g}{a_0} \right)^2 \cos^2 f = 1 - (1 + 2d)q^2 + \left(\frac{1}{3} + \frac{26}{3}d + 4d^2 - 6e - \frac{12}{f}d(e - d) \right) q^4 + O(q^6). \tag{B-10}$$

Thus, the moveout velocity v_{mo} approximation at small phase angles may be stated as follows:

$$v_{mo} = \sqrt{1 + 2d}\, a_0 \left(1 + \frac{(e - d)\left(1 + \frac{2d}{f}\right)}{1 + 2d} q^2 \right) + O(q^4). \tag{B-11}$$

It can also be expressed as a function of f in terms of equation A-9:

$$v_{mo} = \sqrt{1 + 2d}\, a_0 \left(1 + \frac{(e - d)\left(1 + \frac{2d}{f}\right)}{(1 + 2d)^3} f^2 \right) + O(q^4). \tag{B-12}$$

Appendix C

List of the Main Programs Developed in This Research

Computer programs were written by the author to carry out this research. Major programs and their functions are described here for the reader's convenient reference. All programs are held in the Department of Exploration Geophysics, Curtin University of Technology.

Program 1 twophiv.f:

Calculation of the P-wave ray velocity field for a two-layered isotropic or VTI model.

Program 2 phase_ray_path.m

Program to plot the phase and ray velocity fields of P, SV, and SH-waves for a transversely isotropic medium.

Program 3 slow_pola.m

Program to plot the slowness surfaces and polarization vectors of P, SV, and SH-waves for a transversely isotropic medium.

Program 4 sumoveout.c

Calculation of the reflection traveltime for a VTI medium. It also processes moveout correction(NMO, MO), and records the data.

Program 5 parameter.c

Recovery of five elastic parameters a_0, b_0, e, d, g and tilt angle y from the observed velocity fields of P, SV, and SH-waves.

Program 6 interval.c

Recovery of the interval elastic parameters e, d, g of the second layer of a two-layered model. The velocity fields from P, SV, and SH-wave first break times through this two-layered model are required input. The overall elastic parameters and the first layer's parameters need to be known.

Program 7 twoforward.c

Calculation of P, SV, and SH-wave velocity fields for a two-layered isotropic or VTI model. It includes negative offsets. Random noise may be added to the travel times by the program.

Program 8 vspvti_size.c

Calculation of the VSP travel times of transmitted rays in a VTI medium. It simulates physical modelling experiments with larger transducers.

Program 9 datatops

Script file to translate binary data to SU data, and produce a postscript file.

Program 10 invps.m

Matlab program to display inversion results. The plots show the velocity field from observations and that calculated from the inversion results.